Transverse Laser Cooling of Calcium Monohydride Molecules

Sebastián Francisco Vázquez-Carson

Submitted in partial fulfillment of the
requirements for the degree of
Doctor of Philosophy
under the Executive Committee
of the Graduate School of Arts and Sciences

COLUMBIA UNIVERSITY

2022

Abstract

Transverse Laser Cooling of Calcium Monohydride Molecules

Sebastián Francisco Vázquez-Carson

In this thesis, I demonstrate Doppler and Sisyphus cooling of a cryogenic buffer-gas beam of CaH molecules. I detail the construction and optimization of the experimental apparatus, including the cryogenic source, laser systems, vacuum systems and detection schemes. I demonstrate that the cryogenic source produces a bright and slow beam of CaH molecules via ablation of a solid chemical target and thermalization with a He buffer gas. The molecular beam exits the ablation cell with an average forward velocity of 250 $\pm$ 200 m/s and a molecular beam flux per ablation pulse of $\approx 1 \times 10^{10}$ per steradian per pulse. I present the spectroscopic determination of the molecular transitions necessary to pursue laser cooling. These include the $X^2\Sigma^+ \rightarrow A^2\Pi_{1/2}$ and the $X^2\Sigma^+ \rightarrow B^2\Sigma^+$ transitions that each contain two spin-rotation states, $J = 1/2$ and $J = 3/2$, and a further pair of hyperfine states, $F = 0, 1$ and $F = 1, 2$, respectively. Finally, I describe the vibrational repumping transitions between the four hyperfine states of the $J = 1/2$ and $J = 3/2$ branches of the $V = 1$ vibrational state back to the ground state via decay from an intermediary state, $X^2\Sigma^+(V = 1) \rightarrow B^2\Sigma^+(V = 0) \rightarrow X^2\Sigma^+(V = 0)$. I present measurements of the vibrational decay probabilities from the $B^2\Sigma^+(V = 0)$ and $A^2\Pi_{1/2}(V = 0)$ excited states to the $V = 0, 1$ and 2 states of the ground $X^2\Sigma^+$ state. Next, I show that we can achieve a high scattering rate of $\approx 1.6 \times 10^6$ photons/second while cycling on the $X^2\Sigma^+ \rightarrow A^2\Pi_{1/2}$ transition. Finally, I demonstrate the ability to perform transverse cooling of a beam of CaH molecules through both the Doppler mechanism and magnetically assisted Sisyphus

mechanism. With the help of a transverse standing wave of laser light, I show that we are able to lower the molecular beam's transverse temperature from 12.2 ± 1.2 mK to 5.7 ± 1.1 mK. This thesis represents a promising start to laser slowing and magneto-optical trapping of CaH molecules, which could provide trapped ultracold samples of atomic hydrogen upon dissociation of the trapped CaH molecules.

Table of Contents

List of Figures

Acknowledgements

I would like to thank my parents that have always believed in me and given me the strength to continue through any adversity. I would never have come this far without you.

I would also like to thank my advisor Tanya Zelevinsky for supporting me during my transition from High Energy Nuclear physics to the wonderful world of Atomic, Molecular, and optical physics. She has been an inspirational teacher, allowing me to flourish under her guidance and mentorship.

I would like to thank everyone in the Zelevinsky lab for all their advice and help over the years — Rees McNally, Ivan Kozyrev, Debayan Mitra, Qi Sun, Kon Leung, Jinyu Dai, Stan Kondov, and Konrad Wenz, all sources of innumerable lessons.

I would like to thank my thesis committee for their time, confidence and mentorship during the evolution my research.

I want to thank my friends — Bill, Ashley, and Purple for accompanying me on the often solitary road of research during Covid. I am grateful to have had your loyal friendship and support during the good and bad times.

Finally, I want to thank mi amor de mi vida, Naya. My biggest supporter, my therapist, my advocate, and my joy.

Chapter 1: A Molecular Path to Ultracold Hydrogen

Experimentalists throughout the ages have been in pursuit of knowledge regarding the laws of nature and how to manipulate matter for the advantage of mankind. Over the course of history, man has gained mastery of more and more complex technologies -from torches to lasers, from daVinci's flying machines to rockets. Scientists and engineers of antiquity applied their knowledge of the laws of nature to increasingly complex systems and these efforts have greatly improved the quality of human life. Scientists in the twentieth century unlocked the quantum power of the atom, a development that has propelled a new age of information; first through semiconductors and now through quantum information. Inspired by this long tradition, I decided to laser cool molecules and further develop a technology that may be of value to my fellow man. It is my hope that the knowledge I learn in the cooling of the two alkali-earth hydrides CaH and BaH can be put to use in future tests of fundamental physics, quantum information, or chemistry. In this chapter, I will begin by motivating why obtaining quantum control of molecules is necessary and will describe the likely impacts of this technology. I will describe in the following chapter, the relevant quantum structure of the molecules used for the research presented in my thesis. Next, I will demonstrate how the experimental apparatus I built takes advantage of this quantum structure to exchange momentum with molecules through optical cycling using a laser. I will go in detail regarding the molecular properties of CaH relevant to molecular laser cycling. I will show how I spectroscopically identified the transitions necessary for laser cooling. Finally, I will discuss how I used this knowledge to produce both Doppler and Sisyphus cooling in CaH molecules

1.1 Motivation for Cooling Alkali-Earth Hydrides

Modern physics and chemistry implements creative experimental protocols to probe and manipulate complex quantum objects such as atoms and molecules in order to investigate fundamental physics, realize the dream of quantum information, and study chemistry at ultracold temperatures. Atomic physicists have developed techniques using electric [1], magnetic [2], and optical [3] traps to isolate a growing array of molecular species, which include diatomic [4, 5, 6, 7, 8, 9], triatomic [10, 11, 12], and symmetric top molecules [13]. Cold molecules can be used as pristine quantum laboratories with access to electric and magnetic fields of extreme strength and impeccable precision. These unique qualities make molecular systems prime candidates to test fundamental physics and search for physics beyond the Standard Model [14, 15, 10]. Molecules also can provide tuneable long range interactions, which offer the ability to perform quantum logic and later the potential to store fragile qubit superpositions in a protected quantum state that can be selectively decoupled from other qubits [16, 17, 18, 19]. This would provide strong coupling with neighbors during gate operations while the molecules are in a polarized state. After completing the gate protocol, the molecular qubit can be put into an unpolarized state that protects information from environmental noise and nearby gate operations. Finally, precise quantum control of molecules will grant the ability to create or break molecular bonds at will. The potential merit of applying this technology to physical and organic chemistry will be immense as it would allow atom-by-atom engineering of increasingly complex compounds unattainable through thermodynamic channels.

1.1.1 Fundamental Physics

The Standard Model represents the total culmination of mankind's theories regarding the physical world. The Standard Model is so accurate in its representation of the universe that it can even predict physical structure to better than 10^{-13} [20, 21]. In spite of this precision, the Standard Model does not represent a complete description of the laws of nature due to its lack of a proven description of key phenomena such as dark matter, dark energy, or observed matter-antimatter

asymmetry. Cold molecule experiments are pushing the frontiers of precision measurement to test the Standard Model and are sensitive to certain SUSY theories or to time drifts in fundamental constants or discrete symmetry violations [22, 23, 24]. Up until this point in the history of physics, testing fundamental physics theories had been the privilege of high energy particle super-colliders; however, this approach has reached an asymptotic limit due to the exponential cost associated with linear improvements in sensitivity. On the other hand, ultracold atomic and molecular physics can take advantage of techniques like Ramsay spectroscopy of clock transitions to measure the internal energy structure of atoms to a previously unimaginable precision [25]. Molecules promise the capability to push this sensitivity and precision to all new limits. [26]

The research of this thesis provides the groundwork for the development of a machine capable of producing a trapped ultracold sample of hydrogen that can be used to set new limits on the proton radius, the fine structure constant, and the Rydberg constant. [27]

1.2 Fundamental Physics

1.2.1 Proton-Electron Mass Ratio

Different types of quantum transitions in molecules can be used to search for time variation in the fine structure constant and the proton electron mass ratio. Electronic transitions are sensitive to the exact value of the fine structure constant α, while rovibronic transitions can be used to test the proton-electron mass ratio μ.[27, 28, 29]

$$\frac{\Delta\mu}{\mu} \propto \frac{\Delta\alpha}{\alpha} \tag{1.1}$$

Due to the higher sensitivity of the proton-electron mass ratio to changes in the fundamental underlying physics, it is logical to begin our search for beyond the Standard Model physics by identifying molecules with structures sensitive to changes in the proton-electron mass ratio. Thus, we must consider how a measurement of the reduced mass will scale with respect to a stabilized frequency probe. The literature on the subject [30] derives this sensitivity scaling as:

$$\frac{\delta\mu}{\delta t}\frac{1}{\mu} = \frac{\delta\nu}{\nu}\frac{1}{K_\mu \Delta t} \tag{1.2}$$

Given that the frequency probe is stabilized to $\frac{\delta\nu}{\nu}$, then the sensitivity of the transition of the reduced mass will be given by K_μ

$$K_\mu = \frac{\mu}{E_e - E_g}\left(\frac{dE_e}{d\mu} - \frac{dE_g}{d\mu}\right) \tag{1.3}$$

This inverse dependence of $\frac{1}{E_e - E_g}$ leads one to the conclusion that molecules with nearly degenerate energy levels will provide the best sensitivity to variations in the proton-electron mass ratio. Highly symmetric diatomics and polyatomic molecules promise to be a fantastic candidate for one of these time variation searches [30, 31, 32, 33]. In particular, the rovibronic transitions of SF_6 have already been probed in a cryogenic supersonic beam to set a lower limit on the time variation rate of the proton electron mass ratio of $\approx 10^{-13}$ per year [34]. Meanwhile, deep space methanol lines have spectroscopically probed the time variation of $\frac{\Delta\mu}{\mu}$ back 7×10^{-9} years [35]. While ultracold laboratory samples of these molecular species do not provide the same window into the distant past of that astronomical spectroscopy provides, lab samples promise to reach an astounding level of precision vastly surpassing that of the best astronomical observations [36].

1.2.2 Violations of Fundamental Symmetries

The Standard Model posits that fundamental particles, such as electrons, exist as infinitesimal objects with a lack of volume and should not posses an Electric Dipole Moment (EDM). A measurement of a non-zero EDM would imply that the electron's charge is separated over a volume of space and prove that the electron has volume and perhaps internal structure. There exist many theories that allow for permanent electric dipole moments through high order virtual loop couplings [37, 38, 39]. These theories rely on discrete symmetry breaking in electro-weak forces acting on the electron [39]. There have been many searches using atoms [40, 41], diatomics [42, 43], and polyatomic molecules [42, 44, 45]; each successively pushing the exclusion bound for symmetry

violating exchanges well beyond the reach of the LHC, high into the TeV mass range [39]. These experiments leverage the extremely strong internal electric field of a polarizable molecule and then look for variations in electron or nuclear spin procession frequency about an externally applied electric field [37]. The accuracy of this frequency measurement will be described as a Poissonian process and the limit of the uncertainty in frequency will depend on the number of molecules N and the interrogation time of the measurement τ:

$$\Delta\omega = \frac{1}{\tau\sqrt{N}} \tag{1.4}$$

Experiments have been competing against each other to achieve the highest molecule flux and the longest experimental lifetime possible. Most of the AMO experimental approaches can be divided into two different techniques. The first is a trapped molecular ion sample within an optical lattice that achieves a very long lifetime but is limited by a the low number of trapped molecules [43]. The second technique consists of cryogenic molecular beam experiments that make up for a low interrogation time with high molecule number of up to 10^{10} molecules per steradian, a high repetition rate, and a long beam length [42, 46, 39, 47, 48].

The future of these experiments will likely utilize laser cooling and trapping to prepare samples of suitable molecules simultaneously providing a high number of molecules and the maximum interrogation time [10, 49]. At this time, the molecules that have been successfully trapped [50, 51, 6, 52, 7, 13] are paving the way for cooling the molecules more suitable for testing fundamental physics such as ThO [53]. All of the previously cooled and trapped molecules have in common, low masses and highly diagonal branching ratios, which have made extended optical cycling more approachable. These initial molecules serve to refine the cooling techniques that will be required to cool molecules more suitable for fundamental physics. CaH, as discussed in this thesis, represents a unique opportunity to test fundamental physics due to its ability to cycle thousands of photons and produce samples of ultracold hydrogen that can be trapped in a magneto-optical trap (MOT) [54].

1.2.3 Ultracold Hydrogen Spectroscopy

BaH and CaH, in particular, probe fundamental physics by providing a pathway to trapped samples of ultracold hydrogen, whose experimentally measured quantum structure can be compared to that predicted by the Standard Model. While it may seem like a lot of extra work to cool a molecule just to break it apart and keep the atomic hydrogen, the properties of hydrogen, such as its UV cycling transition wavelength and high recoil velocity, make direct laser cooling very challenging. Degenerate samples of hydrogen have previously been made in magnetic traps [55], but the large number of atoms used to evaporate the heat away leaves a very dense atomic sample. The high density guarantees that any measured transitions are broadened by collisions past the required sensitivity. Cryogenic beam experiments have set the spectroscopic limit on the $1S \rightarrow 2S$ transition to beyond 10^{-15} [56]. These beam experiments are, however limited by Doppler broadening arising from the relatively high temperature of the sample due to its high velocity.

Our experimental plan is to slow and trap a molecular hydride into a MOT and dissociate the molecules to isolate the sample and retain the hydrogen. The other experiment in the Zelevinsky group adiabatically photo-dissociates Sr dimers trapped in a magic wavelength optical lattice. This carefully chosen magic trap induces an identical light shift for the ground and excited states, making transitions insensitive to laser intensity fluctuations. By driving coherent transitions to the exact dissociation threshold, the quantum information of the grounds state is preserved after dissociation and the wavefunctions can be seen in the momentum of the Sr atoms as they drift apart. My experiment plans to apply this in-house expertise to photo-dissociate the molecule without adding extra energy to the hydrogen, ensuring the coldest hydrogen sample possible. The left-over hydrogen can then be placed in a magic wavelength trap, amenable to precise measurements of the transitions with Ramsay spectroscopy. Photo-dissociation will begin with molecules in thermal equilibrium. If dissociation is performed correctly, the atomic components of the molecule have the same temperature as the sample set by Boltzman's relation.'

$$T = \frac{M v_p^2}{2K_b} \tag{1.5}$$

This means that after breaking apart the molecule, the temperature of the alkali-earth metal and the hydrogen will scale by their fractional mass relative to the molecule as follows [57, 54] :

$$T_A = \frac{T_{AB}}{M_{AB}/M_A} \tag{1.6}$$

The inverse scaling on molecular mass implies that using the heaviest alkali-earth metal will ultimately provide the coldest sample of hydrogen. Barium is nearly 140 times heavier than hydrogen and thus could provide hydrogen at temperatures of hundreds of nanokelvin [54]. However, there is some subtlety in choosing the optimal alkali-earth metal because the increased mass of BaH coupled with the relatively long natural lifetime of 137 ns, lower the trap loading efficiency and trap depth. We discovered this significant obstacle after laser cooling a cryogenic buffer gas beam of BaH and decided we needed to try a new molecule. Calcium strikes a good compromise as it will still lower the hydrogen's temperature by an order of magnitude, but its much shorter natural lifetime 33ns and lower mass make it much easier to slow and trap [58].

The lessons learned from dissociating the molecular bonds will provide valuable insight into the techniques future generations of physicists could use to assemble and destroy molecules piece by piece. This could provide a mechanism by which physicists could prepare exotic molecules to study at ultracold temperature. This opens the door to the field of experimental quantum chemistry and will illuminate the transition from quantum physics to chemistry. Observing molecular collisions at an ultra-low temperature will allow experimentalists to watch chemistry take place atom by atom, bond by bond, ultimately allowing us to apply the precision of fundamental physics to the field of chemistry.

1.3 Quantum Chemistry

Classical chemical reaction barriers are characterized by Arrhenius' Law, which states that reactions become exponentially more likely as the thermal energy of the reactants approaches the chemical energy barrier called the activation energy

$$k(T) \propto \exp\left(-\frac{E_A}{k_B T}\right) \tag{1.7}$$

This classical picture leads one to believe that chemical reactions stop as one cools towards absolute zero. However, it has been demonstrated that molecules become sticky at these temperatures and chemistry still takes place. It is clear that as the deBroglie wavelength grows at low temperatures, quantum effects dominate their classical counter parts and chemistry takes place as a result of tunneling, entanglement and state-dependent collision cross sections [59, 60]. Recent studies have investigated the formation of long lived intermediary three and four body states that exist during the collisional phase of the chemical reaction [61]. In classical chemistry, the reagent collisions and recombination take place over picoseconds. In contrast, at ultracold temperatures, the intermediate states can last up to half a millisecond [62, 63]. Further, it has been shown that the distribution of intermediate states (two-body, three-body, etc) can be tuned using external lasers, magnetic fields, and electric fields applied during the collision [60, 64, 65, 66].

1.3.1 Quantum Engineered Reactions

Another application of cold molecules is to test how chemistry proceeds when reactions take place in exotic regimes not probed by chemists. This includes out of thermal equilibrium reactions, hyperfine dependent reactions, or the partial scattering wave regime [67]. The reactant samples could be prepared in two different quantum states that are out of thermal equilibrium and the final state of the reaction products could be measured as a function of the reactant states.

There are theory proposals that indicate that external optical, electric, or magnetic fields could also impact the intermediate state chemistry and affect the final products of diatomic reactions [68,

69, 70]. The application of these external fields can change the molecular reaction potentials by several kelvin, facilitating so one may careful probing of the effect of the reaction barrier on every part of the chemical reaction [71]. Physicists have already experimentally observed that spin-state preparation can be used to suppress the reaction $N + H \rightarrow NH$ at several hundred millikelvin [72]. There are a number of atomic experiments that are already using Feshbach resonances to carefully control the production of diatomic molecules [73, 74] . Thus, externally applied electromagnetic fields are already in use to enhance or suppress certain chemical pathways.

The formation of organic molecules at low temperatures in outer space is also of significant interest to the quantum chemistry community. The precursors of the large organic molecules that gave rise to life are thought to be short hydrocarbon chains such as methanol that undergo oxidation during collisions with hydroxide radicals. These collisions can give rise to larger molecules as the reagents tunnel through the reaction barrier and stick together [75]. This tunneling reaction has already been experimentally probed, leading to the conclusion that oxidization of hydrocarbons at low temperatures via tunneling of hydroxide radicals is much more probable than previously thought. Studies such as these can help us to imagine mechanisms by which simple organic molecules may have been born from lifeless gases in the freezing vacuum of space.

1.4 Application of Molecules to Quantum Information

Experimental quantum information can be separated into two classes of projects which differ in the type of "quantum computer" they attempt to create. There are programmable quantum simulators that aim to replicate a specific theoretical Hamiltonian whose behavior is non-analytic and difficult to calculate using traditional methods [76, 77]. Next, there are general quantum computers that seek to string together quantum logic gates into programmable circuits to realize algorithms [78, 79, 80]. This is similar to the design philosophy of classical computers that have integrated circuit chips with logic gate arrays that can be programmed using some base operating software.

Most of the theory proposals describing how to make quantum information devices do not rely

on exactly which quantum object serves as the basis architecture of the qubit. Rather, the qubit is treated like a black box and all that matters is the ability to encode information into a qubit state that can interact with the energy levels of the surrounding qubits. As a result there have been attempts to create these logic interactions with a wide variety of qubit technologies, ranging from superconducting magnetic qubits [81], ion qubits [82], neutral atom qubits [83], diatomic molecules [84, 85, 86], or even within the same macromolecule [87, 88, 89, 90].

1.4.1 Quantum Simulators

The most commonly proposed use of quantum simulators is to emulate the interactions arising from a relatively simple interaction Hamiltonians that lack analytic solutions describing the time evolution of states. This computational approach was first proposed by Feynman in the 1980's [91]. Feynman stated that while computers using binary linear algebra reach their limit for most calculations involving non-linear differentials, nature routinely evolves under such interactions. As a result, if one can precisely engineer the interaction between quantum objects, the qubit's interactions represent the outcome of that specific Hamiltonian evolution.

The 2D Fermi-Hubbard model is the simplest Hamiltonian lacking analytic solutions that has been successfully modeled with an experimental quantum simulator [82]. The 2D Fermi-Hubbard model describes the onsite interactions of Fermions constrained to a lattice, and poses a simple interaction Hamiltonian believed to give rise to the phenomenon of superconductivity. Neutral atoms have also been used to provide solutions to quantum phase transitions in an Ising system in (2+1) dimensions.[92] These advances reveal the potential of the nascent field of quantum simulation.

Molecular tunable dipole interactions are of particular interest to the field of quantum simulation. Controllable dipolar interactions between qubits can be turned on and off depending on the internal quantum state of the molecule. One such scheme uses the spin interactions of the hyperfine levels to produce state dependent forces between qubits [93]. Transferring one of the molecules to the $m_j = 0$ hyperfine state turns off the interaction, while flipping from $m_j > 0$ to $m_j < 0$ flips the sign of the NMR-based interaction. [94] Another scheme uses an unpolarized ground state that

lacks an intrinsic dipole moment. In this case, interactions are turned on by exciting to a long-lived state that is either intrinsically polarized or is polarized by an external electric or magnetic field [79]. This gives rise to a dipole-dipole interaction over long ranges that resembles

$$V_{dd}(\vec{r}) = \frac{C_{dd}}{4\pi} \frac{1 - 3\cos^2\theta}{r^3} \tag{1.8}$$

This non-trivial long-range interaction allows physicists to simulate a whole new range of Hamiltonians [95, 96]. These qubits can easily be made at ultra-low temperatures and high densities by cooling atoms initially, then loading the atoms into a lattice, before associating the atoms into molecular dimers. This approach has the benefit of achieving near deterministic lattice filling via light assisted collisions [82]. This efficient single-site filling is key to a robust simulation protocol.

1.4.2 General Quantum Computers

The construction of a general quantum computer requires many logic gate qubit arrays. [97, 91, 98, 99, 100] These gates rely on the conditional state of one of the input qubits to determine whether there is a change of state of the output qubit. Several key requirements must be satisfied for such a computer to be possible. First, the qubits need to posses stable “shelving states" that are resistant to error introduced through the environment. [101] Second, the qubits should have interacting states with long coherence times that allow for high fidelity gate operations. Third, the underlying qubit architecture needs to be scalable and compact in order to realize the millions of qubits required for quantum logic algorithms and error correction protocols [102, 103]. There have been several successful trapped atom experiments that have set the limits of logic gate fidelity [61]. This approach seems promising due to the development of miniature chip-based traps and optical tweezers arrays generated by electro-optical deflectors (EOD’s) or spatial light modulators (SLM’s) [104, 105]. Long coherence times together with scalable architecture will allow for the construction of quantum circuits with the millions of qubits required for even the simplest quantum algorithms and error correction. [106]

Molecular qubits are attractive candidates for quantum computing as they can be turned on and off at command. [107] However, this comes at a significant increase in experimental complexity compared to neutral atoms. By polarizing the molecule or putting it in a non-polarized ground state, the computer operator can allow the qubit to interact only during the logic operation. The rest of the time the molecule will sit in the lattice site in its non-interacting, non-polarized state, where superposition states can be stored with minimal decoherence. Limiting the period of time that the qubits are interacting with each other and the environment promises to improve the information fidelity of the qubits and reduce the amount of quantum error correction required to complete a calculation. The use of tunable long-range interactions when coupled to the implementation of optical tweezers will allow for unparalleled scalability, while guaranteeing that qubit information can be stored long-term while other operations take place. At the end of the calculation, the information can be accessed again with state-selective rapid readout and the single site resolution of quantum gas microscopes [108].

1.5 Production of Cold Molecular Gasses

Multiple techniques have been implemented to create cold and ultracold samples of gaseous molecules. One such approach begins by laser cooling atoms and trapping them before they are assembled into molecules [25, 109]. Other techniques attempt to cool the molecules directly using a combination of cryogenic production and optical cycling [110]. I will briefly discuss four of the most common direct molecule cooling techniques – supersonic beam expansion cooling, electro-optical cooling, polychromatic cooling, and buffer gas cooling [111, 112, 113]. This section will focus on those techniques that employ direct laser cooling on molecules, because my thesis research falls into this category. There are other proposed techniques for cooling molecules that may be appropriate in specific circumstances. The following techniques are generally applicable to a large class of molecules of varying structures and high masses.

1.5.1 Supersonic Beams

Supersonic expansion, one of the oldest techniques in molecular cooling, has been used for decades to perform spectroscopy on molecules of interest [114]. Supersonic cooling makes use of the decrease in temperature resulting from the expansion of a high pressure gas as it enters a low pressure region [115, 54]. The resultant change in volume takes energy out from the rotational and vibrational modes, and concentrates the energy into kinetic energy in the beam axis direction. This results in forward velocities that can be thousands of meters per second, whereas the transverse and internal temperatures are in the hundreds of millikelvin [116].

Supersonic samples are cold, but their high forward velocities are far from the Doppler limit. These supersonic beams are not ideal sources for generating molecules that can be laser cooled and loaded into a trap due to the high forward velocity. To load a trap, one must scatter away all of forward momentum. For high forward velocity beams, this requires a very extended slowing distance over which most of the molecules would be lost before ever reaching the trap. The most successful attempts to load traps with these beams have used supersonic expansion only to cool the internal degrees of freedom, while electric or magnetic fields are used to retard the molecules enough that a magneto-optical trap or an ion trap can hold them [117, 118]. Stark decelerators have already been demonstrated to be effective at cooling diatomic and polyatomic samples, but have provided a low trapped yield [119, 120]. Magnetic Zeeman slowers have also been shown to be effective for specific molecules with a simple hyperfine structure [121].

1.5.2 Electro-Optical Cooling

Specific classes of molecules possess low-field-seeking ladders of states that can be used to exert forces on the molecules. By applying a strong external electric field and using polarization or magnetic fields to strategically transfer molecules between high-field and low-field seeking states, one may induce a position dependent Stark shift that slows the molecular velocity distribution to the point that it can be trapped. When the molecular population is transferred into a polarized state, the Stark effect shifts the energy as:

$$E_{Stark} = -\mu_{eff}^{el} E = -\frac{KME\mu^{el}}{J(J+1)} \tag{1.9}$$

Where μ_e is the electric dipole moment of the state in question and J is the rotational angular momentum index. The coupling of the rotational angular momentum to the spin of the molecule means that electro-optical cooling is optimized for one spin-rotation state at a time. Therefore, efficient state preparation is required to guarantee the most coolable molecules as possible. Not all molecules possess linear stark shifts because levels that are too close together can push against each other as the high field seeking states of one transition mix with the low field seeking state of a neighboring transition.

It is most common for electro-optical cooling to be used in conjunction with other techniques because there is a practical limit to the size of the Stark shift that can be applied in the laboratory. Velocity filtering or preliminary buffer-gas cooling work well with electro-optical cooling. As a result there have been some instances of electro-optical cooling of molecules [122].

1.5.3 Polychromatic Cooling

Traditional slowing techniques rely on sustained scattering of light off of atomic or molecular beams prepared in a vapor oven or ablation cell. To reduce the overall forward momentum of the beam sufficiently low to be held in a trap, thousands of photons must be scattered as rapidly as possible. The rate of cycling is ultimately limited by the natural lifetime of the excited state, which determines the spontaneous decay rate back to the ground state. The electron excited by each scattering event absorbs a photon and receives a momentum kick equal to the momentum of the photon, $\hbar k$. After some amount of time characterized by the excited state's natural lifetime, the electron decays and isotropically radiates momentum away in the form of a fluoresced photon. If the electron decays back to the original ground state, a resonant laser can drive the same transition and repeat the momentum exchange cycle. On the other hand, the scattering cycle is broken if the electron decays to any other state but the original, thus halting any further manipulation via the original laser. In large part, the difficulty associated with this traditional form of scattering is

directly dependent on how likely the system is to decay back to the original ground state. Atoms and molecules are considered “amenable to laser cooling" if one can engineer within them a “two-level system". A two-level system is defined as one in which excited electrons always decay back to their original state. However, as this technology has matured, physicists have developed techniques for creating quasi two-level systems by adding repumping lasers that return electrons from the previously unaddressed dark states back into the scattering cycle. This is a difficult technique to scale up in complexity as the number of repumper lasers exponentially increase with the increasing degrees of freedom, becoming untenable using modern experimental practices. Molecules lack selection rules that determine the vibrational decay channels. The decay probability known as the Frank-Condon factor (FCF) is calculated as radial overlap integral between the excited state wave function and the vibrational ground state. The FCF’s of molecules that are “easy" to laser cool are as close to 1 as possible, usually better than 0.98. As a result, traditional molecular laser cooling experiments spend most of their time spectroscopically identifying these leaks and plugging them with dedicated lasers. The number of repumping lasers is also dependent on how many photons you plan to scatter to achieve the required experimental temperatures. Showing 1D cooling takes on the order of 10^2 scatters, loading a MOT requires about 10^4 photons, while keeping the molecules in a trap requires at least 10^5 photons. Scattering hundreds of photons might require one repumper, while sustained trapping can require upwards of three for even simple molecules. Recent proposals [112] suggest the use of high-intensity multi-frequency lasers, which drive pi pulses to transfer all of the molecules to the excited state and then stimulate their decay back down again to the original ground state. This offers two benefits. First, by utilizing coherent population transfers rather than relying on spontaneous decay, one almost entirely eliminates any chance of the molecule decaying into an undesired state that must then be repumped. Second, with sufficiently high laser power the transition can be driven much faster than the natural lifetime of the excited state. These techniques have been demonstrated in SrOH molecules. [123] As the technology matures, coherent molecule cooling will represent the best approach for laser cooling of large and complex molecules. [124]

1.5.4 Buffer Gas Cooling

Buffer-gas cooling has become one of the preferred methods of producing a cold, dense beam of molecules at moderate forward velocities for ultracold trap experiments and is gradually replacing supersonic beams. The principle is relatively simple at its core [110]. A hot sample of molecules is initially produced through laser ablation of a solid sample target or through reagents flowed into a cryogenic chamber. As the molecular sample expands in the buffer gas cell, the molecules collide with a steady-state vapor of cold helium or another noble gas like neon. The collisions dissipate the heat of ablation and cool the sample to the ambient temperature of the chamber, which is between 2-6 K. The buffer gas cell is designed with an aperture on one side that allows buffer gas to flow out into the vacuum chamber of the experiment. The molecular sample becomes trapped in the buffer gas flow. After it thermalizes, this mixture of buffer gas and molecular sample is ejected down the beam line. This hydrodynamic entrainment enhances the number of molecules that flow down the experiment beam-line by an order of magnitude, and can be seen by changing the rate at which buffer gas flows into the cell.[110, 125] A high flux coupled with the relatively low forward velocity on the order of 100 m/s is the reason that my experiment uses a buffer gas beam. This technology is quickly becoming an integral part of molecule experiments ranging from EDM searches to quantum chemistry in optical tweezers.[126]

Some buffer gas cells have an additional chamber after the first cell that is kept at a pressure between the high pressure of the primary cell and the low pressure of the vacuum. This allows the inner cell to run at a higher pressure, improving the efficiency of thermalization and the extraction of the molecular sample. The lower pressure second cell retards the significant forward velocity that arises from a high pressure primary cell [110]. Some natural collimation arises in the molecular beam due to the hydrodynamic entrainment of beams originating from both single stage and dual stage buffer gas cells. Additional collimation is afterwards provided by collimating apertures [110], magnetic lenses [30] , or even 2D MOTs

1.6 Looking Towards the Future

The modern field of Atomic Molecular and Optical Physics was born from the revolutionary advancements in atomic physics at the turn of the century that permitted laser cooling and trapping of cold atomic samples at high densities. Developments in this field have led to orders of magnitude improvements in spectroscopy and made it possible for small-scale table-top physics to contribute to fields traditionally dominated by billion-dollar international super-collider collaborations. Ultracold atomic quantum gasses have pioneered breakthrough discoveries in fields like high energy particle physics [127], condensed matter [77, 128], and information science [129]. Advancements from atomic physics have even found application outside of physics in rocketry, earth sciences, and metrology [130, 131]. Moreover, precision atomic time keeping gave rise to precision navigation by permitting GPS protocols. The changes in modern technology enabled by early advances in AMO were not anticipated by the physicists that first invented these techniques. These researchers were motivated by a passion for research and a love of the elegance of nature. It is my hope that the advances in molecular cooling that I have contributed to with this thesis will extend far beyond my foresight, impacting future generations in a positive manner.

Chapter 2: The Structure of Diatomic Molecules

2.1 Introduction

The theoretical framework for discussing the quantum structure of molecules is fundamentally the same as the theory developed to describe atoms. At the core of the description is the Schrödinger equation, which reveals that quantum energy levels are eigenstates of the system's Hamiltonian. The eigenvalues of the Hamiltonian operator are the quantized energies of the system. The Hamiltonian is an operator defined as the total energy of the system including both the kinetic energy and the potential energy arising from the internal interactions of the system. When solving the Schrödinger equation, we make use of the Born-Oppenheimer approximation to separate the wavefunctions into a product of radial and angular wavefunctions. These independent wavefunctions are ultimately multiplied back together to provide the complete quantum state of the molecule as a whole. Compared to atoms, the primary difference in the theoretical description of molecules in the additional degrees of freedom that grow exponentially as the number of particles increase and their interactions grow exponentially in complexity. This makes analytic solutions nearly impossible. Additional modes such as rotational and vibrational modes in molecules give rise to new manifolds of quantum states that must be navigated to optically pump the molecule between desired states.

Within the field of molecular cooling, there are largely two classes of molecules – the diatomic molecules and the polyatomic molecules. By far, the most explored class of molecules are diatomic molecules such as the alkaline earth monohalides like CaF [4], SrF [132], BaF [133], and RaF [134]. Diatomic alkaline earth monohydrides are a subset of diatomic molecule that has been successfully cooled, with the first result for BaH published by Rees McNally and myself in 2020 [135]. Significant advancements have been made in the field of polyatomic cooling, with

recent success including linear polyatomics such as SrOH [11] and symmetric top polyatomics such $CaOCH_3$ [13]. There are significant differences in the cooling schemes required for cooling these different classes of molecules, due to the different degrees of freedom and internal couplings that vary among species. The primary difference that must be accounted for between diatomics and polyatomics is the presence of additional vibrational modes. Diatomic molecules only posses stretching modes, but polyatomic molecules can bend in addition to stretching, which further enriches their structure.

In the following section, I lay out a brief description of the transitions present in diatomic molecules. I begin from the Schrödinger Equation and then describe implementation of the Born-Oppenheimer approximation as defined by Hund's cases that govern the ways in which the various angular momenta couple. Then having derived the relevant transition manifolds within CaH, I will describe the optical cycling and repumping scheme used to apply radiative pressure to the molecules by scattering hundreds of photons.

2.2 Electronic Structure of Diatomic Molecules

As with any quantum system, the mathematical description of the molecule's structure begins with the Schrödinger equation:

$$\hat{H}_{mol}\Psi_{mol} = E_{mol}\Psi_{mol} \tag{2.1}$$

where the Hamiltonian H is the sum of the kinetic energy and the potential energy arising from the interactions of the particles that make up the molecule. This energy landscape gives rise to the molecular wavefunctions, in which the molecule resides either in a pure state or a superposition of molecular energy eigenstates Ψ_{mol}. When I refer to a transition throughout this thesis, I am referring to a change from molecular energy eigenfunctions with a initial energy E_g to an excited energy eigenstate with a different energy E_e. The Hamiltonian can be expressed generally as a sum of the kinetic energies of the electrons and nuclei in addition to the attractive interactions between

the nuclei and the electrons and the repulsive interactions between particles of the same charge as follows:

$$\hat{H}_{mol} = \hat{T}_{nuc} + \hat{T}_{el} + \hat{V}_{nuc,nuc} + \hat{V}_{el,el} + \hat{V}_{nuc,el} \tag{2.2}$$

The interactions between the electronic and nuclear spins have been neglected for now, due to their small contribution to the energy of each state. The nuclear and electronic kinetic energies are of course:

$$\hat{T}_{nuc} = -\frac{\hbar^2}{2}\sum_{j=1}^{J_{nuc}}\frac{1}{M_j}\nabla_j^2 \tag{2.3}$$

$$\hat{T}_{el} = -\frac{\hbar^2}{2m_e}\sum_{i=1}^{N_{el}}\nabla_i^2 \tag{2.4}$$

where M_j is the mass of the j^{th} nucleon and m_e is the mass of the electron. The interaction energy operators can be expanded into sums of the interactions of each particle with every other particle. Due to their similar negative charge, the electrons exhibit a repulsive force between them that is inversely proportional to the distance between each of the electrons $R_{i,i'}$. This interaction energy is:

$$\hat{V}_{el,el} = \frac{e^2}{4\pi\epsilon_0}\sum_{i'>i}^{N_{el}}\sum_{i=1}^{N_{el}}\frac{1}{R_{i,i'}} \tag{2.5}$$

Each pair of protons is repulsive with an energy that scales inversely with $R_{k,k'}$ the distance between each of the two nucleons:

$$\hat{V}_{nuc,nuc} = \frac{e^2}{4\pi\epsilon_0}\sum_{k'>k}^{K_{nuc}}\sum_{k=1}^{K_{nuc}}\frac{Z_k Z_{k'}}{R_{k,k'}} \tag{2.6}$$

Finally, the molecule is held together by the attractive potential between the net positively charged nucleons and the negatively charged electrons. This interaction scales inversely with the separation between each nucleon and each electron $r_{i,k}$:

$$\hat{V}_{nuc,el} = -\frac{e^2}{4\pi\epsilon_0} \sum_{k=1}^{K_{nuc}} \sum_{i=1}^{N_{el}} \frac{Z_k}{r_{i,k}} \tag{2.7}$$

This expression for the Hamiltonian should, in theory, be sufficient to fully characterize the spectrum of any molecule once spin interactions are included as a perturbation on the coulombic eigenvalues. However, for even the simplest molecules and most atoms, no analytic solutions can be derived, and theoretical descriptions require numerical methods. However, one may make physically motivated assumptions in order to simplify the problem enough to get some analytic solutions.

2.3 Assumptions

As stated previously, one can safely assume that the spin interactions between the nucleons and electrons are much smaller than the Coulomb attraction between the nuclei and the electrons. The intra-nuclear interactions can be neglected due to the short range action of the nuclear forces. In addition, one may assume that each electron cloud adiabatically follows the motion of the nearest nucleus as it vibrates in the molecular potential. This allows us to simplify the Hamiltonian to describe the electron's motion about the nuclei independent from the nuclear vibration. This separated Hamiltonian is as follows:

$$\hat{H}_{el} = \hat{T}_{el} + \hat{V}_{nuc,el} + \hat{V}_{el,el} \tag{2.8}$$

This allows us to now solve the Schrödinger equation to look for energy eigenstates $\Psi_{el}(r, R)$, where R is the vector between the pair of nuclei.

$$\hat{H_{el}}\Psi_{el}(r, R) = E_{el}\Psi_{el}(r, R) \tag{2.9}$$

The motion of the electron clouds around the nuclei of the atoms occurs at a much higher frequency than the vibrational motion of the molecule. This allows us to make use of the Born-Oppenheimer approximation to solve for vibrational wavefunctions independently of the electronic

wavefunctions. This approximation separates the coupled differential equation describing the molecule and simplifies it into a product between the energy eigenstates of the electron $\Psi_{el}(r)$ and the energy eigenstates of the nuclei $\Psi_{nuc}(R)$. The energy of the molecular product wave function can be expressed as:

$$E_{el} = T_{el} + V_{nuc,nuc} \tag{2.10}$$

Putting this together, we can now write the description of our system as a pair of differential equations that we may solve separately.

$$(\hat{T}_{nuc} + U)\Psi_{nuc}(R) = E_{nuc}\Psi_{nuc}(R) \tag{2.11}$$

Then, to calculate the total energy of the system for a given energy eigenstate of the molecule, one must add together the energies obtained by solving the differential equations for the nuclear motion and the electronic motion. Thus, the total energy for each state inhabited by the molecule is given by the following:

$$E_{mol} = E_{el} + E_{nuc} \tag{2.12}$$

2.4 Angular Momenta of the Diatomic Molecule

Up until now, I have neglected to account for the various ways that the numerous angular momenta of the molecule can couple together. Understanding the variations of how the angular momenta can couple is necessary to further simplifying and solving the electronic Hamiltonian. The couplings lead to conserved quantities, which can be taken advantage of to construct a quasi-two level system that can be used to cycle thousands of photons for slowing and trapping. These angular momentum couplings can be extended to describe specific states of polyatomics, but this discussion will focus on the application to diatomics.

Most of the electronic structure of the molecule is a consequence of the various angular momen-

tum couplings between the rotational angular momentum of the molecule and the orbital angular momentum of the electron. The notation used to label the molecular angular momenta is reminiscent to that used for atoms. Here, I familiarize the reader with the labels conventionally used to label the relevant angular momenta [136].

	Atomic property		Molecular projection	
Description	Symbol	Values	Symbol	Values
Electronic spin	$\boldsymbol{S}$	$0,\frac{1}{2},1,...$	$\boldsymbol{\Sigma}$	$0,\frac{1}{2},1,...$
Electronic orbital angular momentum	$\boldsymbol{L}$	s,p,d,...	$\boldsymbol{\Lambda}$	$\Sigma,\Lambda,\Delta,...$
Total angular momentum	$\boldsymbol{J}$	$0,\frac{1}{2},1,...$	$\boldsymbol{\Omega}$	$0,\pm\frac{1}{2},\pm1,...$

Molecular states have electronic spin that is labeled **S** and orbital momentum labeled **L** like their atomic counterparts. Despite the similarity, there are significant differences in how the projection axes of the angular momenta are chosen which depend on how much angular momentum there is in the electronic states. Atoms in general benefit greatly from the spherical symmetry of their Hamiltonians, but molecules have much more limited symmetry that varies between classes of molecules. Thankfully, diatomic molecules are among the most symmetric molecules due to their axial cylindrical symmetry. This makes the choice of the momentum projection axis simpler. The projection of electronic spin **S** and the orbital angular momentum **L** on to the internuclear axis are labeled Σ and Λ respectively. The sum total of the electronic and angular momenta is $J = S+L$, whereas the sum of the projections is $\Omega = \Sigma + \Lambda$. The nuclear spin I in addition to the electronic and orbital angular is labeled $F = I + J$. Finally, the rotational angular momentum of the molecule about its center of mass is also quantized and labeled **R**. Below, I list the various angular momenta of the molecule and the symbols used to denote them [136]

Angular momenta	Quantum number	Expression
Electronic spin	$\boldsymbol{S}$	
Nuclear spin	$\boldsymbol{I}$	
Electronic orbital angular momentum	$\boldsymbol{L}$	
Total angular momentum	$\boldsymbol{J}$	
Total angular momentum excluding electronic spin	$\boldsymbol{N}$	$\boldsymbol{N = J - S}$
Rotational angular momentum of the nuclei	$\boldsymbol{R}$	$\boldsymbol{R = N - L}$
Grand total angular momentum	$\boldsymbol{F}$	$\boldsymbol{F = I + J^*}$

2.5 Molecular Term Symbols

It is key that one understand the different ways that the molecular angular momentum couple together, because these differences give rise to different combinations of angular momentum being conserved depending on the specific state in consideration. We use an additional state label indicating the coupling present in the state of interest. This new molecular term symbol is given bellow:

$$^{2S+1}\Delta^{\pm}_{\Omega} \tag{2.13}$$

This term symbol specifies the total spin S, the projection of the orbital angular momentum Δ, and the projection of the total angular momentum Ω onto the internuclear axis. The molecular term symbol also defines the reflection symmetry $(+/-)$ of the state about a plane containing the axis of symmetry. This is different from the parity traditionally considered for atomic orbitals. Δ denotes the magnitude of the projection of the orbital angular momentum onto the internuclear axis. This projection in molecules is labeled by the Greek letters $\Delta = \Sigma, \Pi, \Delta, \ldots$ corresponding to = 0,1,2,... quanta of angular momentum. These labels are analogous to the atomic labels of S, P, D, ... indicating = 0,1,2,... quanta of angular momentum.

2.6 Hund's Cases: Molecular Angular Momentum Couplings

Hund's cases are the limiting cases of the different ways that the angular momenta couple, and are a guide to choosing the appropriate quantum numbers to define your state by. There are two Hund's cases relevant to the cooling of CaH – Hund's case (a) and (b) – which are defined by the relative alignment between the electro-orbital angular momentum and the molecular internuclear axis. That is to say, Hund's case (a) considers a state where the electronic orbital angular momentum is strongly coupled to the internuclear axis. Hund's case (b) considers a state in which the electronic orbital angular momentum L and the nuclear angular momentum R are strongly coupled. [124]

Coupling case	Good quantum numbers	Requirements
(a)	$\Lambda, S, \Sigma, J, \Omega$	$A\Lambda \gg BJ$
(b)	Λ, N, S, J	$A\Lambda \ll BJ$

Figure 2.1: The appropriate state labels for Hund's cases a and b. [124]

2.6.1 Hund's Case (a): The CaH $^2\Pi_\Omega$ States

Throughout the work demonstrated in this thesis, I worked extensively with the CaH $A^2\Pi_{1/2}$ states. Shown in the figure below is Hund's case (a). In this limit, the electronic-orbital angular momentum is strongly coupled to the internuclear axis and is called spin-orbit coupling. The strong coupling gives rise to pairs of states that are separated by large splittings relative to the rotational spacing that can be seen in CaH by the large splitting between the $A^2\Pi_{1/2}$ and $A^2\Pi_{3/2}$ states. This coupling scheme results in **L** and **S** processing around the internuclear axis rapidly, that Ω and **R** process about **J** much slower.

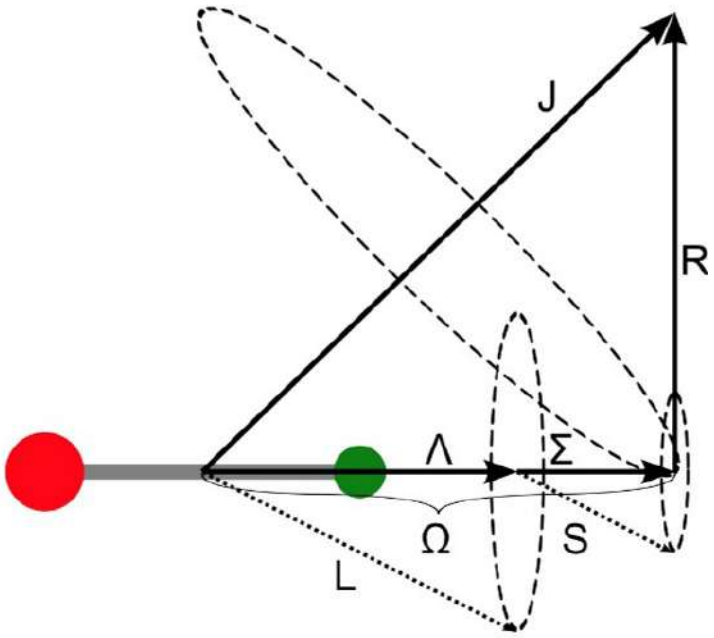

Figure 2.2: The figure above illustrates the angular momentum coupling associated with Hund's case a. [136]

2.6.2 Hund's Case (b): The CaH $^2\Sigma^+$ States

The other class of states used throughout the cooling of CaH are the $^2\Sigma$ states. The $X^2\Sigma^+$ ground state of the cycling scheme and the state used for repumping and detection are all $^2\Sigma$ states. In the $^2\Sigma$ states, the electronic-orbital angular momentum is again strongly coupled to the internuclear axis, though now the splittings are smaller than for the $^2\Pi_\Omega$ states. Next Λ, **R**, and **N** are all coupled to **J**. The higher number of couplings in Hund's case (b) means that Ω is not well defined and is not an appropriate quantum number.

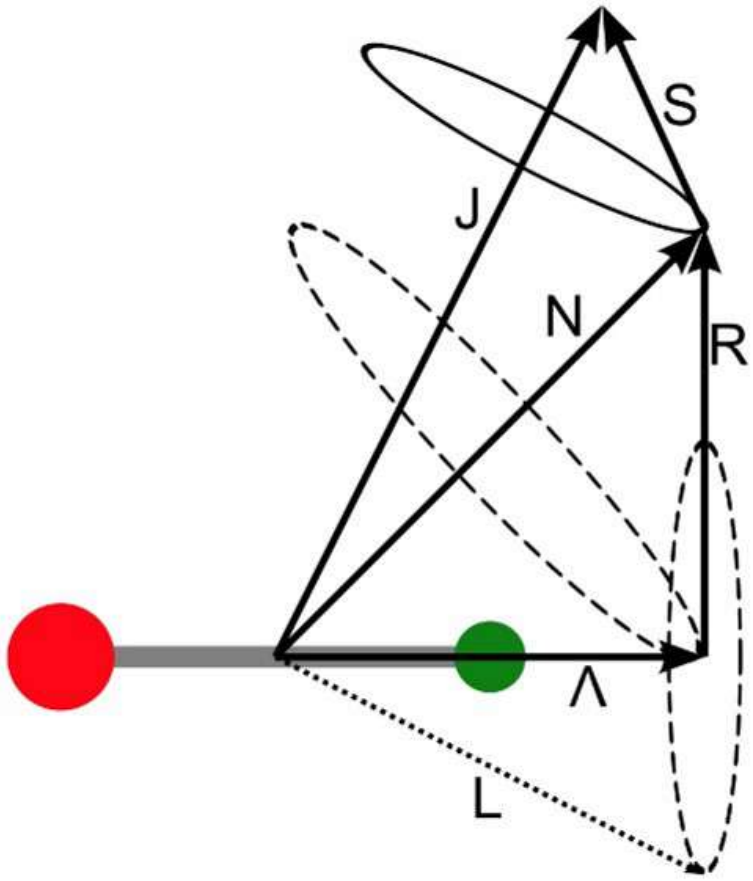

Figure 2.3: The figure above illustrates the angular momentum coupling associated with Hund's case b. [136]

2.6.3 Transitions between States of Different Hund's Case

The work outlined in this thesis used molecular states well-described by Hund's cases (a) and (b). These states are used for producing sustained photon cycling, imaging the molecular beam, and vibrational repumping. Transitions between different Hund's cases can broadly be classified into two classes, $^2\Sigma^+ \rightarrow^2 \Sigma^+$ and $^2\Sigma^+ \rightarrow^2 \Pi_{1/2}$. This means that I was utilizing transitions from Hund's case (b) to Hund's case (b) in addition to transitions from Hund's case (b) to Hund's case (a). The theoretical description of these types of transitions is best found in the textbook *Molecular Spectra and Molecular Structure* by Gerhard Herzberg [137] and the following is a synopsis of his work as applied to the cooling of CaH.

$^2\Sigma^+ \rightarrow^2 \Sigma^+$ Transitions

The most commonly used transitions in this thesis were transitions between $^2\Sigma^+$ states. I used the $X^2\Sigma^+(V = 0) \rightarrow B^2\Sigma^+(V = 0)$ transition for fluorescence spectroscopy to detect the molecular beam. I also used the $X^2\Sigma^+(V = 1) \rightarrow B^2\Sigma^+(V = 0)$ to repump molecules that decayed to the first excited vibrational state back to the ground vibrational manifold.

The selection rules for these types of transitions are more straight forward. Conservation of angular momentum requires that the molecules change rotational states by ± 1. This forbids transitions in which the rotational quantum number does not change by one ($\Delta N \neq 0$). Herzberg further divides these transitions into two classes, R and P type transitions. R type transitions are those in which the transition increases the rotational quantum number by one ($R \rightarrow \Delta N = +1$), while P type transitions decrease the rotational quantum number by one ($P \rightarrow \Delta N = -1$). Finally the R and P transitions are further divided into three classes of transitions based on how the spin rotation quantum number J changes. ΔJ may take one of three values, $\Delta J = 0, \pm 1$. A subscript of 1 on the R or P transition indicates that $\Delta J = +1$, whereas a subscript of 2 indicates that $\Delta J = -1$. Finally, a Q_{12} subscript on the R or P denotes that $\Delta J = 0$. Herzberg defines all these transitions and their subscripts in the following chart. I have highlighted the transitions I used in this experiment in red.

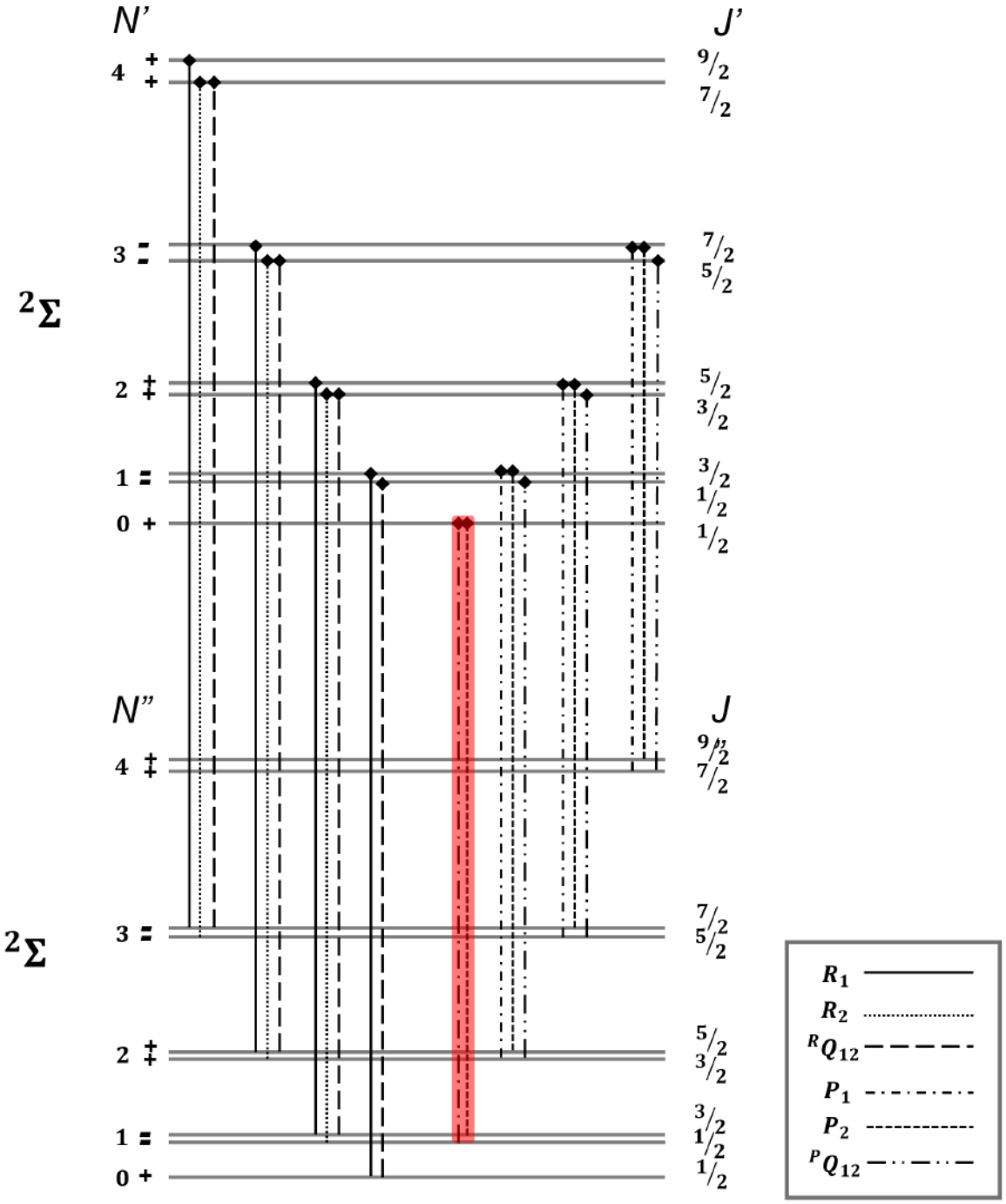
N'
J'
4 +
9/2
7/2
3 =
7/2
5/2
2Σ
2 ‡
5/2
3/2
1 =
3/2
1/2
0 +
1/2
N"
J
4 ‡
9/2
7/2
3 =
7/2
5/2
2Σ
2 ‡
5/2
3/2
1 =
3/2
1/2
0 +
1/2
R1
R2
RQ12
P1
P2
PQ12

Careful consideration of these selection rules reveals that transitions from the first excited rotational state to the rotational ground state have only one decay path that is back to the original rotational state. This can be seen in the diagram through the presence of only P type transitions between a $N = 1$ ground state and a $N = 0$ excited state. The closure provided by this selection rule provides the motivation for choosing the $N = 1$ state as the ground state addressed by the CaH cooling laser.

Through out my thesis I found evidence of additional loss channels from the $B^2\Sigma^+(V = 0, N = 0)$ state. I would lose about 30% of the molecules after fully depleting the V=0 band and finally repumping V=1 through the $B^2\Sigma^+(V = 0, N = 0)$ state. One possible explanation of this is that the nearby $A^2\Pi_{1/2}(N = 1, V = 1)$ perturbs the $B^2\Sigma^+(V = 0, N = 0)$ state, effectively mixing the two states and destroying rotational closure. We also considered the possibility that the excited $B^2\Sigma^+(V = 0, N = 0)$ somehow couples to the continuum, leading to predissociation on this state. It was for this reason that I chose to use the $B^2\Sigma^+(V = 0, N = 0)$ state as little as possible. This topic will be further discussed in the section of the thesis elaborating the repumping experiments I performed while optimizing my experiment.

$^2\Sigma^+ \rightarrow ^2\Pi_{1/2}$ Transitions

Arguably the most important transition used in the cooling of CaH was the $X^2\Sigma^+(V = 0, N = 1) \rightarrow A^2\Pi_{1/2}(V = 0, N = 0)$ transition. This was the transition that was ultimately chosen to scatter several hundred photons off the molecules and cool them. This transition will become even more important to the future of the experiment as it will be the primary slowing and trapping transition when CaH progresses towards a MOT.

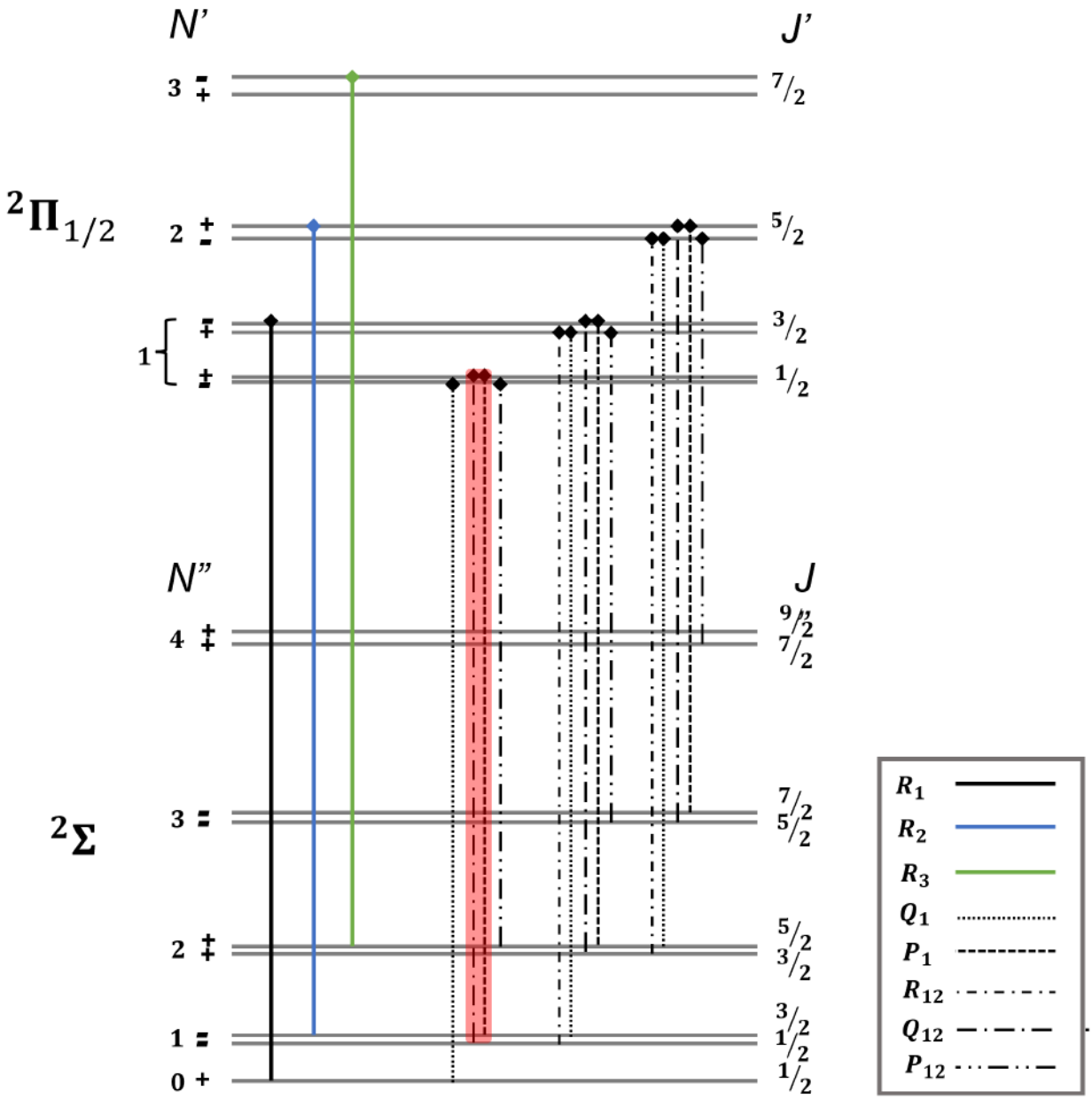
N'
J'
3 ∓ ±
7/2
2Π1/2
2 ± ∓
5/2
1
∓
±
3/2
1/2
N"
J
4 ‡
9/2
7/2
2Σ
3 =
7/2
5/2
2 ‡
5/2
3/2
1 =
3/2
1/2
0 +
1/2
R1
R2
R3
Q1
P1
R12
Q12
P12

The transition between $^2\Sigma^+ \rightarrow ^2\Pi_{1/2}$ possess additional complexity due to the strong coupling between the electronic spin-orbital angular momentum and the internuclear axis present in the $A^2\Pi_{1/2}(V = 0)$ excited state. This creates two well separated branches of states depending on the direction of the electronic orbital angular momentum, and destroys the selection rule that controlled the values ΔN could take. The only remaining angular momentum rules are those that require $\Delta J = 0, \pm 1$. This leads to 12 possible transitions, and one must take advantage of the parity selection rules to guarantee closure. The only set of states which can be used to create a system capable of sustained optical cycling are the positive parity states of the $A^2\Pi_{1/2}$ branch in combination with the negative parity of the $X^2\Sigma^+(V = 0, N = 1)$ states. These are labeled as the P_1 and Q_{12} transitions and are highlighted in the chart shown above.

2.7 Rotational Energy Levels of CaH

Creating a quasi-two level state capable of scattering many photons requires a good understanding of the available rotational states, as described in the section on Hund's cases and the transitions between different angular momentum coupling schemes. Without rotational closure, cooling and trapping diatomic molecules using radiation pressure would be impossible.

The rotations of a diatomic molecule can be well approximated by treating the molecule as a rigid rotor with cylindrical symmetry. This approximation begins to break down at higher rotational energies, but remains a good description for the first few quantum rotational levels used in this thesis. The moment of inertia of a quantum rigid rotor about its center of mass is given by the product of the reduced mass and the square of the distance between the point masses (nuclei):

$$I = \frac{m_1 m_2}{m_1 + m_2} r^2 \tag{2.14}$$

The Hamiltonian then can be expressed in the rest frame of the center of mass as: :

$$\hat{H_{el}}\Psi_{el}(\theta, \phi) = E_{el}\Psi_{el}(\theta, \phi) = E_{el}\Theta(\theta)\Phi(\phi) \tag{2.15}$$

Recalling that the radial distance r_0 is constant in the rigid rotor, we may express this Hamiltonian in spherical coordinates as:

$$-\frac{\hbar^2}{2I}\left[\frac{\delta}{\delta r_0}\cancel{r_0^2}\cancel{\frac{\delta}{\delta r_0}}^{0}+\frac{1}{sin(\theta)}\frac{\delta}{\delta\theta}+\frac{1}{sin(\theta)}\frac{\delta^2}{\delta\phi^2}\right]\Theta(\theta)\Phi(\phi)=E_{el}\Theta(\theta)\Phi(\phi) \tag{2.16}$$

Solving the Schrödinger equation will provide a quadratic ladder of states N that quantize the energy of the system as follows:

$$E_{rotation}(N)=\frac{\hbar^2N(N+1)}{2I} \tag{2.17}$$

For a more accurate description of the rotational spacing, the change in the moment of inertia due to the centrifugal force must be taken into account in addition to the spin rotation coupling. Through spectroscopic measurements, the scientific community has compiled tables of spectroscopic molecular constants quantifying the distortion of the molecule. Expressed in terms of these spectroscopic constants, the rotational spacing is given by one of the following expressions depending on the alignment of the spin relative to the rotational angular momentum.

$$F_1(N)=B_v''N(N+1)-D_v''N^2(N+1)^2+\frac{\gamma_v}{2}N \tag{2.18}$$

$$F_2(N)=B_v''N(N+1)-D_v''N^2(N+1)^2-\frac{\gamma_v}{2}(N+1) \tag{2.19}$$

Below, I list the experimentally measured [138, 139, 140, 141, 142, 143] rotational potential spectroscopic constants available on the NIST website:

$B\,^2\Sigma^+$ (4p)	15762	1285	20		[4.3410] 15	0.116		[2.020] 15 16		1.974_4	B ↔ X V	15754.9_6 15
	↳Hulthen, 1927; Watson and Bender, 1930; *missing citation*; Liberale and Weniger, 1969; Berg and Klynning, 1974; Berg and Klynning, 1974, 2											
State	**T_e**	**ω_e**	**$\omega_e x_e$**	**$\omega_e y_e$**	**B_e**	**α_e**	**γ_e**	**D_e**	**β_e**	**r_e**	**Trans.**	**ν_{00}**
$A\,^2\Pi_i$ (4p)	14413 17	1333	20		$[4.3476_9]$ 15	0.106		[1.883] 15 18		1.974_0	A ↔ X V	14430.39 15
	↳Hulthen, 1927; Watson and Bender, 1930; Mulliken and Christy, 1931; Liberale and Weniger, 1969; Berg and Klynning, 1974; Berg and Klynning, 1974, 2											
$X\,^2\Sigma^+$	0	1298.34 Z	19.10		4.2766 19	0.0970		1.837 20		2.0025 21		

2.7.1 Thermal Distribution, rotational spacing in Kelvin

As with most quantum thermal ensembles, a rotational temperature may be defined, resulting in thermal distribution governing the probability of each molecule populating a given rotational state. I outlined in the section on Hund's cases and rotational angular momentum that optical cycling is only possible when driving the $N = 1 \rightarrow N = 0$ transition. Therefore, I needed to maximize the natural thermal population that resides in the $N = 1$ state to ensure that there was the highest number of molecules available for laser cooling. Maximizing the number of molecules in $N = 1$ also maximizes the number of molecules that can be slowed and loaded into the MOT.

Ablation in the cryogenic cell produces a dense plume of extremely hot CaH molecules (and other ablation byproducts like calcium or hydrogen radicals) at a temperature of several thousand kelvin. At this point in time, hundreds of rotational levels are populated. If I were to try optical cycling at a high rotational temperature, there would be so few molecules in the $N = 1$ state that cooling would effectively be undetectable. Therefore, one must cool the ablation plume down to compress the rotational population into the lowest levels. Rotational cooling is achieved through the injection of gaseous He at around 12K into the cryogenic cell, which is maintained at 6K by a closed loop liquid helium refrigerator. As the ablation plume expands, the CaH molecules collide with the helium buffer gas and rapidly thermalize to the temperature of the buffer gas. One may tune the temperature of the cell and the gas to optimize the population in the $N = 1$ rotational level.

Recalling statistical mechanics, we know that the of the probability of each rotational level being populated is a product of the multiplicity of that state by a decaying exponential containing the energy of each rotational state and the temperature of the system. When using the eigenenergies of the quantum rigid rotor, this probability resembles the following unnormalized expression [57]:

$$P_N \approx (2N + 1)\exp\left(-\frac{\Delta E}{kT}\right) \tag{2.20}$$

Solving for the temperature which maximizes the population in $N = 1$ gives about 14K. If we plot the state population in the first few energy level at 14K and compare that to the state population at

1000K, the effect of rotational cooling is clearly seen.

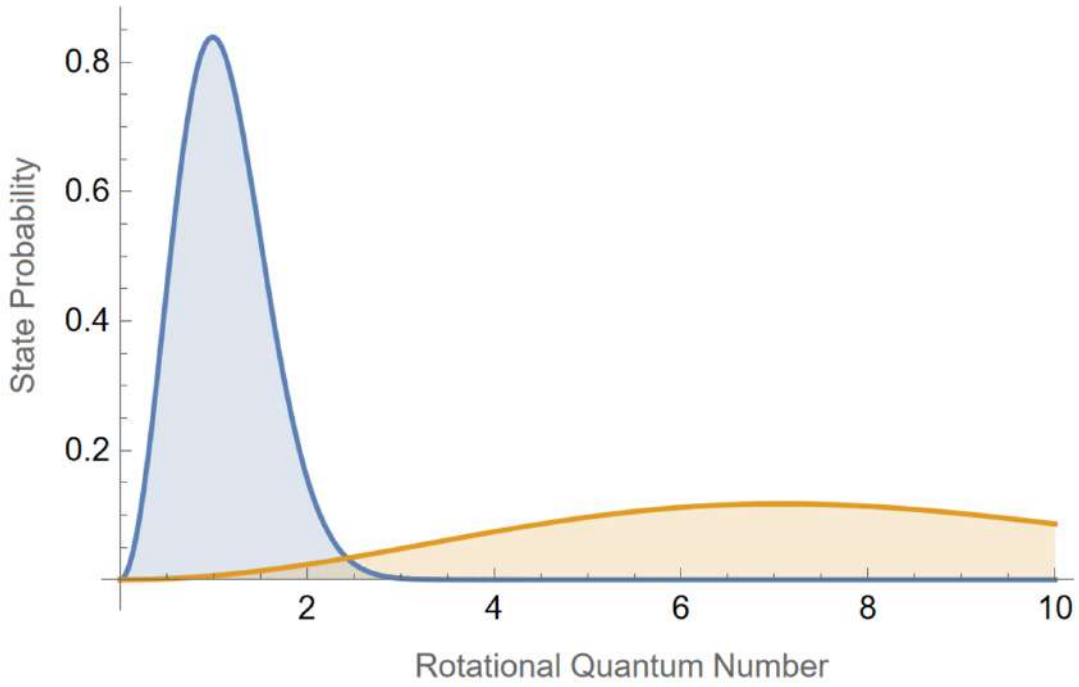

2.8 Vibrational Energy Levels of CaH

In addition to the electronic and angular degrees of freedom discussed above, molecules also have the freedom to vibrate. From an intuitive perspective, we know that a diatomic molecule is a bound state in which two different atoms reside at a bond length that balances the repulsion of their nuclei with the attraction of the nuclei with the other atom's electron cloud. The deepest point of the molecular potential is quadratic, producing a linear restoring force that maintains the atoms preferred position. I show in figure2.4 some of the theoretically predicted molecular states that have been calculated *ab initio* for CaH by Shayesteh et al.[144] The state label using the roman alphabet (X, A, B, C ...) merely indicates the order in which those states were spectroscopically first detected. This label is not indicative of the relative ordering of the energy hierarchy.

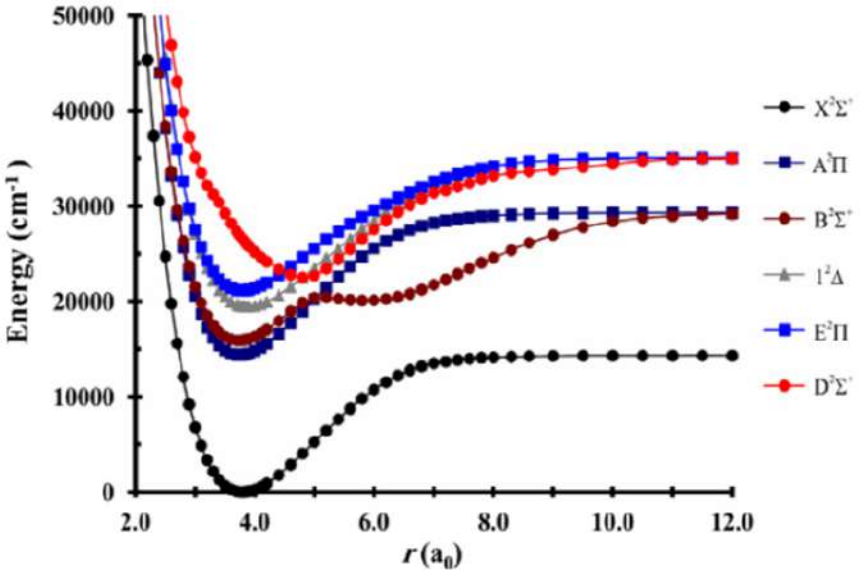

Figure 2.4: The molecular states of CaH as calculated by Shayesteh et al. [144] Note the avoided crossing between the B and D states which perturbs the B state.

Recalling the quantum harmonic oscillator, we expect a ground state with a non-zero energy and a ladder of equally spaced states growing from the ground state. This intuition is of course only accurate to a point; a more thorough description of the energy levels of the diatomic molecule requires adding higher order corrections to account for the an-harmonic scaling of high energy states. This an-harmonic behavior is due to the change in the restoring strength for high frequency and amplitude vibrations. Additionally, the harmonic oscillator analogy breaks down due to the infinite binding potential of the harmonic oscillator, which is not reflected in real molecules that posses finite binding energies. In nature, molecules have an energy past which the molecule breaks free from its electrostatic binding potential, called the dissociation energy. The an-harmonic oscillator is the simplest theoretical description that can estimate a dissociation energy and the increasing density of vibrational states as the vibrational quantum number increases. The first few terms of the expansion of the vibrational potential, written as a power series in the vibrational quantum number, is as follows:

$$E_{vibrational}(v) = \omega_e(v + 1/2) - \omega_e x_e(v + 1/2)^2 + \omega_e y_e(v + 1/2)^3 + ... \tag{2.21}$$

Here ω_e is the vibrational constant, $\omega_e x_e$ is the harmonic distortion constant, and $\omega_e y_e$ is the an-harmonic distortion constant. These constants have been experimentally measured and can be found on the NIST website [138, 139, 140, 141, 142, 143]. A few of the vibrational constant values are show in the table below for the states that are used in this thesis.

$B\,^2\Sigma^+$ (4p)	15762	1285	20		[4.3410] 15	0.116		[2.020] 15 16		1.974_4	B ↔ X V	15754.9_6 15
	↳Hulthen, 1927; Watson and Bender, 1930; *missing citation*; Liberale and Weniger, 1969; Berg and Klynning, 1974; Berg and Klynning, 1974, 2											
State	**T_e**	**ω_e**	**$\omega_e x_e$**	**$\omega_e y_e$**	**B_e**	**α_e**	**γ_e**	**D_e**	**β_e**	**r_e**	**Trans.**	**ν_{00}**
$A\,^2\Pi_i$ (4p)	14413 17	1333	20		[4.3476$_9$] 15	0.106		[1.883] 15 18		1.974_0	A ↔ X V	14430.39 15
	↳Hulthen, 1927; Watson and Bender, 1930; Mulliken and Christy, 1931; Liberale and Weniger, 1969; Berg and Klynning, 1974; Berg and Klynning, 1974, 2											
$X\,^2\Sigma^+$	0	1298.34 Z	19.10		4.2766 19	0.0970		1.837 20		2.0025 21		

The anharmonic oscillator is a great tool to gain intuition into the behavior of the first few vibrational levels, but the anharmonic oscillator has some significant shortcomings when comparing its spectra for high V. Namely, the anharmonic oscillator underestimates the binding energy and so it should be thought of as a functional model for the first 5 or so vibrational levels.

Further improvements to the molecular binding potential can be attained by modeling the binding energy as a Morse Potential, named after physicist Philip Morse. This potential can be accurately fit to provide a reasonable estimate for the binding energy, while accounting for anharmonic behavior of the higher lying vibrational states. This Morse potential can be expressed as:

$$V(x) = D_e(1 - e^{-\alpha x})^2 \tag{2.22}$$

Where $x = r - r_e$ is the change in molecular bond length from the minimum of the potential. D_e is the dissociation energy, $a = \sqrt{\frac{k_e}{2D_e}}$, and $k_e = \frac{d^2V}{dx^2}$. We can derive vibrational wavefunctions by taking this potential and solving the Schrödinger equation:

$$-\frac{\hbar^2}{2m}\frac{d^2\Psi}{dx^2} + V(x)\psi = E\Psi \tag{2.23}$$

Solving this gives a set of solutions for the eigenfunctions of the following form:

$$\psi_v(z) = N_v z^{\lambda-v-1/2} e^{-z/2} L_v^{2\lambda-2v-1}(z) \tag{2.24}$$

Where $L_v^{(a)}$ is a series of generalized Laguerre polynomials.

$$L_v^{\alpha} = \frac{z^{-\alpha} e^z}{v!} \frac{d^v}{dz^v}(z^{v+\alpha} e^{-z}) \tag{2.25}$$

Where I have defined the normalization factor N_v and the parameters λ and z

$$N_v = \sqrt{\frac{v!(2\lambda - 2v - 1)}{\Gamma(2\lambda - v)}} \tag{2.26}$$

$$\lambda = \frac{\sqrt{2mD_e}}{a\hbar} \tag{2.27}$$

$$z = 2\lambda e^{-x} \tag{2.28}$$

Figure 2.5 beautifully illustrates the difference in the wavefunctions for the harmonic oscillator compared to the Morse potential wavefunctions, plotted for nitrogen molecules. [145] The different spacings of the wavefunctions of each potential are clear. The harmonic oscillator has equally spaced energy levels, while the Morse potential spacing becomes more dense as the vibrational quantum number increases. In addition, it is clear that the low energy wavefunction closely resembles a harmonic oscillator, while the higher energy wavefunction becomes prominently anharmonic.

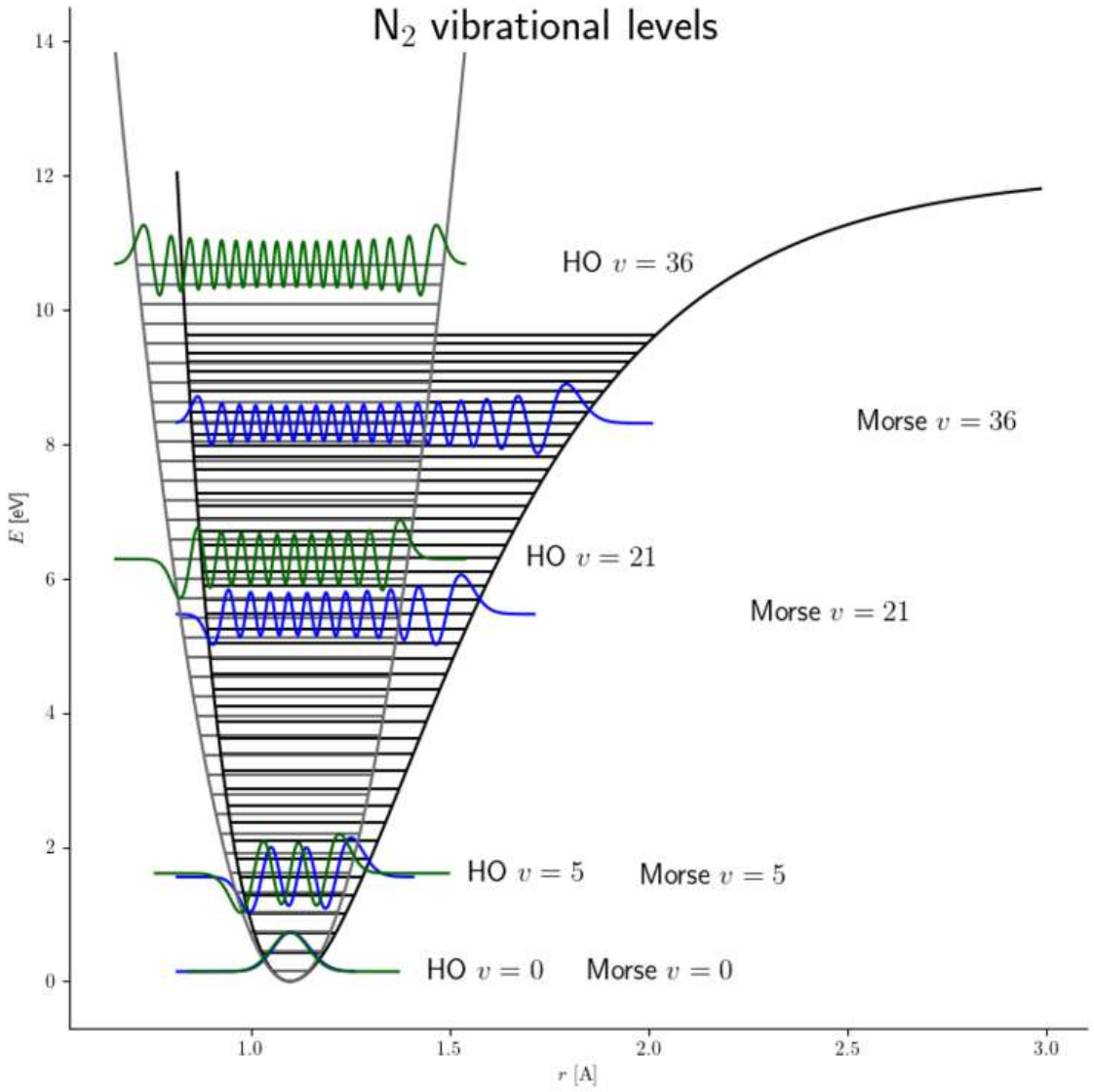

Figure 2.5: A plot showing the harmonic oscillator potential and the Morse potential along with their corresponding wavefunctions. [145] Note the equal spacing of the harmonic oscillator energy eigenstates, whereas the Morse potential energy eigenstates grow closer together towards the top of the potential. In addition, the wavefunctions are very similar for the lowest energy eigenstates while the wavefunctions begin to differ significantly for the higher levels. Finally, note that the harmonic oscillator has an infinite binding potential while the Morse potential has a finite binding energy.

An important feature of the Morse potential is that its solutions are mutually orthogonal, which mathematically prohibits decays between different vibrational levels. However, different electronic states have different molecular binding potentials that provide different vibrational solutions with slightly different Laguerre polynomials for each binding potential. Therefore, there is a small

chance for molecules to be lost into other vibrational states. As a result, transitions between the vibrational states of different electronic states are not forbidden. This is a major obstacle for everyone trying to apply radiative pressure to molecules. Molecules excited with the $X^2\Sigma^+(V = 0) \rightarrow A^2\Pi_{1/2}(V = 0)$ or the $X^2\Sigma^+(V = 0) \rightarrow B^2\Sigma^+(V = 0)$ transition are most likely to decay back to the $V = 0$ state, but have a non-zero probability of decaying to higher lying vibrational states ($V \geq 2$). The decays scale by the frequency of the transition cubed ω^3 and the Frank Condon Factor (FCF). The FCF is calculated as the overlap integral of the excited state wave function with the wave function of the vibrational state in question as is shown below:

$$q_{v',v''} = \int_0^{\inf} \psi^*_{v'}\psi_{v''}dr \tag{2.29}$$

The only solution to recover molecules that decay to the wrong vibrational state is to optically pump them back into the V=0 state with a repumping laser via an off-diagonal transition. I measured the vibrational branching ratios for each of the first three vibrational state decay channels for molecules decaying from either the A of B states. The closer the V=0 FCF is to one, the more photons one is able to scatter on that transition before the molecule can decay into an excited vibrational state. I measured the vibrational decay probabilities for the A and B states. In figure 2.6 I have listed the FCF's below while comparing them to the theoretically predicted values. [146, 147, 148, 149, 58, 150]

Transition	Lifetime τ (ns)	Vibrational Quanta (v'')	Transition wavelength (nm)	FCF Theory ($f_{0v''}$)	FCF measured ($f_{0v''}$)
$A \rightarrow X$	33(3)	0	695.13	0.953	0.9572(43)
		1	761.87	0.0439	0.0386(32)
		2	840.07	2.74×10^{-3}	$4.2(3.2)\times10^{-3}$
		3	932.80	2.3×10^{-4}	-
$B \rightarrow X$	58(2)	0	635.12	0.9856	0.9807(13)
		1	690.37	0.0132	0.0173(13)
		2	753.97	1.1×10^{-3}	$2.0(0.3)\times10^{-3}$
		3	827.84	1×10^{-4}	-

Figure 2.6: The lifetimes, wavelengths, theoretical FCF's , and measured FCF's for the two V=0 excited states used in this thesis as reported in my most recent paper. [146]

Inspection of the measured FCF of the B state shows that one would expect it to be the preferred state for cooling due to is better $V = 0$ FCF. However, the A state posses fairly good FCF's and double the scattering rate. This contributed to why we ultimately chose to use the A state for laser cooling and relegate the B state to repumping and imaging.

2.9 Spin-Rotation and Hyperfine Energy Levels of CaH

The electronic energy levels of CaH are further split by two additional angular momentum couplings – the spin-rotation coupling and the hyperfine nuclear spin coupling arising from the unpaired proton that is the hydrogen nucleus. For the X state, the spin-rotation Hamiltonian can be expressed as:

$$H_{SR} = \gamma_{vN} S \cdot N \tag{2.30}$$

Where γ_{vN} is an the spin-rotation coupling constant. The hyperfine interaction is well captured by the following Hamiltonian:

$$H_{HFS} = b_{vN} I \cdot S + c_{vN} (I \cdot \hat{z})(S \cdot \hat{z}) \tag{2.31}$$

expressed in terms of the hyperfine constant b_{vN} and the dipole contact constant c_{vN}. In CaH the couplings of the spin-orbit interaction are at least an order of magnitude larger than the hyperfine interaction. The spin rotation-splitting in the ground state is ≈ 1.86 GHz, whereas the hyperfine splitting is at most 101 MHz without a strong external B field to Zeeman-shift the magnetic sub-levels. It is for this reason that in my experiment, I chose to address each spin-rotation state with its own laser with the addition of AOM sidebands to address the hyperfine levels.

2.10 Parity

As mentioned above, the parity selection rule $- \rightarrow +$ is essential for creating the quasi two-level system that is required for sustained photon cycling. [124] The parity eigenfunctions for the

Σ^+ and Π states are written as sums of the molecular basis state wavefunctions [151].

$$\left\langle {}^{2S+1}\Lambda_{\Omega\pm}\right| = \frac{\left\langle {}^{2S+1}\Lambda_{\Omega}\right|}{\pm}(-1)^{J-2\Sigma+S}\left\langle {}^{2S+1}\Lambda_{-\Omega}\right|\sqrt{2} \tag{2.32}$$

Parity states are eigenfunctions of the inversion operator E^* which takes $r \rightarrow -r$

$$E^*\left\langle {}^{2S+1}\Lambda_{\pm\Omega}\right| = \pm\left\langle {}^{2S+1}\Lambda_{\pm\Omega}\right| \tag{2.33}$$

This can be simplified for transitions where $\Lambda, \Sigma,$ and Ω remain constant, because all the total parity is only changed by J. [152] This experiment's parity wavefunctions can be written in terms of the angular momentum states of the system:

$$\left\langle {}^2\Sigma^+_{1/2}(e/f)\right| = \frac{\left\langle {}^2\Sigma^+_{1/2}\right| \pm \left\langle {}^2\Sigma^+_{-1/2}\right|}{\sqrt{2}} \tag{2.34}$$

$$\left\langle {}^2\Pi^+_{1/2}(e/f)\right| = \frac{\left\langle {}^2\Pi^+_{1/2}\right| \pm \left\langle {}^2\Pi^+_{-1/2}\right|}{\sqrt{2}} \tag{2.35}$$

2.11 Choosing the appropriate cycling scheme for laser cooling

The relevant energy levels for CaH cooling are shown below. The vibrational decay probabilities to the three lowest vibrational $X^2\Sigma^+(N = 1, V = 0, 1, 2)$ states are also shown. Molecules begin the cooling process in the $X^2\Sigma^+(N = 1, V = 0)$ from where we excite them to either the $B^2\Sigma^+(N = 0, V = 0)$ or the $A^2\Pi_{1/2}(J = 1/2, V = 0)$ states. Rotational closure is guaranteed by only using molecules in the $N = 1$ rotational state of the $X^2\Sigma^+(V = 0)$ potential and driving transitions to the $N = 0$ excited states of opposite parity. Finally, we create a quasi two-level system by repumping molecules that decay to the V=1 vibrational level, back into the V=0 band by repumping via the off diagonal $X^2\Sigma^+(V = 1, N = 1) \rightarrow B^2\Sigma^+(V = 0, N = 0)$ transition.

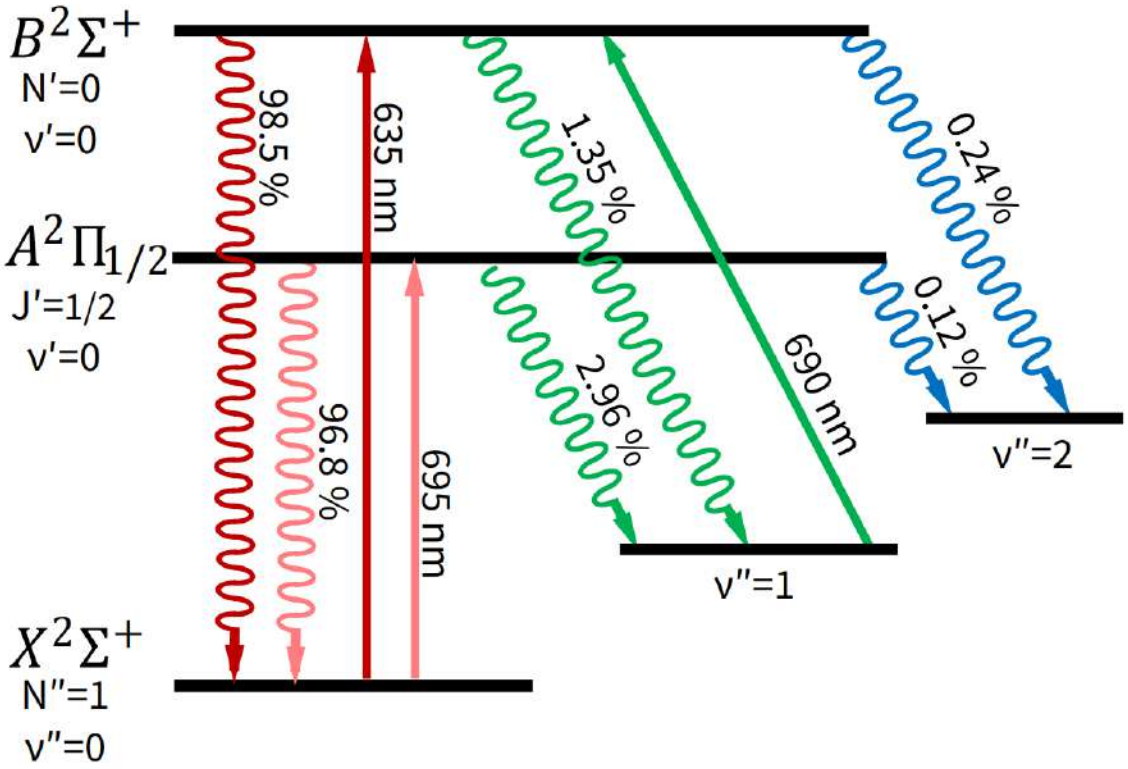

The $N = 1$ ground state manifold of the $X^2\Sigma^+$ is split into two states (1.86 GHz apart) by the coupling of the spin to the rotational angular momentum of the $N = 1$ state. Hyperfine interactions of the electron and nuclear spins further split those levels in half and are labeled as $F = 0, 1$ for the $J = 1/2$ state and $F = 1, 2$ for the $J = 3/2$ state. Each spin rotation state is addressed by a separate laser and can be seen in figure 2.7. The hyperfine splittings are 54 MHz and 101 MHz respectively and are addressed by sidebands generated by AOMs. Each hyperfine state posses $2F + 1$ Zeeman levels that are effectively degenerate for the experiments described in this thesis. This scheme allowed my experiment to cool CaH by cycling ≈ 200 photons at a peak scattering rate of 1.6×10^6 photons per second.

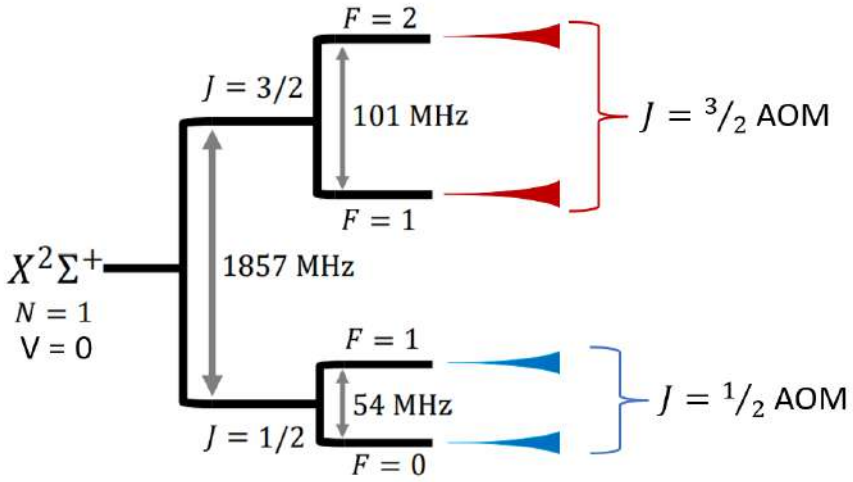

Figure 2.7: The hyperfine structure for the two spin-rotation components of the V=0 X $^2\Sigma^+$ground state. The F=1,2 states of the J=3/2 state are split by 101 MHz, while the F=0,1 states of the J=1/2 state are split by 54MHz. Each spin-rotation state is addressed with its own AOM.

Chapter 3: Experimental Apparatus

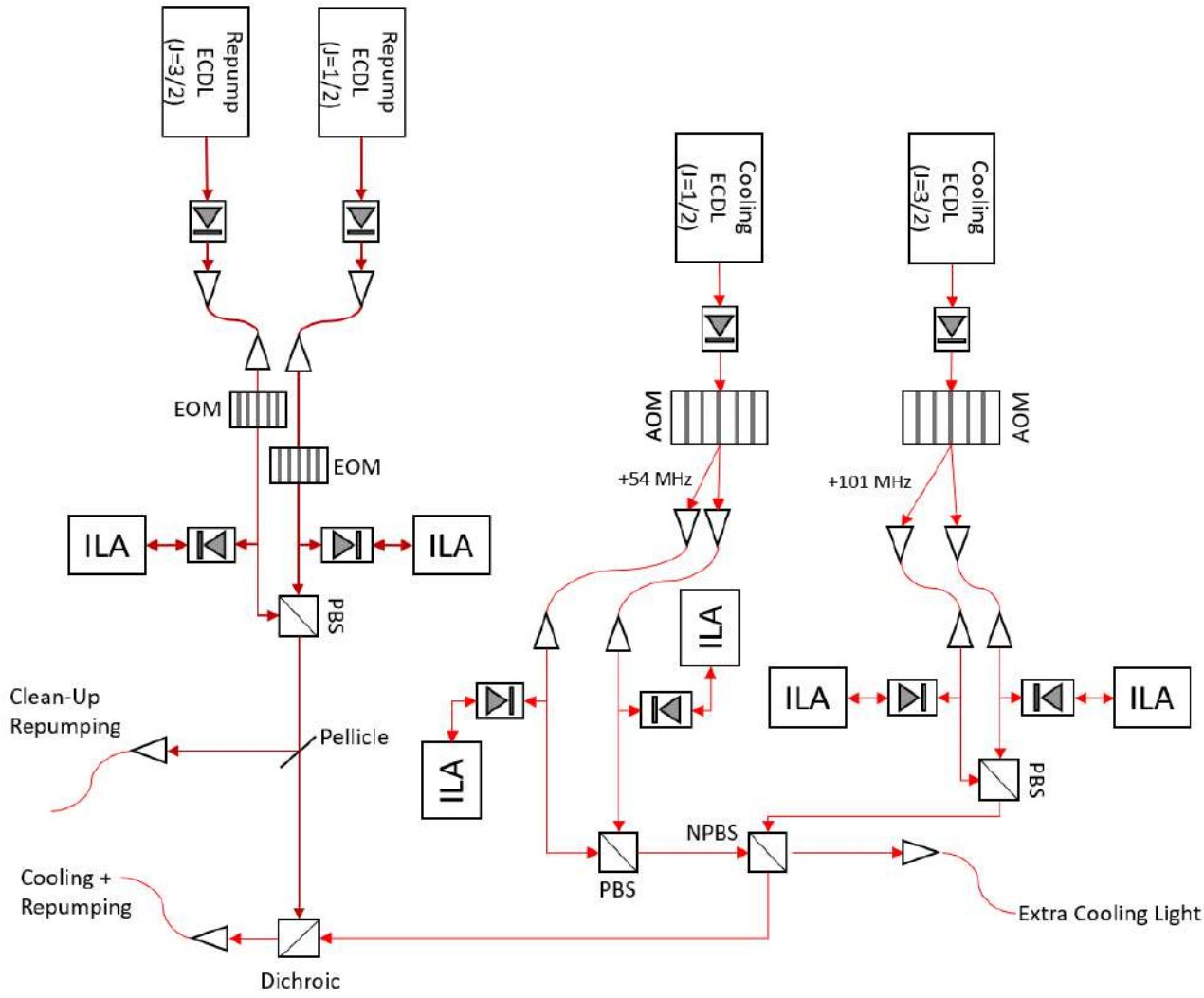

A photo of the laser system used to cool CaH. This system provides three amplified output beams that are fiber coupled and transferred to the experiment. One fiber carries coaligned cooling and repumping light, a second fiber carries cooling light alone, while a third fiber carries isolated repumping light.

3.1 Introduction

There are a multitude of experimental apparatus that must be constructed and seamlessly coordinated to create a system capable of direct laser cooling, slowing, and trapping molecules. The experimental apparatus I developed can be divided into five main subsystems – the cryogenic system, the vacuum system, the laser system, the detection system, and the computer control system. All of these systems must be maintained and optimized to accomplish one's experimental goals.

A well designed cryogenic buffer gas experiment seeks to provide the densest and coldest beam of molecules possible. A stable and powerful laser system then cools those molecules over a short distance before loading those molecules into a trap. A beam of molecules is produced through laser ablation or chemical production of a molecular sample which produces a hot cloud of molecules. This sample subsequently thermalizes with the buffer gas present in the cell. The helium buffer gas flow collimates the molecular sample into a beam [110, 136, 125]. That beam propagates into an ultra-high vacuum experiment region where lasers are applied transversely to compress the beam [135, 11, 13, 146, 153]. The lasers can also be aligned longitudinally, to slow the beam to the capture velocity of a MOT [154, 7, 6, 111]. After cooling or loading a trap, molecules then must be imaged either onto a camera for spatial information or onto a PMT for time of flight analysis.

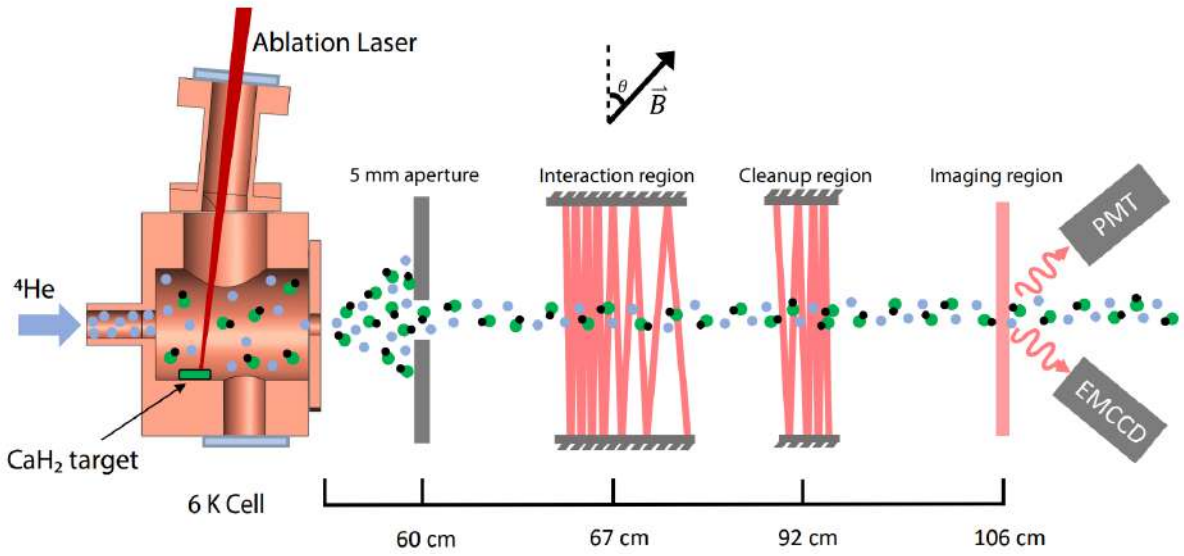

Figure 3.1: I show a diagram of the experiment, indicating where the molecule are exposed to light for cooling, V=1 clean-up, and imaging. Molecules begin in the cryostat and propagate 6cm before passing through a velocity filtering aperture that limits the transverse velocity of the molecular beam. Molecules immediately propagate into the interaction region, who's center is 7cm away, where molecules are exposed to high power lasers used to create Sisyphus cooling. After that molecules proceed 25cm down-beam to the clean up region where any molecules in the V=1 ground state are repumped back into the V=0 ground state to provide the most signal for imaging. Finally, molecules propagate another 14cm to the imaging region where they interact with a laser and fluoresce. This fluorescence is collect by a PMT and an EMCCD camera for analysis of the beam's properties.

The difficulty in designing and fabricating such as system is compounded because many sub-system are home-built or custom fabricated to meet the unique requirements of the experiment. This is compounded by the fact that often, several generations of students [155, 57] are responsible for this development and it is easy to overlook features that would be useful to later generations. As a result, lack of compatibility between systems can commonly be a problem and subsystems must be interfaced using a home-built sequencer written in Labview. Graduate students spend most of their time building new components while maintaining and repairing older component. Only when everything is working perfectly can the physics goals be attempted. In the sections below, I will step the reader through each major subsystem, describing the design philosophy, the fabrication process, maintenance, and finally their use in the experimental sequence.

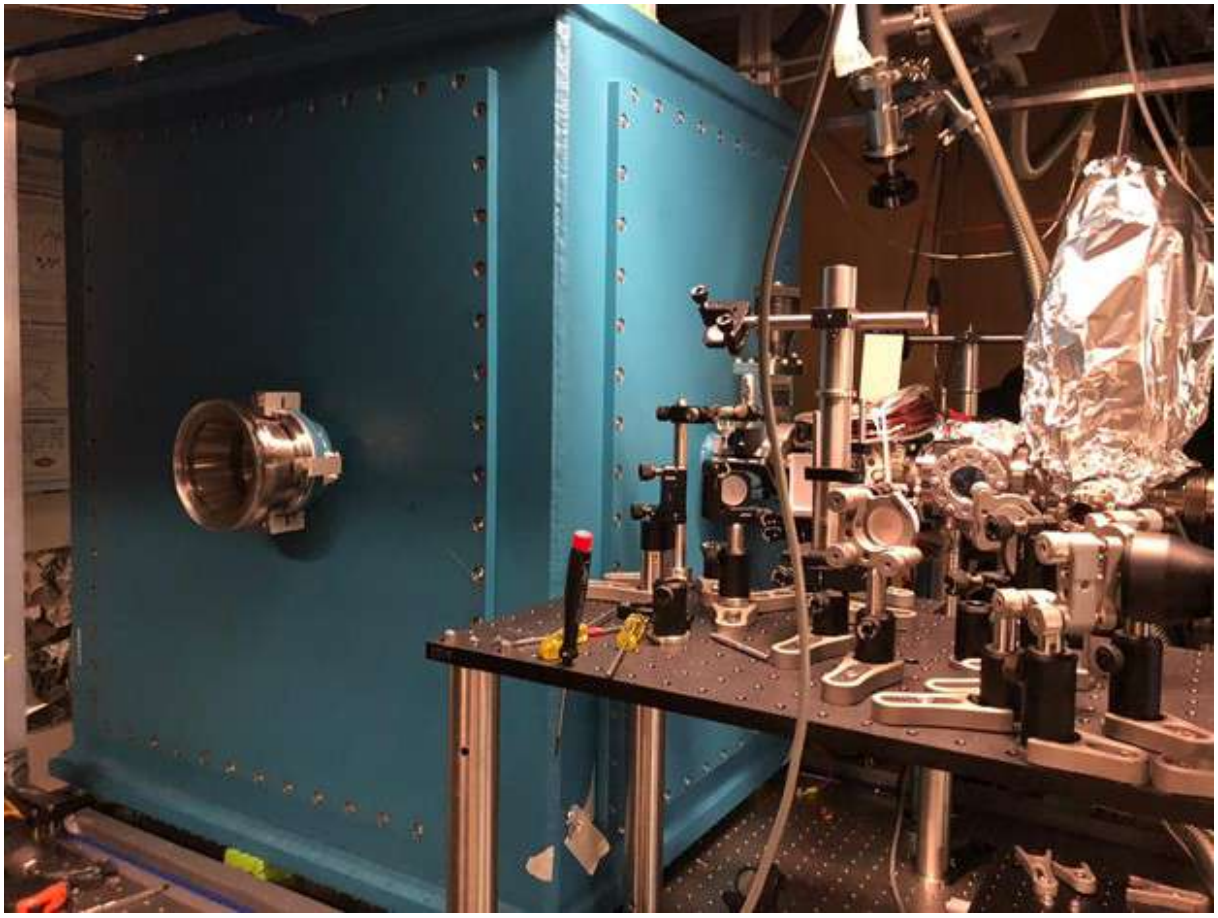

Figure 3.2: A photo of the cryostat in blue. The windows providing optical access to the cell can be seen on the left of the cryostat. The beam region can be surrounded by optics used to probe the properties of the beam.

3.2 The Cryostat

The starting point of any cryogenic buffer gas experiment is the cryostat. It is in the cryostat that the molecules are first produced, cooled, and embedded into a buffer gas beam for use in the rest of the apparatus. As a result, the first ingredient for a successful buffer-gas experiment is a well-designed and functional cryostat. The optimal cryostat design is not identical for every molecular species because different molecules use a variety of production techniques. These different techniques produce beams at a variety of temperatures, buffer gas flow rates, and molecular yields. My experiment optimized the cryostat design and operation for BaH independently from the design used for CaH. A significant part of my time in the lab was spent maximizing the produc-

tion of CaH and and optimizing the rotational temperature and forward velocity distribution of the molecules. It is common to discover small problems after constructing the first cryostat - some of these problems can be addressed with minor upgrades that can be made along the way. Some other design improvements require major redesigns. These large upgrades can require months of design, fabrication, installation, and optimization. I inherited much of the cryostat used in this experiment from the BaH experiment [155, 57, 135]. I will describe the original design and the upgrades I made to transition to CaH cooling.

A molecular buffer-gas cryostat is constructed by building a chamber with excellent thermal shielding, cryogenic refrigeration, and vacuum pumping. The molecular species sample is inserted into the inner-most region of the cryostat in a chamber called the cell. The cell has a gas inlet into which a small amount of He buffer gas is flowed continuously. The cryostat must have optical access to permit the laser ablation of the sample and measure molecule production and dynamics. Finally, the molecular buffer-gas cryostat must be connected to the beam-line of the experiment so that molecules produced in-cell can flow into the experiment region of the vacuum system.

3.2.1 Liquid Helium Cooling and Thermal Shielding

As discussed in chapter 2, optical cycling with CaH requires driving transitions between the $N = 1$ and $N = 0$ rotational bands. Therefore, the molecular ensemble must be at low enough temperature to rotationally cool the ablated molecules and maximize the population in the $N = 1$ rotational level. This immediately eliminates conventional atomic sources such as ovens. A hot cell, will transfer much of the molecular population into states with $N > 1$, while a cell that is too cold will primarily populate the $N = 0$ state. For CaH, the optimal rotational temperature is approximately 14K. Reaching this low temperature requires cryogenic helium refrigerant and high levels of thermal shielding to prevent black body radiation from putting a high thermal load on the cell.

The Pulse Tube Refrigerator

Refrigeration to 4K and below requires the use of liquid helium refrigerant through either a closed loop Pulse Tube Refrigerator (PTR) or through an evaporative open loop refrigerator. Open loop helium refrigerators are very costly to operate because you fill a pot with liquid helium and then pump on it to force evaporate and carry heat with it. At the time of this thesis, the best closed loop PTR systems can reach temperatures of 2K while evaporative Helium fridges can reach several hundred millikelvin. My experiment was initially designed for working with BaH and as such was optimized to run at 4K according to the mass of the molecule and the rotational level spacing [155, 57, 156]. When BaH was abandoned in favor of CaH, I had to reuse much of the core BaH experiment architecture and re-purpose it to the new molecule. I used a two stage PTR manufactured by Cryomech (model number PTR-415) built for the BaH experiment. This model PTR has a 40K stage with 40W of cooling power and a smaller 4K stage with a cooling power of 1.5W.

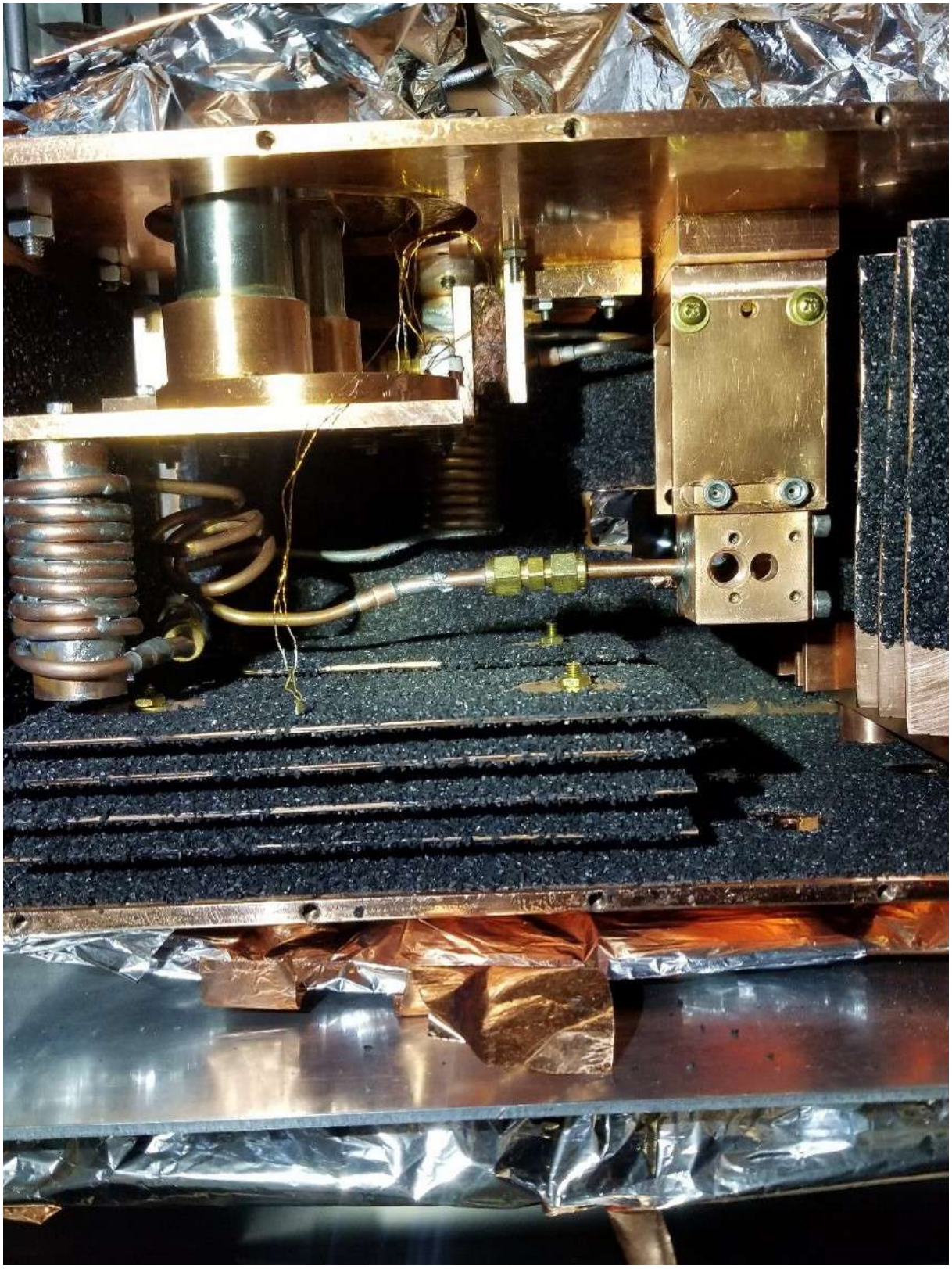

Figure 3.3: I show the 4K region. In the top left 4K PTR head can be seen with the helium bobbins bolted below it. The helium buffer gas line can be seen wound around the bobbins and then connecting to the ablation cell on the right. The cryogenic charcoal sorbs can be seen on the bottom and the right portions of the 4K region. Layers of aluminized mylar can be observed wrapping around the 4K shield.

Shielding

Cooling a cryostat to 4K requires pumping the heat out from it faster than the surrounding environment can flow heat back in. This isolation is primarily accomplished by separating the coldest regions of the experiment from the laboratory environment by placing them in vacuum to eliminate convection and conduction. The next significant source of heat transfer in our cryostat is black-body radiation from the vacuum chamber's room temperature surface. This thermal radiation is eliminated through layers of radiative shielding that the cryogenic cell and PTR assembly reside in. Practically, this is accomplished by placing a 40K box around the cell. The radiative flux Q_{rad} on each shield layer can be calculated as [136]:

$$Q_{rad} = \frac{\sigma A_1 (T_2^4 - T_1^4)}{\frac{1}{\epsilon_1} + \frac{A_1}{A_2}(\frac{1}{\epsilon_2} - 1)} \tag{3.1}$$

where A_1 and A_2 are the inner and outer shield surface areas. T_1 and T_2 are the inner and outer temperatures, while ϵ_1 and ϵ_2 are the emissivity of each surface. The radiative heat load from the room temperature walls of the vacuum chamber is about 30 W. This heat load would overpower the 4K cold head of the PTR. This radiative transfer is eliminated by placing a black body shield between the vacuum chamber walls and the cryogenic cell. This radiative shield consists of an aluminum box thermally anchored to the 40K head of the PTR assembly, which has a much higher heat capacity. This does not eliminate black body radiation from heating the 4K cell, but the 40K surface radiates one thousand times less thermal energy than the room temperature vacuum chamber. The radiative absorption of each layer depends on the shield material and the surface finish. We minimize the absorbance of all inner surfaces by polishing them so they reflect away as much heat as possible. I further reduced the thermal absorption by wrapping the exterior of the 40K shield in aluminized Mylar to reflect some of the room temperature BBR of the vacuum chamber. The addition of shielding lowers the radiative heat load to the 4K region to less than 0.01W. This leaves radiation through the windows that provide optical access to the cell as the largest heat load. This optical access is required and can not be completely eliminated.

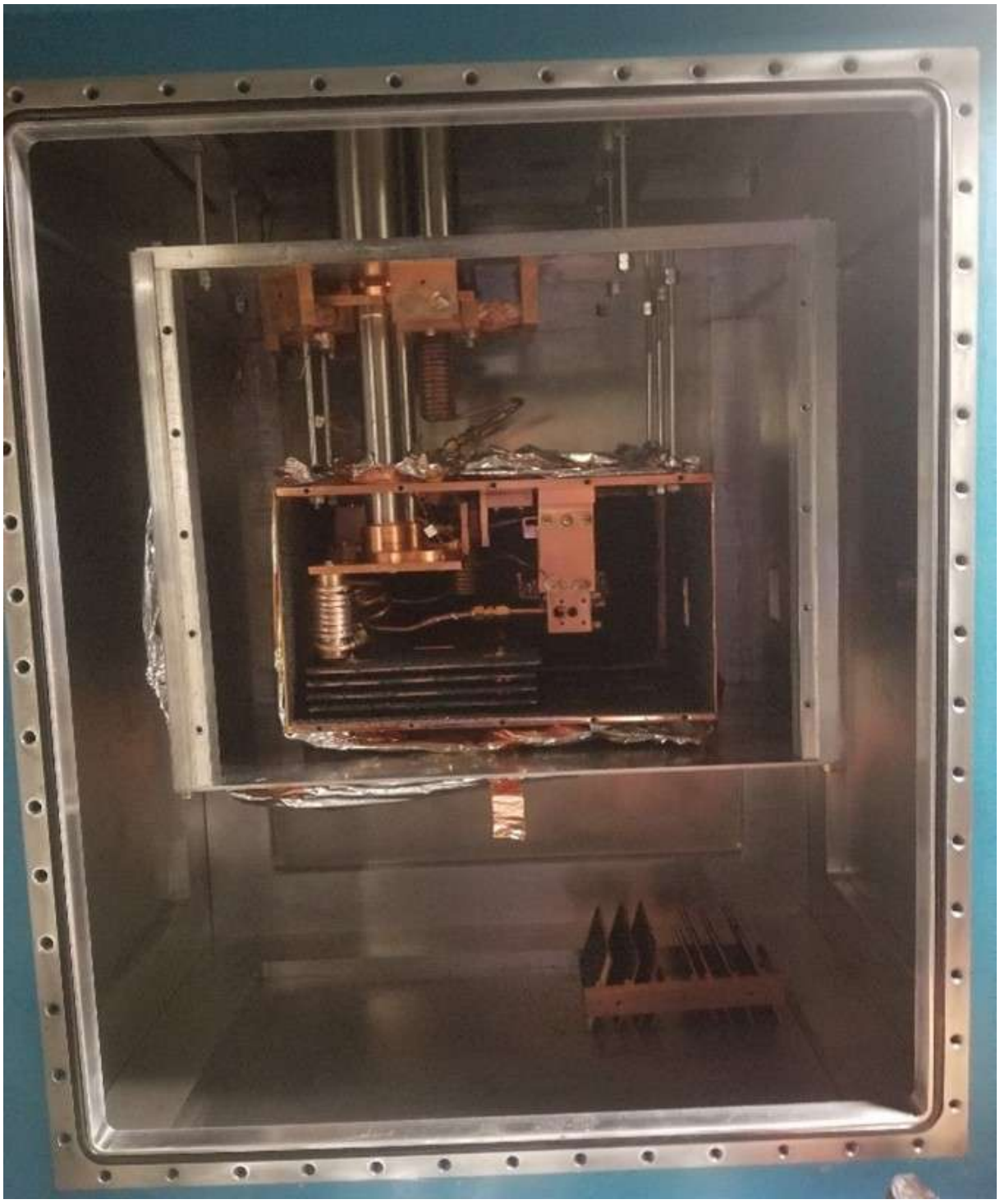

Figure 3.4: I show all the layers of the cryostat after we opened the system for cell maintenance. The room temperature shield can be seen on the outer edge along with the rubber gasket which provides the air-tight seal. A bank of cryogenic charcoal sorb fins can be seen resting on the base of the room temperature shield. Within , the aluminum 40K shield can be seen encasing the copper 4K region. Within, the 4K region one may observe the 4K PTR head, the ablation cell, the helium buffer gas bobbins, and additional charcoal sorbs.

Buffer Gas Injection

Hot molecules produced during ablation rely on the cold helium buffer gas to cool down. Therefore, it is essential to cool the helium buffer gas as much as possible before injecting it into the cell. This is accomplished by winding the buffer gas inlet tubing around bobbins that are thermally anchored to the 40k and 4K shields. The 3/16" inch diameter OFHC copper piping is brazed to one inch copper rods that are bolted to the PTR cold heads. The temperature of the helium when it reaches the cell is approximately 12K based on the rotational spectroscopy we performed, where I assumed that the molecular rotational temperature thermalized to the helium temperature. Further cooling would require extra bobbins in the 4K section, which would not fit in the 4K shield and introduce additional heat load to the PTR.

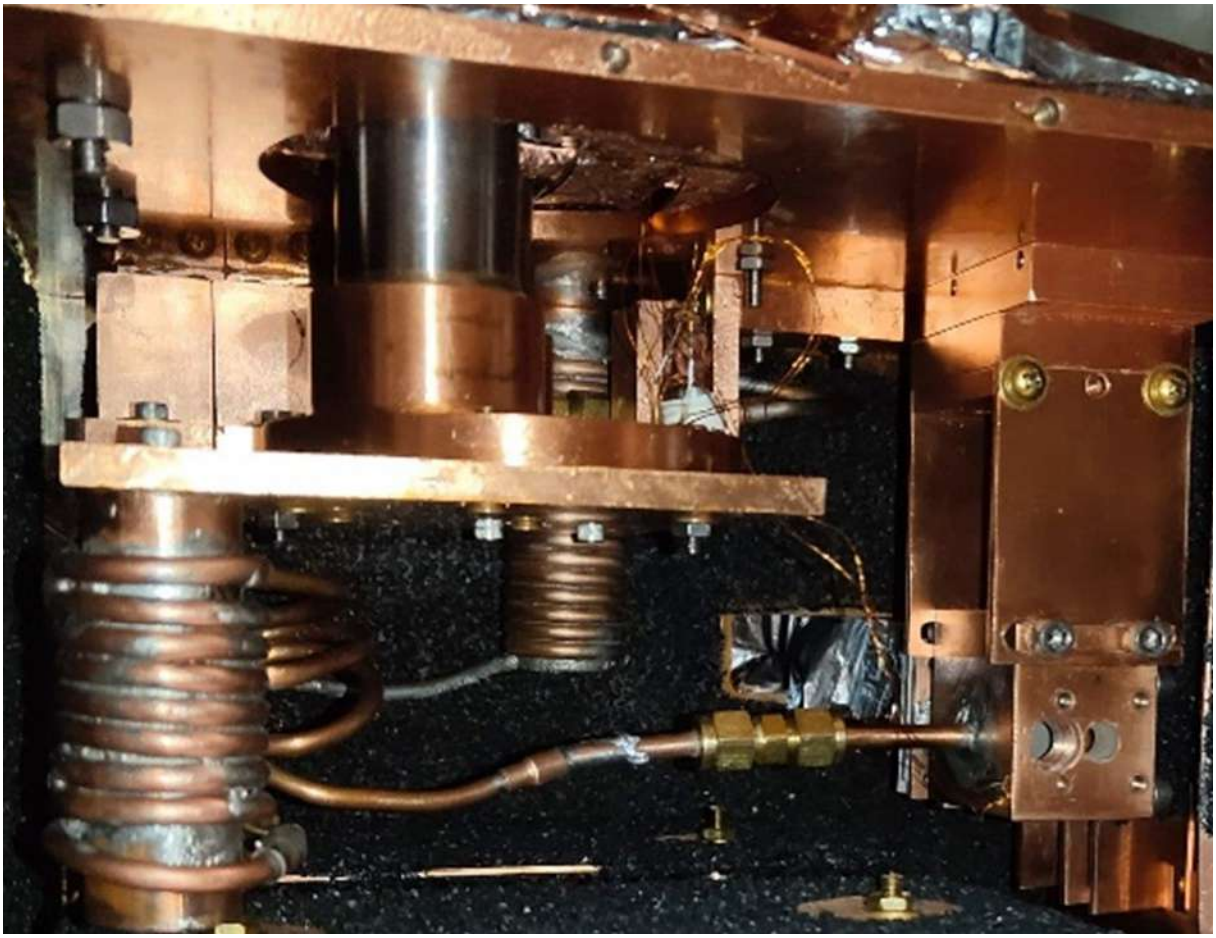

The buffer gas flow was controlled with two different mass flow controllers (AERA FC780C

and MKS 1259C). The mass controllers measure the amount of helium flowing into the cell in units of standard cubic centimeters per minute (sccm) defined as the mass of helium that fills one cubic centimeter at room pressure and temperature. We use the mass controllers to probe two different buffer gas flow regimes. The AERA provided low flow (0-20 sccm) control, while high flow (20-100 sccm) was provided by the MKS controller. The in-cell absorption signal was measured to be proportional to the buffer gas flow rate. Therefore, early in-cell spectroscopic measurements were done in the high flow regime using the MKS flow controller. The in-beam molecule signal was maximized at a helium buffer-gas flow between 1 and 6 sccm with the highest flux of low velocity molecules corresponding to lower He flow. All in-beam data was taken using the AERA controller. Early designs of the buffer gas injection system were often prone to clogs forming from frozen contaminants in the helium line. The cryogenic temperatures within the cryostat will freeze anything other than helium. Any air or humidity that entered the helium line from leaks or swapping helium tanks, would result in a clog. The leaks were remedied by redoing the connections in the helium line and ensuring everything was tight. In addition, the mass controller not in-use was sealed off from room pressure with an angle valve and a cap on the end of the tubing to prevent leaks. However, the contamination from swapping helium bottles will only be fixed when a bleed off valve is added before the mass controllers. This would enable us to bleed off any room air that enters the helium line after swapping He tanks. At the time of this thesis a bleed-off valve has not yet been added because the improvements I made have been enough to prevent clogs.

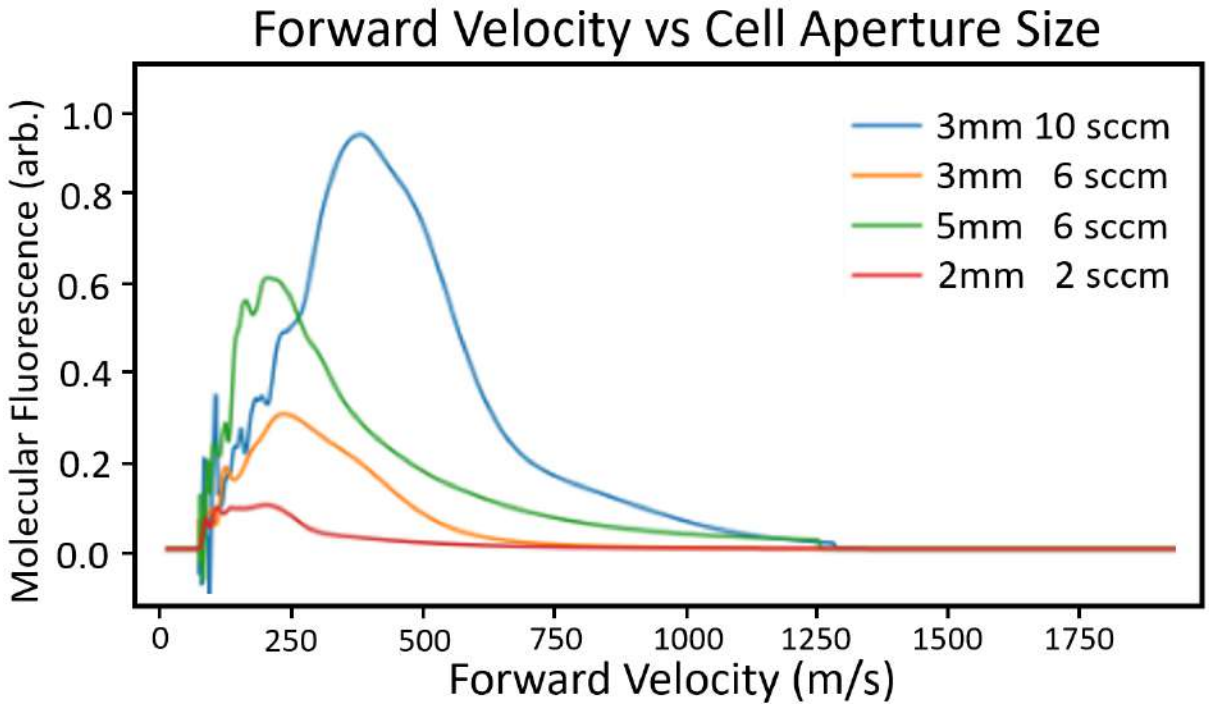

Figure 3.5: I show the effect of three cell aperture sizes at a variety of helium flow rates. We found that the 5mm aperture with 6 sccm of Helium buffer-gas flow produced the densest beam of CaH molecules below 250m/s.

The 4K Cell

The cryogenic cell lies at the core of the experiment, pumping molecules into the experiment region with each ablation pulse. The cell is made with copper 101 (OFHC copper) for the best thermal conduction and has an internal cylindrical chamber with a diameter of 25mm and a depth of 32mm. The CaH_2 target is epoxied onto a copper screw which is inserted into the cell opposite to the ablation laser window. From this position, the ablation laser has full optical access to the sample surface and can be rastered across the sample to average over the local variations between ablation spots. The helium buffer gas inlet is immediately next to the sample holder and continuously flows 1 sccm of helium into the cell. A collimating aperture is opposite to the helium inlet which allows a beam of molecules produced in cell to proceed to the experiment chamber. Due to the radiative flux hitting the chamber through the view ports, the minimum temperature the cell can reach is 6K. Lowering this temperature to the specified 4K would require making the windows to the cell

smaller or adding custom NBK7 windows to the 40K shield.

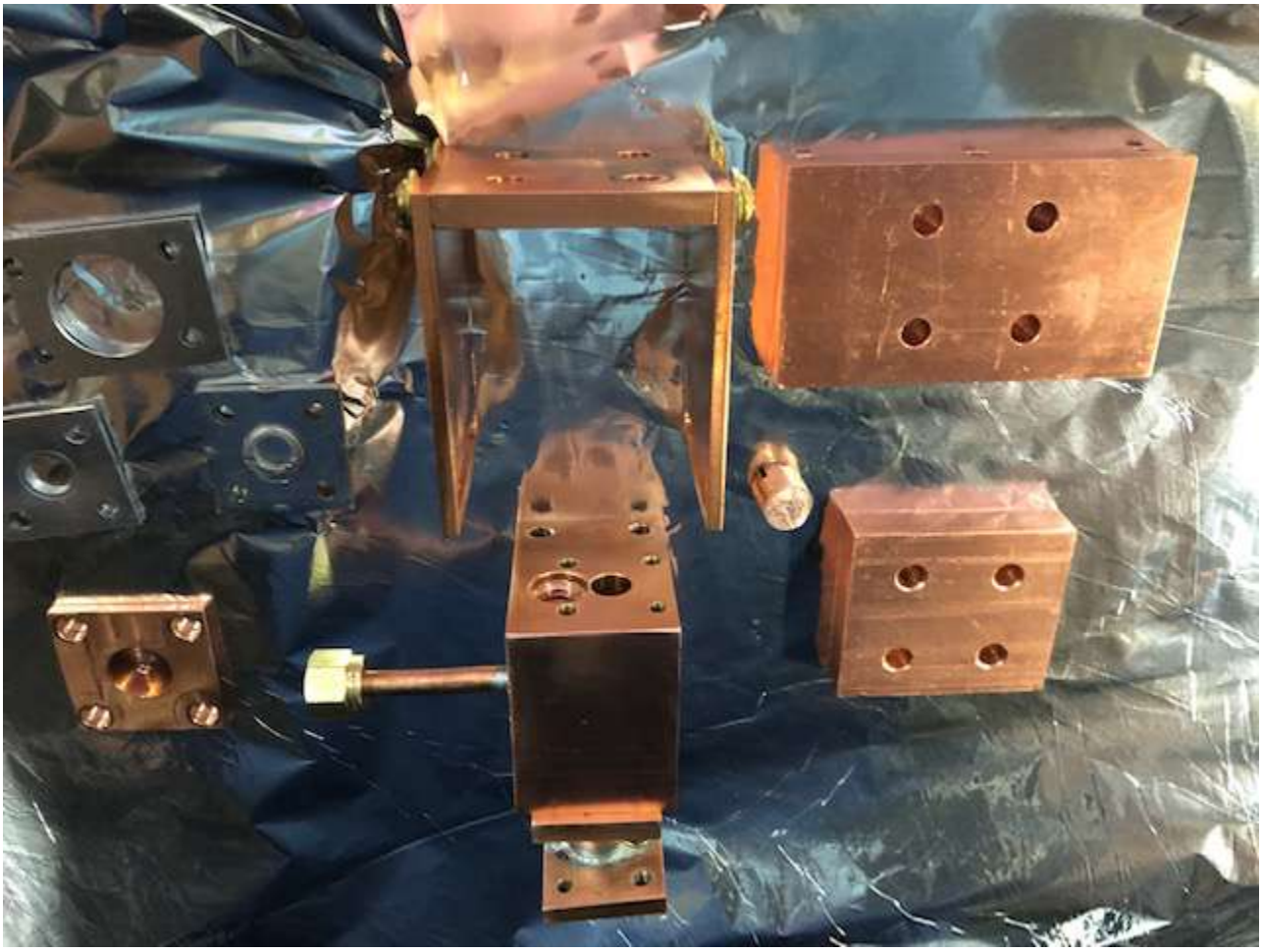

Figure 3.6: I show the components of the cell assembly after it was taken out of the cryostat. I show the cell, the cell windows, the cell aperture, the sample holder, and the thermal coupling plates.

The volume and dimensions of the cell have a significant impact on the molecular yield and temperature in the beamline of the experiment. Intuitively, the smaller the cell volume and the larger the aperture diameter, the higher the flux of molecules that exit the cell. However, one is not seeking to solely maximize the total molecular flux, but rather the molecular flux at low forward velocities [110]. This introduces a new timescale into the system during which the hot ablation plume thermalizes with the cold helium buffer gas. If the cell is too small, the molecules lack sufficient time to thermalize and the cell primarily emits molecules at extremely high velocities. If the cell aperture is too small, molecules diffuse to the cell walls where cryopumping adheres

them to the copper surface. his can significantly decrease the molecular yield of the cell. On the other hand, if the exit aperture is too big, then the extraction time is too short and molecules don't thermalize. The balance between the extraction efficiency and the thermalization efficiency can be characterized as a ratio between the diffusion time τ_{diff} (the time required for thermalization from collisions with the buffer gas) and the extraction time $\tau_{extract}$ [110, 124, 136, 155]. This ratio, labeled γ is given as:

$$\gamma_{cell} = \frac{\tau_{diff}}{\tau_{extract}} \approx \frac{\sigma_0 f_{He}}{L_{cell}\bar{v}_{He}} \tag{3.2}$$

where σ_0 is the collision cross-section of the helium-CaH collisions, while f_{He} is the helium buffer gas flow rate. The extraction time is expressed in terms of the cell length L_{cell} and the average thermal velocity of the helium buffer gas $\bar{v}_{He}$. I experimentally optimized the characteristics of the cell that could be modified without a complete overhaul of the cryostat. Experimental parameters that could easily be varied were the length of the cryogenic cell, the aperture size, the ablation laser power, and the temperature of the cell. The 5mm aperture that was found to maximize the molecule population below 150 m/s. The performance of the cell aperture is very dependant on the helium flow rate into the cell.

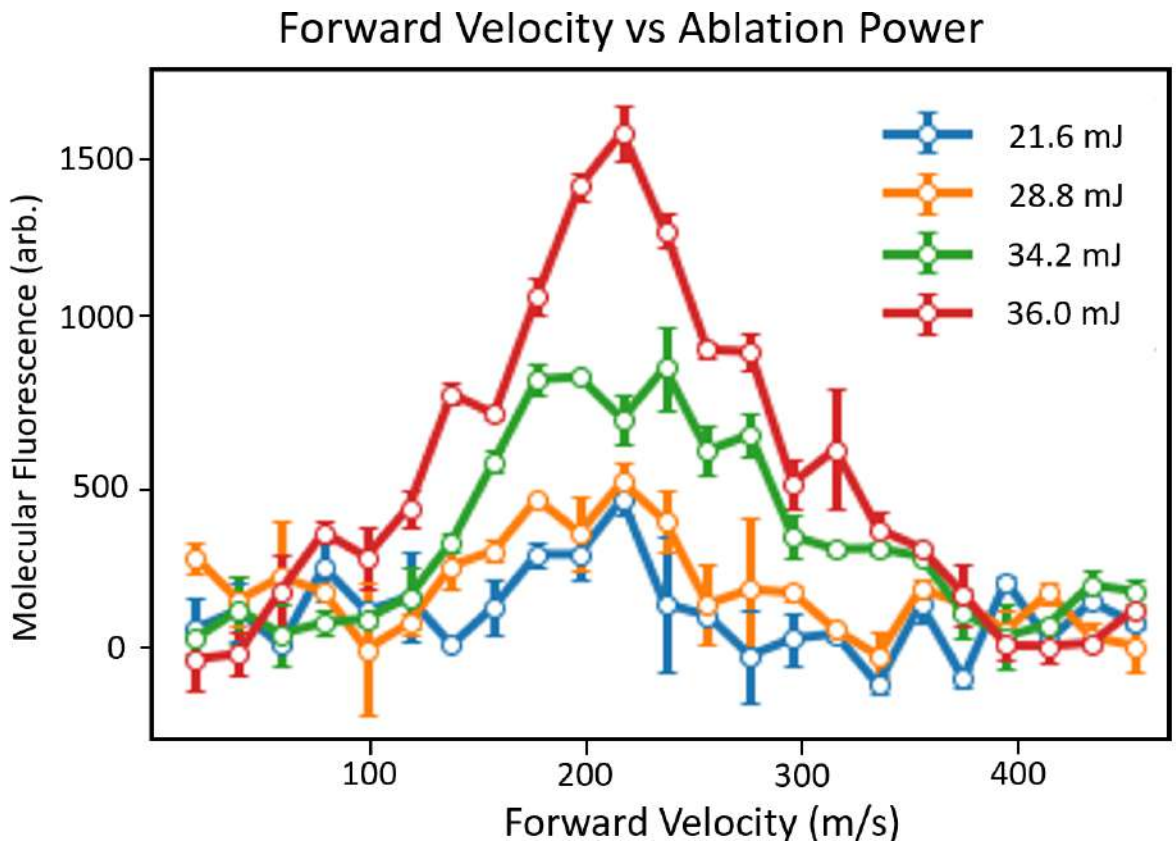

(a) Here I show the effect of ablation laser power.

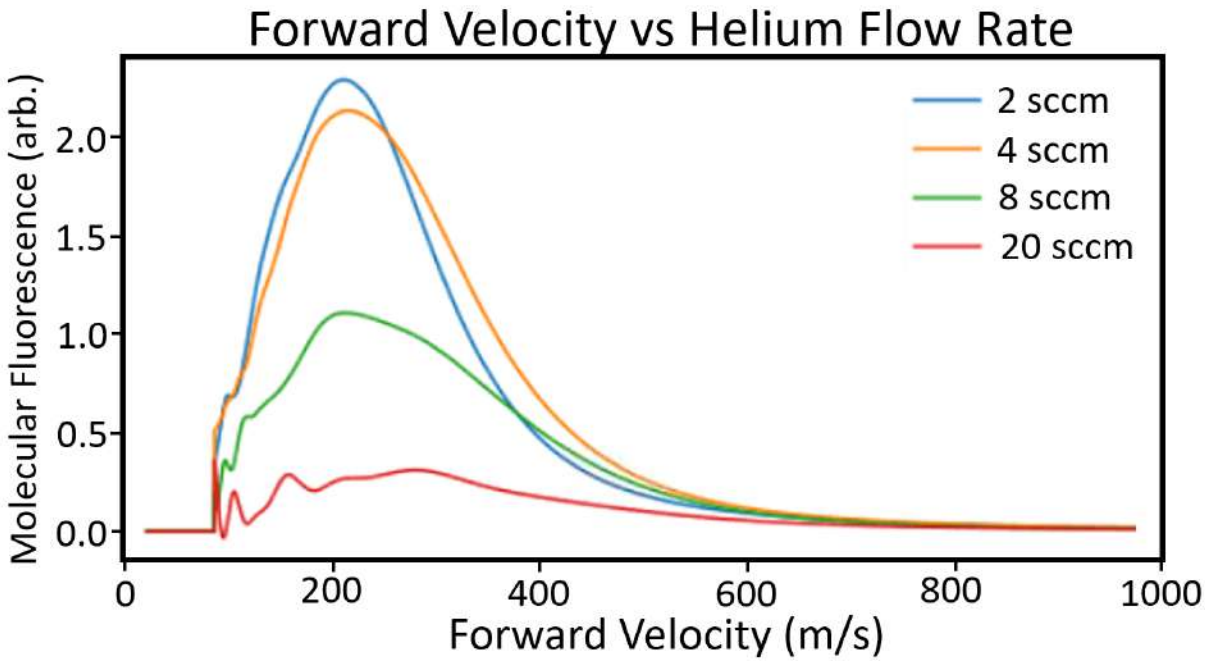

(b) Here I show the effect of ablation helium flow rate.

Figure 3.7: The He flow rate can be seen to greatly affect the velocity distribution, while the ablation laser power effects the molecular yield and had little impact on the velocity profile.

I experimentally optimized the cell temperature to maximize the molecular population in the $N = 1$ rotational state. This optimization was performed by raising the temperature above the cell baseline with cryogenic resistive heaters and then sweeping helium flow rates and ablation energies while measuring the population in the $N = 1$ rotational level. We were unable to lower the temperature of the cell past 6K without significantly redesigning the cryostat. The minimum helium buffer gas temperature was limited at 12K due to the limited time the buffer gas has to thermalize before flowing into the cell. Reducing this temperature would have required adding new bobbins which would not have fit in the 4K shield chamber. This was deemed unnecessary due to the higher $N = 0$ population that was observed when operating at the system's minimum temperature. The primary sources of heating to the cell were the black body radiation from the large optical access windows and the overall large surface area of the 40K shield. A smaller 40K shield would have benefited the cryostat performance but would have required completely reconstructing the cryostat.

I have measured the molecular beam velocity distribution using direct detection of CaH molecules via the $X - B$ transition in addition to Doppler sensitive spectroscopy with Ca atoms. We began with absorption time of flight profiles of CaH molecules detected as they exited the cell aperture and then remeasured the fluorescence of those same molecules 92cm downstream. We calculate the velocity profiles by applying a Weiner deconvolution algorithm to the initial time of flight and the final time of flight profile after the beam's ballistic propagation [155, 57]. The mode of the velocity distribution calculated in this manner was robust against variations in the Weiner parameter and agreed with the mode of the Ca velocity distribution. However, the high velocity portion of the distributions provided by the deconvolution method was found to be very sensitive to the initial values of this parameter. We chose to primarily use the Ca measurement due to its agreement with the deconvolution method, its consistency, and the lack of additional analysis algorithms.

We did not perform Doppler sensitive 45 degree fluorescence directly on CaH because we lacked a well-blackened, low background scatter chamber with this off-axis degree of optical access. Velocity sensitive Doppler spectroscopy requires a high enough signal to noise to detect a

small velocity subset of the molecular beam. However, the lack of an appropriate detection chamber, meant that molecules would not be seen over the background laser scatter in the system. We decided not to invest in a chamber like this because of the good agreement between the two previously described velocity measurement techniques. Finally, we measured the thermalization and extraction dynamics of both Ca and CaH and found that they behaved almost identically in the 0-4 sccm buffer gas flow regime. This is in agreement with our intuition that the two species should display similar thermal properties because the masses of CaH and Ca differ by only one AMU.

Sample Preparation

The chemical sample at the heart of the cyrostat consists of a sample of CaH_2 of greater than 95% purity which is epoxied to the surface of a custom machined 0.75 inch OFHC copper screw. One sample change would often be enough for one to two months of data collection. I also experimented with pressed samples of ultra pure CaH_2 but I found that the pressed targets degraded in about a week of data-taking but provided a small increase in signal when freshly installed. Conversely, the 95% purity samples could last for months, but required a week of ablation to begin producing high yield beams. Samples were purchased from Sigma Aldritch and are available at `https://www.sigmaaldrich.com/US/en/substance/Calciumhydride42097789788`. The solid CaH_2 sample was a mixture of CaH_2 and a non-reactive binding agent of unknown composition that gave the samples the appearance of dry white clay. Higher purity samples are a fine crystalline powder.

The sample of CaH_2 was prepared in a glove box that was pressurized with nitrogen to prevent the contamination of the sample with moisture from the air. Upon opening the sample bottle, small pieces of about 3mm in diameter would be broken off using a dedicated pair of clean wire cutters. Once enough pieces to cover the sample holder tip were broken off, I would coat the tip of the sample holder in Locktight 495 instant superglue and use fine tweezers to gently place the CaH_2 rocks on the tip of the sample holder. I would leave the sample holder in the pressurized glove box for 30 minutes to allow the glue to cure before transferring the sample holder into the cell. The

process of transferring the sample holder from the glove box could be improved to further preserve sample integrity, but my protocol worked fine and was as follows. After allowing the glue to dry, I would begin flowing nitrogen into the 4k cell to displace any air in the cell (one should hear the sound of the nitrogen flowing out from the cell). Next I would remove the sample holder from the pressurized glove box and transport it to the cell while flowing nitrogen across the sample surface with a hand held nitrogen line. We performed tests to determine how quickly the CaH_2 sample would degrade in the presence of lab air. We measured that for the CaH_2 grain sizes used in this experiment, the sample would completely degrade in 45 minutes. Therefore, we do not believe that the 15 seconds required to transport the sample from the glovebox to the cell caused any significant damage to the sample.

The sample would be screwed into the cell as quickly as possible and nitrogen would continue to flow into the cell until all the thermal and vacuum shields were replaced and the scroll pump had been allowed to lower the cryostat pressure to about 1 Torr. At this point, the nitrogen flow to the cell would be turned off to allow the scroll pump to finish pumping down to 10^{-2} Torr. Finally, the turbo would be turned on to pump the chamber down to 10^{-5} Torr, before finally turning on the PTR. After cooling to baseline temperatures, the cryostat pressure was between 10^{-8} Torr and 10^{-7} depending on the state of the charcoal sorbs. The cryostat pressure would improve as contaminants from the room air exited the charcoal after temperature cycling.

Occasionally, I would disassemble the cell for cleaning by removing it from the 4K PTR head. It was our practice going back to the early days of the BaH experiment to clean the cell simply by tapping out the ablation debris and then blowing nitrogen in the cell to remove as much dust as possible. In 2021, we tried sanding away the ablation debris that coated the interior of the cell. This was inspired word of mouth advice from other buffer-gas experiments that were able to lower their beam temperature by exposing the bare copper surface. This however, was catastrophic to our cryogenic cell efficiency. After sanding we were barely able to see in-cell absorption, which had decreased from approximately 25% absorption down to less than 1%. Meanwhile, we were completely unable to see the molecular beam in the experiment chamber. After months of trying

new ablation parameters, we finally recovered the beam and attained comparable in-cell to the previously seen levels. It is not immediately clear what the root cause of the loss of signal was. I suggested testing the reactivity hypothesis by electroplating a spare cell with gold or a CaH paste to eliminate the potential for chemical reactions. We did not attempt either of these ideas due to the long fabrication time of a new cell and by the gradual return of the molecular beam as the interior surface of the cell was re-coated with ablation debris.

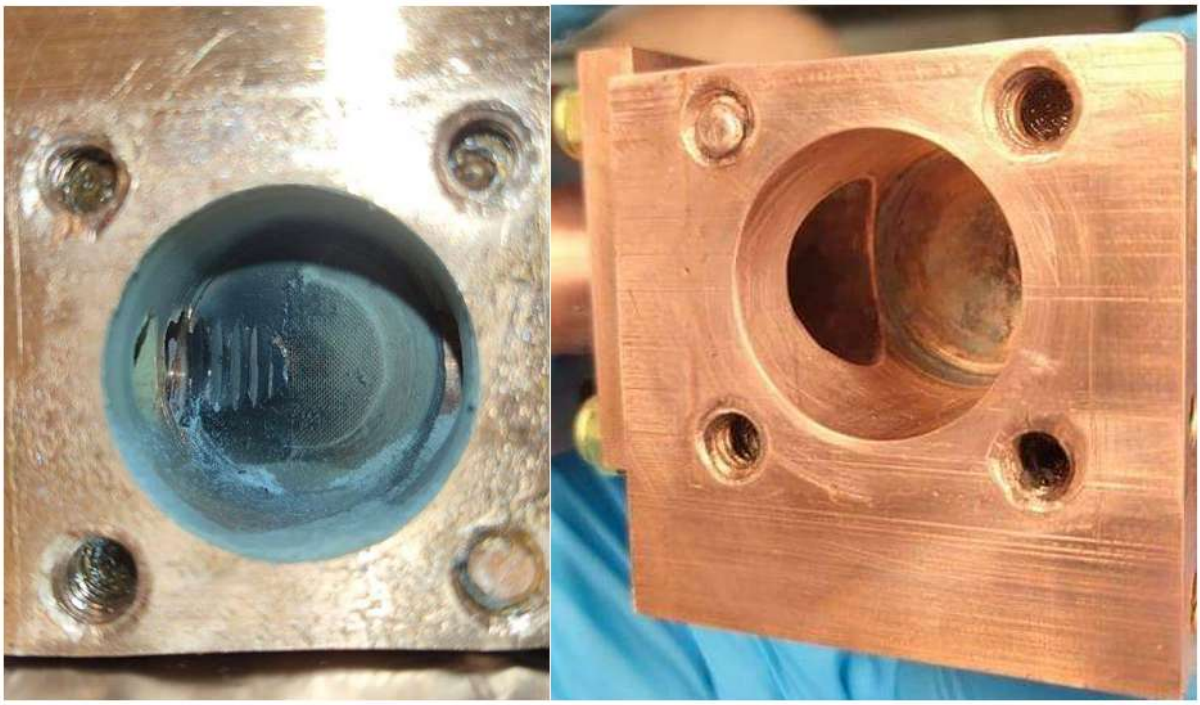

Figure 3.8: On the left, I show images of a cell after weeks of ablation. The powder seen at the bottom of the cell is debris blasted off the sample by the focused ablation laser. On the right, I show the cell after we sanded it and destroyed the beam.

We would change cell windows while the cryostat was open for a sample change. The cell windows quickly become coated with ablation debris, restricting the optical access to the cell. Therefore, it is important to detach them from the cell from time to time and wipe them down with isopropyl alcohol to remove any visible sediment. It is also possible to crack the cell windows with the ablation laser if the laser is accidentally focused onto the window. A cracked cell window must be replaced at the next sample change, but there is no need to panic as I have managed to continue taking data for weeks with a cracked cell window until the sample was naturally depleted.

A cracked window will harm the in cell absorption signal, but should not effect the molecular beam yield. Recently, we modified the ablation laser system, placing the focusing laser on a 1D translation stage. The stage's travel is limited to prevent the laser from ever being focused on the windows.

3.3 Vacuum System

It is essential that the molecular beam experiments take place in a vacuum. Therefore, careful consideration must be given to the design of the system because it will need to pump out all the buffer gas exiting the 4K region to prevent beam collisions. Cryogenic buffer gas experiments operate in two different pressure and temperature regimes. The vacuum system designed for the cryogenic cell must be capable of pumping out high volumes of gas while at 4 Kelvin to compensate for the continuous flow of buffer-gas into the ablation cell. The cryogenic buffer gas system however, does not need to reach as low a pressure as the beam line and is commonly 10^{-6} Torr while flowing He and cold. On the other hand, the beamline is maintained at 10^{-8} Torr. I have seen a complete loss of signal resulting from buffer gas background collisions as the beam exits the cryostat and into the beamline. In the following section I will describe the vacuum system used in both the cryostat and beamline.

Figure 3.9: I show a cross section of a turbo pump. One may observe the many layers of turbo fans that change angle to gradually force gas out from the vacuum system through the flange on the bottom left. [157]

3.3.1 Cryo Vacuum

The cryogenic vacuum is the easier vacuum system to work with due to extremely low temperatures it operates at. At 4K every contaminant except the helium buffer gas sticks to any surface it collides with. The cryogenic temperatures also prevent any contaminants from outgassing. We take advantage of the adhesion of gases at these temperatures to help lower the cryostat pressure. Much of the pumping of the excess buffer gas in the cryogenic chamber is handled by charcoal sorbs placed in the vacuum chamber. The carbon matrix in the charcoal acts as a sponge to trap background gas when the charcoal is maintained at temperatures less than 14 kelvin. Any gas that escapes to the higher temperature regions of the cryostat is pumped on by two turbos. We use a scroll pump to back the turbos that are bolted on the exterior of the vacuum chamber.

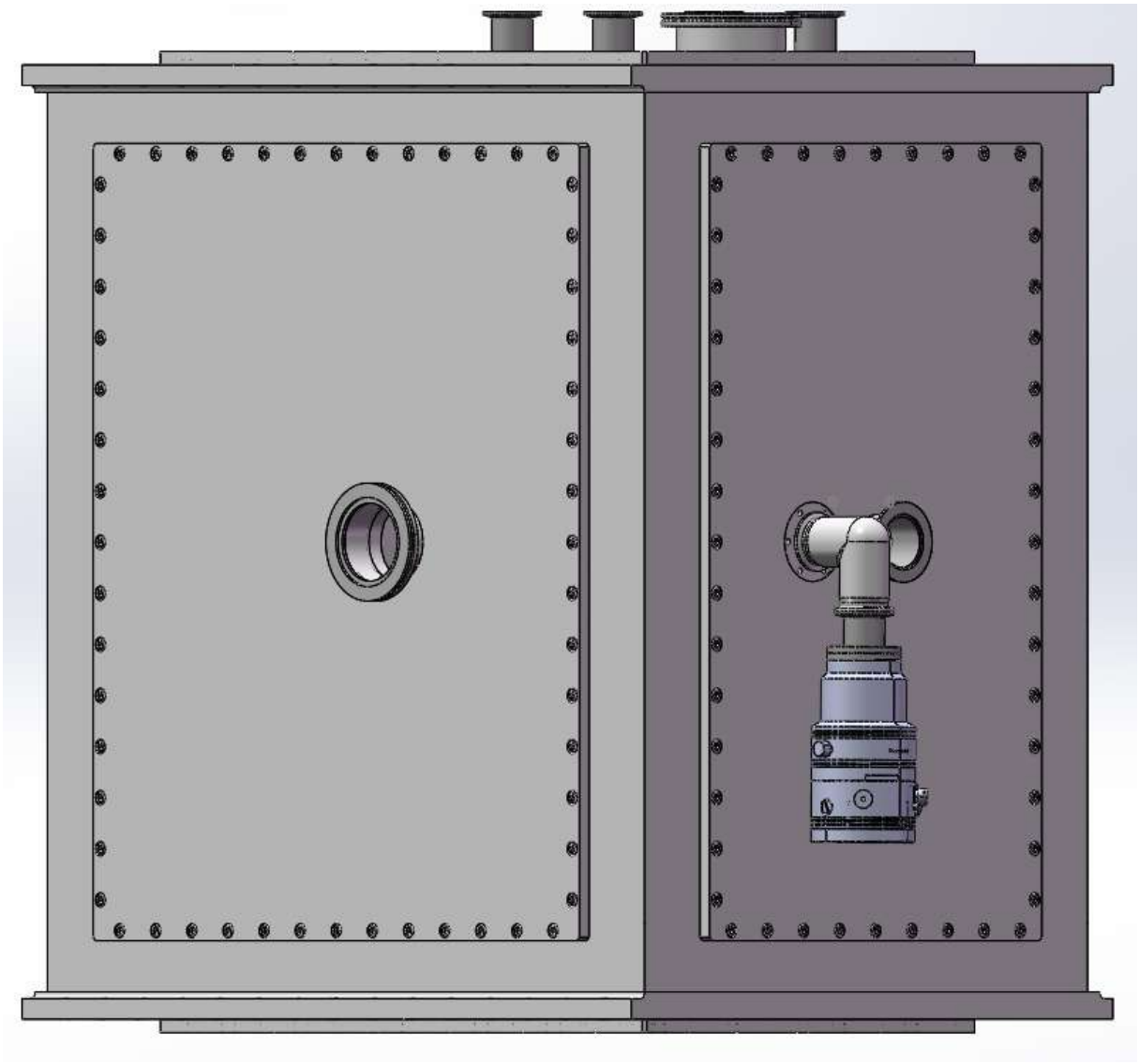

Figure 3.10: Here I show a CAD drawing of the cryostat which has been modified to mount an additional turbo next to the beam-line. We decided to design and manufacture this front panel to try and avoid any pressure build up at the transition from the cryostat to the molecular beam. This upgrade has not yet been implemented but will be added before slowing experiments begin.

Charcoal Sorbs

The charcoal sorbs provide the majority of the vacuum pumping in the 4K region. However, because charcoal sorbs are absorbers, there is a limit to the amount of He gas that can be trapped. The sorbs porous matrix can become saturated and cease to absorb He. When this occurs, the cryostat pressure quickly rises. The increase in pressure can cause thermal coupling between

the cryogenic shield layers, further increasing the temperature of the cryostat. If the cryostat temperature rises past 14 kelvin, the sorbs will begin to release helium. This can be prevented by periodically heating the charcoal to purge the trapped He. All of the trapped helium to escapes the charcoal to be removed by the turbos. I found that increasing the number of charcoal sorbs did not dramatically increase the molecular yield. However, increasing the surface area covered in charcoal dramatically increased the run time of the experiment by increasing the amount of time one may flow helium before warming up the cryostat. Adding cryogenic heaters to the shield layers of the cryostat may reduce the time required to temperature cycle the cryostat and purge the sorbs. Resistive cartridge heaters are sold by Lakeshore Cryogenics and must be epoxied into a copper housing that can be thermally anchored wherever heating is desired. I reduced the temperature cycling time by half by adding heaters to the cryostat, allowing the sorbs to be purged overnight.

Sorbs are constructed by purchasing ultra-high purity charcoal of medium grain-size (approximately 3mm diameter) and then adhering a layer onto OFHC copper sheets using a thermally conductive cryogenic epoxy such as Stycast 2850FT. Multiple copper-sorb sheets are bolted together with copper spacers between them and then thermally anchored to the 4K shield. One should fit as many sorb sheets in the 4K region as are allowed by the cryostat design.

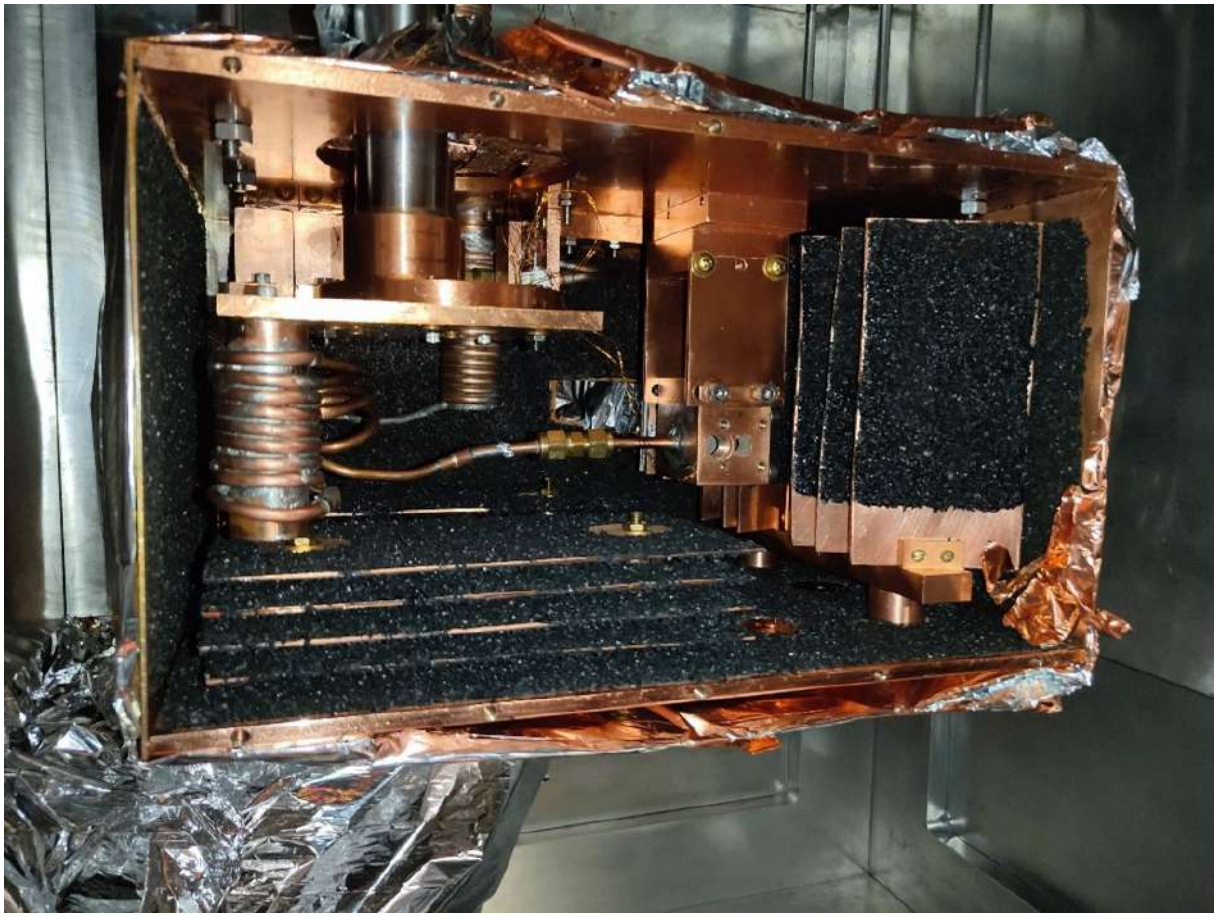

Dual Turbo

Additional vacuum pumps must be placed on the cryostat to remove the helium buffer gas that escapes the 4K regions. This prevents a pressure build up near the room temperature shield that knocks CaH molecules out of the beam and raises the beam-line pressure. Two turbo pumps are bolted to the outside of the vacuum chamber. A Pfieffer TPU-170 turbo pump attached to the top of the cryostat provides the majority of the pumping. I propose an improvement to the cryostat by adding an Agilent TwisTorr 84 to the front panel of the vacuum chamber adjacent to the gate valve connecting to the beam-line chamber. This additional turbo would pump out gas reflected off the velocity filtering aperture prior to the interaction region.

3.3.2 Beam Region Vacuum

The vacuum quality in the beam region of the experiment is key to preventing background collisions and preserving the molecular beam flow. As mentioned earlier, a background gas build up in the vacuum system can completely eliminate the molecule beam. The most recent iteration of the vacuum system is composed of three sub-chambers: the transverse cooling chamber, the clean-up chamber, and the detection chamber. We placed two turbos at the start and end of of the vacuum chamber. The first turbo prevents pressure build up at the beginning of the beamline, while the final turbo pumps out the residual helium at the end of the system. Both turbos used in the beamline are Pfieffer HiPace 300. The combination of these pumps allow us to maintain a baseline beamline pressure of 10^{-8} Torr and a pressure of 10^{-7} Torr while flowing buffer-gas. This vacuum system will need to be modified when including a MOT chamber with the primary change being the addition of a titanium sublimation pump directly attached to the MOT chamber to allow the chamber to reach a pressure less than 10^{-9} Torr.

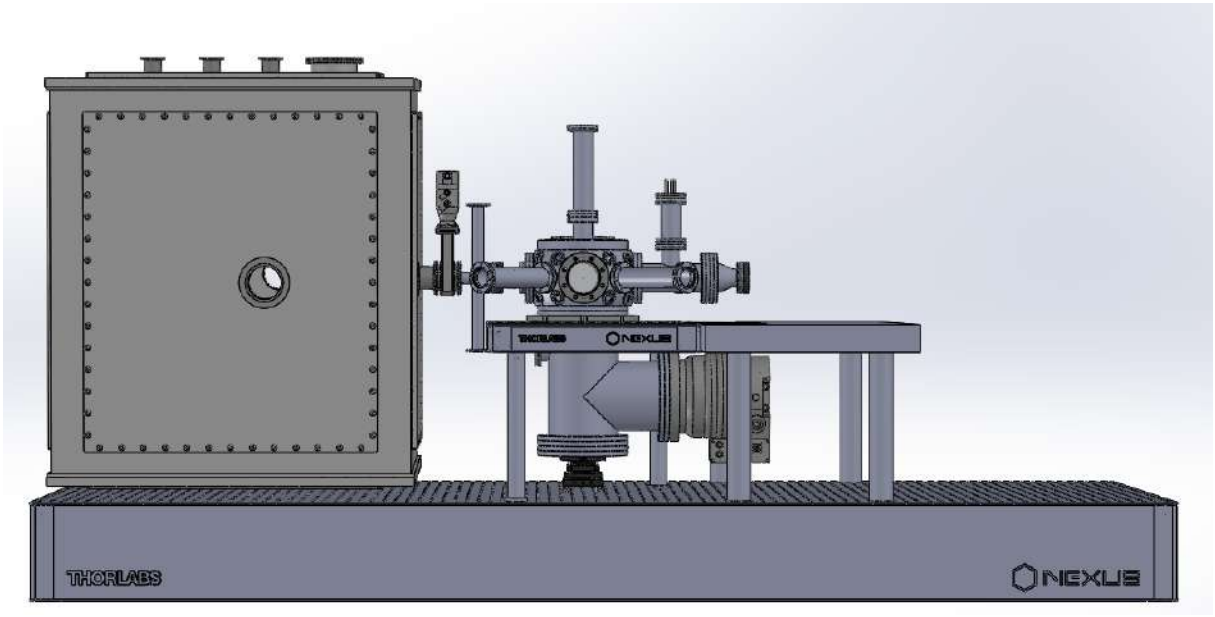

Figure 3.11: A schematic of the planned MOT assembly that I helped design.

Cooling Chamber

I designed and built the transverse cooling chamber with our old post-doc Ivan Kozyrev. The chamber was assembled separately and the vacuum performance was confirmed before installation on the beam-line. The chamber was machined out of 316 stainless steel by Precision Cryo and consists of two KF mounting points to the molecular beam chamber with four custom windows clamped on to provide optical access. The windows are sealed to the chamber with rubber O-rings that provide a seal down to 10^{-8} Torr. These windows were dual antireflection coated for use with red and near infrared lasers. Coating was provided by the company Casix based in China with a pre-COVID lead time of 6 months. Due to supply chain disruptions, it is unclear if replacement windows could be coated at all within a reasonable amount of time. Therefore, these windows must be treated with as much care as possible.

I also wound air-cooled magnetic field coils to remix the molecules for both Doppler and Sisyphus cooling. The top and bottom coils each contain 40 windings made from 15 AWG magnetic wire, while the coils generating the horizontal field only use 10 windings of the same wire. The vertical coils produce the field for magnetically assisted Sisyphus cooling, while the horizontal field coils are used to compensate for the Earth's magnetic field. I chose to make these coils air cooled to reduce experimental complexity and because we only needed a field of a few Gauss for cooling. I have operated these coils all the way up to 10 A, but the system should not be operated for extended periods of time at currents above 7 A due to heating in the coils. When taking high magnetic field data, I would turn on the coils shortly before beginning a data set and immediately turn down the current once the data was recorded. This allowed me to create a maximum field strength of 7 Gauss (10 A).

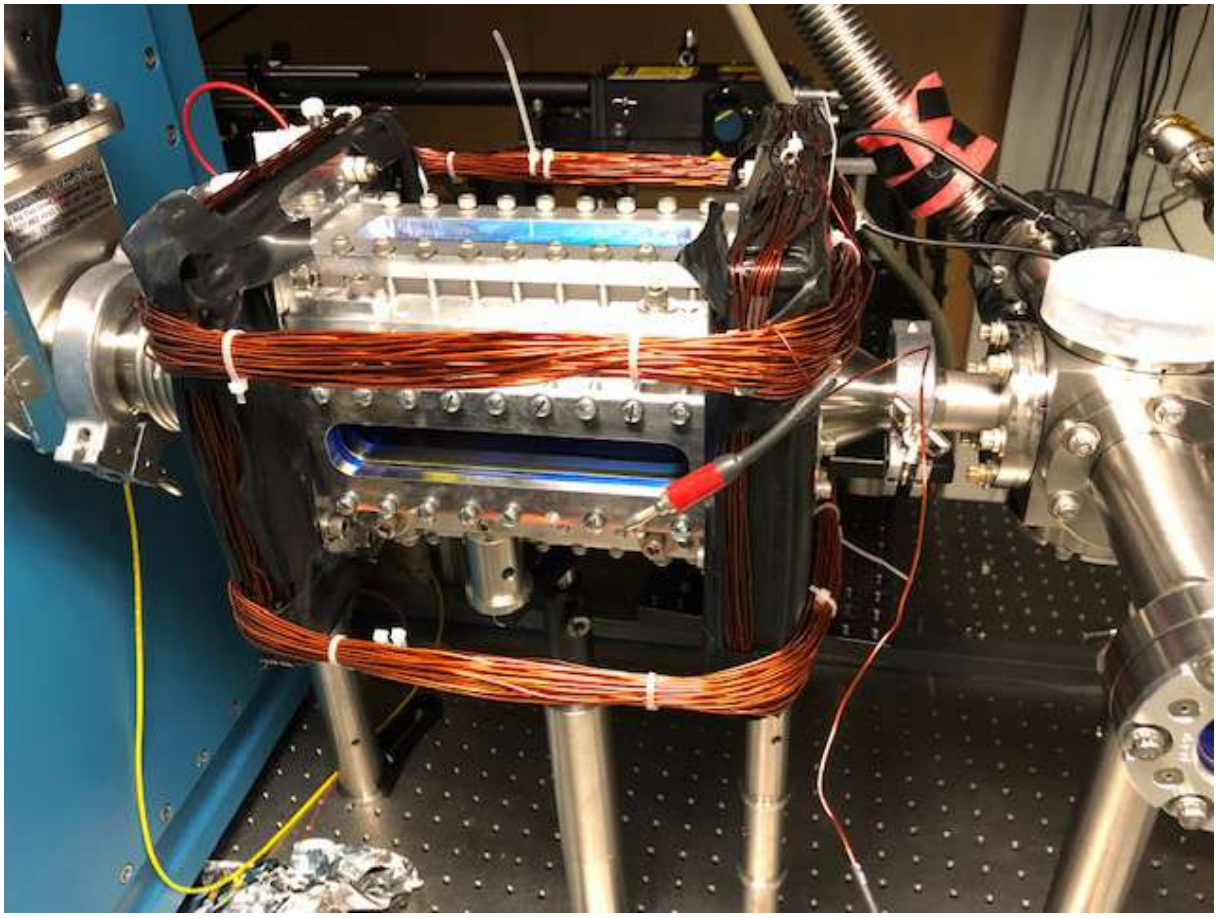

Figure 3.12: I show the interaction region vacuum chamber I helped design and assemble. The 12cm long windows can be seen in addition to the vertical and horizontal magnetic field coils that I wound.

Detection Chamber

Molecules are detected in the final chamber of the beam-line. The detection chamber is built around a CF 2.75 cube. One of the horizontal sides of this cube is used to connect the chamber to the beam line. The opposite face of the cube was used to mount the final turbo pump. The top and bottom faces have AR coated windows. One window provides optical access to the EMCCD collection optics used to measure the geometric properties of the molecular beam. A photomultiplier tube (PMT) is bolted on the other window to provide time of flight information. The imaging system will be described in depth later in this chapter. Finally, the fluorescence detection laser passes through the final pair of horizontal windows allowing us to detect the molecule beam. Background

scatter is a major source of noise when detecting fluorescence at the same wavelength as the probe laser. This laser scatter is mitigated by bolting on 20cm nipples to the chamber and moving the laser windows far from the center of the detection chamber. This eliminates line of sight scatter and massively reduces background scatter. We took it one step further and included light baffles within the 20cm nipples to further eliminate window scatter. Finally, the entire chamber was painted black using UHV compatible black paint. The baffles were blackened by growing copper oxide on the copper gaskets to provide the best absorption.

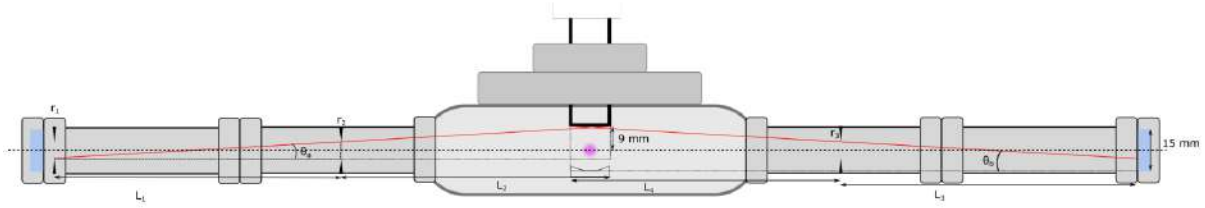

Figure 3.13: I show a transverse cross-section of the detection chamber. The windows are placed 20 cm from the center of the detection chamber using CF nipples. Baffles are placed within the nipples to prevent scatter off the windows from reaching the PMT which is mounted at the top of the figure. [155]

3.4 The Laser System

One of the largest technical challenges associated with the traditional forms of laser cooling is the large number of lasers that must remain well-locked during data collection. The unusually high number of lasers is a consequence of the $\approx$ 2GHz spin-rotation splitting in the ground state and the need for vibrational repumping lasers. This motivated me to build six external cavity diode lasers so that I could scatter the hundreds of photons required for transverse laser cooling. These six lasers drive all of the spin-rotation states but must be frequency modulated to address the hyperfine states within each spin-rotation level. I built an additional six injection locking amplifiers which ultimately provided the experiment with a total of 300mW of cooling light and 150mW of rempumping light because the Sisyphus mechanism requires high intensity for efficient cooling. Additional lasers, such as a Calcium 429nm laser, were also built to measure the cell extraction efficiency and the beam temperature. Finally, all of these lasers were locked using a WS7

commercial Fizeau interferometer wavemeter built by High Finesse. The quality of the injection locking was monitored while taking data using a scanning Fabry-Perot cavity from Thorlabs.

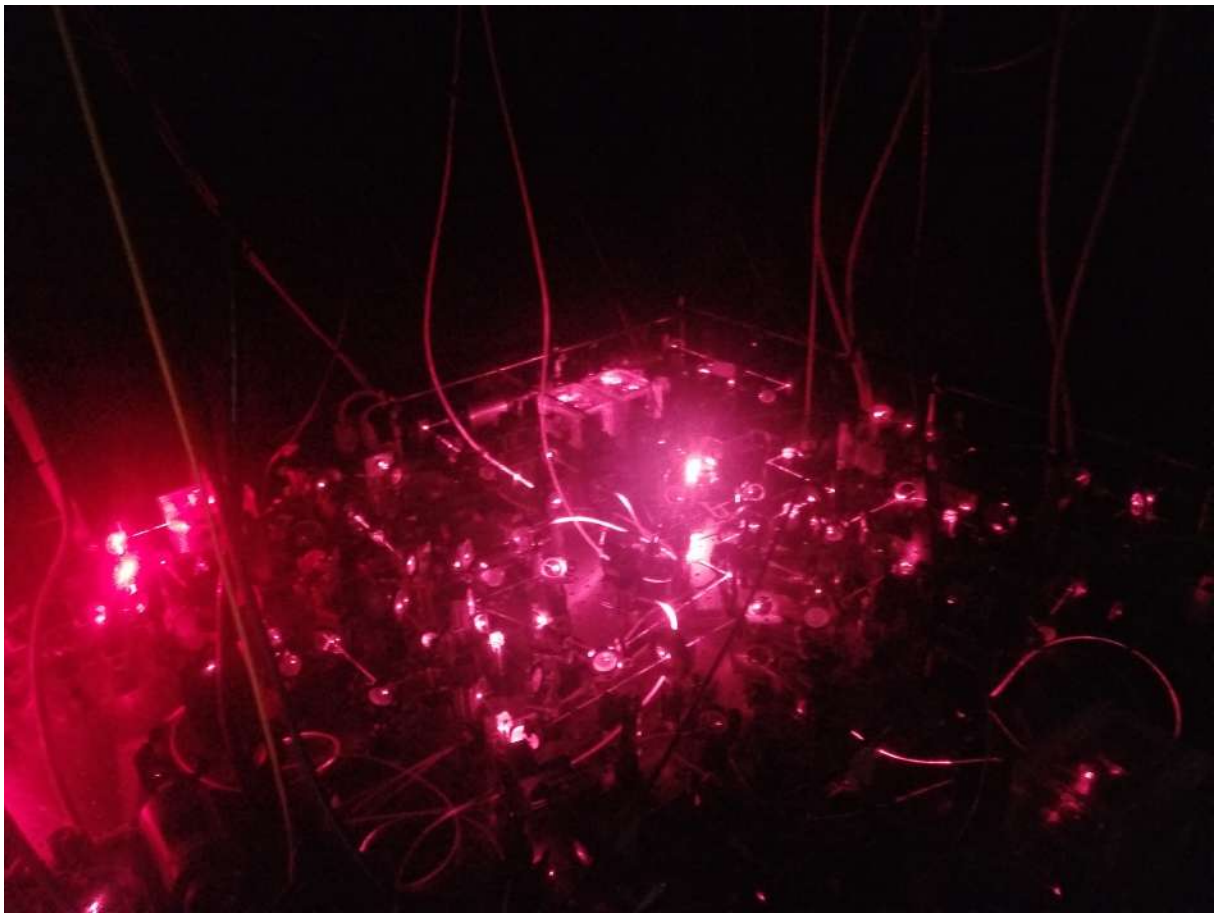

Figure 3.14: I show an image of the laser table where the detection, cooling, and repumping light is generated before it is coupled to single mode fibers to be transported to the experiment table.

3.4.1 Ablation Laser

The ablation laser begins the experimental sequence by blasting away a hot cloud of molecules from the surface of the molecular sample. We use the Ultra CFR pulsed ND:YAG that can emit 50mJ of 1064nm light over 6 nanoseconds. This laser can fire at 20HZ - though at this rate, it quickly heats the cryogenic cell. Therefore, we operate the ablation laser at 2 Hz while taking data. After six years of heavy use, we found that the ablation energy dropped from the advertized 50mJ, but still produced an acceptable 36mJ of energy. This degradation is likely a result of deterioration of the non-linear Nd:YAG crystal that is optically pumped to produce the laser pulses.

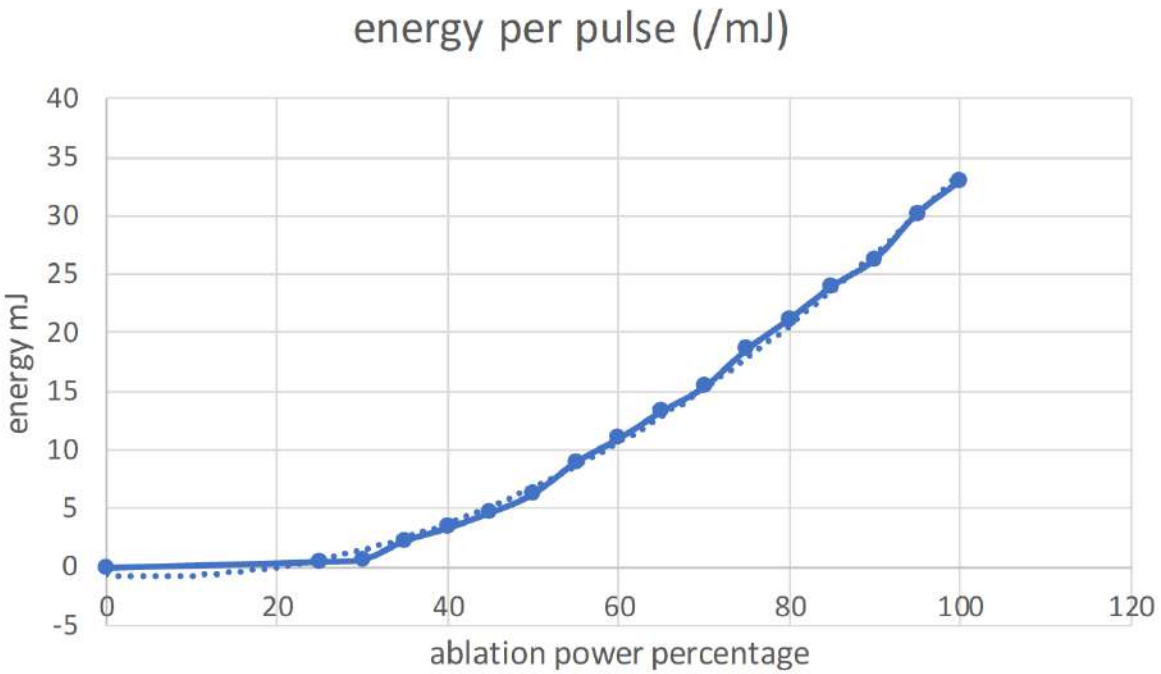

Figure 3.15: I show the measured ablation power as a function of the sequencer power percentage setting.

An internal pockel cell is use to dump all the built up laser power within the laser cavity. After exiting the laser housing, the light passes through a plano-concave lens with a focal length of 1.5 m. This lens allows us to control the ablation intensity to maximize the molecule production. This lens is mounted on a linear translation stage which not only precisely controls the lens's position, but also serves as a travel limiter. This prevents the ablation laser from being focused onto the cell window and cracking it.

After passing through the lens, the laser is reflected off a rastering mirror that is programmed to sweep the ablation light over the sample surface to average away the local inhomogineities of the CaH_2 solid target. Before incorporating the rastering actuators, we found that the molecule yield of one point on the sample surface would quickly be depleted over the course of a hundred shots. This made differential measurements nearly impossible because we did not know if the change in the detected fluorescence was due to a quantum population transfer or simply a change in the local yield of the solid CaH_2 target. However, the rastering mirror allows the sample to be used for several hours before we detect any drop in the molecular signal. The sample can be "refreshed" by

prolonged rapid ablation of the sample surface while the rastering mirror sweeps over the surface. We believe that this roughs up the sample surface to facilitate ablation when data is being taken.

3.4.2 Home Built ECDLs

All of the seed lasers used in this experiment are home built ECDLs based on the Littrow-DeMille design. [136]. I chose to utilize this design because I needed as much power as possible for cooling. The Littrow design provides more feedback power that allowed me to use non-antireflective coated diodes. Not only do non-AR coated diodes offer an order of magnitude more power than their AR coated counter parts, but non-AR coated diodes are significantly cheaper. Internal mode competition is the challenge of using non-AR coated diodes and one must provide more feedback power to out-compete the internal cavity modes. This is easily mitigated by using the Littrow design; but Littrow lasers, are not perfect - they output a broader laser linewidth compared to Metcalf lasers. Additionally, the maintenance of a Littrow system is much more work compared to a Littman-Metcalf system. Any re-tuning of the horizontal feedback of the laser grating, changes the output beam angle and all of the optics downstream must be realigned. The Littrow-DeMille design incorporates a steering mirror attached to the grating flexure to limit the downstream misalignment from horizontal tuning. While this does limit the resulting shift in beam angle, it does not completely eliminate the misalignment and one must still slightly realign all of the optics. The 5MHz linewidth of the Littrow design is an acceptable compromise for our experiment due to the 6MHz linewidth of the main cooling transition. I had little choice in which ECDL design to use due to the very limited availability of power at 690nm. We learned to live with a more labor intensive laser system. We mitigated the amount of laser tuning that had to be done by encasing all of our seed lasers in temperature-stabilized home-built acrylic cases. These cases limit the effect of temperature and pressure fluctuations within the lab. I was able to achieve a mode hop free tuning range of up to 500MHz with this design if the laser was properly tuned. In fact, the size of the mode-hop-free tuning range is a good diagnostic for the overall quality of the laser mode. If the mode-hop-free tuning range is less than 500MHz, one should consider

retuning the grating feedback and verify that the laser temperature is stable. It is worth noting that the addition of a feed-forward circuit would significantly expand the mode-hop-free tuning range allowing GHz of tuning. The only time we scan the frequency of our lasers over more than 100MHz is when performing spectroscopy. After spectroscopy is complete, our lasers would not be moved by more than ±50MHz. Therefore, we decided that we did not need the feed forward circuit at this stage and it would be possible to retroactively add into the system. Below, I show the CAD drawings for this modified Littrow-DeMille laser and I provide a list of the diodes used in this experiment. We got a bit lucky because initially, high power diodes were only available for the 635nm X-B transition. Only 10mW diodes were available for the 695nm X-A transition and the 690nm repumping transitions. Shortly after beginning the CaH experiment, the diode manufacturer Ushio announced a prototype single mode diode at 690 capable of outputting 250mW. We reached out to Ushio and explained our requirements. In response, Ushio kindly sent us some of their engineering sample diodes. Without these single mode, high power, non-AR coated diodes, observing Sisyphus cooling would have been nearly impossible.

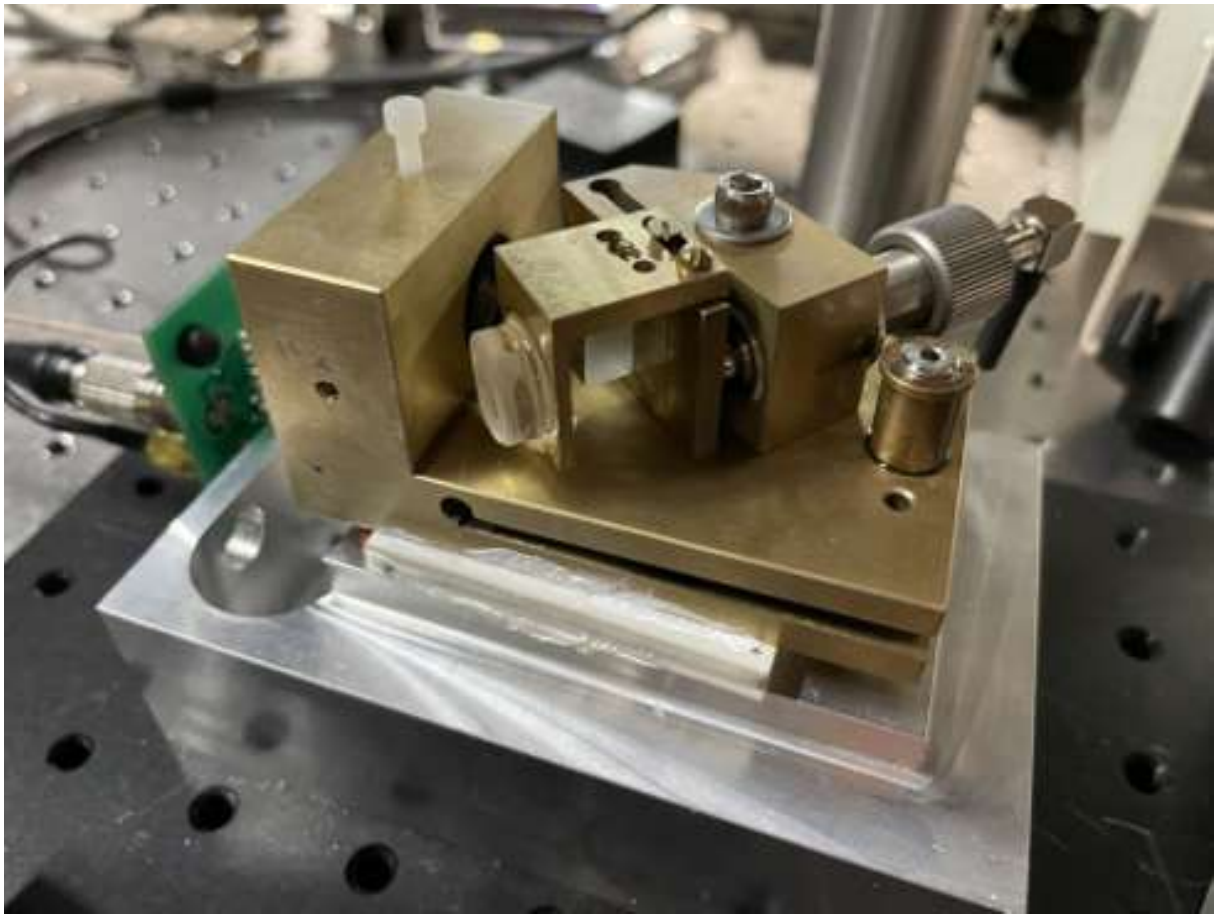

Figure 3.16: I show a close up of the home-built Littrow-DeMille ECDL used in this experiment. One can see the TEC used to stabilize the laser temperature, the brass diode housing, the feed-back grating, piezo actuator, and the steering mirror that directs the laser towards the rest of the optics system.

High power lasers are one of the aspects of AMO physics where being at the best funded lab makes everything much easier. Commercial fiber lasers outputting watts of power are available at the wavelengths used in this experiment, but cost a hundred thousand dollars. Even after I spent months building 6 injection lock amplifiers, our laser system was more than an order of magnitude lower power than those offered by commercial fiber amplifiers.

Temperature Tuning with Thorlabs OSA

All lasers, whether home-built or commercial, must be temperature stabilized to be useful in quantum physics. However, temperature tuning is even more important when working with a non-

AR coated diode because locking the laser requires out-competing the internal cavity modes of the diode. The key to a stable non-AR coated ECDL lock is to first tune the free spectral distribution of the diode to the desired laser frequency, before including the feedback grating. This guarantees that the internal cavity modes will be near the wavelength you lock at and those internal modes will not effect your lock as much. The effect of temperature tuning is most obvious when measuring the mode-hop-free tuning range. A laser that is not well temperature tuned, will have a mode-hop-free tuning range of tens of MHz, while a properly stabilized ECDL will be able to tune well over 500MHz.

The most valuable tool for temperature tuning is the Thorlabs USB Optical Spectrum Analyser (OSA). Before installing the grating into the laser housing, one simply aligns the output from the diode to the OSA. The fiber sensor of the OSA is insensitive to alignment, making alignment trivial and saving time. The proprietary Thorlabs OSA software will then display the spectral distribution of the output light and the software will calculate the peak frequency of the distribution. From that point, one can simply adjust the temperature to move the spectral distribution to the desired locking frequency. Temperature tuning, has its limitations - diodes can only operate within a certain range of temperatures given on the diode spec sheet. Additionally, tuning the temperature to either extreme has its risks. Tuning the temperature too high will severely impact the longevity of the diode. Meanwhile, cooling the diode too much can cause humidity to condense on the diode and ruin it. This condensation can be avoided by maintaining the diode above the lab's dew point or by placing the laser in a housing filled with a dry gas.

3.4.3 Wavemeter Locking

All of the lasers used in this experiment are locked using a WS-7 Fizeau interferometer made by High Finesse rated to 60MHz absolute accuracy between 330nm and 1180nm. The wavemeter posseses an internal HeNe laser reference used to calibrate the spectral response on a daily basis, but as I will discuss in the subsequent section, this calibration technique was found to be sensitive to daily fluctuations of the temperature and pressure in the lab.

Figure 3.17: I show a photo of the wavemeter used to lock the lasers in this experiment. [158]

We supply light to the wavemeter via an eight channel high-speed fiber switch, which allows us to lock up to eight lasers at a time. The wavemeter is capable of measuring the laser frequency at up to 500Hz if all of the switch channels are power saturated. Normally, we operate closer to 100Hz because we choose to save as much laser power as possible for the experiment. We have been able to lock our lasers to ±1MHz of the frequency set point, with this wavemeter. At one point, we also attempted to use the wavemeter to lock a near UV Calcium laser, but the UV light quickly damaged the fiber switch channel to the point where we needed to increase the wavemeter exposure time to unusable levels. I recommend purchasing the UV upgrade package if UV capabilities are required. Repairing a damaged wavemeter channel is both costly and time consuming.

Wavemeter Isolation and Sr Reference

One of the best improvements made to the laser locking system was to isolate the wavemeter from the lab by placing it in a custom vacuum chamber. The HighFinnesse WS-7 claims to be temperature stabilized and capable of automatically compensating for barometric fluctuations. However, even with this stabilization, the wavemeter was found to drift by as much as 20MHz day to day. The addition of the vacuum chamber allows the internal pressure and temperature to be decoupled from the daily fluctuations in the lab's atmospheric conditions. The chamber was maintained at room pressure and we found this to be sufficient to prevent day to day drifts in the

wavemeter. Further improvement could be had by pumping the air out of this chamber. Before making this upgrade, we needed to perform daily spectrums of the detection transition to measure that day's frequency offset and apply it across all laser set point. Not only is this time consuming but it makes it very difficult to reproduce results from the previous day as all the resonance frequencies shift.

We found the wavemeter's accuracy and precision was also improved by periodically calibrating it to high precision external reference. We borrow the $Sr^{88}\ ^1S_0 \rightarrow^3 P_1$ (434.829050Thz) laser from our molecular clock neighbors to calibrate the wavemeter. We chose to use this laser because it is PDH locked to a ULE cavity and has a very well known frequency. This reference confirms that the wavemeter has not drifted and we have not seen a daily frequency offset greater than a few MHz after making these improvements.

3.4.4 Laser Amplification

Low power lasers are suitable for use in spectroscopy because one wants to limit the power broadening. Less power is required for Doppler cooling as tens of mW per hyperfine state is enough to saturate the transition. However, Sisyphus cooling requires high laser intensities to generate a significant stark shift in the hyperfine levels of the molecule. We had three options for generating enough 690nm power for cooling - tapered amplifiers (TAs), injection locking amplifiers (ILAs), and commercial fiber lasers. Both tapered amplifiers and injection locking amplifiers offer the advantage that they can both be assembled in-house and both cost just a fraction of the price of a commercial fiber laser. The home-built tapered amplifiers and injection lock amplifiers output about 200mW per amplifier which is enough the begin to see Sisyphus cooling, but this was not enough to saturate the effect in CaH. However, this is much too little power for white light slowing. A fiber amplifier will need to be purchased for this experiment to execute on its long term objective to trap CaH and eventually dissociate the molecules to isolate hydrogen atoms.

I council the reader to use an injection locking amplifier rather a tapered amplifier whenever possible. Tapered amplifiers are fundamentally unstable devices and burning out the TA chip is

very easy if the amplifier is not seeded correctly. The gain medium of the tapered amplifier is also much more expensive - the TA chips available at 690nm are several thousand dollars. I spoke with Eagleyard about their 690nm TA chips when I was designing the amplification system and their sales representative strongly discouraged me from buying their TA chip due to its fragility and high price. TA chips at different wavelength are more durable and we successfully used TA chips at 1060nm to laser cool BaH. However, the alignment and mode shaping for TA's is more complex. The injection locking amplifier's optical mode quality is much higher, this saves time in mode shaping, and ultimately allows for a much higher fiber coupling efficiency. Finally, TA's require higher power current supplies and temperature controllers which add to the cost of these systems.

ILA

Here I will describe the two different ILA designs that I used to cool of CaH. One design utilized a proprietary Thorlabs temperature-controlled mount for TO-can laser diodes. The other design made use of a brass housing designed for the Littrow-DeMille ECDL but repurposed to house the ILA diode. Both ILA designs shared identical diodes, Thorlabs temperature/current drivers, and colimation aspheric lenses. I found the home-built ILA housing to be the most stable, which I attribute to three factors. First, the home-built design has a higher thermal mass, giving better temperature stability. Second, the home-built ILA housing is more mechanically stable because it is bolted directly to the optics table. The thorlabs design is placed on optics posts, creating a cantilever with significant mechanical resonances that destabilize the seed alignment. Finally, the asphere is separate from the diode mount, making aligning the asphere to the diode more challenging. The home-built ILA mount uses a standard thorlabs colimation package, in which the diode and asphere are threaded in the same optics tube and very well centered relative to each other. Five out of the six ILA's used to cool CaH were home-built, while only one used the thorlabs mount.

Now I will briefly describe the two different optical systems used to seed the injection locking

amplifiers and how the master laser is coupled to the amplifier diode. There are two variations of the ILA seeding system. The $X(V = 0) \rightarrow A(V = 0)$ cooling laser system consists of four ILA's that address each hyperfine state of the ground state. The other system uses two ILA's to address the $X(V = 1) \rightarrow B(V = 0)$ rempumping transition and each ILA addresses both hyperfine states of the V=1 ground state. I address the V=1 hyperfine states by seeding the ILA with EOM modulated light. The EOM adds sidebands at ±56MHz or ±104MHz according to the spin rotation state it is addressing. This design benefits from a simpler optical system, but it outputs a spectrum with an extra sideband. This wastes power and exposes the molecules to a more complicated spectrum. The repump lasers are always held on resonance, so the extra EOM sidebands are far from resonance. However, Doppler or Sisyphus cooling requires detuning the laser off resonance to achieve the maximum force. Thus, the extra sidebands from the EOM compete with the sidebands in use. For example, the optimal Sisyphus cooling occurred at +20MHz. At this detuning, the extra EOM sidebands are detuned by -30MHz and begin to produce a force of the opposite magnitude on the molecules. This suppresses the cooling. For this reason, I designed the cooling ILA system to be seeded by single frequency light at exactly the frequency desired for cooling. I generate these discrete frequencies by adding an AOM to the seed ECDL. The AOM gives light at +0MHz and at +56MHz for the J=1/2 state and at +0MHz and at +101MHz for the J=3/2 state. This perfectly addresses hyperfine structure without adding any unneeded frequencies to the system. After the AOM splits the seed laser into two beams, each of these is coupled to its own fiber that seeds one hyperfine ILA. The light addressing the hyperfine states is combined with its other hyperfine component using a polarizing beam splitter. Next, the spin-rotation states are combined on a non-polarizing beam splitter. Finally, the cooling and repumping light is combined on a dichroic filter that reflects 695nm light but transmits the 690nm repumping light. Below I have drawn a diagram to show how all six ILA's are seeded, combined, and fiber-coupled. This system provided the experiment with up to 300mW of cooling light and 200mW of repumping light. This power is more than enough for Doppler, but was barely enough to produce a robust Sisyphus signature.

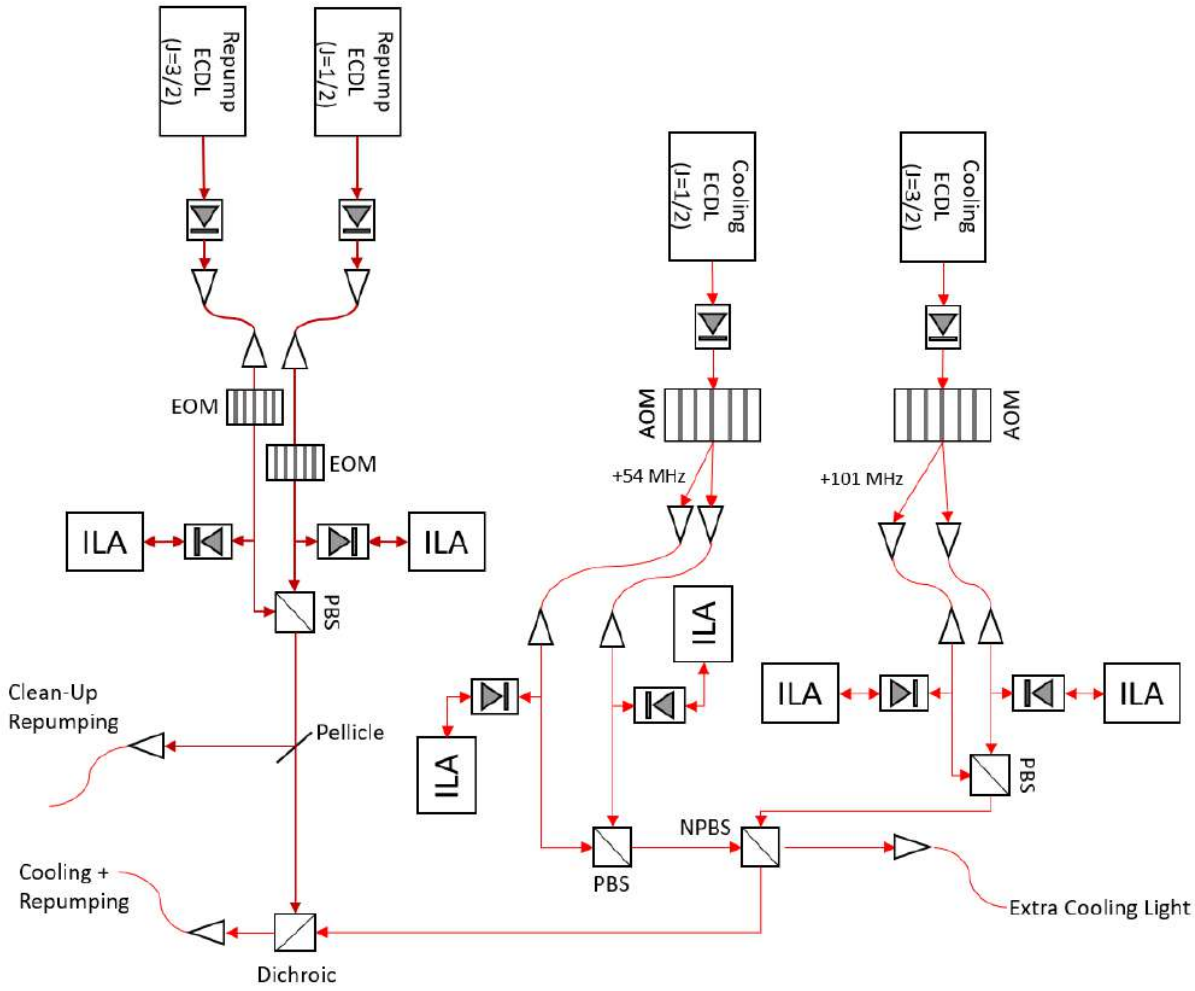

Figure 3.18: The laser diagram used in this experiment to generate the cooling and repumping light.

The key to achieving a stable lock when using an injection locking amplifier, is to mode match the seed beam and the amplifier beam. The best way to quantify the mode matching is to measure the back-coupling efficiency of the ILA light through the seed fiber. After the amplifier light passes through the isolator, most of the light will be deflected by the polarizing beam splitter towards the experiment fiber. However, a small percentage of the amplifier light will pass through the PBS back towards the seed fiber. Simply place a power meter on the ECDL side of the fiber and measure how much ILA light comes out. A stable lock will be possible if the back-coupled ILA light efficiency is greater than 60% and there is at least 2mW of single frequency seed power. If seeding the amplifier with EOM modulated light, 10mW of seed light will guarantee that all of the EOM

sidebands are amplified.

3.4.5 Frequency Modulation

We address the hyperfine states of the V=0 and V=1 $X^2\Sigma^+$ ground state using a combination of home-built EOM's and commercial AOMs. The EOMs and AOMs require an RF drive frequency which is generated by a pair of direct digital synthesizers (DDS) from NovaTech. The modulators require about 500mW of RF power. The DDS outputs microwatts of RF power; therefore, we use inline RF amplifiers from mini-circuits to generate enough power. This creates 50MHz or 100MHz sidebands as appropriate for each spin rotation state's hyperfine splitting. The resulting modulated spectra are as follows:

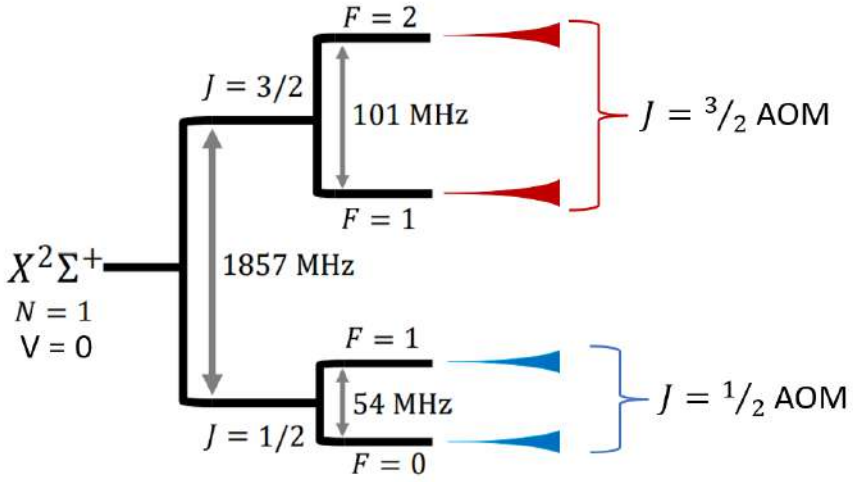

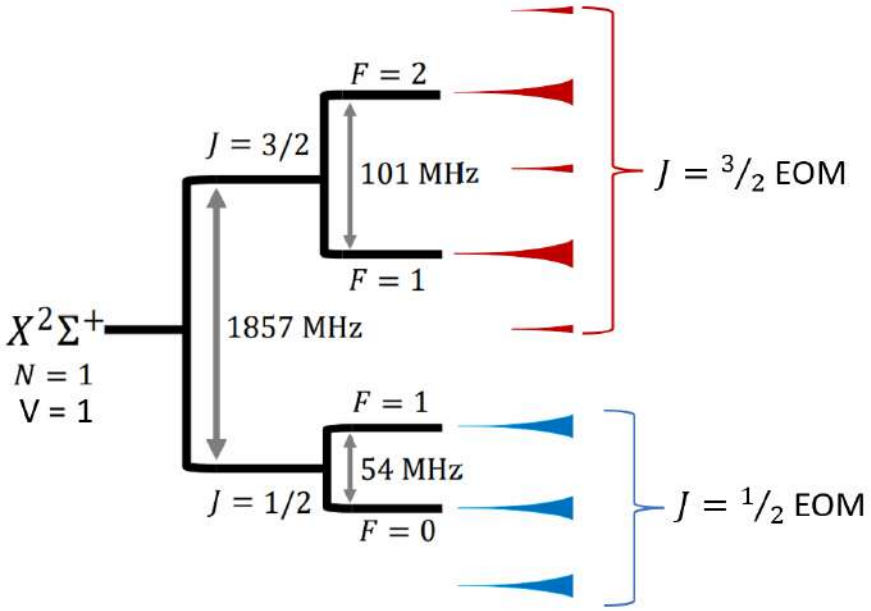

Figure 3.19: On top, I show the hyperfine structure for the two spin-rotation components of the V=0 X $^2\Sigma^+$ground state. The F=1,2 states of the J=3/2 state are split by 101MHz, while the F=0,1 states of the J=1/2 state are split by 54MHz. Each spin-rotation state is addressed with its own AOM. On bottom, I show the hyperfine structure for the two spin-rotation components of the V=1 X $^2\Sigma^+$ground state. Each spin-rotation state is addressed with its own EOM.

3.4.6 RF Sources

We drive our frequency modulators using a pair NovaTech 409B direct digital synthesizers controlled by our sequencer computer via USB. This can easily generate single frequency sine waveforms, but also offer the flexibility of arbitrary waveform generation that may be needed as the experimental sequence grows more complex.

The NovaTech DDS's output a maximum frequency of 250MHz. Therefore, I needed to build a voltage controlled oscillator (VCO) to drive a 350MHz waveform for bichromatic slowing with barium hydride. This system used a VCO and a double pass AOM to generate 700MHz side-bands which would provide the beat note needed to drive stimulated excitation and decay. To my disappointment, we never further investigated bichromatic cooling as the fiber amplifier that we borrowed from the CENTREX collaboration arrived broken. By the time I got it repaired, CEN-TREX needed it back. I believe bichromatic and polychromatic slowing are the most promising

techniques for slowing complex molecules with sub-optimal vibrational branching ratios. As high power lasers become more readily available, I foresee this technique becoming a staple of molecular cooling experiments.

Home-Built EOMs

EOMs function based on the Pockel effect within a non-linear Lithium Tantalate crystal in which the light is phase modulated to provide symmetric sidebands about the carrier frequency. By modulating the electric field within the EOM crystal, one creates a periodic change in the index of refraction of the crystal. This in-turn modulates part of the carrier wave's phase as defined by Carson's Rule [159].

The periodic modulation of the complex phase of a monochromatic laser, can be derived as follows [160]. We write the laser's electric field as:

$$E(t) = Ae^{i(\omega t + D sin(\Omega t))} \tag{3.3}$$

where A is the amplitude of the laser, ω is the laser carrier frequency, D is the modulation depth, and Ω is modulation frequency. The beauty of this expression is that it may be expanded as a sum of Bessel functions J_n [57]. This expansion into Bessel functions is called the Jacobi-Anger function and is given as:

$$E(t) = Ae^{i\omega t}(J_0(D) + \sum_{n=1}^{\infty} J_n(D)e^{in\Omega t} + \sum_{n=1}^{\infty}(-1)^n J_n(D)e^{-in\Omega t}) \tag{3.4}$$

This expansion revels that the addition of this phase creates symmetric Bessel function sidebands about the carrier frequency ω and the dominant Bessel function is determined by the modulation depth D.

We are using two variations of home-built EOMs on this experiment. The EOM shown on the left was the I built to be used for cooling, while the EOM on the right is the white-light slowing EOM that I helped the junior grad student Jinyu build. Both EOM designs use a Tank circuit to

create an impedance-matched LC resonator at the desired frequency, which drives the periodic electric field in the crystal. The capacitance of the system is set by the dimensions and dielectric properties of the crystal in addition to the stray capacitance of other components in the EOM housing. The primary difference between the cooling EOM and the white-light slowing EOM is the quality factor to which the resonances were tuned. In general, the more sidebands that one wishes to add, the better the circuit Q must be.

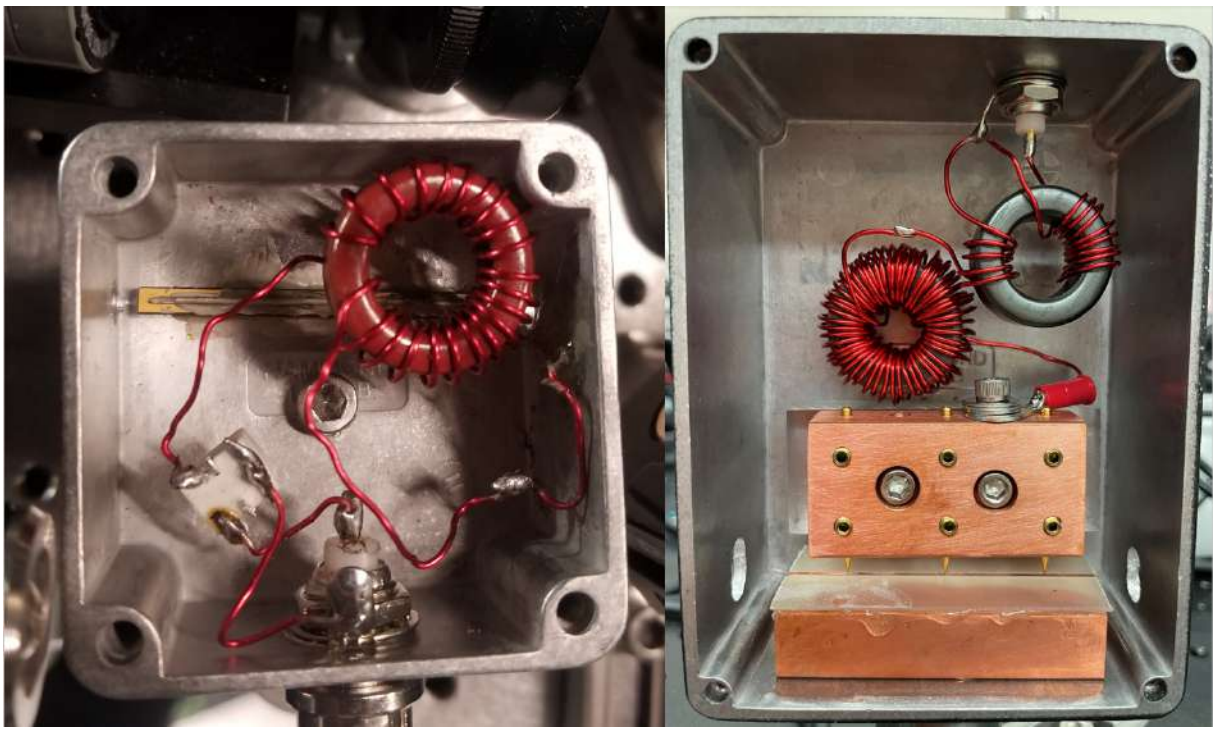

Figure 3.20: On the left, I show the interior of one of the home-built EOMs used to add frequency sidebands to the repumping and imaging lasers. The inductor component of the tank circuit can be seen as a red wire wrapped around the red inductor core. The EOM crystal is seen beneath the EOM crystal. On the right, I show the high Q EOM used to add sidebands to the cooling light. Here a much longer crystal is used to drive high order Bessel functions. The inductor is the densely wrapped torus and the impedance matching transformer can be seen as the less densely wound ring. The winding of the inductor is tuned to create a 1MHz resonance, while the transformer winding is tuned to minimize the reflected waveform and create a 50 Ω input impedance at a 1MHz drive frequency.

A low Q circuit can also drive higher order Bessel functions, but will require much more power and the inefficiency of the circuit will cause overheating. The Q of the cooling EOMs was about 50 after tuning, though I found the Q to drift closer to 30 after installation. I attribute this to

the movement of components within the housing upon installation and possibly due to the stray capacitance of the optics table. Meanwhile, the Q of the white-light slowing EOM was tuned to 2000. This high Q value was needed to create $n \geq 200$ sidebands. Choosing a modulation frequency of ≈ 1 MHz and driving the higher order Bessel functions creates “white" light. The light is called white because the laser is broadened across hundreds of MHz. The light is still red to the human eye, but to an AMO physicist, this might as well be white. This broad spectrum is designed to keep molecules on resonance as they experience a large Doppler shift as they decelerate. The downside of such high modulation, is that it spreads the laser power over several hundred MHz and the power at one frequency drops by two orders of magnitude. I strongly advocate moving away from ILA amplification for slowing because broadening the lasers by this amount will provide less than one mW per sideband. A high power fiber laser would provide tens of mW per sideband and make Doppler slowing easier.

One of the benefits of EOM modulation is that phase modulation does not interfere with the ability to seed a injection locking amplifier. This is not possible with AOMs. Initially, I thought I might be able to modulate all of my cooling and repumping lasers with one EOM by using the $n = 2$ Bessel function with a modulation frequency of 50MHz. This modulation would give sidebands at $0, \pm 50, \text{and} \pm 100 MHz$ and would address all of the hyperfine states. This did not work for this experiment because the spin rotation states are 2 GHz apart and are addressed by two separate lasers that are combined on a PBS, which forces their polarizations to be orthogonal. This method of combining lasers was our only option due to the power constraints and the splitting between the spin rotation states. After the PBS, laser polarizations are orthogonal and only one of the polarization can be modulated by the electric field inside an EOM. Therefore, I chose to modulate each spin rotation independently and accept a slightly more complex optics system.

AOMs

AOMs use a radio frequency piezo to generate sound waves in a crystal that make use of Bragg diffraction to control the intensity of a laser or to add asymmetric sidebands to a monochromatic

laser. [161, 162]

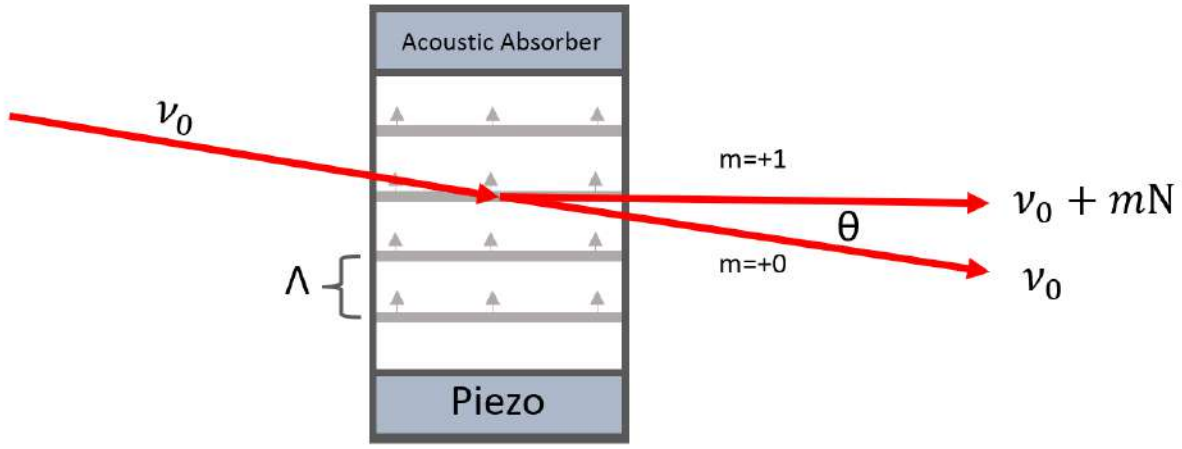

When the incident laser angle satisfies the Brag condition [163, 164], the input laser will be diffracted into separate beams according to the following expression:

$$2\Lambda sin\theta = m\frac{\lambda}{n} \tag{3.5}$$

where $\Lambda(N)$ is the wavelength(frequency) of the sound wave in the AOM crystal with an index of refraction n, m is the diffraction order $(..., -2, -1, 0, +1, +2, ...)$ of the incident light of wavelength λ. For all this experiment's applications we always used the $m = 0, \pm 1$ orders. One may express the intensity of the ± 1 order as:

$$\frac{I_{\pm 1}}{I_0} = sin^2(\frac{\Delta\phi}{2}) \tag{3.6}$$

In practice we control the ratio of the diffraction order intensities by varying drive power of the AOM crystal with higher drive powers, diverting more power to the higher order diffraction modes.

We use AOMs to add sidebands that address the hyperfine states of our $X \rightarrow A$ cooling lasers. We initially attempted cooling with EOM sidebands due to the simpler optics system, but we found that while performing frequency sweeps, the unneeded sidebands competed with each other effectively canceling out any heating or cooling. Therefore, it was decided that it was essential to

only generate the needed sidebands using an AOM. The drawback of this method is that one will need to double the ILAs in the optical system and waste 50% of the output power. It is also worth noting, that AOMs, unlike EOMs, can not seed a tapered amplifier or an injection locking amplifier with two frequencies because the seed frequencies compete and destabilize each other.

3.5 Detection Hardware

One can not discuss the experimental apparatus without going into detail concerning the specifics of how we detect the molecules. Through out this experiment, we use four different kinds of detectors depending on the specific application - USB cameras, fast photo-diodes, photo-multiplying tubes, and an electron multiplying charge-coupled device (EMCCD) camera.

3.5.1 Thorlabs USB Camera

(a) The ThorCam CCD

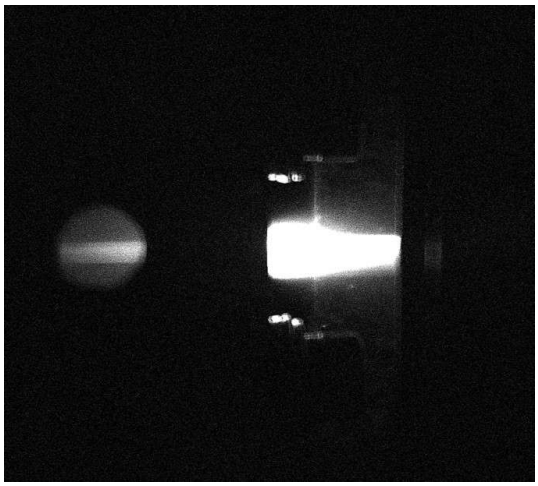

(b) An Image of the cryogenic beam taken with the ThorCam.

The Thorlabs USB camera is one of the most affordable and useful optical detection devices used in this experiment. We use this camera to detect in-cell Calcium production; in addition to general laser diagnostics, such as beam profiling or colimation. This camera is suitable for

applications where one is imaging a bright source and wishes to preserve the spatial information from the object being imaged. The Thorcam program also contains built-in fitting functionality, allowing one to quickly extract geometric properties from the images. This camera is unsuitable for applications requiring sub-millisecond time information. This camera lacks significant signal amplification or active noise reduction. As a result, this camera is not suitable for low light imaging applications such as molecular fluorescence imaging, where one requires single photon sensitivity. However, the Thorcam can easily be used to image atomic fluorescence due to the much higher fluorescence of atoms. We used the Thorcam to image Calcium atoms both in cell and shortly after the Calcium atoms extracted into the beam. This allowed us to measure the beam freezing zone and observe the transition from the high collision cell region to the collision-less beam.

3.5.2 Fast Photo-Diodes

We use InGaAs fast photo-diodes from New Focus, for applications where we do not need amplification but still require sub-millisecond time resolution. The fast photo-diodes were key for in-cell spectroscopy, where they were used to identify the molecular transition frequencies. They are used in conjunction with low pass RF attenuators to monitor in-cell molecule production by resonant absorption. Finally, fast photo diodes can be used for Doppler free absorption locking or for phase-locking applications where one is stabilizing to a beat-note at less than 150MHz.

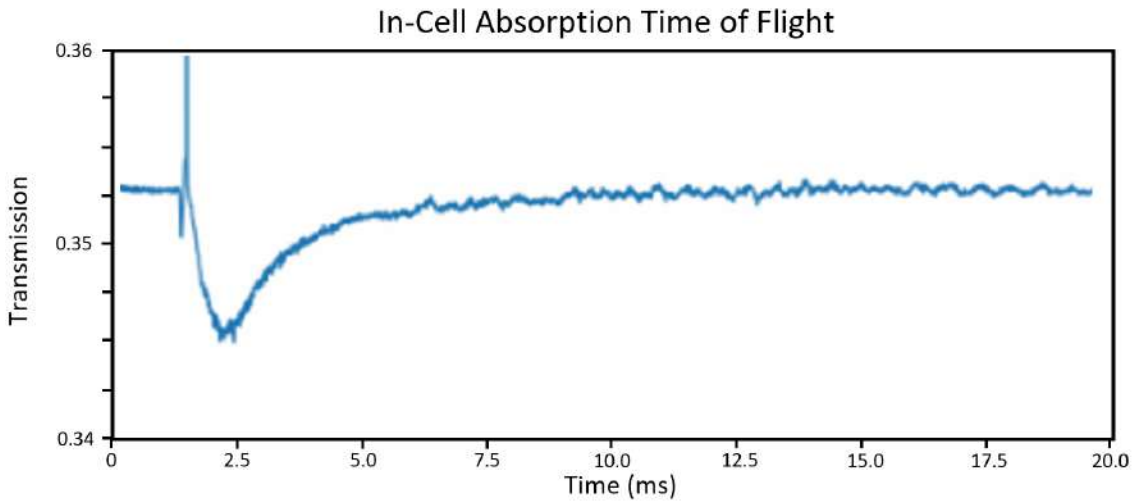

Figure 3.21: InGaAs fast photo-diode (top). [165] An example time of flight in-cell absorption trace recorded with a InGaAs fast photo-diode.

3.5.3 PMTs

PMTs are a form of photo-vacuum tube. They consist of a photo-cathode with a series of amplifying dynodes within a very high electric potential ($\approx$ 2kV). Electrons are ejected from the photo-cathode via the photoelectric effect and then focused onto the dynodes where they collide with the metal fins and generate an avalanche of electrons that ultimately are collected at the PMT anode. This secondary emission amplification technique can amplify single electrons from the photo-cathode by as much as 10^8 allowing scientists to detects single photons. This extreme sensitivity spans from the UV to the near infrared and as a result PMTs are used in almost every field of experimental physics[166].

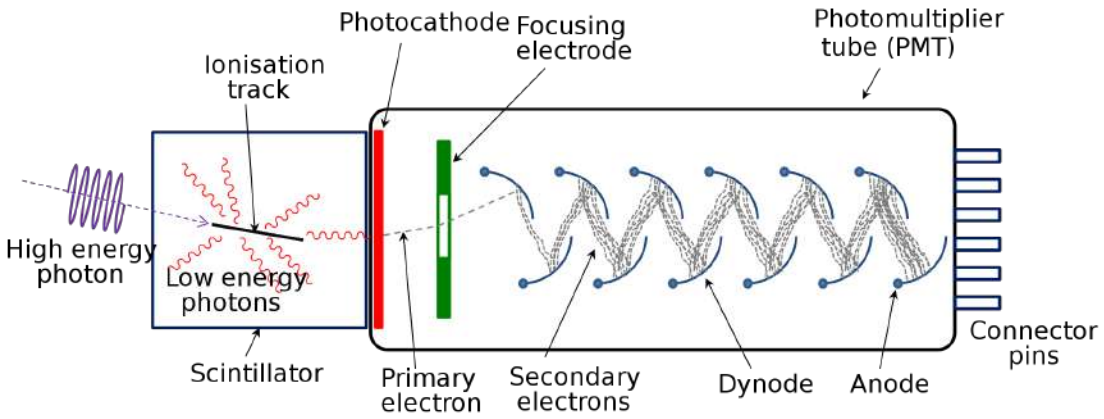

Figure 3.22: The internal architecture of a PMT [167].

We use PMTs when we require high signal amplification, sub-millisecond time resolution, and are willing sacrifice spatial information. Therefore, we use PMTs when detecting molecular time of flight fluorescence. PMTs are also used for in-beam fluorescence spectrums to measure the hyperfine splitting frequencies, in Doppler sensitive velocity measurements, in $V = 0$ depletion measurements, and finally vibrational branching ratio measurements [146].

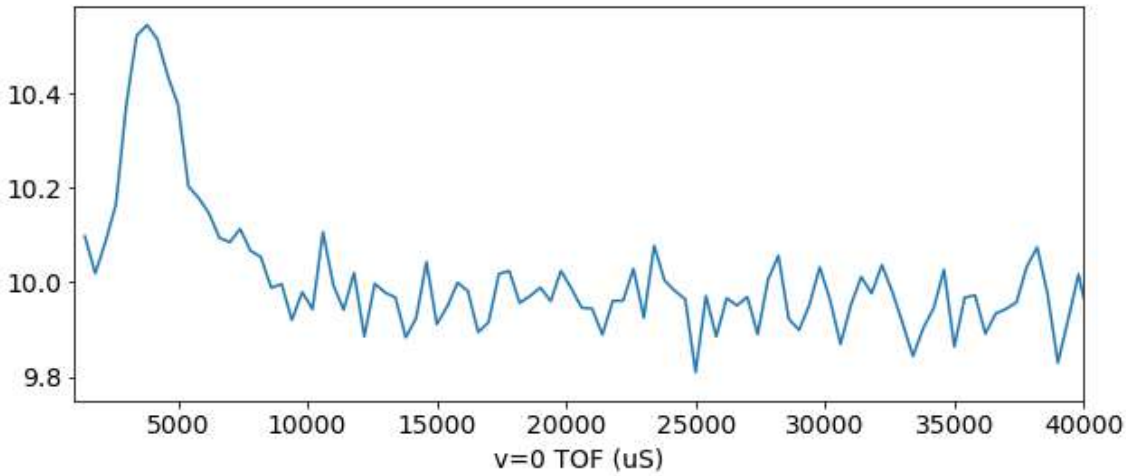

Figure 3.23: I show the time of flight trace of molecules fluorescing under the interaction with the detection laser as detected by the PMT.

The PMTs used in this experiment are a voltage amplifier and PMT combination made by SenseTech (models P30PC-01 and PSWPC-01).

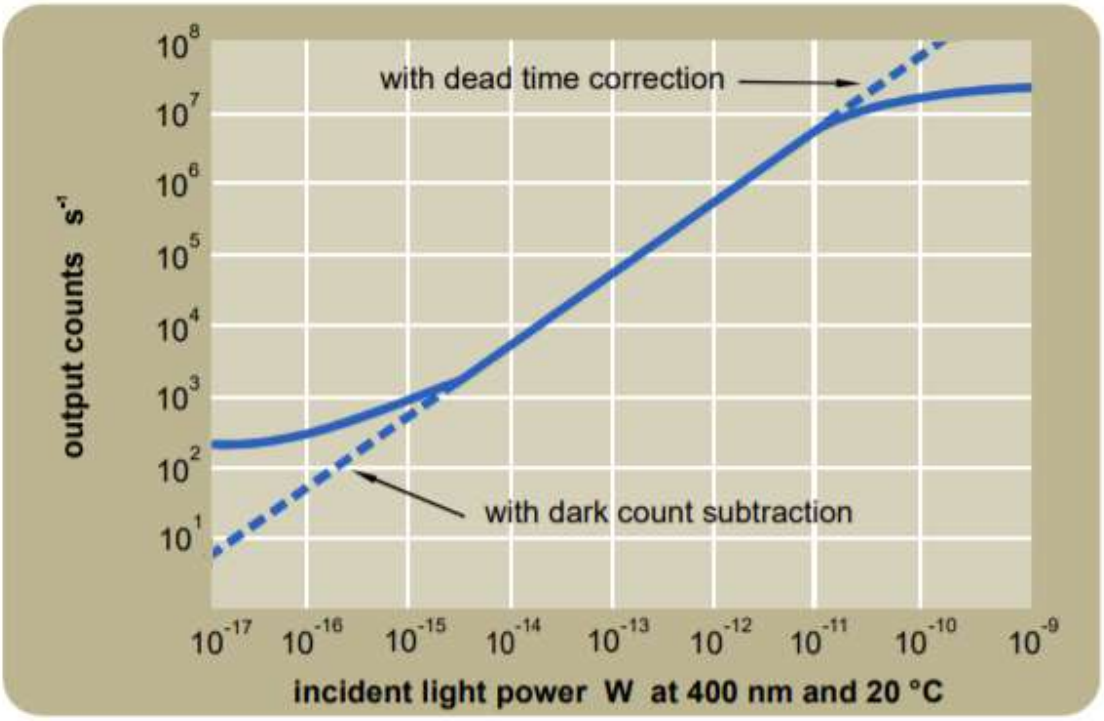

Figure 3.24: The advertised PMT sensitivity of the SenseTech P30PC-01 is shown below for 400nm light [168].

3.5.4 EMCCD

An EMCCD is similar to a standard CCD camera, but with an additional electron multiplying gain register [169]. This provides the sensitivity benefits of a PMT, but preserves the geometric information of the molecular beam necessary to observe cooling. EMCCDs use a cascade register that amplifies the signal from the pixel serial register before passing the pixel's amplified signal to an output node. As each pixel passes through the cascade register, the signal is amplified by a variable amount that can be set by the user. This flexibility allows the EMCCD to be used in variable light conditions - from room light down to single photon counting. One of the primary benefits of an EMCCD is that it is not readout noise limited because the signal is amplified before the signal is ever recorded. The EMCCD used in this experiment, the iXon Ultra 888 by Andor, also allows the user to water cool the pixel serial register down to -70 Celsius to suppress dark counts and minimize readout noise.

(a) The iXON Ulra 888

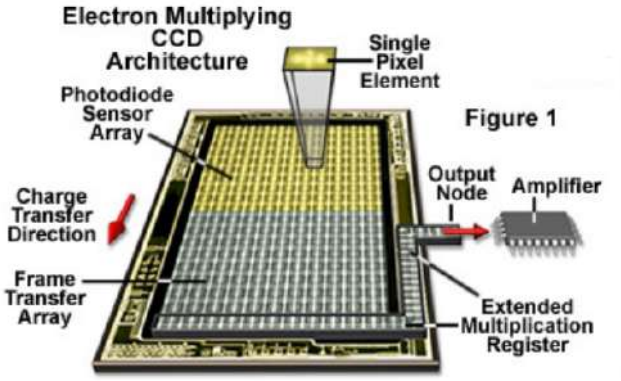

(b) EMCCD Architecture [170]

3.6 LabView Sequencer and DAQ

The LabView VI's used in this experiment controls the pulse tube (PTR), the helium buffer-gas, the ablation laser, the laser lock, and the PMT time of flight signal. It should be noted that in the future, the experiment will switch the sequence control to Cicero so I will focus on the parts of the sequencer that will remain after those upgrades.

I wrote the LabView VI which controls the PTR via RS232 connection. This VI allows one to monitor and record the temperatures of the 40K PTR head, the 40K shield, the 4K head, and the 4K cell. One is also able to program PTR temperature cycles to turn on and off the PTR automatically. Finally, the PTR VI monitors the PTR internal temperatures and oil pressures, which are a useful diagnostic for a malfunctioning PTR. In my experience, PTR breakdowns are almost always a result of the chiller in the mechanical room overheating due to excessive heat build up in the pre-lab.

The LabView sequencer also includes VI's which manage the MKS and AERA mass-flow controllers with 0-5V analogue control signals. This allows one to flow between 0 and 200 sccm of helium depending on which mass-flow controller is used. Caution must be exercised if flowing more than 20 sccm for an extended period of time, as this will exceed the charcoal sorbs ability to pump and the 4K region will thermally couple to the 40K region. This can cause the sorbs to heat up and out-gas all of the helium they have trapped. Finally, there is about a 30 second lag between

turning on He flow and the cell pressure equilibrating. I recommend allowing at least 30 seconds between turning on the helium flow and beginning ablation and data acquisition.

Another key functionality of the LabView sequencer is the control of the BigSky ablation laser energy and repetition rate via a USB serial connection. The sequencer also relies on the Q switch trigger from the ablation laser to begin recording data. Despite the ablation laser being capable of firing at 10Hz, the experimental and DAQ sequence takes about 300ms to complete. This limits our experimental rep rate to 3Hz.

We have a separate LabView VI that controls the PID piezo locking of the ECDL seed lasers. This VI runs on a separate computer to avoid memory bottle necks during the data acquisition, which dramatically decrease the PID lock rate. The locking VI is capable of communicating with the AttoCube ANC300 chassis piezo controller, but recently we added the ability to use the Pilot PZ controller for additional locking channels. The external control of the Pilot PZ with home-built lasers requires that one enters “0x534c" as the Userkey to unlock the software. When I first joined the experiment, both the sequencer and the locking VI were running on the same computer and once the experimental sequence began, the laser PID would effectively freeze and the lasers would be drifting. Now that we operate the locking VI on a separate computer we have eliminated this catastrophic locking lag. Now, the locking rep rate is limited almost entirely by the exposure time of each laser on the wavemeter. If all eight channels are properly exposed, the channel exposure time is one millisecond, giving a maximum locking rate of 125Hz.

The final component of the LabView computer control system is the DAQ card and BNC break-out board. These are the components that distribute the triggers from the sequencer to the various experimental apparatus and record the digital or analogue data from the experiment. We use the PXIe-6363 DAQ card from National Instruments in conjunction with a BNC-2110 shielded BNC connector block.

Chapter 4: In-Cell Dynamics and Spectroscopy

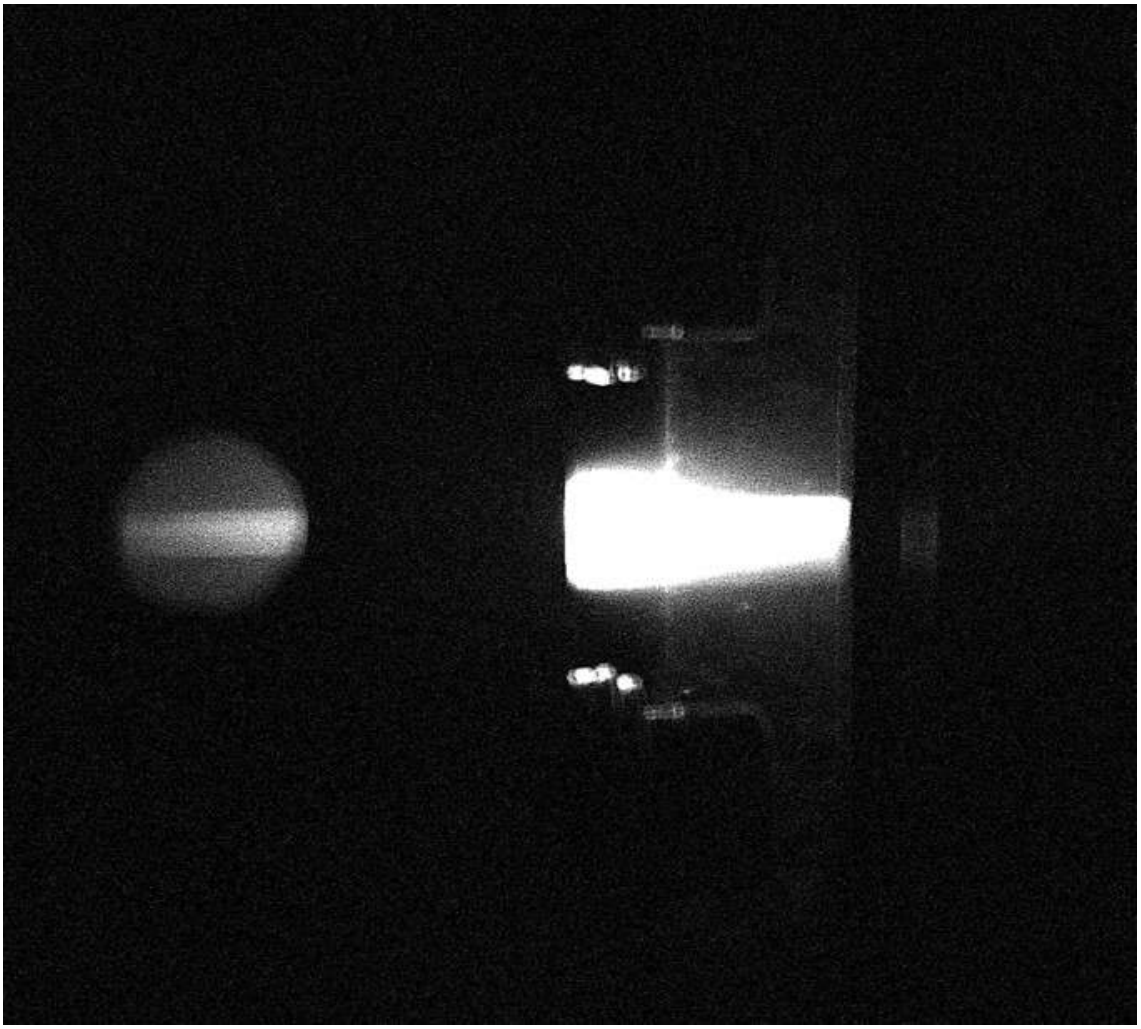

Figure 4.1: A photo of the ablation plume.

Our experiment begins in the cryogenic buffer gas cell. The molecular beam used for cooling is generated through the ablation of solid CaH_2 samples within the frigid environment of the cell. Molecules are ejected from the ablation plume at thousands of degrees, and cooled through collisions with the surrounding buffer-gas that continuously flows into the cell. As the molecules

expand and cool, they become hydrodynamically entrained in a flow of He and exit through the cell aperture into the experiment chamber [136, 57, 155]. The properties of the molecular beam downstream are very sensitive to the conditions within the cryogenic cell; thus, the first step towards laser cooling is optimizing cell conditions to produce the brightest and slowest beam possible. A cool and slow beam is important because it facilitates laser cooling and loading into a MOT. In this chapter, I will lay out the series of experiments by which we optimized the cell's production. First, we had to spectroscopically identify the cooling, detection, and repumping transitions. Having identified the frequencies, we proceeded to vary the size and temperature of the cell, the size of the cell aperture, the ablation energy, and the helium flow rate. Finally, we performed measurements of the beam velocity immediately outside of the cryogenic cell.

4.1 In-Cell Spectroscopy

The transitions necessary for molecular cooling are easiest to identify within the cryogenic cell. Doppler and collisional broadening widen transitions across hundreds of MHz, thereby allowing rapid identification of the correct frequency. Spectroscopic searches rely on theoretical predictions or previous spectroscopy data to provide an estimate of the transition frequency [147, 148, 171, 149, 150, 58]. Due to the complexity of molecules, these predictions have uncertainties of hundred of MHz or even GHz. Identifying transitions can be a slow and arduous process, as each step of the spectrum probes a few MHz at a time. The broadened lines within the cell allow one to take larger frequency steps without the risk of scanning over a transition without seeing anything.

Molecules ejected from the CaH_2 sample by the ablation laser thermalize and expand into the path of the absorption probe laser. If the probe laser is far from resonance, the molecules pass through the laser without interacting. However, as we sweep the laser frequency, eventually the ablation laser scans over the molecular resonance. The high number of molecules interacting with the resonant probe laser absorb the laser light and the photo-diode will record a time-dependent absorption signal. This signal is integrated to give the total absorption at a given laser frequency. One such time of flight absorption trace is shown in Figure 4.2.

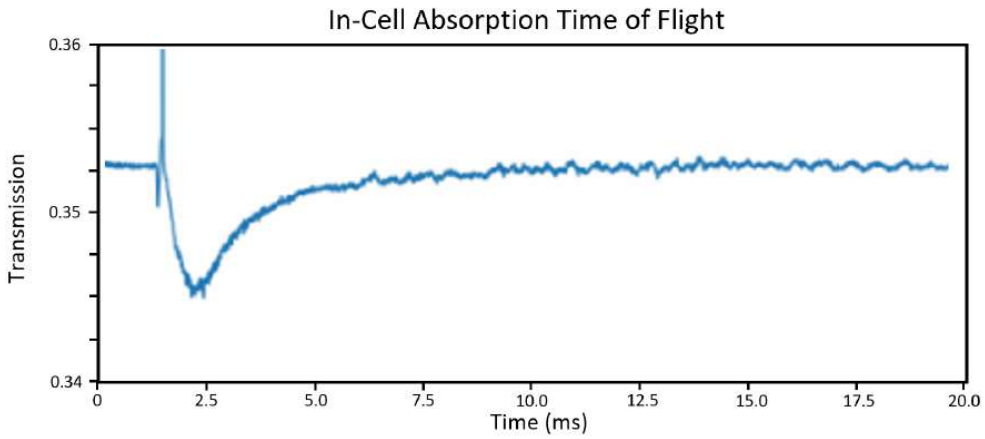

Figure 4.2: A time of flight absorption trace.

We probe the transitions in-cell by shining the spectroscopy laser through the windows of the cell and looking for the frequency dependent absorption of that laser. We further amplify the magnitude of that absorption, by double passing the laser onto itself; this doubles the effective path length, and doubles the absorption signature. Double passing is accomplished by using a PBS and a $\frac{\lambda}{4}$ waveplate to separate the co-aligned passes and reflect the probe laser onto a InGaAs photo-diode. A dichroic is placed in-front of the photo-diode to separate the probe laser light from the room light. Finally, we place a Mini-Circuits 1MHz low pass filter on the photo-diode output to suppress any beat notes from the laser interfering with itself. This optical setup can be seen in figure 4.3. This absorption trace is an invaluable source of knowledge regarding not only the frequency of the transitions, but also the cryogenic cell's dynamics, as discussed in the latter half of this chapter.

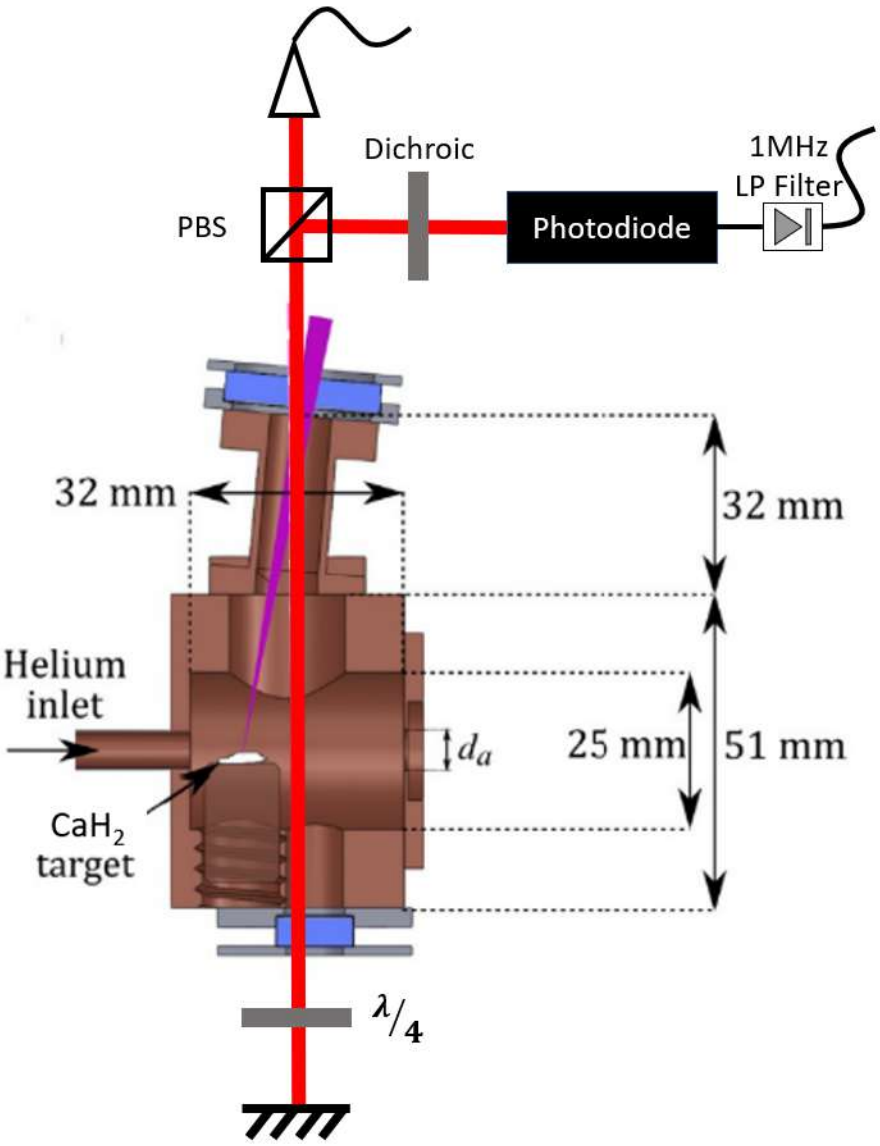

Figure 4.3: The in-cell absorption probe used for the initial absorption spectroscopy of the molecular transitions.

4.1.1 $X^2\Sigma^+(V = 0, N = 1) \rightarrow B^2\Sigma^+(V = 0, N = 0)$

The first set of lasers I built in 2019 were used to search for the $X^2\Sigma^+(V = 0, N = 1) \rightarrow B^2\Sigma^+(V = 0, N = 0)$ transition via in-cell absorption. We were guided by previous measurements [58] and quickly found this transition by probing the cryogenic cell with 100 micro-watts and the resulting spectrum is shown in figure 4.4. We intentionally used a very small amount of power to avoid saturating the transition. Surpassing the saturation intensity does not increase the absolute

absorption, but decreases the absorption percentage and make the signal harder to see.

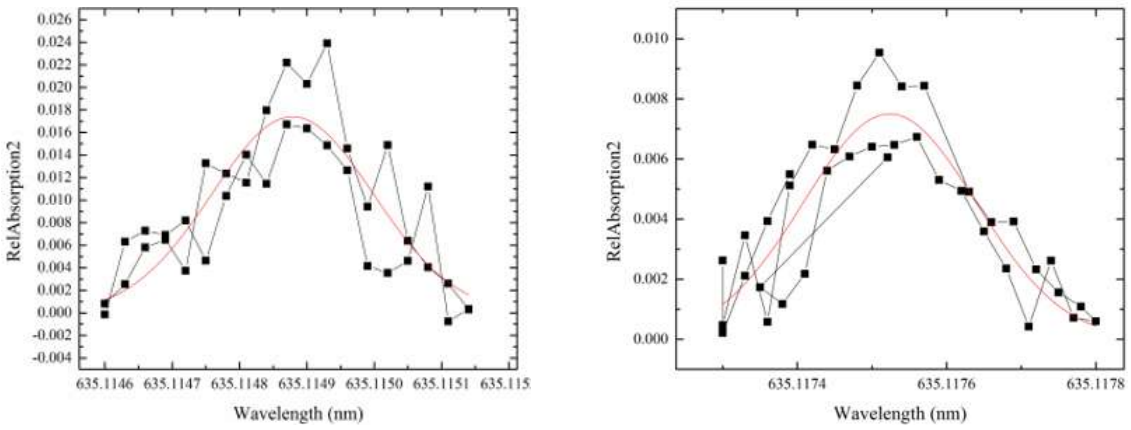

(a) $X^2\Sigma^+(J = 1/2) \rightarrow B^2\Sigma^+$ *Absorption* (b) $X^2\Sigma^+(J = 3/2) \rightarrow B^2\Sigma^+$ *Absorption*

Figure 4.4: In-cell absorption spectra of the J=1/2 and J=3/2 branches of the $X^2\Sigma^+ \rightarrow B^2\Sigma^+$ transition.

Basic AMO physics teaches that transitions can be Doppler broadened, producing a profile of the following form: [151]

$$\frac{I_\nu}{I_{total}} = \frac{c}{\nu}\sqrt{\frac{m}{2\pi kT}}e^{-\frac{mc^2(\nu-\nu_0)^2}{\nu^2 2kT}} \tag{4.1}$$

This Gaussian form has a full width half maximum of:

$$FWHM = \frac{2\lambda_0}{c}\sqrt{\frac{2kTln2}{m}} \tag{4.2}$$

Using these expressions, we fit and estimate that the molecular temperature is about 11K.

4.1.2 $X^2\Sigma^+(V = 0, N = 1) \rightarrow A^2\Pi(V = 0, J = 1/2)$

I built ECDLs to address the $X^2\Sigma^+(V = 0, N = 1) \rightarrow A^2\Pi(V = 0)$ transition. In accordance with previous observations, by Bernath et al.[58], we found this line within a few days of searching and the spectra as shown in Figures 4.5 and 4.6.

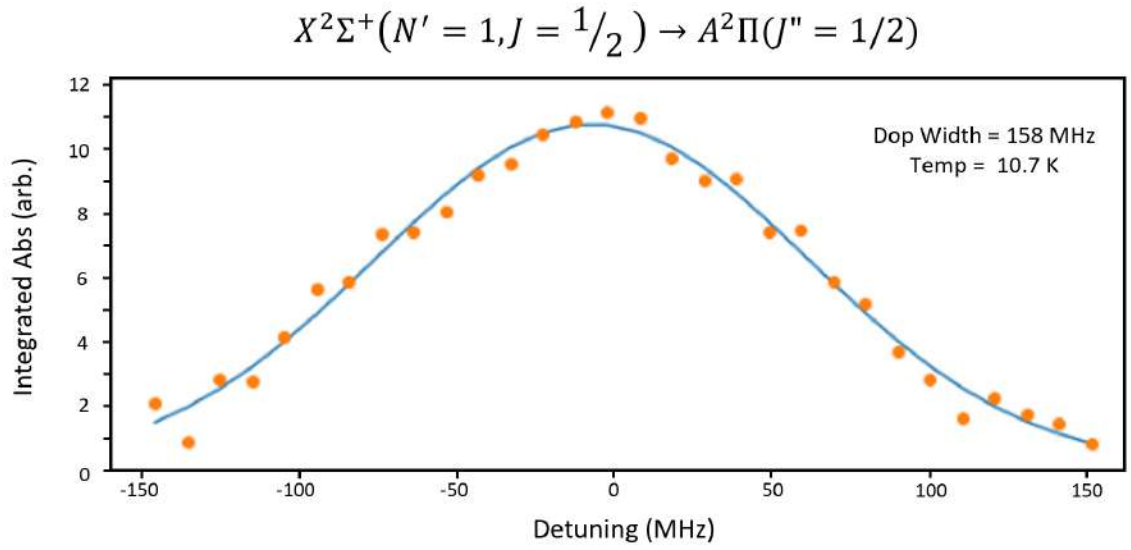

Figure 4.5: An absorption spectrum of the J=1/2 branch of $X^2\Sigma^+ \rightarrow A^2\Pi$ transition. A Gaussian fit gives a temperature of 10.7K

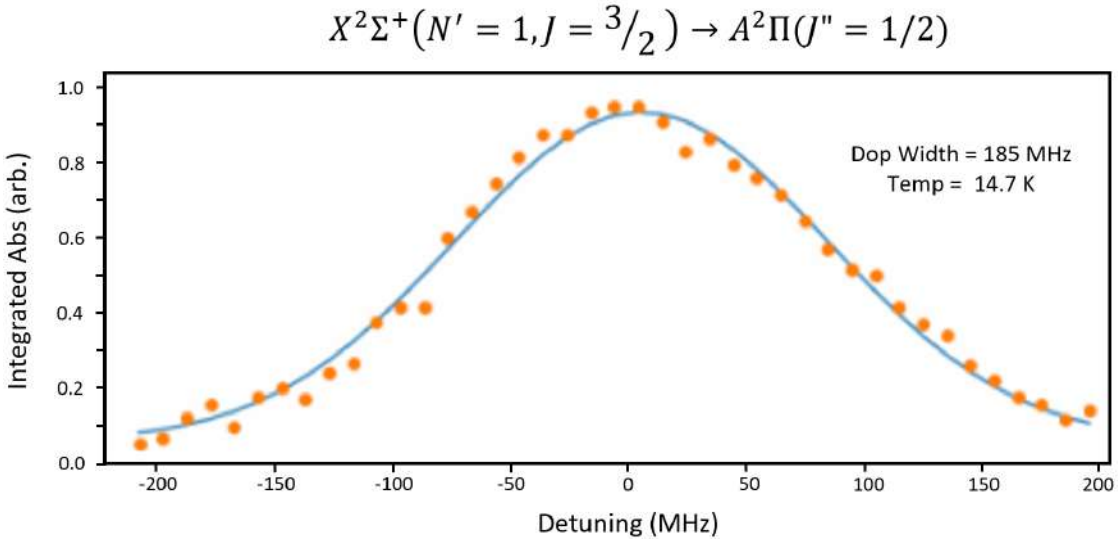

Figure 4.6: An absorption spectrum of the J=3/2 branch of $X^2\Sigma^+ \rightarrow A^2\Pi$ transition. A Gaussian fit gives a temperature of 14.7K

After fitting the spectra, we were pleased that the temperatures were very close to those previously measured with the $X^2\Sigma^+(V = 0, N = 1) \rightarrow B^2\Sigma^+(V = 0, N = 0)$ transition. [58]

4.1.3 $X^2\Sigma^+(V=1, N=1) \rightarrow B^2\Sigma^+(V=0, N=0)$

The final set of transitions required to start laser cooling were the two spin rotations states of the first vibrational repumping transition, $X^2\Sigma^+(V=1, N=1) \rightarrow B^2\Sigma^+(V=0, N=0)$. This transition was much more difficult to detect via absorption, because collisions with the helium buffer gas relaxed the population from the higher-lying vibrational states to the vibrational ground state. This is favorable for laser cooling because it maximizes the molecules available for cooling, but it leaves very few molecules in the $V=1$ ground state that can absorb the spectroscopy laser. After weeks of searching, it occurred to me that we could directly populate the V=1 state by driving off diagonal transitions from the $X^2\Sigma^+(V=0, N=1)$ state to the $A^2\Pi(V=1)$ state (637.7 nm). Because this transition is suppressed by the vibration branching ratios by a factor of 10^{-2}, we needed as much power as we had available to populate the $V=1$ band. This optical transfer scheme is shown in Figure 4.7.

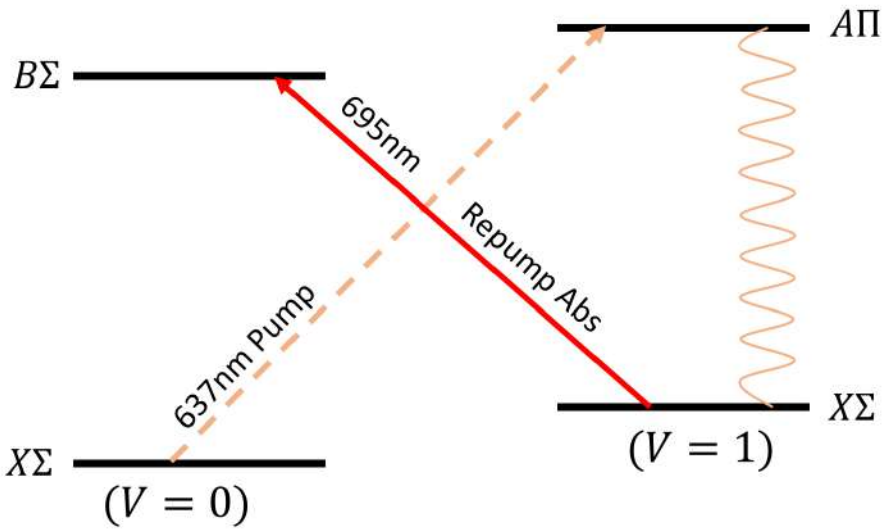

Figure 4.7: Shown in orange, is the pumping scheme used to populate the V=1 ground state. Absorption spectra were performed on the off-diagonal transition (shown in red) to return molecules in the V=1 X $^2\Sigma^+$to the V=0 band through the intermediary B $^2\Sigma^+$.

We used predictions from Bernath [151] as well as other research [149, 150] to guide our search for this transition. We found the $V=1$ pumping transition at 637.7 nm. Once we locked the $V=1$ pumping laser to resonance, the enhancement to the $V=1$ population was clear since

the population in this state increased significantly. A similar direct pumping method may help identify the $V = 2$ repumping transition at a later stage. Direct V=1 pumping could have been used to measure the vibrational branching ratios, but we determined that it would be significantly more precise to directly measure the fluorescence from molecules decaying to the $V = 1$ band as a result of cycling on the $V = 0$ band. Further discussion of the vibrational branching ratios will be offered in chapter 5.

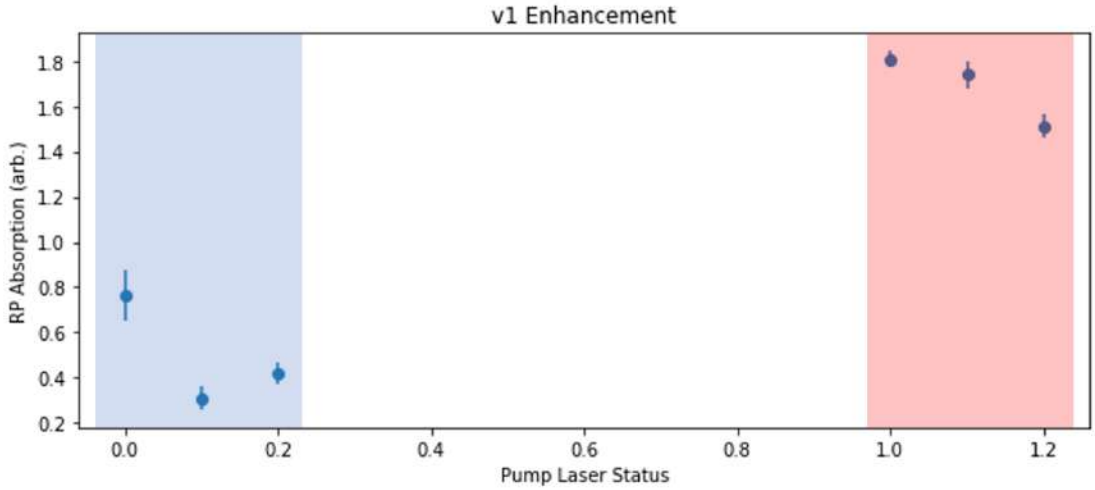

Figure 4.8: I show the effect on the repump absorption of adding the $V = 1$ pumping laser on the integrated absorption. Data points on the left (highlighted in blue) are the integrated repump absorption without the $V = 0 \rightarrow V = 1$ pump, while data points on the right (highlighted in red) show the enhancement to the $V = 1$ population after turning on the pump.

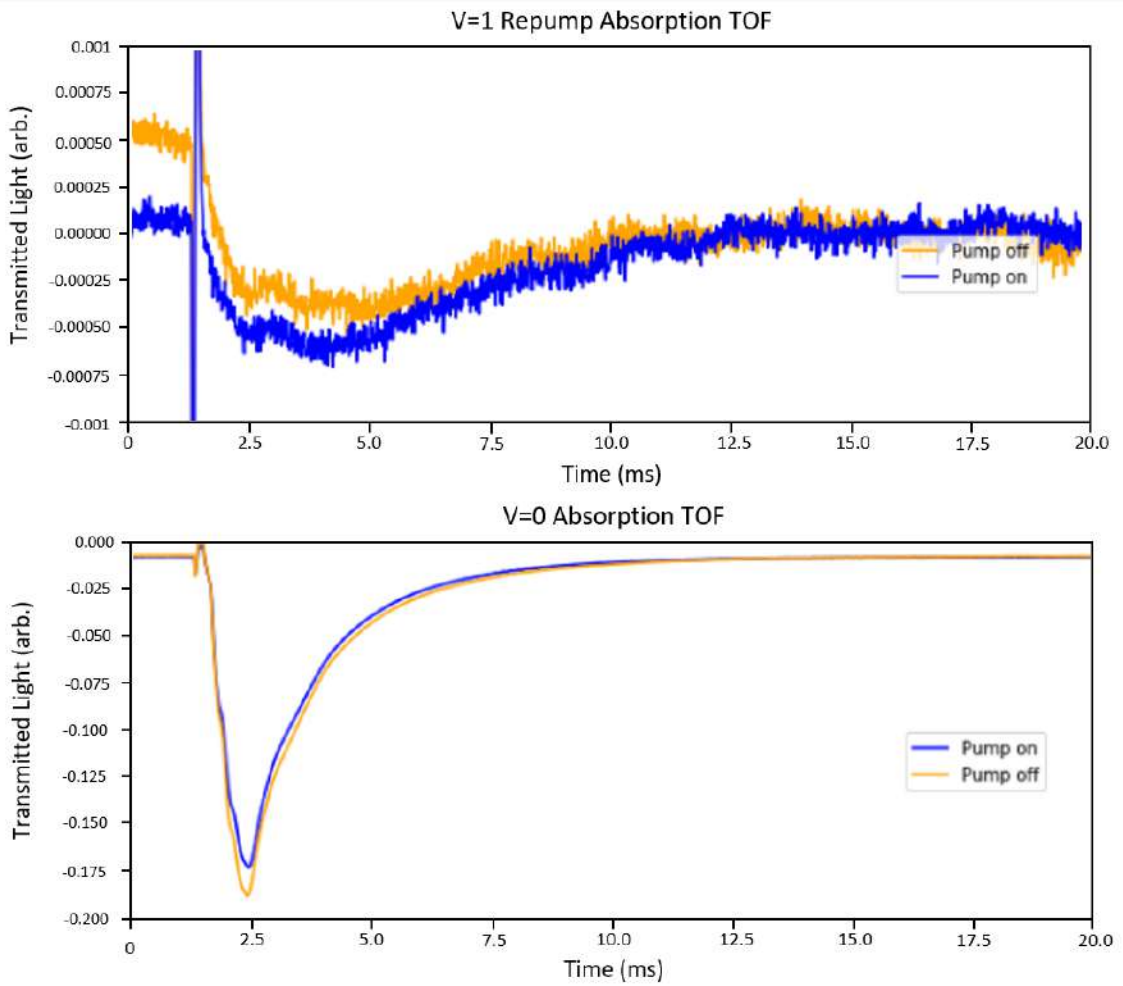

Figure 4.9: This figure shows the effect on the repump absorption time of flight by adding the V=1 pumping laser. The top plot shows the time of flight enhancement as detected through absorption on the $X^2\Sigma^+ \rightarrow B^2\Sigma^+$. The bottom plot shows the time of flight depletion of the $V = 0$ ground state when the $V = 1$ pump is turned on. The orange plots corresponds to the absorption signal without the $V = 1$ pump, while the blue trace shows the time of flight when the $V = 1$ pump is turned on. These are single shot absorption traces.

Figure 4.10, shows a spectrum in which both spin-rotation components of the $X^2\Sigma^+(V = 1, N = 1)$ are visible. Inspection of the spectrum reveals that the higher-lying $J = 3/2$ state ($\delta = 0$) produces significantly higher absorption than the $J = 1/2$ state (δ = 1860MHz).

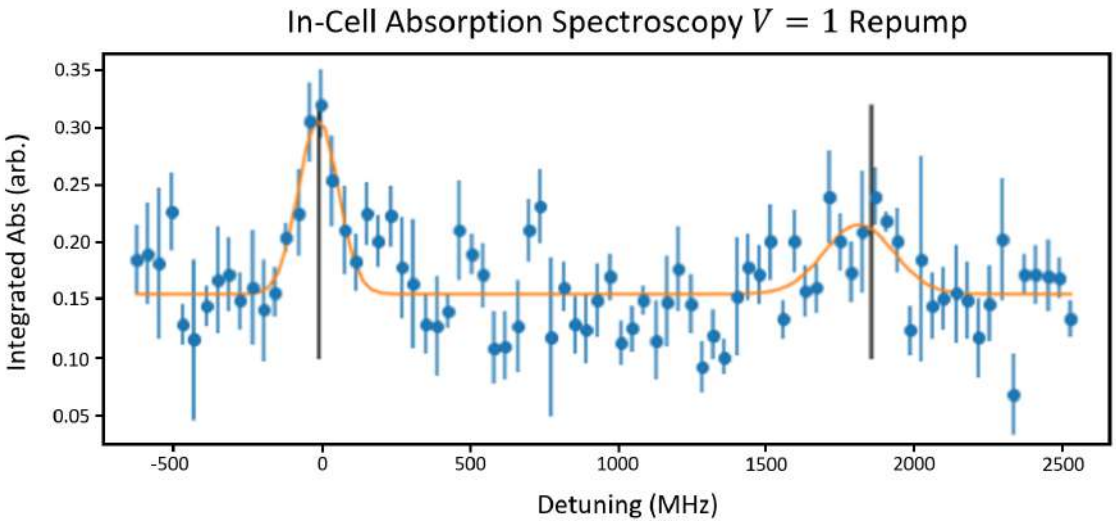

Figure 4.10: A 3GHz wide in-cell absorption spectrum in which both spin rotation states of the $X^2\Sigma^+(V = 1) \rightarrow B^2\Sigma^+(V = 0)$ repumping transition can be seen. Two Gaussians have been fit to the resonances to guide the reader's eye and fit the center of each transition.

The difference in transition strength can be explained by considering the multiplicity of states for each spin rotation state. The ratio of these transition strengths scales as the ratio of Zeeman sublevel multiplicities ($N_{m_f} = 2F + 1$) for each state. The J=3/2 state has F=1,2, giving eight Zeeman sublevels, while the J=1/2 state has four. The expected strength of $J = 1/2$ absorption should be $\approx \frac{1}{3}$ the absorption of the $J = 3/2$ state, which is consistent with our findings.

4.2 In-Cell Dynamics

An absorption probe can be used to measure the translational temperature, rotational temperature, extraction time, and extraction efficiency. The process of ablation is not well described by theory [110] and as a result, designing the best cell for the experiment relies heavily on the experimental optimization of the cell. The ideal cell has a high molecular yield at very low forward velocities, while maximizing the molecular population in the $N = 1$ rotational level used for photon cycling. Herein I will discuss our experimental optimization as we strove to strike a balance between high molecule yield and low beam forward velocity.

Molecules are ejected from the solid CaH_2 sample at thousands of degree kelvin shortly after ablation, but as the ablation products expand, they collide with cold helium buffer gas and thermal-

ize to the ambient He temperature. The rate at which the molecules thermalize is a key parameter to optimize, because unthermalized molecules present in the molecular beam will be at such high temperatures that they will boost the rest of the molecules to higher velocities. One must ensure that the rate at which molecules thermalize is faster than the rate at which molecules exit from the cell. I show the results of the measurements of the thermalization and the extraction time follow.

4.2.1 Kinetic Thermalization

We measured the thermalization time scale by examining the spectroscopic properties of the molecules via in-cell absorption. Specifically, we looked at how the width and center frequency of the molecular resonance changes as a function of time following ablation. Given that, as the molecular velocity distribution cools, the absorption resonance will narrow as the thermal broadening decreases with an absolute lower limit defined by the hyperfine structure and the natural linewidth [155, 57, 136]. In addition, the resonance center stabilizes to the resonance of the rest frame as the molecules loose any collective transverse flow and the effects of the different velocity classes of the molecular ensemble cancel out. We reanalyze data from the previous absorption spectra, but now instead of integrating the entire time of flight signal, we integrate the signal over a much smaller time window. Each class of this time-dependent series of spectrums is fit with a Gaussian to extract the center and width. Figure 4.11 shows the result of this time dependant analysis for the two different spin rotation components of the $X^2\Sigma^+((V = 0, N = 1)) \rightarrow A^2\Pi(V = 0, J = 1/2)$ transition.

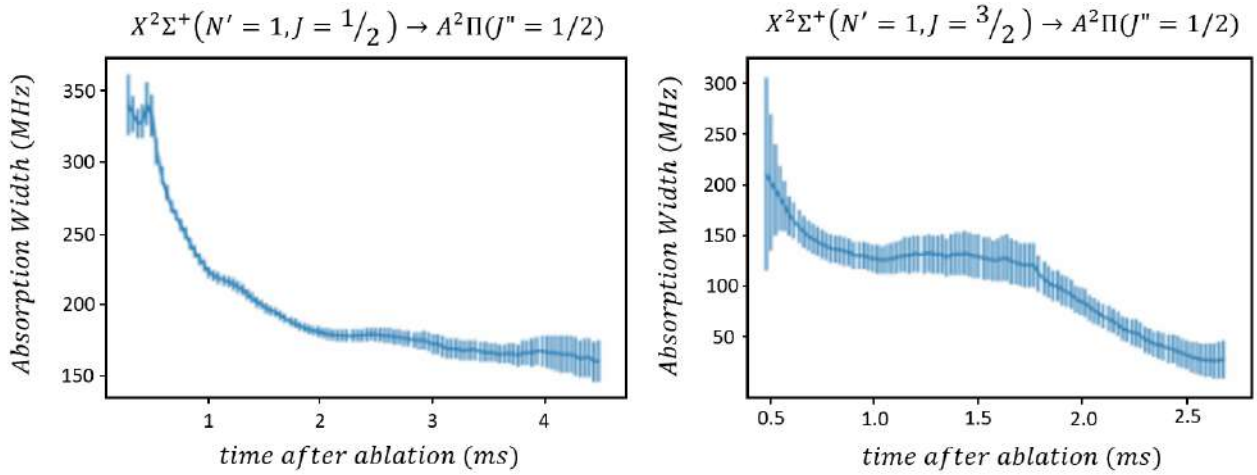

Figure 4.11: The fitted width of the two spin-rotation components of the $X^2\Sigma^+ \rightarrow A^2\Pi$. The width can be converted to the temperature ablation plume. A decreasing width corresponds to cooling and thermalization with the buffer gas. The different cooling timescales indicate different dynamics that depend on the collisional cross-section of each spin-rotation state.

Examination of these thermalization profiles reveals that each spin rotation state has its own dynamics. The $X^2\Sigma^+(J = 1/2, v = 0, N = 1) \rightarrow A^2\Pi(J = 1/2, V = 0)$ state has a clear exponential decay corresponding to thermalization through collisions with the buffer gas, but the $X^2\Sigma^+(J = 3/2, V = 0, N = 1)$ state has a different relaxation rate. I suspect that this is due to the specific collisional cross-sections of each state. It is a well established fact that thermalization rates are dependant on the quantum state of the molecule [110, 124, 126]. The thermalization rate is directly related to the diffusion rate of the molecules within the buffer gas. The thermalization rate is described in the following manner [110, 136] :

$$\frac{dT_a(N)}{dN} = -\frac{T_a(N) - T_b}{C} \tag{4.3}$$

where $T_a(N)$ is the translational temperature of the molecular species after N collisions and T_b is the temperature of the buffer gas. Finally, C is defined as:

$$C \equiv \frac{(m_a + m_b)^2}{2m_a m_b} \tag{4.4}$$

The number of collisions before the ablation plume thermalizes N_{therm} can be calculated as:

$$N_{therm} \equiv C\ ln\left(\frac{T_a(t=0)-T_b}{T_b}\right) \approx Cln\left(\frac{T_a(t=0)}{T_b}\right) \tag{4.5}$$

Therefore, the thermalization timescale is:

$$\tau_{therm} = \frac{N_{therm}}{R_a} \tag{4.6}$$

where the buffer gas collision rate is $R_a \approx n_b \sigma_{ab} \overline{v}_b \sqrt{1+\frac{m_b}{m_a}}$. This equation can be used to derive the "optimal" buffer-gas density n_{Th} for thermalization to take place in under 1ms.

$$n_{Th} \geq \frac{2C}{\sigma_{ab} L_c \sqrt{\frac{m_a}{m_b}+1}} ln\left(\frac{T_a(t=0)-T_b}{T_b}\right) \tag{4.7}$$

Fitting the absorption width, we see that the $X^2\Sigma^+(J=1/2, V=0, N=1)$ state thermalizes in 1.5ms while the $X^2\Sigma^+(J=3/2, V=0, N=1)$ thermalizes in 1ms. This is borderline as we will see extraction from the cell takes place over a comparable timescale. The implications of faster thermalization will be discussed in the extraction section.

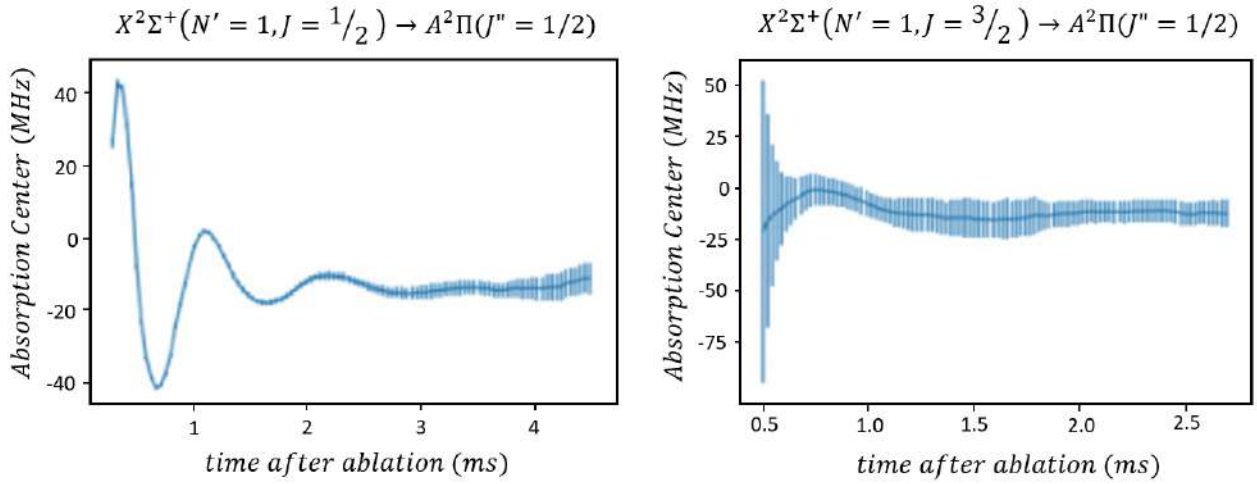

Figure 4.12: The fitted center of the transition resonance for both spin rotation branches of the $X^2\Sigma^+ \rightarrow A^2\Pi$ is shown. The fitted center shifts due to the Doppler shift in the resonance frequency arising from collective flow of the CaH molecules after ablation. The flow begins orthogonal to the sample surface, but is quickly dispersed through collisions with the Helium. One obvious feature of these plots is the characteristic curve of the damped harmonic oscillator. The different damping rates in each spin-rotation state indicated different collisional dynamics that depend on the spin-rotation coupling of that state. The J=3/2 state is damped much faster than the J=1/2 state, indicating a larger collisional cross-section.

The absorption center measurement points to some interesting thermalization dynamics taking place. Any physicist looking at the behavior of the absorption center will recognize the curve of a damped oscillator. This arises as a result of the damping of the initial molecular plume which is ejected from the sample surface with a preferential flow direction away from the sample surface. As the molecules collide with the buffer gas, this initially uniform jet thermalizes until the molecular motion is purely random in the transverse direction.

Again the $X^2\Sigma^+(J = 3/2, V = 0, N = 1)$ is damped away faster, while the $X^2\Sigma^+(J = 1/2, V = 0, N = 1)$ oscillates for a longer period of time. This observation corroborates our earlier conclusion that the collisional cross section of the $X^2\Sigma^+(J = 3/2, V = 0, N = 1)$ state is higher.

4.2.2 Rotational Thermalization

Optimization of the rotational temperature is key to producing a bright beam of molecules that reside in the $N = 1$ rotational level. We probed the thermalization of the rotational levels

by directly measuring the population residing in each of the first few rotational levels via in-cell absorption. We tried to be consistent across all the rotational levels by driving the Q1 transition from the highest-lying spin-rotation state of each rotational state. These transition frequencies are summarized below:

	SR Transition	Freq (nm)
N=0	J=1/2 Q1	431.5023501
N=1	J=3/2 Q1	431.6027651
N=2	J=5/2 Q1	431.6968431
N=3	J=7/2 Q1	431.7863016
N=4	J=9/2 Q1	431.8728397

We found the thermal distribution to heavily favor the rotational ground state, with a significant fraction of the population remaining in the desirable $N = 1$ state. This is consistent across all of the ablation energies that we tested (ablation energies less than 70% failed to produce any molecules). This implies that the buffer gas cell is too cold and collisions with the helium buffer gas are concentrating the rotational population to a rotational temperature of 7K.

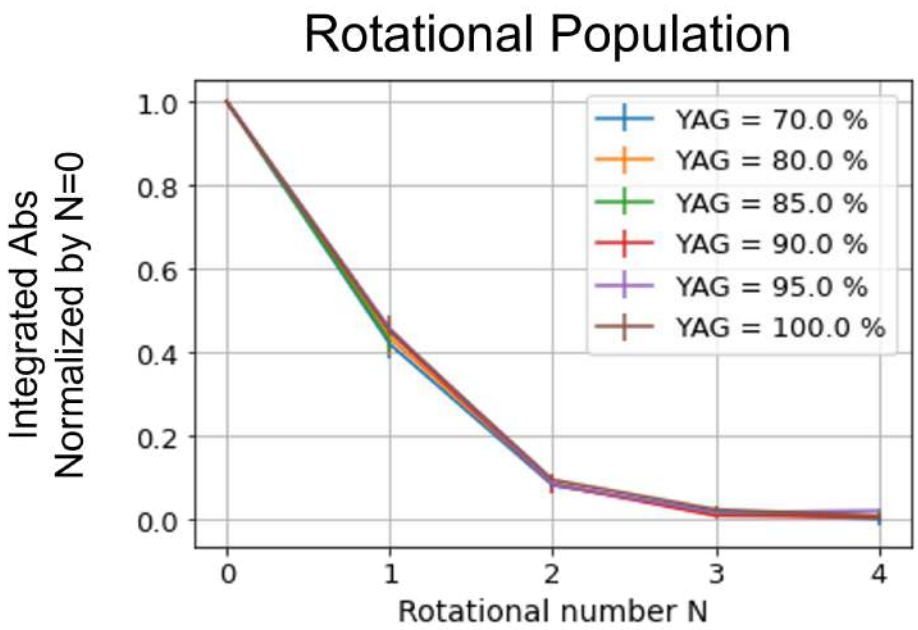

Figure 4.13: The integrated in-cell absorption of the Q1 transitions of the first four rotational levels of CaH after normalization by the $N = 0$ signal. The magnitude of the absorption is proportional to the population in that specific rotational level. The data reveals that the cell is producing primarily $N = 0$ molecules, indicating that the cell is too cold. Attempts to heat the cell and produce more $N = 1$ molecules lead to a significant loss of molecular yield, so we decided to leave the cell at 6K.

Our natural response to this measurement was to heat the cell, hoping this would transfer the $N = 0$ population to the $N = 1$ level. This was done by flowing current through a resistive cartridge heater from Lakshore Cryotronics that I embedded into a block of high purity oxygen-free copper and bolted onto the cell to provide good thermal coupling. The cell thermistors reflected an increase in temperature. However, the rotational population failed to respond in the manner that we anticipated; we found that heating the cell only served to suppress the molecular yield.

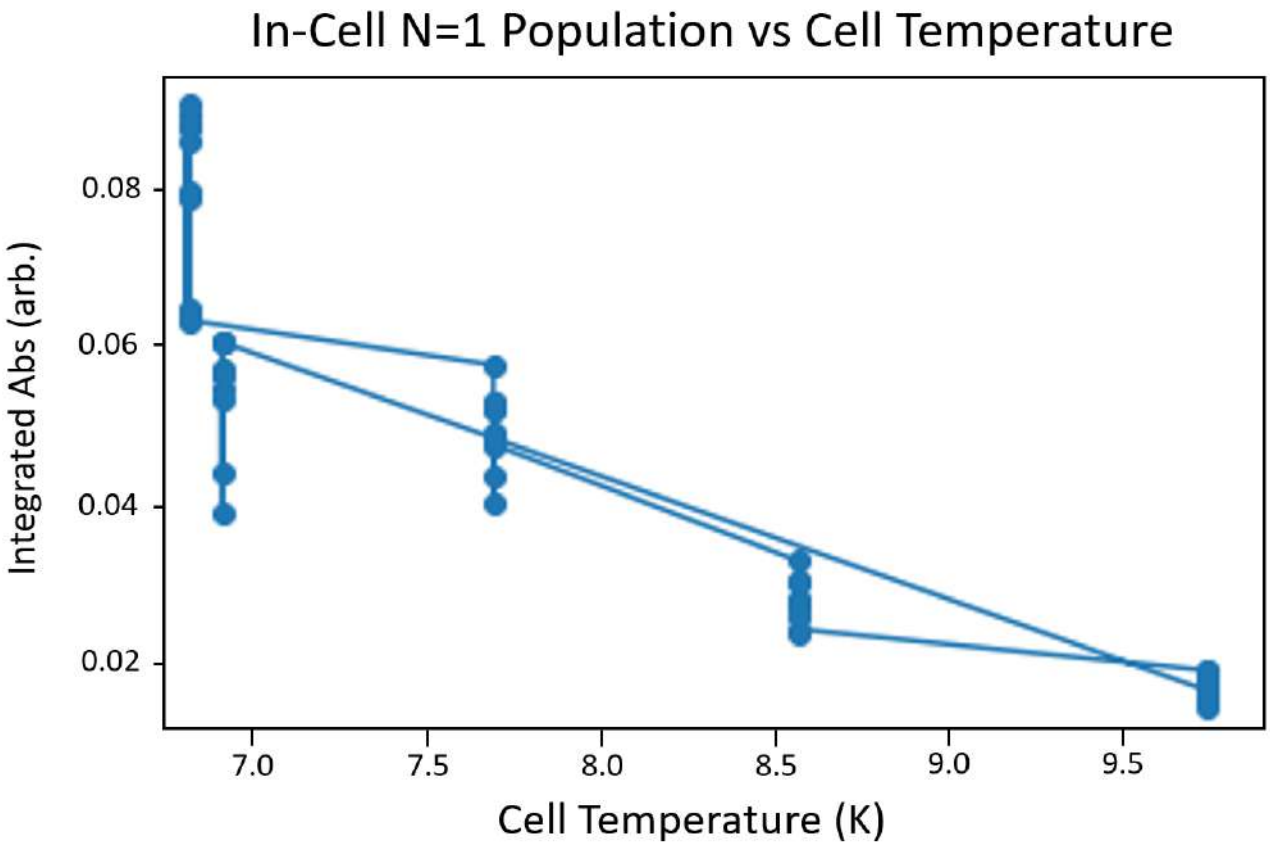

Figure 4.14: The effect on the production of molecules in the $N = 1$ rotational level. Heating the cell only reduced the population in $N = 1$, so we decided to leave the cell at 6K.

The reduction in the $N = 1$ may have been because we heated the cell walls rather than the helium that was flowing into the cell. We chose to heat the cell rather than the helium line directly because the helium line is braised onto 4K bobbins and we did not poses any way of changing the helium temperature without significantly reconstructing the cryostat. Due to the significant population remaining in the $N = 1$ level, we decided to leave the bobbin unchanged and prioritize moving towards a cooling result. The rotational production of the cell should be revisited before longitudinal slowing and MOT loading as this could double the number of available molecules that can be potentially trapped.

4.2.3 Molecular Beam Extraction

Having discussed the relevant thermalization timescales, it makes sense to think about the extraction of the thermalized molecule beam from the buffer gas cell. After molecules ejected during ablation are cooled via collisions with the He buffer gas, the molecules begin to flow out from the cell; molecules that diffuse to the walls of the cell stick to the 4K surface, before they have a chance to exit via the cell aperture. The balance of the diffusion time with the extraction time determines the efficiency of the molecular source.

The diffusion time is given by [110]:

$$\tau_{Diff} = \frac{16}{9\pi} \frac{A_{cell}\, n_{0,b}\, \sigma_{b-s}}{\overline{v}_{0,b}} \tag{4.8}$$

where A_{cell} is the cross-sectional area of the cell, $n_{0,b}$ is the steady state buffer-gas number density, σ_{b-s} is the collisional cross-section of the $X^2\Sigma^+(V = 0, N = 1)$ state, and $\overline{v}_{0,b}$ is the steady-state thermal velocity of the buffer-gas.

extraction rate can be expressed as:

$$\frac{dN_b}{dt} = \frac{1}{4} N_b \overline{v}_{0,b} \frac{A_{aperture}}{V_{cell}} \tag{4.9}$$

giving an extraction time constant of:

$$\tau_{pump} = \frac{4V_{cell}}{\overline{v}_{0,b} A_{aperture}} \tag{4.10}$$

Hutzler et al. define two regimes within buffer gas cells, which are defined by the ratio γ of the extraction and diffusion time constants [110]:

$$\gamma_{cell} = \frac{\tau_{diff}}{\tau_{pump}} \approx \frac{\sigma_{b-s} f_{0,b}}{L_{cell} \overline{v}_{0,b}} \tag{4.11}$$

For $\gamma_{cell} \leq 1$ molecules diffuse faster than they extract. Cells in this regime will have low forward velocities, but a low molecular yield as molecules reach the wall faster than they exit the cell.

Increasing the buffer-gas number density n_b slows down the diffusion time and increases the extraction efficiency of the beam. On the other hand, for $\gamma_{cell} \geq 1$ the extraction time is much faster than the diffusion time and an extraction efficiency between 10% and 40% can be achieved [172, 173]. However, the trade off can be a significant boosting of the molecular velocity distribution and a higher than optimal beam temperature. Using either protocol, the thermalization time should be much faster than extraction or diffusion times.

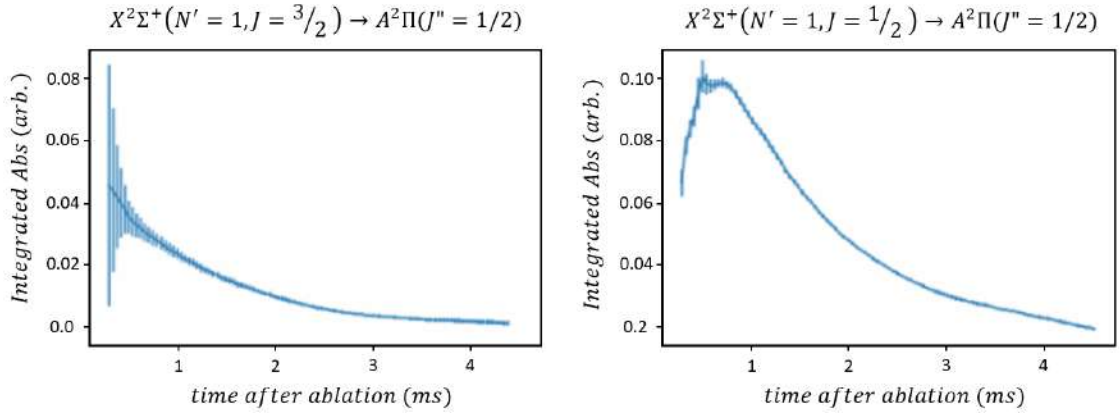

Figure 4.15: The integrated in-cell absorption as a function of time after ablation. Molecules are seen exiting the cell after $\approx$ 2 milliseconds.

We measured the extraction time by fitting a decaying exponential to the in-cell absorption traces of the $X^2\Sigma^+(J = 1/2, V = 0, N = 1)$ and $X^2\Sigma^+(J = 3/2, V = 0, N = 1)$ excited states. We see that both states give a similar extraction time constant of 2ms. While this is longer than the thermalization time, ideally thermalization should occur even faster. In the following section, I will discuss our attempts to improve the diffusion time and the effect it had on the yield of the molecule beam.

4.2.4 Early Beam Dynamics

We investigated the properties of the molecular beam during in-cell thermalization, after extraction from the cell, and the effect the in-cell changes had on the molecular beam in the experimental region. Ablation energy, cell aperture size, and the helium flow rate are the parameters that we can easily change. These measurements are obtained by in-cell absorption and out-of-cell fluo-

rescence. We measured the out of cell absorption by shining a probe laser directly in front of the aperture where the beam density is the highest. This detection scheme is shown in Figure 4.16.

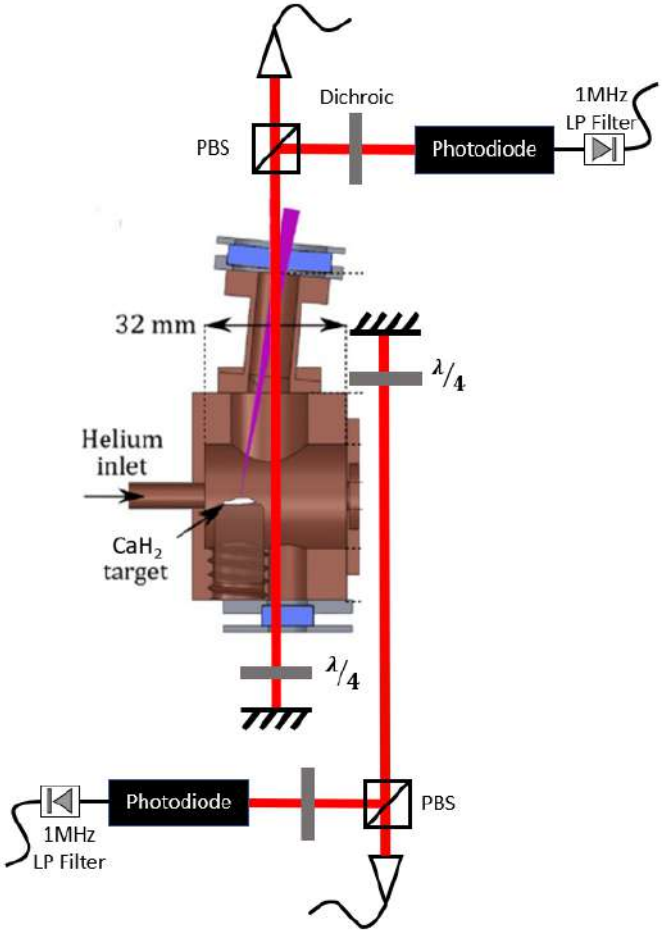

Figure 4.16: The position of the in-cell and out-of-cell absorption probes used to measure the extraction efficiency and the dynamics of the molecules at the onset of beam propagation.

Variations in ablation energy produced the clearest trend in molecule production. Ablation energy is controlled with the LabView sequencer and the impact on molecular yield is clear as shown in 4.17. There is a clear energy threshold which must be surpassed for molecules to be produced in any meaningful quantity. This energy threshold corresponds to the energy required to heat the sample such that there is enough energy to break the adhesion between the crystallized CaH_2 molecules and the binding agent. After surpassing the crystalline binding energy, the in-cell absorption plateaus. However, the out of cell absorption rises linearly with the ablation energy. In light of this, we decided to use the maximum ablation energy to maximize the molecular yield in

the experimental chamber.

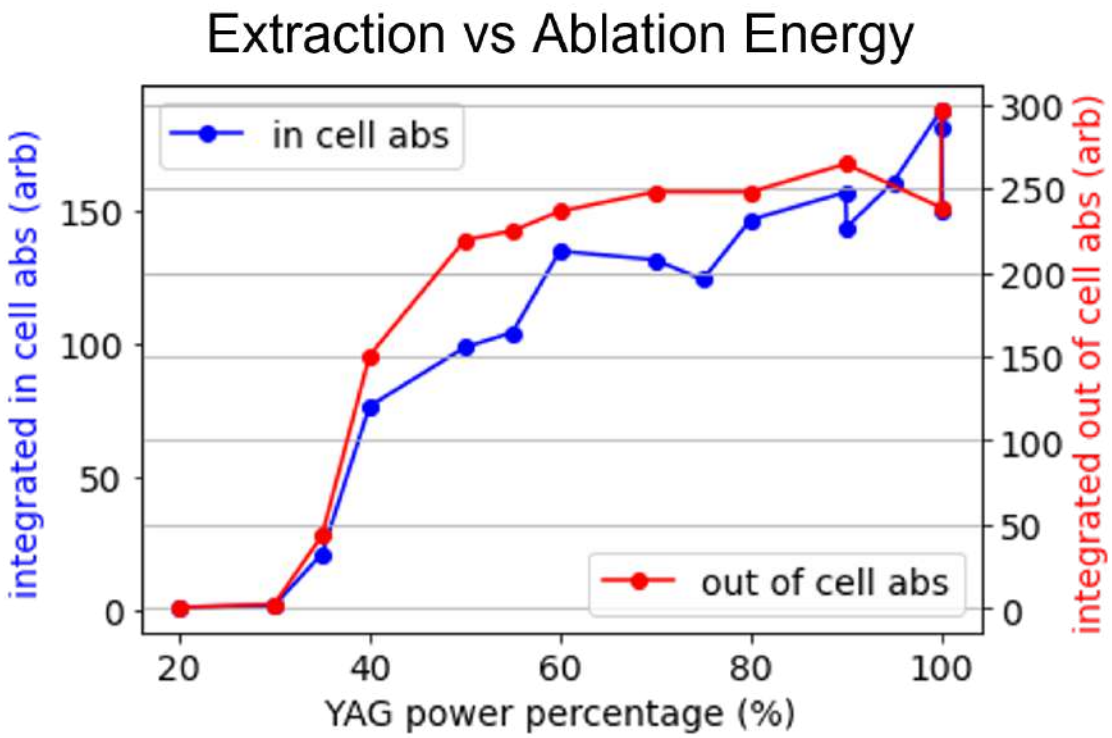

Figure 4.17: The effect of in-cell production and out-of-cell extraction as a function of ablation energy percentage (100% corresponds to 36mJ). In-cell production benefits from increasing the ablation power as high as possible, whereas the beam yield plateaus after 60% (21mJ).

Helium flow rate was also optimized. Increasing the helium flow rate decreases the mean-free path within the cell. This has the effect of decreasing the thermalization time while increasing the diffusion time. The effect on the extraction efficiency is less intuitive because one would expect the extraction efficiency and the beam yield to increase with higher flows, but experimental results paint a murkier picture. The in-cell and out-of-cell absorption both increase linearly with flow rate, but the extraction efficiency (the ratio of the two absorption signals) remains constant. The most interesting result from Helium flow optimization is the observed drop off in beam signal in the experimental region when the in-cell pressure becomes too high. The loss of beam signal was likely due to pressure building up at the transition from the cryostat to the experimental chamber. It is also possible that the increased helium flow knocks the light CaH molecules out of the beam. In other words, as the pressure of the cell increases, collisions occur among the beam particles at further

distances from the cell aperture. Thus increasing the the molecule beam's angular dispersion.

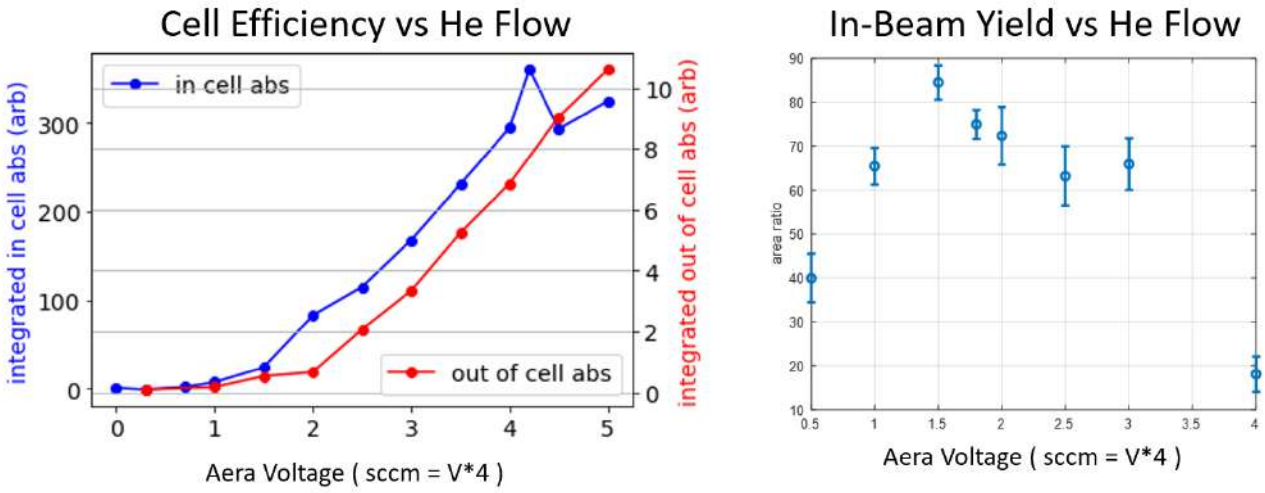

Figure 4.18: The effect of in-cell production and out-of-cell extraction as a function of Helium flow rate. In-cell production grows linearly with Helium flow, but the beam yield is maximized between 4 and 12 sccm of flow.

Another way of examining the molecular beam's dynamics shortly after exiting the cell is to image the fluorescence of calcium atoms that are embedded in the beam as a byproduct of ablation. Calcium is a better probe for this type of measurement because it fluoresces brighter than CaH. This allows one to see the atoms with a standard CCD camera rather a PMT or the EMCCD. We believe that Ca is a good proxy for CaH molecules due to their nearly identical masses, which should give rise to similar collisional dynamics. One such image can be seen in Figure 4.19; the ablation plume is so bright that it saturates the CCD. Calcium fluorescence can also be seen illuminating the interior of the cell. While this image is beautiful, it captures the frustration of the molecular AMO physicist, as it drives home how much more responsive atoms are to laser manipulation.

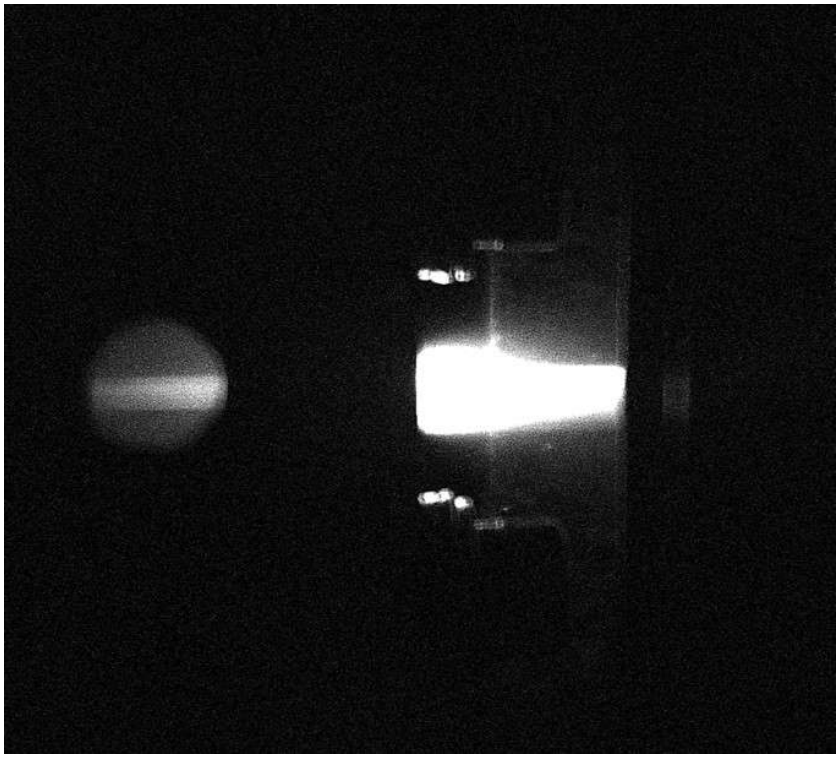

Figure 4.19: The ablation plume as imaged through Ca fluorescence.

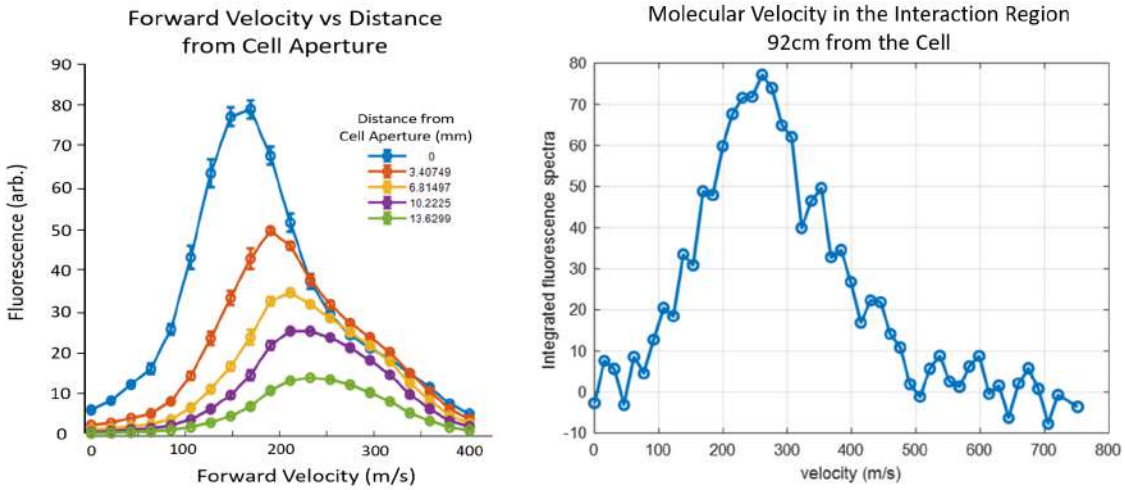

Figure 4.20: The effect of beam velocity boosting that occurs 16mm after the cell aperture, referred to as the zone of freezing. On the left I show a CCD image with the five regions over which the Ca fluorescence signal was integrated as a function of laser frequency to provide the velocity profiles shown on the right. An increase in the mean velocity and the decrease in beam density can be seen as the beam continues to collide with the buffer gas and expands into the beam region.

Lowering the laser power prevents the CCD from saturating. We can then isolate the fluores-

cence of the ablation jet as it exits the aperture by cropping the CCD image. We perform forward velocity dependent spectra to measure the molecular beam velocity as it exits the cell. In this configuration, a laser is shone anti-parallel to the beam direction. The high velocity of the Ca molecules as they exit the cell produce Doppler shift in the transition resonance. Due to the abundance of signal we can take it one step further and look at the Doppler-dependent fluorescence as a function of distance from the cell. We found that the molecular beam velocity distribution changes as a function of distance from the cell. The region in which the velocity distribution is modified by collisions in the “zone of freezing". After the beam density decreases, the molecules transition to a ballistic, collision-less environment where we perform our experiments. We can clearly observe that the molecular beam is boosted to higher velocities as it propagates away from the aperture. The initial velocity distribution peaked below 100 m/s at the cell aperture, but increases to a mean velocity of 150 m/s after 13mm of boosting. This boosting is reduced by some groups through the use of a two stage cell. The second stage is maintained at a lower pressure than the first cell, but as molecules propagate through this region they isotropically collide with the buffer gas and boosting is reduced [110, 174]. It is important to note that the beam density drops as a result of the collisions with the buffer gas. I performed some direct Monte-Carlo hydrodynamic simulations using the DS2V program to see if the addition of deLaval bell nozzles would help collimate this beam. Unfortunately, the simulations did not reveal any promising results at the aperture pressures we require. A thorough discussion of the effects of such nozzles in higher pressure regimes can be found in a paper by Takahashi et al [125].

The final parameter that we could vary without building a new cell and 4K shield region was the cell aperture. Again, the results were not the most intuitive. As we expected that decreasing the aperture size should raise the pressure within the cell, increasing the diffusion time to allow for better thermalization at the cost of decreasing extraction efficiency. One may vary the helium flow rate at each aperture size to try and distinguish between the effects, as can be seen in Figure 4.21.

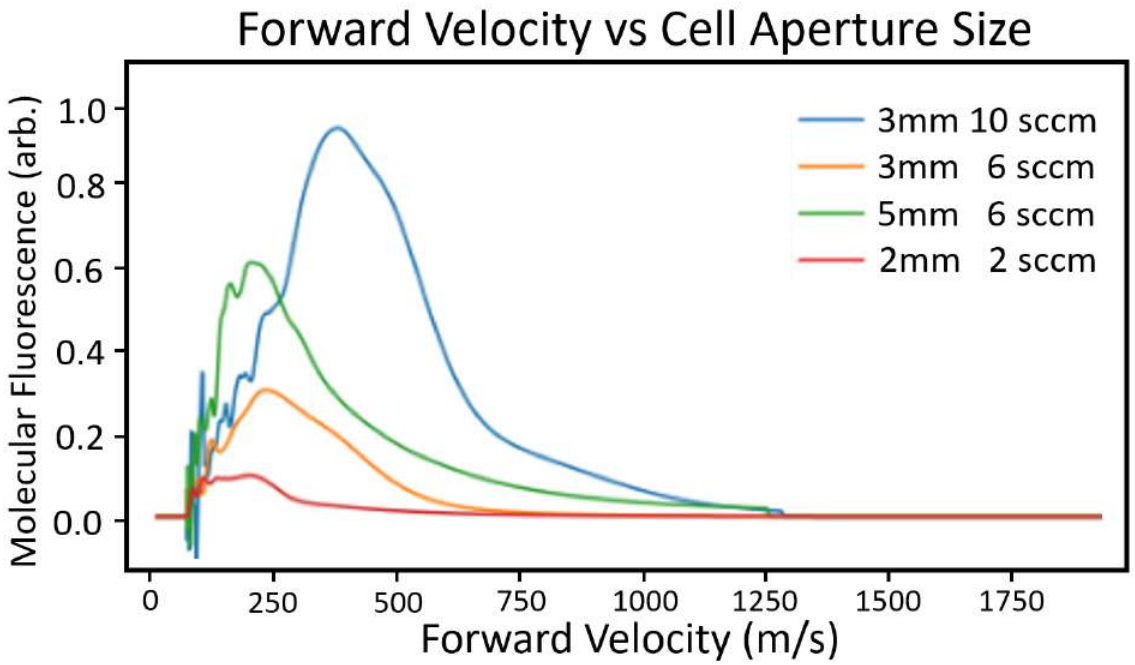

Figure 4.21: I show the effect of the cell aperture size for different He flow regimes. We seek to optimize the molecular yield at low velocity. Therefore, we chose to operate the cell with a 5mm aperture while flowing 4sccm of He.

This measurement shows a significant broadening of the thermal distribution as aperture size increases as molecules are able to exit the cell faster and thermalize less. Larger apertures increases the population at high velocity, but also increases the population at lower velocities. Thus, we chose to operate with the 5mm aperture. We also attempted a 7mm aperture, but found that this size aperture did not allow enough time for thermalization, and the velocity distribution produced by the 7mm aperture was not appropriate for our applications. Finally, I would like to call attention to the difference between the 3mm aperture at medium flow (4 sccm) when compared to the velocity distribution at high flow (8 sccm). Here we see the effect of too much buffer gas and the resultant velocity boosting that was discussed in the prior section.

Chapter 5: Beam Measurements, Scattering Rate Optimization, and Vibrations Branching Ratios

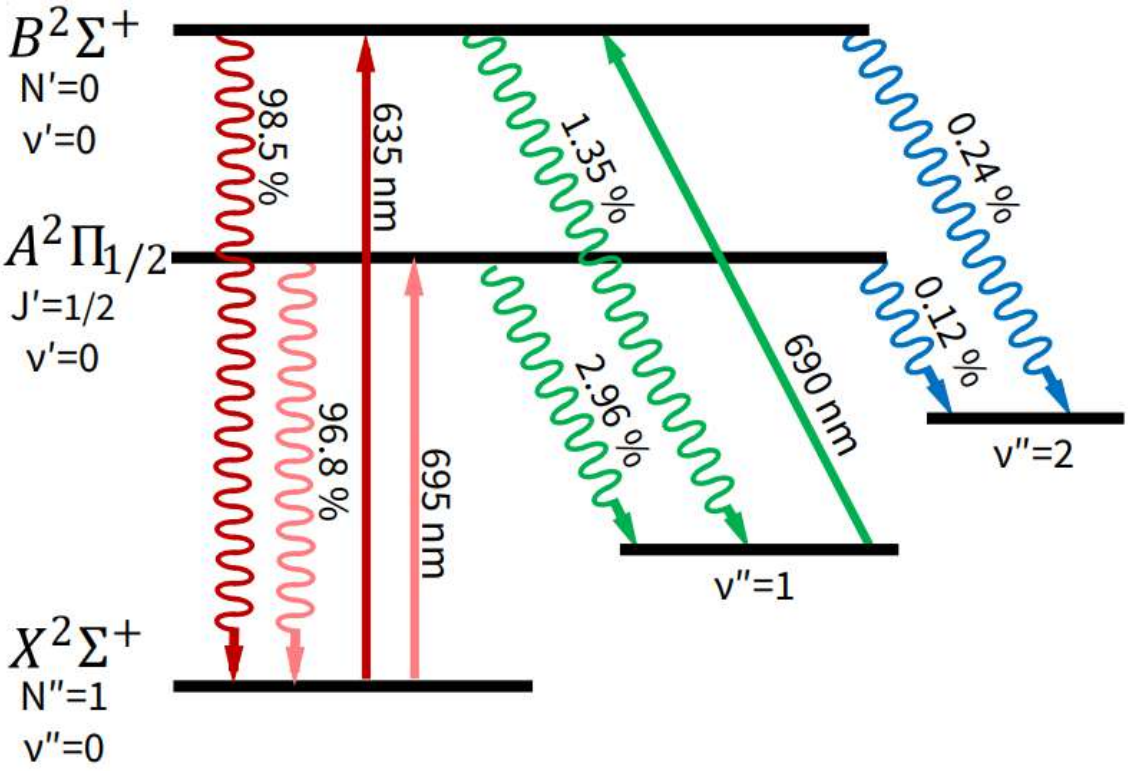

Figure 5.1: I show a diagram of the cooling (pink), imaging (red), and repumping (green) transitions used in this experiment. The decays from the excited states to the $V = 0, 1, 2$ states are represented as wavy lines.

5.1 Introduction

In this section, I will present the in-beam experiments used to characterize the transitions necessary for transverse laser cooling. Laser cooling requires that we scatter as many photons as possible from the molecular beam as quickly as physically possible. Therefore, one must understand the properties of the cooling, imaging, and repumping transitions to maximize control of the system. Sisyphus cooling has a very small margin for error, and when attempting this type of cooling with limited laser power, the settings of the experimental apparatus must approach perfection.

I began this painstaking experimental optimization by performing high resolution spectroscopy to identify the hyperfine structure for each of the transitions. Next, I measured the vibration branching ratios of each transition by directly detecting fluorescence as the molecule relaxed from the $V = 0$ band to the $V = 1$ and $V = 2$ bands. Then, I demonstrated the ability to cycle photons within the $V = 0$ band by addressing both spin-rotation components of the $X^2\Sigma^+(V = 0, N = 1)$ ground state. Subsequently, I measured the saturation intensity. I put together these results to measure the depletion rate of the $V = 0$ band over many passes of the $X - B$ and $X - A$ lasers that filled the interaction region. Finally, I used the vibrational branching ratios to convert the sustained depletion rate into the sustained scattering rate.

5.2 In-Beam Spectroscopy

I located the transitions needed for transverse laser cooling in the cryogenic cell in chapter 3 using absorption spectroscopy. However, the high density and relatively high temperatures produced significant collisional and thermal broadening of the transitions, making it impossible to resolve the hyperfine structure of the two spin-rotation components of the $X^2\Sigma^+$ ground state. To prevent population pile up in the unaddressed hyperfine state; it is necessary to address the hyperfine states of each spin-rotation level. Therefore, the first logical step toward optical manipulation of the molecules in-beam was to spectroscopically identify the hyperfine states of the $X^2\Sigma^+(V = 0, N = 1)$ and $X^2\Sigma^+(V = 1, N = 1)$ states. I needed to ensure that the excited states

did not possess a hyperfine structure that would need to be considered. I addressed the hyperfine resonances with EOMs or AOMs to match the measured electronic ground state splittings. In this section, I will present the experimental methodology by which we performed this spectroscopy in addition to the results of that spectroscopy.

5.2.1 Experimental Set-Up

The experimental configuration used to measure the molecular hyperfine structure is a simplified version of the experiment ultimately used for sisyphus cooling. Molecules are produced via ablation of a solid target of CaH_2 within the 6K cryogenic buffer gas cell. The pulsed 1064nm Nd:YAG laser produces a 30 mJ, 10 nanosecond pulse focused to a waist of 1.5 mm. After ablation, the internal rotation and vibration states of the CaH molecules thermalize via collisions with the buffer gas. The cool molecules are embedded in the flow of helium exiting the 5 mm cell aperture with a forward velocity of 250 ± 200 m/s [146]. The transverse velocity of the molecules is limited by placing a 5 mm aperture 60 cm away in the path of the molecular beam. The location of the velocity skimming aperture can be seen in Figure 5.2. This aperture only permits molecules with an average transverse temperature $\leq$ 12 mK to pass into the beam chamber. This transverse temperature corresponds to a $\frac{1}{e^2}$ transverse velocity of ± 3 m/s. This lowers the fluorescence signal detected by the spectroscopy PMT. However, it also reduces the thermal broadening of each transition, giving more precise knowledge of the hyperfine splitting frequencies.

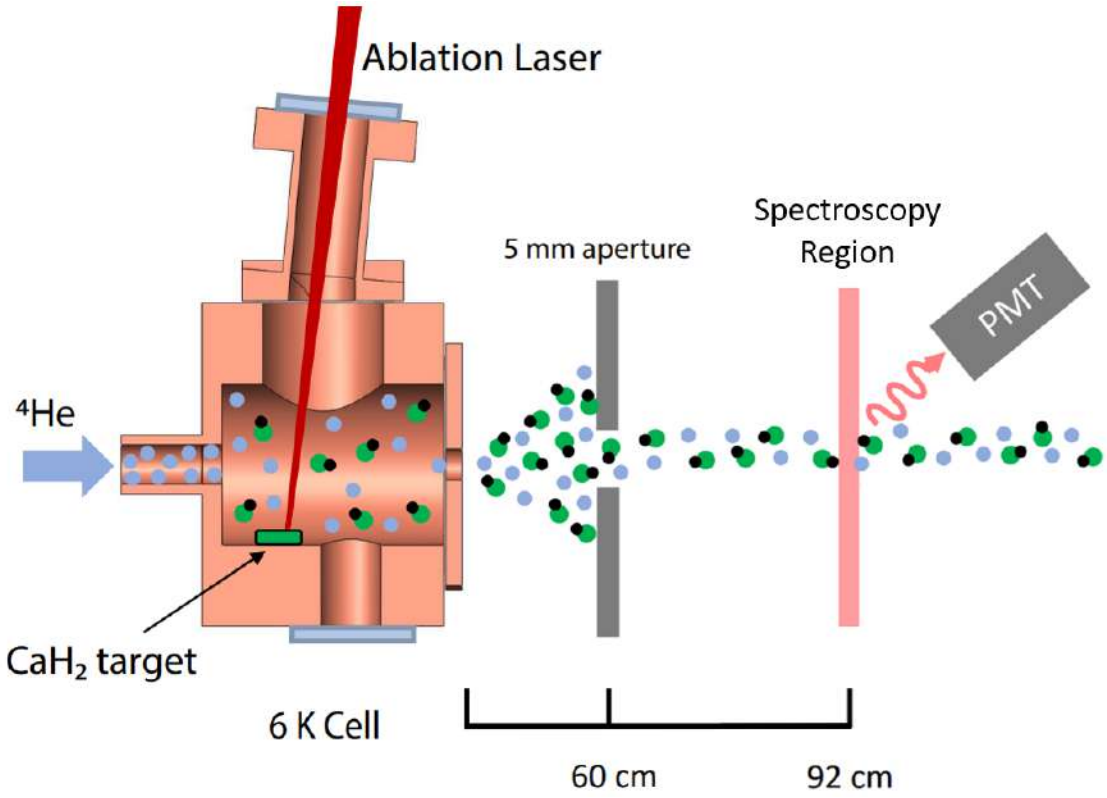

Figure 5.2: Shows the experimental set up used to perform in-beam spectroscopy. The molecules leave the cryogenic cell and propagate 60 cm before passing through a 5 mm velocity filtering aperture that limits the molecular beam's transverse velocity. The beam propagates another 32 cm before a transverse spectroscopy laser interacts with the molecules. Fluorescence from the molecules is collected by a 60 mm focal length planoconvex lens before it is focused onto the PMT's active area.

After passing through the transverse temperature filter aperture, molecules ballistically propagate an additional 32 cm before entering the spectroscopy chamber, where the molecules are exposed to a probe laser with $\Delta f_{laser} \approx 1$ MHz. The chamber is a CF-2.75 6 way cube with blackened 20 cm nipples placed horizontally that limit the background scatter by moving the laser windows far from the detection region. When the laser frequency is on resonance with each of hyperfine states, the molecules fluoresce isotropically. The power broadening of the lines was limited by exposing the molecules to $\approx$ 3 mW of laser power. A 60 mm focal length A coated, planoconvex lens is mounted outside the chamber to collimate this light, before a second lens focuses the fluorescence through a dichroic filter onto the active area of the PMT. The dichroic filter serves to isolate the molecular fluorescence from the external light of the lab. The PMT signal recorded

by the National Instruments DAQ is saved on the computer for analysis. The frequency dependant fluorescence is calculated by recording the time of flight signal, subtracting the background, and integrating over the duration of the molecular pulse. The hyperfine splittings are then fitted out to provide the relative splittings.

5.2.2 $X^2\Sigma^+(V = 0, N = 1) \rightarrow B^2\Sigma^+(V = 0, N = 0)$ Spectroscopy

The first set of transitions to be spectroscopically probed were the $X^2\Sigma^+(V = 0, N = 1) \rightarrow B^2\Sigma^+(V = 0, N = 0)$ states. We create a partially closed cycling transition that can only leak via vibrational decay by driving $\Delta N = \pm 1$ rotational transitions between the ground state and the second lowest electronic state of opposite parity ($B^2\Sigma^+$). We chose to investigate these states first due to the higher power non-antireflective coated diodes that were available at the transition wavelength. The Senstech P30PC-01 was used in combination with a FL635-10 Thorlabs dichroic filter, and the quantum efficiency of the detection system was found to be 3.75% at 635 nm. These transitions are at approximately 635.12 nm and the spin rotation states are split by 1.86 GHz. The initial measurements of the hyperfine structure of CaH were provided by Bernath et al. in their 2013 paper [58]. The J=1/2 spin rotation state is split into $F = 0$ and $F = 1$ sublevels, with a total of $2F + 1 = 4$ m_F sublevels that are unresolved. Meanwhile, the J=3/2 spin rotation state is split into two F sublevels, $F = 1$ and $F = 2$ with a total of $2F + 1 = 8$ m_F sublevels that are unresolved. Our measured hyperfine splittings of 54 MHz (J=1/2) and 101 MHz (J=3/2) were found to be in agreement with previous measurements [58]. Note that the relative strengths of the various F sublevels are in good agreement with the $N_{mf} = 2F+1$ multiplicities of the m_F sublevels for each F state.

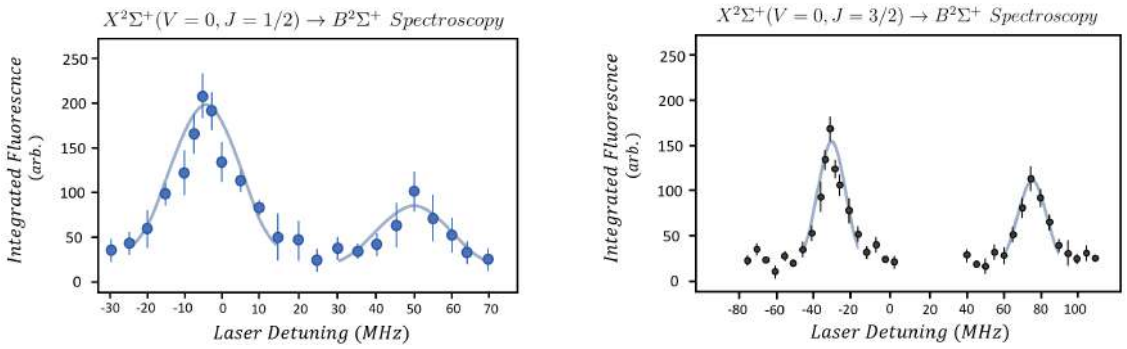

(a) J=1/2 (b) J=3/2

Figure 5.3: In-beam spectroscopy used to identify the hyperfine states of both the J=1/2 and J=3/2 branches of the $X^2\Sigma^+ \rightarrow B^2\Sigma^+$ transition.

5.2.3 $X^2\Sigma^+(V=0,N=1) \rightarrow A^2\Pi(V=0,J=1/2)$ Spectroscopy

Next we measured the $X^2\Sigma^+(V=0,N=1) \rightarrow A^2\Pi_{1/2}(V=0,J=1/2)$ hyperfine splittings of the primary cooling transition. While this was not strictly necessary, as this transition and the $X^2\Sigma^+(V=0,N=1) \rightarrow B^2\Sigma^+(V=0,N=0)$ transitions share the same ground state and hyperfine states, it confirmed the hyperfine splitting previously measured. It also provided us with confirmation that the lowest lying J=1/2 branch of the A state did not have a resolvable structure that would need to be accounted for.

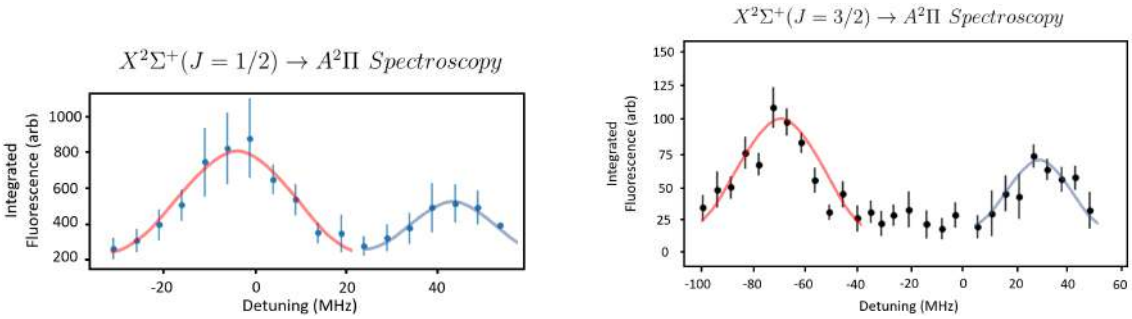

(a) J=1/2 (b) J=3/2

Figure 5.4: In-beam spectroscopy used to identify the hyperfine states of both the J=1/2 and J=3/2 branches of the $X^2\Sigma^+ \rightarrow A^2\Pi$ transition.

We used the SenseTech P30PC-01 PMT with the Semrock FF01-692/40-25 dichroic filter to

isolate the fluorescence of the transition from the room light. The quantum efficiency of the detection system was dominated by the PMT photocathode assembly that was experimentally measured to be 1.75% at the transition wavelength of 695.13 nm. Again, this transition makes use of the $\Delta N = \pm 1$ rotational selection rule to ensure a quasi two level cycling system with similar $F = 0, 1$ ($F = 1, 2$) hyperfine levels for the J=1/2 (J=3/2) states. The analysis of the fluorescence confirmed the measurements performed with the B state and showed no resolvable hyperfine structure in the excited state.

5.2.4 $X^2\Sigma^+(V = 1, N = 1) \rightarrow B^2\Sigma^+(V = 0, N = 0)$ Spectroscopy

The X $^2\Sigma^+(V = 1, N = 1)$ spin-rotation manifold was the final set of states that we needed to spectroscopically identify for this work. Due to the vibrational deformation of the spin-rotation coupling, we expected different spin-rotation splittings in the first excited vibrational state. Upon finding the transitions and fitting the spin-rotation splitting, we confirmed that the first vibrational level was deformed, giving a splitting of 1.894 MHz. The hyperfine splitting was measured to be 56 MHz for the $J = 1/2$ state, while the $J = 3/2$ state was split by 110MHz.

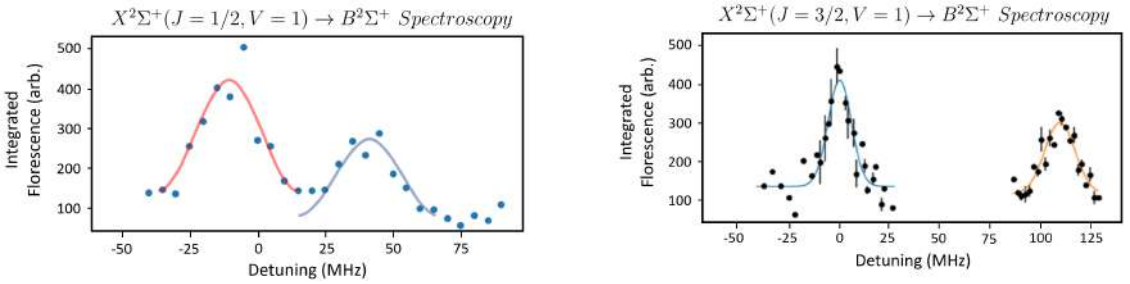

(a) J=1/2 (b) J=3/2

Figure 5.5: I show the in-beam spectroscopy used to identify the hyperfine states of both the J=1/2 and J=3/2 branches of the repumping X$^2\Sigma^+(V = 1) \rightarrow$ B$^2\Sigma^+(V = 0)$ transition.

5.3 Vibrational Branching Ratios

Angular momentum selection rules can be used to engineer a quasi-two level system suitable for photon cycling between molecular rotational states; however, there are no selection rules that

govern the vibrational decay channels. Rather, the vibrational decay probabilities are determined by the overlap integral of the excited state with the vibrational ground state of interest. This integral is called the Frank-Condon Factor (FCF), and can be written in the following form:

$$f_{v'v''} = \int_0^{\inf} \psi_{v'}^* \psi_{v''} \, dr \tag{5.1}$$

The decay probability also scales with the frequency of the decay ($\omega_{v'v''}$) cubed. This normalized decay probability, including the frequency scaling, is called the vibrational branching ratio (VBR) and can be calculated from the FCFs ($f_{v'v''}$) as follows [175]:

$$q_{v'v''} = \frac{f_{v'v''} \times \omega_{v'v''}^3}{\sum_{n=0}^{\inf} f_{v'n} \times \omega_{v'n}^3} \tag{5.2}$$

Cooling molecules requires scattering hundreds of photons, and slowing molecules to MOT capture velocities requires around ten thousand photons. Therefore, it is essential to know, 1^{st}, the decay probability to the first few excited vibrational states, and 2^{nd}, to close these leaks with sufficient repumping lasers in order to reach the required number of photons. [176, 177, 111]. If the vibrational branching ratios are not sufficiently suppressed, the number of repumping lasers becomes excessive and laser cooling is essentially precluded. The vibrational branching ratios for all of the laser cooled molecules such as CaF [5, 51], SrF [111], YbF [5, 153], and YO [7, 178] are all characterized by their highly diagonal VBR values. The VBRs of CaH have been calculated theoretically [179, 150, 149] (shown in Figure 5.6) and strongly support the possibility of laser cooling. In the following experiments, we measured the vibrational decays to the first three vibrational levels. These measurements show that laser slowing of CaH molecules is possible.

Transition	Lifetime τ (ns)	Vibrational Quanta (v'')	Transition wavelength (nm)	FCF Theory ($f_{0v''}$)
$A \rightarrow X$	33(3)	0	695.13	0.953
		1	761.87	0.0439
		2	840.07	2.74×10^{-3}
		3	932.80	2.3×10^{-4}
$B \rightarrow X$	58(2)	0	635.12	0.9856
		1	690.37	0.0132
		2	753.97	1.1×10^{-3}
		3	827.84	1×10^{-4}

Figure 5.6: I show the properties of the two excited electronic states used in this experiment. I give the lifetimes of the excited states and then give the transition wavelengths associated with the decays to different vibrational levels. In the final column, I give the theoretical Franck Condon Factors as reported by previous studies [179, 150].

5.3.1 Experimental Set-Up

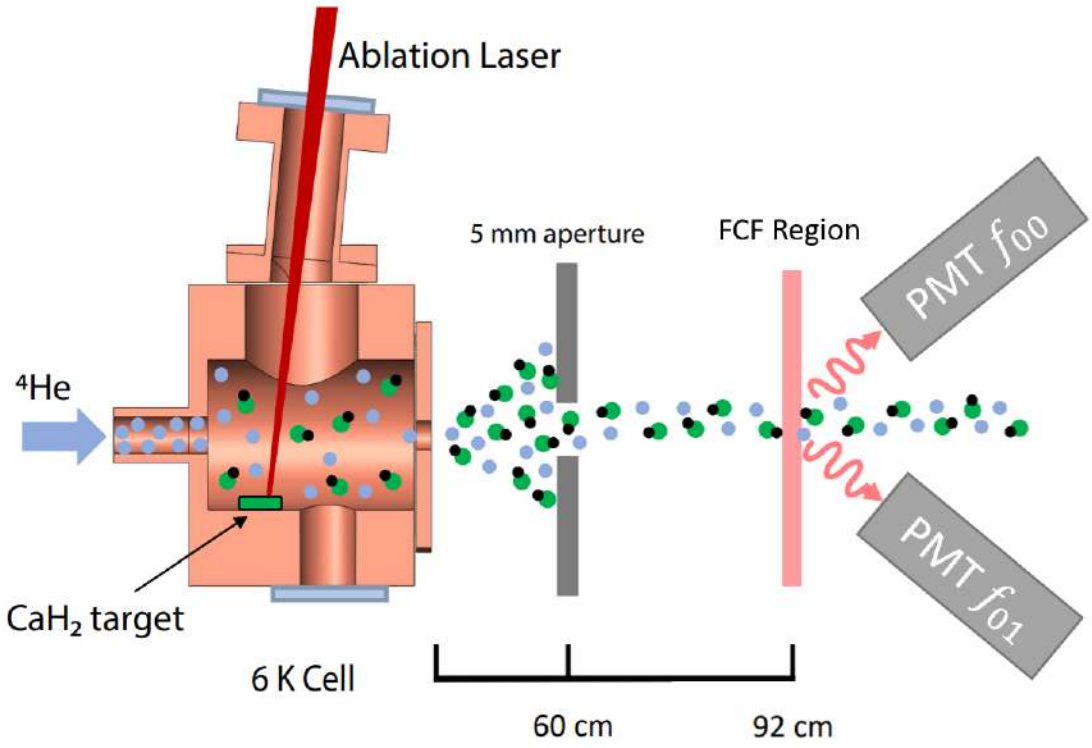

Figure 5.7: I show the experimental setup used to perform in-beam measurements of the vibrational branching ratios. The molecules leave the cryogenic cell and propagate 60cm before passing through a 5mm velocity filtering aperture that limits the molecular beam's transverse velocity. The beam propagates another 32cm before a transverse excitation laser interacts with the molecules driving either the $X^2\Sigma^+ \rightarrow A^2\Pi$ or $X^2\Sigma^+ \rightarrow B^2\Sigma^+$ transition. I placed two PMTs in the detection chamber, each with different dichroic filters to isolate the fluorescence of one of the vibrational decay channels. Fluorescence from the molecules is collected by a 60mm planoconvex lens before it is focused onto the PMT's active area.

In Figure 5.7, I show the experimental setup used to directly measure the vibrational branching ratios. Molecules are ablated from a solid CaH_2 target within the cryogenic cell. These molecules thermalize and exit the cell in a plume of He buffer gas through the 5 mm cell aperture. The molecule beam proceeds to propagate freely for 60cm from the cell aperture before passing through an additional 5mm aperture that limits the transverse velocity to ± 3m/s. Molecules then proceed to the measurement chamber, which is composed of a CF-2.75 six way cross with horizontal 12 inch long nipples that separate the laser windows away from the detection region to reduce scatter.

A laser pumps either the $X^2\Sigma^+(V=0) \rightarrow B^2\Sigma^+(V=0)$ or the $X^2\Sigma^+(V=0) \rightarrow A^2\Pi(V=0)$ transition, from which molecules can decay back to the original $X^2\Sigma^+(V=0)$, the $X^2\Sigma^+(V=1)$, or the $X^2\Sigma^+(V=2)$ vibrational states. We control which decay pathway we detect on the photon counting PMTs with dichroic line filters available from Semrock and Thorlabs listed in Figure 5.8.

	F_1	F_2	F_3
$A^2\Pi_{1/2}$ q_{01}	FF01-692/40-25	FF02-684/24-25	FF01-760/12-25
$A^2\Pi_{1/2}$ q_{02}	FF01-692/40-25	FF02-684/24-25	FF01-840/12-25
$B^2\Sigma^+$ q_{01}	FL635-10	FF01-630/20-25	FF01-690/8-25
$B^2\Sigma^+$ q_{02}	FL635-10	FF01-630/20-25	FF01-760/12-25

Figure 5.8: I list the dichroic filter sets used to isolate the fluorescence from each vibrational decay channel so that we can measure the vibrational branching ratios.

We use two PMTs to simultaneously measure the florescence to the different vibrational ground states. These PMTs are the Senstech P30PC-01 and the Hamamatsu R13456, both operated in photon counting mode. The decays to the first excited vibrational level ($V=1$) are the product of 200 shots, while to detect the minuscule decay to the V=2 state with confidence required 700 shots.

5.3.2 Measurement of the Vibrational Branching Ratios

We first compute the ratio R_0 of the PMT time of flights corresponding to $V=0$ decay. This ratio, written in terms of the experimental parameters and the vibrational branching ratios, is:

$$R_0 = \frac{N q_{00} \Omega_{P_2} T_{F_{2,\lambda_{00}}} Q_{P_{P_2 \lambda_{00}}}}{N q_{00} \Omega_{P_1} T_{F_{1\lambda_{00}}} Q_{P_{1,\lambda_{00}}}} \tag{5.3}$$

Here, the P_1 and P_2 subscripts denote PMTs one and two, while F_1 and F_2 indicate the dichroic filters. N is the number of photons detected by each PMT, q_{00} is the $V=0$ vibrational branching ratio of interest, Ω is the geometric collection efficiency, T is the transmission efficiency of the dichroic on each PMT, and Q represents each PMT's quantum efficiency at the decay wavelength. We account for the different collection efficiencies of the PMT mounting optics and the different

quantum efficiencies of the two PMTs by performing differential measurements. This means that we take a repeat of each measurement after swapping the dichroic filters, and then we take a ratio of these measurements to divide away the unique efficiencies of the detection hardware. We proceed to measure the decays to the excited vibrational state, we replace filter F_2 with F_3, which transmits, λ_{01} to measure $V = 1$ decay or λ_{02} to measure $V = 2$ decay. We record the fluorescence time of flight and take the following ratio:

$$R_{V''} = \frac{N' q_{0V''} \Omega_{P_2} T_{F_{3,\lambda_{0V''}}} Q_{P_{P_2,\lambda_{0V''}}}}{N' q_{00} \Omega_{P_1} T_{F_{1\lambda_{00}}} Q_{P_{1,\lambda_{00}}}} \tag{5.4}$$

where v'' can be either $V = 1$ or $V = 2$. Finally, we can combine these two ratios and rearrange to get the ratio of the vibrational branching ratios:

$$\frac{q_{0V''}}{q_{00}} = \frac{R_{V"} Q_{P_{2,\lambda_{00}}} T_{F_{2,\lambda_{00}}}}{R_0 Q_{P_{2,\lambda_{0V"}}} T_{F_{3,\lambda_{0V"}}}} \tag{5.5}$$

The final step is to assume that the sum of the first three vibrational branching ratios must sum to one. This assumption is well motivated, because the VBR's fall off exponentially as V'' increases. As a result, the $V = 3$ VBR is less than the statistical uncertainty of each of the first three measurements. This final requirement is expressed as:

$$\sum_{V''=0}^{2} (q_{0V''}) \ = 1 \tag{5.6}$$

In Figure 5.9, I show an example of the PMT time of flights when detecting the $V = 0$ and $V = 1$ decay of the $B^2\Sigma^+(V = 0)$ [146]. The blue trace is the $V = 0$ decay detected by the PMT 1 (P_2), whereas the orange line is the time of flight fluorescence to the first excited vibrational level ($V = 1$) by PMT 2 (P_2). The orange points in the inset show the flouresence signal of the molecules that decay to the $V = 1$ state. The blue trace shows the expected decay given the vibrational branching ratio. The agreement between the orange and blue plots of the inset demonstrates good agreement between the extrapolated vibrational branching ratios and the experimentally measured decay.

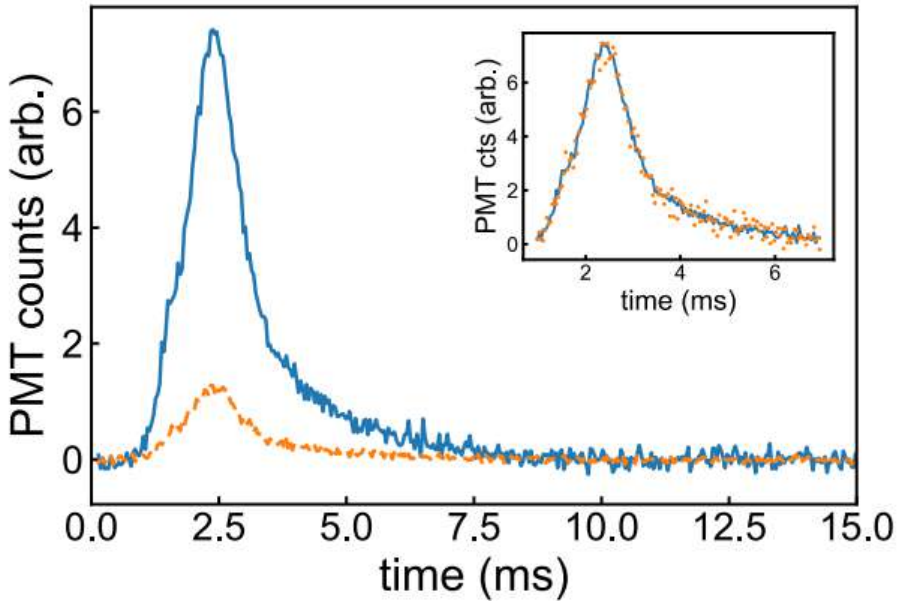

Figure 5.9: I show two PMT traces corresponding to the fluorescence of the molecular beam as it decays to the $V = 0$ ground state (blue) and the $V = 1$ ground state (orange). The inset shows the detected fluorescence to the $V = 1$ band, and the expected fluorescence as calculated from the reported vibrational branching ratio and the observed the $V = 0$ fluorescence [146].

$A^2\Pi_{1/2}(V = 0, J = 1/2)$ Vibrational Decay

The experimentally measured values of the vibrational branching ratios of the $A^2\Pi_{1/2}(V = 0)$ state are summarized in Figure 5.10. The error corresponds to the standard statistical error.

$A^2\Pi_{1/2}$ q_{01}	**value**	**error**
R_0	1.575	0.013
R_1	0.0410	0.0017
$Q_{P_2,\lambda_{01}}/Q_{P_2,\lambda_{00}}$	0.73	0.04
$T_{F_3,\lambda_{01}}/T_{F_2,\lambda_{00}}$	1.17	0.06
q_{01}/q_{00}	**0.0306**	**0.0025**

$A^2\Pi_{1/2}$ q_{02}	**value**	**error**
R_0	1.363	0.015
R_2	0.0007	0.0005
$Q_{P_2,\lambda_{02}}/Q_{P_2,\lambda_{00}}$	0.167	0.008
$T_{F_3,\lambda_{02}}/T_{F_2,\lambda_{00}}$	1.15	0.06
q_{02}/q_{00}	**0.0025**	**0.0019**

Figure 5.10: I report the ratios of the of the fluorescence signal from the $A^2\Pi$ as detected by the PMT's in the experiment region. In addition, I show the ratio of the quantum efficiencies for each decay channel as well as the ratios of the filter transmission efficiencies used to isolate the fluorescence of those decay channels. Finally, I show the detected vibrational branching ratios from $A^2\Pi(V = 0)$ to the $V = 1$ and $V = 2$ levels in the $X^2\Sigma^+$ ground state [146].

The exponential suppression of non-diagonal vibrational decays can be seen in the following

plots of the $A^2\Pi(V = 0)$ VBR's in figure 5.11. The increasing fractional error is attributable to the decreasing signal associated with the higher order decay probabilities and decreasing fluorescence.

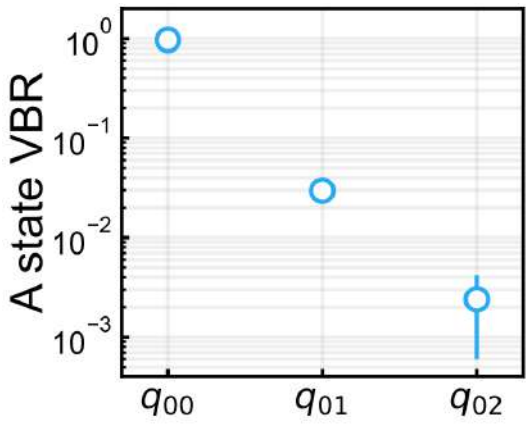

Figure 5.11: I show the measured vibrational branching ratios $q_{0,v'}$ from the $A^2\Pi(V = 0)$ state to the first three vibrational decay channels as plotted on a log scale. This demonstrates the exponentially decreasing probability of decaying to the excited vibrational ground states [146].

$B^2\Sigma^+(V = 0, N = 0)$ Vibrational Decay

In Figure 5.12, I show the experimentally measured vibrational branching ratios of the $B^2\Sigma^+(V = 0)$ state. Again, the errors are standard statistical errors due to fluctuations in detected signals.

$B^2\Sigma^+$ q_{02}	value	error
R_0	5.83	0.03
R_2	0.0040	0.0005
$Q_{P_2,\lambda_{02}}/Q_{P_2,\lambda_{00}}$	0.56	0.03
$T_{F_3,\lambda_{02}}/T_{F_2,\lambda_{00}}$	1.00	0.05
q_{02}/q_{00}	**0.00125**	**0.00019**

$B^2\Sigma^+$ q_{01}	value	error
R_0	5.83	0.05
R_1	0.0696	0.0021
$Q_{P_2,\lambda_{01}}/Q_{P_2,\lambda_{00}}$	0.86	0.05
$T_{F_3,\lambda_{01}}/T_{F_2,\lambda_{00}}$	1.01	0.04
q_{01}/q_{00}	**0.0137**	**0.0011**

Figure 5.12: I report the ratios of the of the fluorescence signal from the $B^2\Sigma^+$ as detected by the PMT's in the experiment region. In addition, I show the ratio of the quantum efficiencies for each decay channel as well as the ratios of the filter transmission efficiencies used to isolate the fluorescence of those decay channels. Finally, I show the detected vibrational branching ratios from the $B^2\Sigma^+(V = 0)$ excited state to the $V = 1$ and $V = 2$ levels in the $X^2\Sigma^+$ ground state [146].

Again, we see the exponential suppression of the higher order decays.

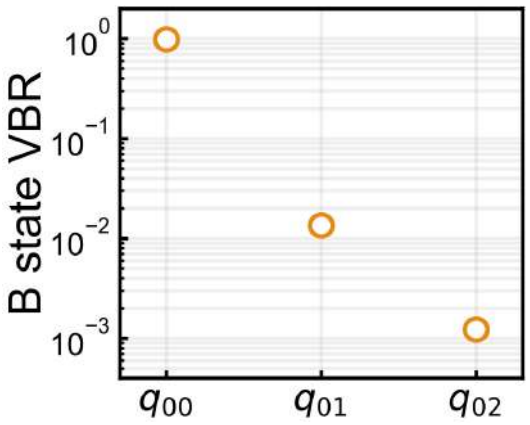

Figure 5.13: I show the measured vibrational branching ratios from the $B^2\Sigma^+(V = 0)$ excited state to the first three vibrational decay channels as plotted on a log scale. This demonstrates the exponentially decreasing probability of decaying to the excited vibrational states [146].

5.4 Scattering Rate Optimization

The scattering rate of a system reliant on spontaneous decay is dependent on saturating the population in the excited state. This is fundamentally limited by the natural lifetime of the excited state $1/\Gamma$. Further consideration of the system reveals that coupling the ground and excited states with a non-coherent monochromatic laser field further limits the maximum scattering rate to be less than the natural lifetime [180]. To understand why this is, I present a brief argument based on the rate equations in which the excited and ground state populations are joined by a laser with Rabi rate Ω, and the rate of excitation ($\frac{d\rho_e(t)}{dt}$) and decay ($\frac{d\rho_g(t)}{dt}$) are coupled. This relationship is expressed in the following differential equations [181]:

$$\begin{aligned} \frac{d\rho_g(t)}{dt} &= -\Omega\rho_g(t) + (\Gamma + \Omega)\rho_e(t) \\ \frac{d\rho_e(t)}{dt} &= \Omega\rho_g(t) - (\Gamma + \Omega)\rho_e(t) \end{aligned} \tag{5.7}$$

The steady state population can be found by imposing requirements that the sum population between the ground and excited states is one, as well as setting the time derivatives to zero. This gives the following expression for the excited state population:

$$\rho_e = \frac{\Omega}{\Gamma + 2\Omega} \tag{5.8}$$

Upon inspection, we see that as the Rabi rate increases, the excited state population saturates, and the population is split equally between the ground state and the excited state. This was derived for a two-level system, but generalizing this derivation shows that the maximum excited state population at high laser power is limited to the number of excited states divided by the total number of states in the system. The angular momentum selection rules that allow for sustain cycling in molecules require driving the $N = 1 \rightarrow N = 0$ rotational transitions, resulting in a type-2 level structure. In short, there will be more ground states than excited states due to the higher rotational angular momentum of the ground state. This inverted level hierarchy further limits the scattering rate.

5.4.1 Magnetically Assisted Dark-State Remixing

Dark-states arise because of the linearly polarized lasers that are used to drive cycling in the type-2 level system. Due to the significant number of lasers required for cycling, we must be creative in how these lasers can be co-aligned to the same fiber before shining them upon the molecules. The A state, B state, and the repumper are spectrally separated enough to combine using narrow band dichroic filters. However, the relatively small splitting of the spin rotation components of the ground state requires us to combine the spin rotation states on a polarizing beam splitter. This co-alignment method requires linearly polarized light for each laser, which is orthogonal relative to the other spin rotation component. The combination of linearly polarized light with the type-2 cycling structure leads to the creation of hyperfine dark-states.

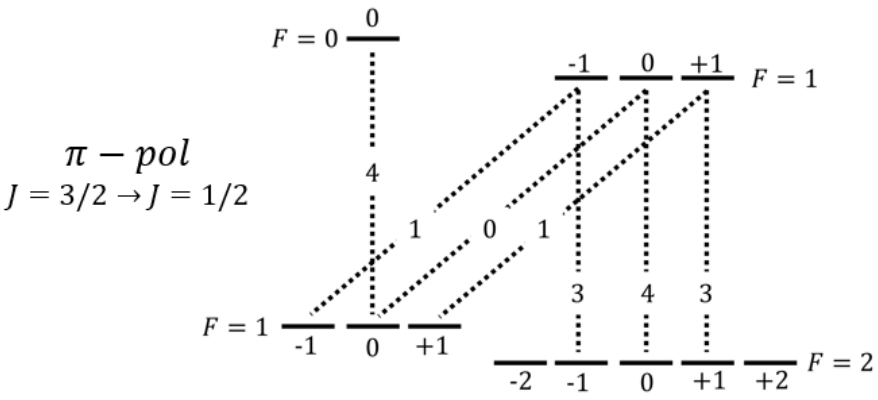

Figure 5.14: I show the permitted hyperfine transitions and the transitions strengths from a $F = 1, 2$ ground state to a $F = 0, 1$ excited state when the transition is driven by linearly polarized light [180]. I show the transition strengths as the numbers on the dotted lines.

The possible transitions obtainable with linearly polarized light are shown in Figure 5.14 [180]. Spontaneous decay can populate all of the hyperfine levels of the $F = 2$ state; however, our lasers can no-longer excite the $m_f = \pm 2$ states. One might choose to remix the hyperfine levels with a Pockels cell, but a Pockels cell was incompatible with the orthogonal polarization scheme used to combine the lasers. Rather, we choose to remix the dark-states by applying an external magnetic field that is held at 45 degrees relative to each spin rotation component. This magnetic field angle defines a new quantization axis, about which the states with $m_F \neq 0$ precess at the Larmor frequency associated with their magnetic moment. The effect of this magnetic field remixing can be seen in Figure 5.15. I plot the depletion rate of the ground state (inversely proportional to the scattering rate) as a function of the relative angle between the magnetic field and the $J = 3/2$ laser polarization. When the magnetic field and the polarization vector are parallel (0 and 90 degrees), the ground state is depleted more slowly. This lower depletion corresponds to a slower scattering rate. Meanwhile, if the magnetic field and the polarization vector are at 45 degrees, the dark states are efficiently remixed, leading to a much higher scattering rate. We do not expect this plot to go to 1 at an angle of 0 because the $J = 1/2$ spin rotation state is still remixing, leading to some depletion of the ground state.

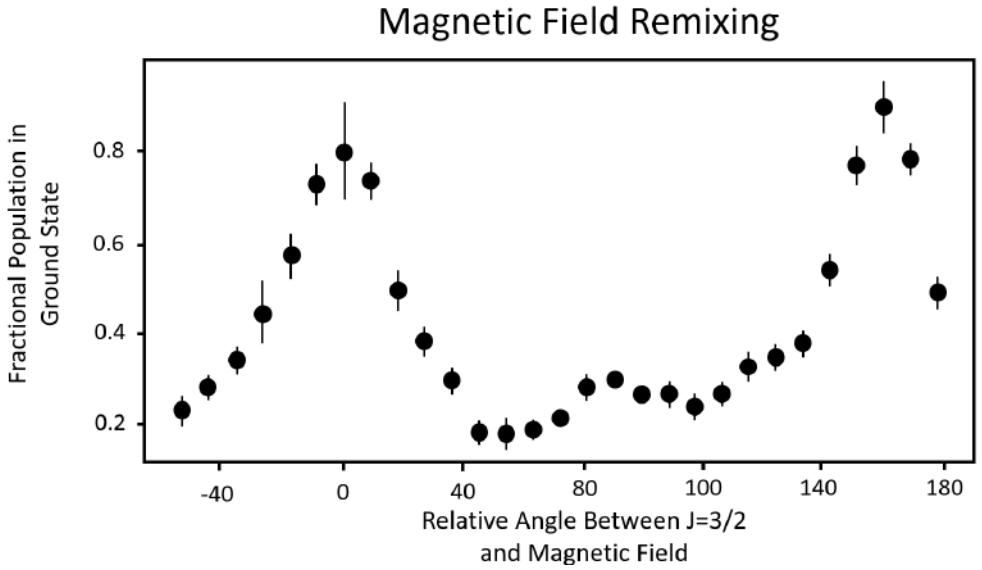

Figure 5.15: I show the fluorescence from the $X^2\Sigma^+ \rightarrow B^2\Sigma^+$ as a function of the angle between the $J = 3/2$ laser and the externally applied field. This was used to measure the molecular population remaining $V = 0$ ground state as a function of laser polarization angle. The population remaining in the ground state is minimized when the scattering rate of the $X^2\Sigma^+ \rightarrow A^2\Pi$ state is maximized, leading to transfer of the molecular population from $V = 0$ to the $V = 1$ band. The scattering rate is maximized when the $J = 3/2$ laser is 45 degrees relative to the remixing magnetic field.

5.4.2 Demonstration of Rotational Cycling

We demonstrate that the spin-rotation states of the ground state are correctly identified and that hyperfine states are well addressed by our AOMs/EOMs. This test relies on the rapid population transfer to any unaddressed ground state in the system. We show that each spin rotation component by itself scatters no more than 5 photons before completely populating the other spin rotation state and becoming dark. Naturally, we expect the $J = 3/2$ states to scatter more photons due to the higher multiplicities of their Zeeman levels. However, by coupling both spin rotation states to the excited states, we expect an order of magnitude more fluorescence as photons cycle between the states and the signal is limited only by the decay to the higher lying vibrational levels and the interaction time. We can expect an average of $\langle N_{ph} \rangle$ photons to scatter when both spin rotation components are addressed before reducing the $V = 0$ population by 1/e. In terms of the VBRs, the expected number of photons is given as:

$$\langle N_{ph} \rangle \approx \frac{1}{1 - \sum_{V''=0}^{2} (q_{0V''})} \tag{5.9}$$

where $q_{0V''}$ are the vibrational branching ratios of the excited state in question. Therefore, we expect to scatter 31 ± 3 photons off of the A state and 68 ± 5 photons off of the B state. If we close the first vibrational decay pathway with a repumping laser, we expect to scatter 400 photons off of the A state and 800 photons off of the B state. In Figures 5.16 and 5.17, I show the effect of addressing both spin-rotation components of the ground state without including any repumping lasers.

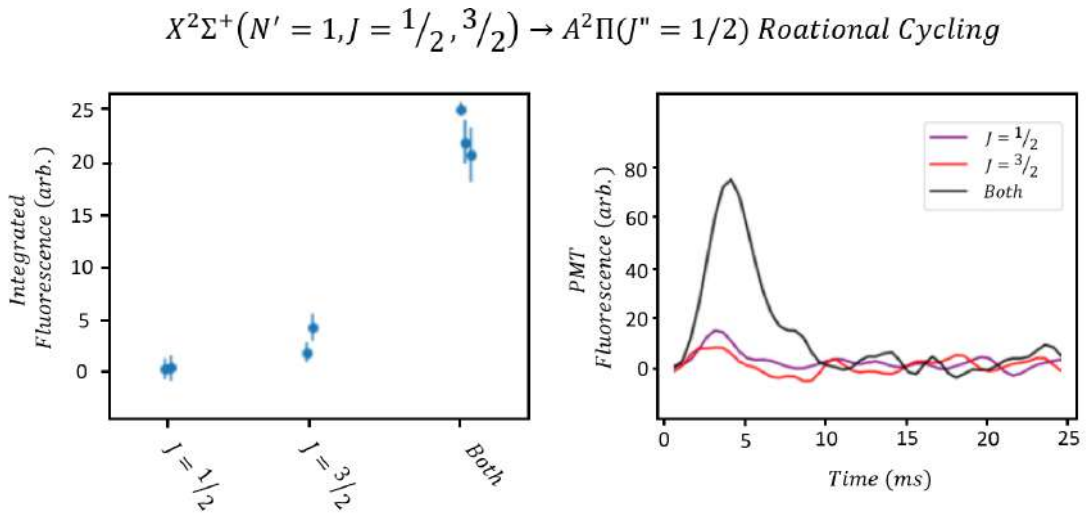

Figure 5.16: On the left, I show the molecular fluorescence from driving the $J = 1/2$ or $J = 3/2$ branch of the $X^2\Sigma^+ \rightarrow A^2\Pi$ transition. I also show the enhanced fluorescence when both spin-rotation components are addressed, indicating that molecules were being transferred between the spin-rotation states rather than being pumped into a dark state. On the right, I show the time of flight data corresponding to the integrated signals shown on the left.

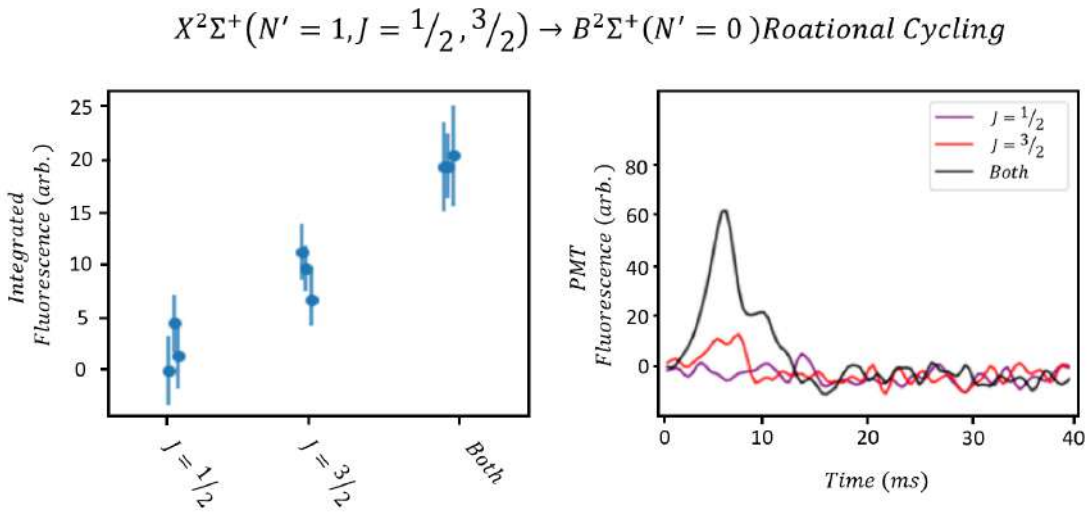

Figure 5.17: On the left, I show the molecular fluorescence from driving the $J = 1/2$ or $J = 3/2$ branch of the $X^2\Sigma^+ \rightarrow B^2\Sigma^+$ transition. Then, I show the enhanced fluorescence when both spin-rotation components are addressed, indicating that molecules were being transferred between the spin-rotation states, rather than being pumped into a dark state. On the right, I show the time of flight data corresponding to the integrated signals shown on the left.

In both of these measurements, we see that we fall short of the 6-fold increase in photons scattered for the A state and the 10-fold increase in photons off of the B state. This indicates that this experiment was interaction time-limited, but the effect of addressing the spin-rotation components is still clear. A more thorough discussion of the cycling rate is presented in the section on depletion measurements taken in a configuration that was not interaction time-limited.

5.4.3 Saturation Intensity

The final step to maximizing the effective scattering rate Γ_{eff} is to saturate the scattering rate by applying sufficient laser power. We experimentally measured the saturation intensity by exposing the molecules to a cycling laser (either the $X - A$ or the $X - B$), and then increasing the power until fluorescence ceases to increase with power. From here, dividing the total laser power by the 1/e beam area gives the saturation intensity. In Figures 5.18 and 5.19, I show the results of such experiments:

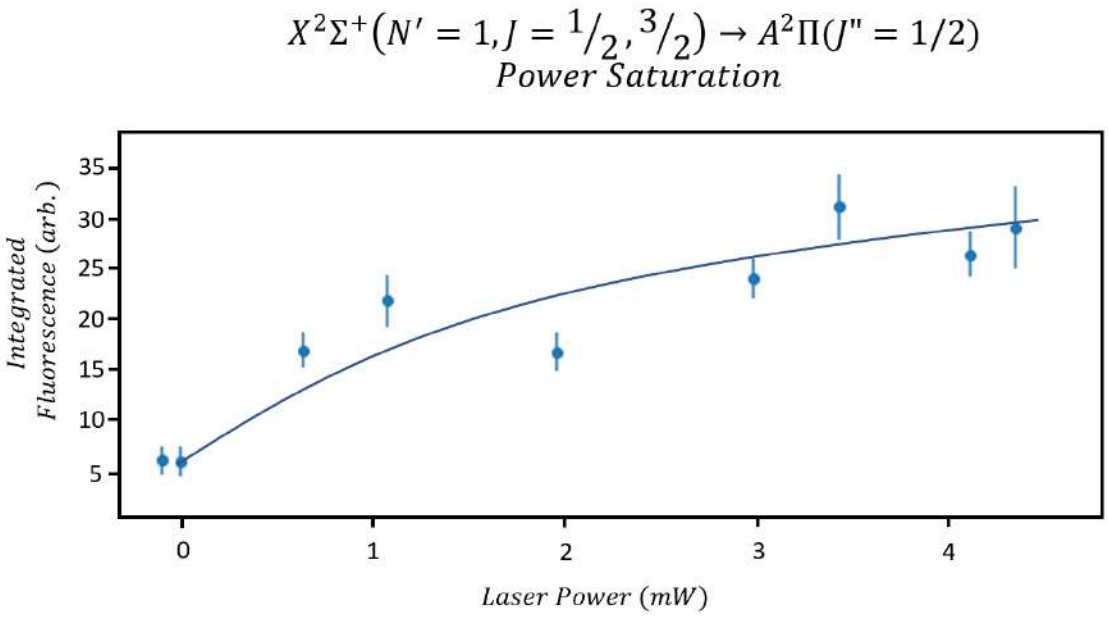

Figure 5.18: I show the integrated fluorescence of the $X^2\Sigma^+ \rightarrow A^2\Pi$ transition as a function of power. The data shows saturation at $\approx$ 3mW corresponding to an intensity of 66mW/cm^2.

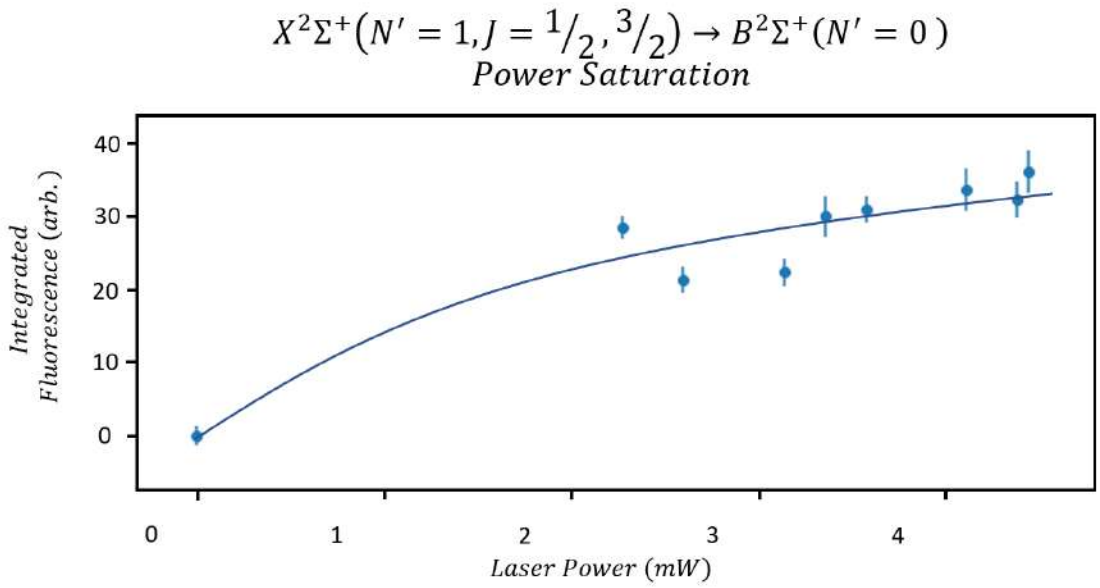

Figure 5.19: I show the integrated fluorescence of the $X^2\Sigma^+ \rightarrow B^2\Sigma^+$ transition as a function of power. The data shows saturation at $\approx$ 1.5mW corresponding to an intensity of 50mW/cm^2.

We measure the laser waist with the Thorlabs USB camera. Figure 5.20 shows the beam profiles.

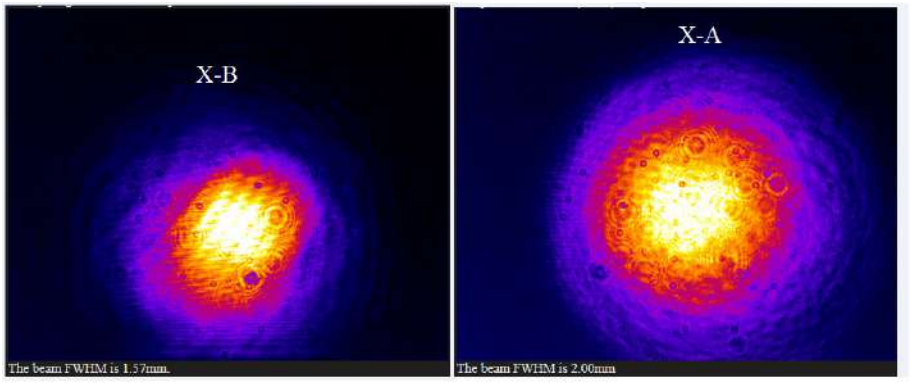

Figure 5.20: Images from the Thorcam CCD camera of the probe beams used to measure the saturation intensity for the $X^2\Sigma^+ \rightarrow B^2\Sigma^+$ (left) and the $X^2\Sigma^+ \rightarrow A^2\Pi$ (right).

Converting power to intensity shows saturation at 66mW/cm^2 for the A state and 50mW/cm^2 for the B state. The shorter natural lifetime of the A state compared to the B state (33 ns vs 58 ns) requires almost double the intensity to saturate that transition. This is in good agreement with our experimental measurements.

5.4.4 Sustained Scattering Rate

Efficient MOT loading requires preserving as many of the molecules that exit the cell as possible. This can be accomplished by adding repumping lasers. Moreover, the MOT loading efficiency is also reliant on slowing the beam as quickly as possible to limit the inherent dispersion of the molecular beam as it propagates. The 250m/s forward velocity of the molecular beam and the average momentum exchange per cycle reveals that we must scatter $\approx 2 \times 10^4$ photons. We can quickly meet this scattered photon requirement through power saturating the transition and efficiently remixing the dark-states through an externally applied magnetic field. The combination of sufficient power and optimal magnetically assisted remixing results in a maximum effective scattering rate, $R_{sc\ max}$ [180]:

$$R_{sc\ max} = \Gamma_{eff} = \frac{1}{\tau} \frac{n_e}{n_e + n_g} \tag{5.10}$$

where n_e and n_g are the total excited and ground states including the hyperfine manifold, which are coupled by the laser field. For CaH, there are $n_e = 4$ hyperfine states in the excited state and there are $n_g = 12$ hyperfine states . τ is the natural lifetime of the state based on the line-width of the transition.

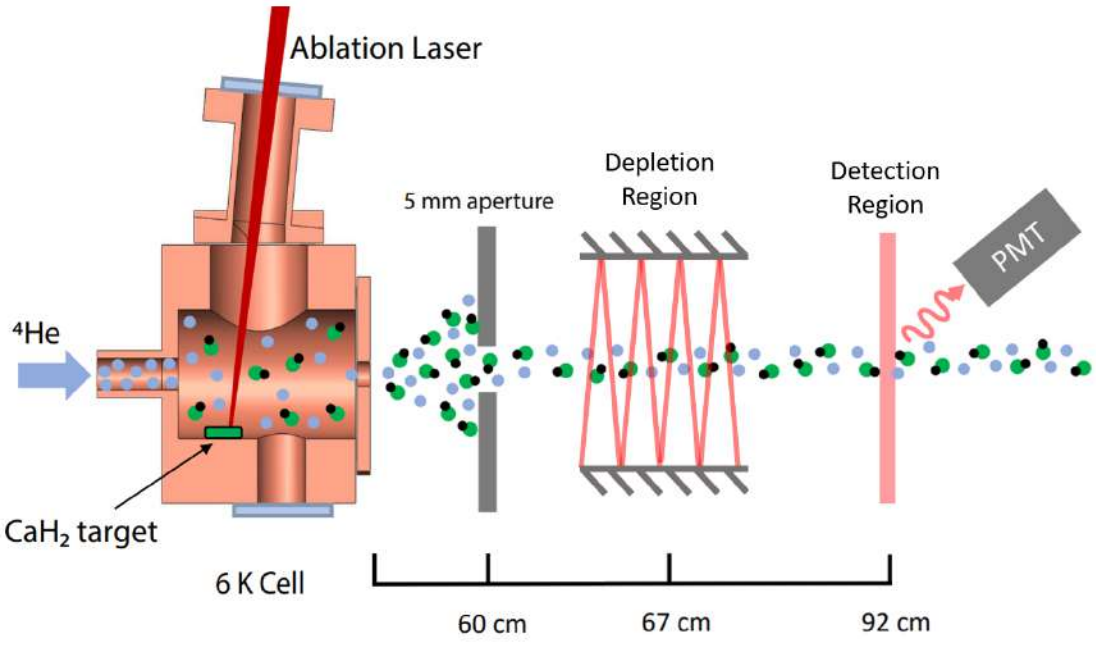

The experimental apparatus used to measure the scattering rate is similar to the other systems described in this chapter. The molecules are ablated in the cell and propagate into the chamber through a 5 mm velocity skimming aperture. However, there are two notable changes. First, we installed the custom built interaction chamber that I designed with Ivan Kozyrev. Second, we multi-pass the cycling laser to fill the interaction chamber. This laser bounces back and forth between two 15cm long custom mirrors. We use a beam block to vary the number of laser passes (i.e. the interaction time). Both the chamber windows and the extended mirrors were purchased from Casix.

After exiting the interaction chamber, molecules propagate to the blackened detection chamber with the 12 inch long nipples, where we use the other $V = 0$ transition to detect the molecular population remaining in the ground state. To normalize the fluorescence signal and account for shot-to-shot fluctuations in the molecular beam yield, we alternate the depletion laser on an off every other shot . The ratio of the remaining ground state population can be used to calculate the number of scattered photons, because we precisely measured the decay probabilities to the excited vibrational states. Written in terms of the vibrational branching ratios and the number of scattered photons ($N_p(t)$), the remaining fraction (f_{rem}) of the ground state population is given by [146]:

$$f_{rem}(t) = \frac{N_{mol}(t)}{N_{mol}(t=0)} = \left(\sum_{V''=0}^{V_a} (q_{0V''}) \right)^{N_p(t)} \tag{5.11}$$

Then, we can measure the laser beam waist and use the beam velocity to calculate the interaction time. Using an exponential fit, we can extract the exponential constant t_d corresponding to the decrease in population. The decay constant is used to calculated the scattering rate, as follows:

$$R_{sc} \approx \frac{1}{\tau_e(\sum_{V''=0}^{V_a}(q_{0V''}))} \tag{5.12}$$

In Figure 5.21, I show two decaying ground state populations. The repumping laser is left off in the case plotted in orange, while the $V = 1$ repumper is added in the blue plot. The addition of the $V = 1$ repumping transition greatly reduces the depletion rate of the $V = 0$ band.

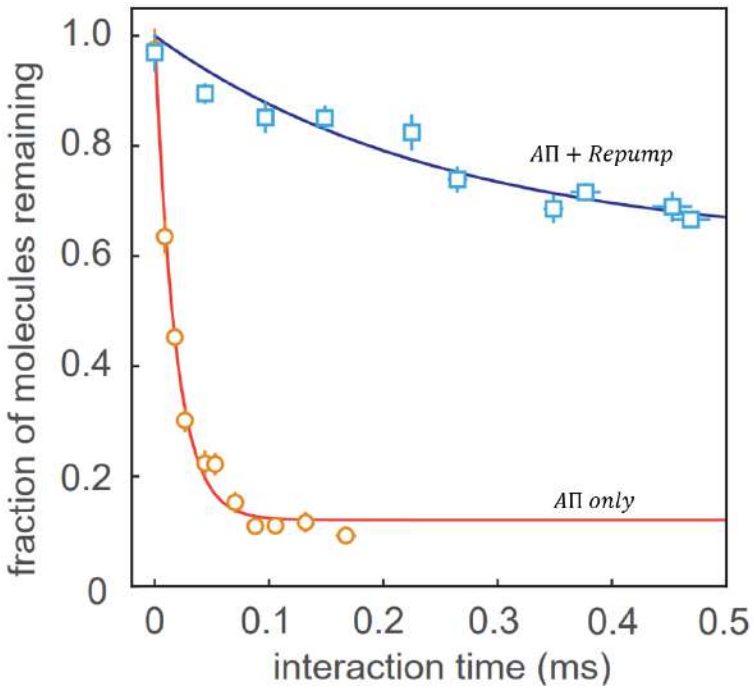

Figure 5.21: I show the depletion of the ground state when driving the $X^2\Sigma^+(V = 0) \rightarrow A^2\Pi$ alone (orange trace). Depletion of the ground state when driving the $X^2\Sigma^+(V = 0) \rightarrow A^2\Pi$, while simultaneously applying the $X^2\Sigma^+(V = 1) \rightarrow B^2\Sigma^+(V = 0)$ repumping laser (blue trace). The decay seen in the blue plot is due to the decay to the $V = 2$ vibrational band.

Experimental Depletion Measurements

We ensure that we saturate the scattering rate by applying the maximum power available in the experiment (80mW for the $X - A$ transition and 40mW for the $X - B$ transition). Each pass with the interaction laser is spatially separated, so that the interaction time is well defined and the laser has a $1/e^2$ radius of 0.55mm. Simultaneously, we apply an external magnetic field of 3 Gauss to remix the m_F manifold dark states.

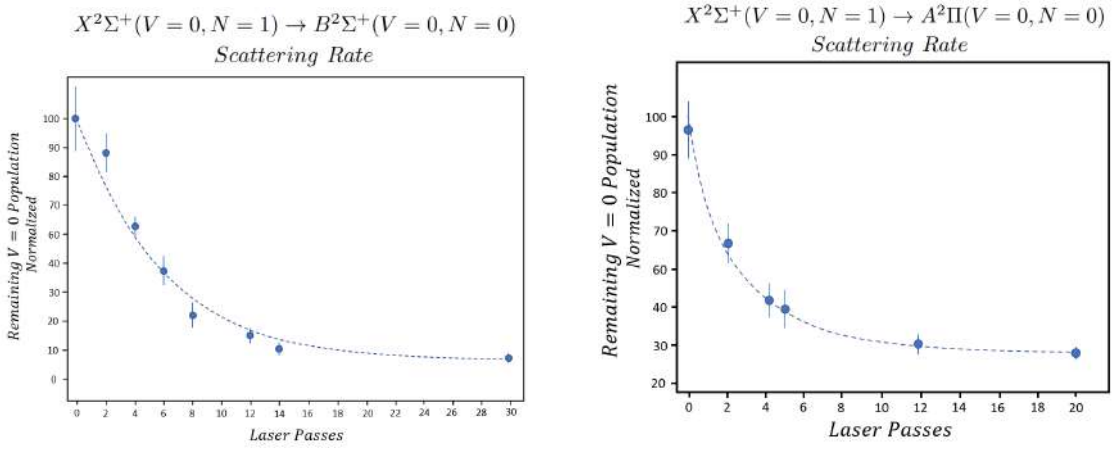

(a) $B^2\Sigma^+(V=0,N=0)$ Scattering Rate

(b) $A^2\Pi(V=0)$ Scattering Rate

Figure 5.22: On the left, I show the depletion of the $V = 0$ ground state to higher-lying vibrational states by cycling on the $X^2\Sigma^+ \rightarrow B^2\Sigma^+$. On the right, I show the depletion of the $V = 0$ ground state to higher-lying vibrational states by cycling on the $X^2\Sigma^+ \rightarrow A^2\Pi$. The A state decays faster than the B state corresponding to its larger vibrational branching ratio to the excited vibrational states.

Using the measured VBRs and the interaction time of the molecules with the laser, we determine that the A state is capable of scattering at $1.67(15) \times 10^6$ photons per second and a scattering rate for the B state of $0.85(3) \times 10^5$ photons per second. We find that over the maximum interaction time, molecules scatter 150^{+500}_{-70} photons. The maximum Γ_{eff} given by scaling $1/\tau$ by the ratio of excited states to total states is 7.6×10^6 photons per second for the A state, and 4.3×10^6 photons per second for the B state. We attribute the lower experimental scattering rates to experimental imperfections such as an inhomogeneous remixing B field, laser frequency instability, power fluctuations, and laser/molecular beam misalignment. This is consistent with the maximum experimental scattering rates reported by other experiments with diatomic and polyatomic molecules, which at most achieve a sustained scattering rate of $\approx 2 \times 10^6$ photons per second and also never achieve the maximum theoretical scattering rate [13, 11, 111, 6].

Experimental Repumping Measurements

Finally, we measure the time required to repump molecules from the $V = 1$ band to the $V = 0$ band after molecules have been pumped into the $V = 1$ band . To do this, we fully transfer the $V = 0$ population to the $V = 1$ ground state by cycling on the $X - A$ transition. Then, we vary the interaction time of the repumping laser to determine the interaction time needed to fully transfer the population back to $V = 0$. This measurement allows us to know how much power and interaction time is needed after cooling or depletion to return remaining $V = 1$ population back to $V = 0$. This ensures that all the molecules are in the $V = 0$ band where we can image them for the best signal to noise. It does not make sense to define a scattering rate in this system, because this is a single photon process and there is no cycling taking place.

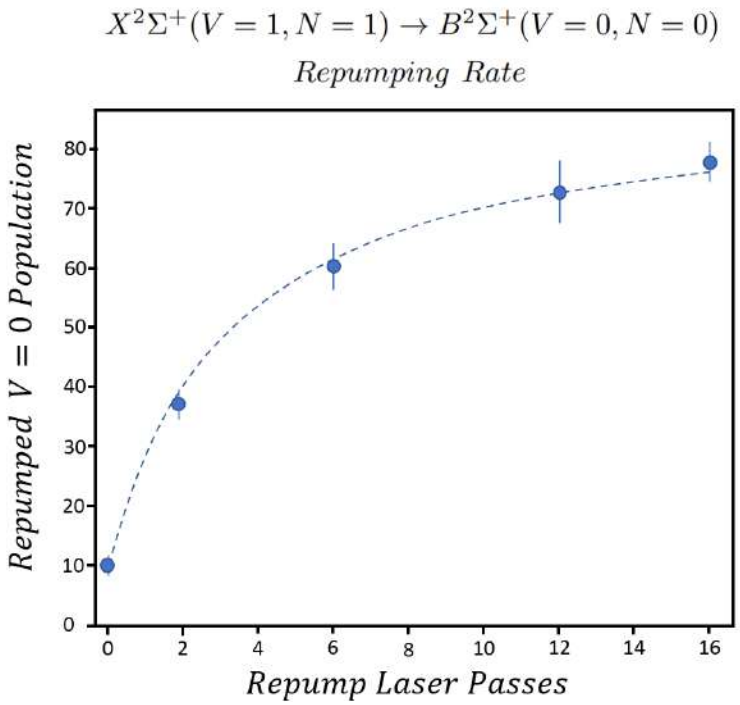

Figure 5.23: I show the number of laser passes required to repump all of the molecules from first excited vibrational state to the vibrational ground state. A fully depleted population requires at least 16 laser passes to fully transfer the population back to the $V = 0$ state.

We gather that 16 passes of our repumping laser is sufficient to clean up all molecules in the $V = 1$ band. In actual cooling measurements, the remaining population in the $V = 0$ after cooling

approximately 50%. Therefore, we are confident that 16 passes is more than enough to transfer all of the molecules back into $V = 0$, where they can be detected.

Chapter 6: Laser Cooling of Calcium Monohydride

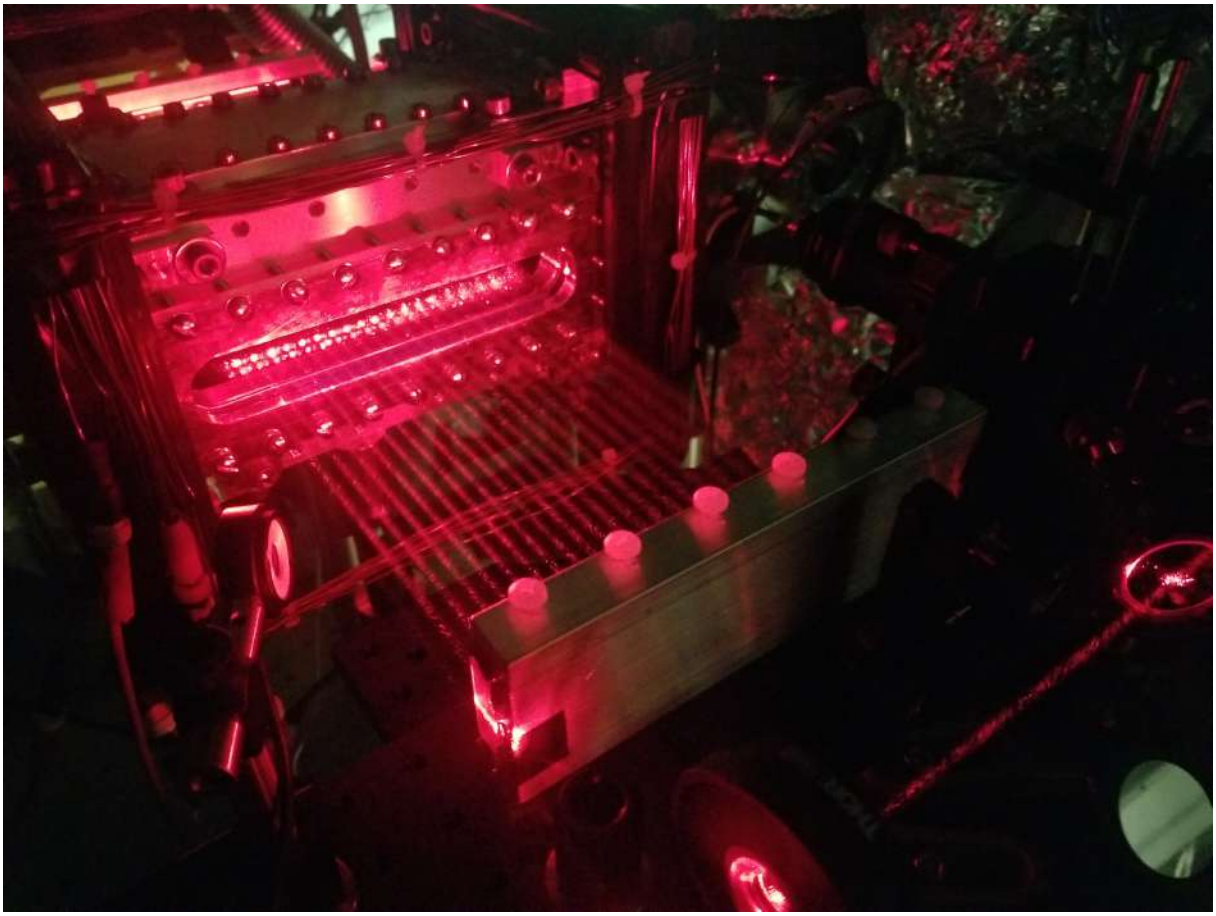

Figure 6.1: A photo of the multipassed $A^2\Pi$ laser shining into the interaction chamber in the configuration used to demonstrate Doppler cooling on CaH.

6.1 Introduction

The final experimental configuration used for the measurement of Doppler and Sisyphus cooling, including the laser system, as well as the imaging system will be described in the following chapter. I lay out the sequence of Sisyphus cooling results I gathered over the past two years. In addition, I discuss the improvements made to the experiment that have ultimately given the best Sisyphus signal to date [146]. This chapter represents the culmination of my thesis effort, and represents years of work spent building the laser and vacuum systems that were used to identify and characterize the molecular transitions required for laser cooling.

In the past decades, robust techniques have been developed for laser cooling atoms [182, 183]. These developments have enabled incredible progress by applying these techniques to fundamental physics and quantum information [184, 185, 186, 187]. The AMO community has logically sought to apply these atomic techniques to molecules, since this advancement represents both the next level in experimental complexity, and because molecules offer properties suitable for metrology and quantum information that capitalizes on the advances already made with atoms. However, the application of atomic techniques to molecules has proven to be difficult, as molecules posses more complex quantum structure and lack selection rules that govern the vibrational decay pathways [188]. We firmly believe that the complexity of molecules is worth overcoming, since molecules posses enhanced sensitivity to fundamental constants [42, 15, 10], and promise enhanced coherence times desirable for quantum computing [16, 17, 18] and tunable long-range interaction due to the intrinsic dipole moments of certain excited states [17, 19]. All of these properties rely on cooling the molecules to gain access to the benefits of cold quantum systems. The technique of buffer gas cooling has been a milestone in the field of molecular physics because it handles the bulk of the cooling, lessening the reliance on laser cooling to the final reduction of temperature from 4K down to the millikelvin regime [110, 173]. The combination of buffer gas cooling and laser cooling, since its invention, has been implemented to cool diatomics [4, 5, 6, 7, 135], triatomics [10, 11, 12], and symmetric top molecules [13]. I am proud to add CaH to this list of molecular

species successfully cooled by the combination of cryogenic buffer gases and laser cooling [146].

In this chapter, I recount the process I used to induce optical cycling and the sub-Doppler cooling of CaH. Knowledge of the vibrational branching ratios and the conditions needed to maximize the scattering rates allowed us to scatter $\approx$ 200 photons with the magnetically assisted Sisyphus effect. We created a standing wave by retro-reflecting the cooling laser onto itself, which lowered the molecular beam's transverse temperature from 12mK to 5.7mK.

6.2 Experimental Set Up

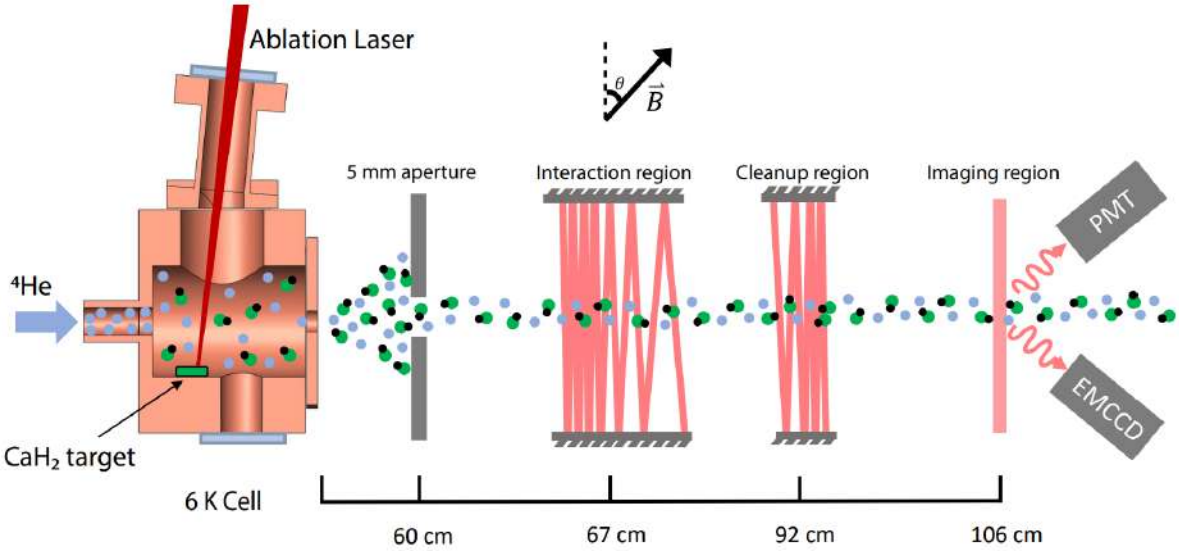

Figure 6.2: A diagram of the experiment, indicating where the molecules are exposed to light for cooling, $V = 1$ clean-up, and imaging. Molecules begin in the cryostat and propagate 6cm before passing through a velocity filtering aperture that limits the transverse velocity of the molecular beam. Afterwards, molecules propagate into the interaction region, where they are exposed to high power lasers used to create Sisyphus cooling. Molecules then proceed 25cm downstream to the clean up region where any molecules in the $V = 1$ ground state are repumped back into the $V = 0$ ground state to provide the most signal for imaging. Finally, molecules propagate another 14cm to the imaging region where they interact with a laser and fluoresce. This fluorescence is collect by a PMT and an EMCCD camera for analysis of the beam's properties.

The experiment begins with the ablation of a CaH_2 sample of 95% purity. Ablation is performed by a pulsed Nd:YAG 30mJ laser at 1064nm in the 6K cryogenic cell at the center of the cryosta [110, 173, 135]. It is worth noting that we tried using CaH_2 samples of higher purity, but

found they did not improve the molecular yield. These higher purity powder samples were pressed by us at only 2 Ton force and hence disintegrated under ablation much faster than the 95% pure sample that possesses a binding agent to keep the sample from breaking apart. I should also point out that the ablation laser produced the best molecular yield when it was slightly defocused and the ablation power was spread over the maximum sample area. Molecules produced in the ablation processes thermalize via collisions with the ^{4}He buffer gas that flows into the cell immediately adjacent to the CaH_2 sample. The temperature of the cell was selected to maximize $N = 0$ and $N = 1$ rotational states and the $V = 0$ vibrational ground state.

Molecules exit the cryostat through a 3mm aperture in the cell and enter the experimental vacuum chamber. Before the molecular beam passes into the interaction chamber, we reduce the transverse velocity distribution to ± 3m/s $1/e^2$. We include this aperture because Sisyphus cooling has a small capture velocity range over which it is effective, and by eliminating the higher velocity molecules, the visible effect of Sisyphus cooling is pronounced. We varied aperture sizes to select the slowest molecules. The 2mm was the smallest aperture we tried, but we found that this caused a build up of pressure on the cryostat side of the aperture. This increase in pressure severely attenuated the molecular yield in the interaction chamber, despite mounting a turbo pump directly adjacent to the aperture on the high pressure side. The velocity was confirmed with time of flight CaH flouresence traces, analyzed with a Wiener deconvolution to extract the mode of the velocity distribution (250m/s). Because this method failed to consistently reproduce the wings of the velocity distribution; instead, we used Ca atoms as a proxy to study the velocity characteristics of the beam. I reason that this was appropriate, given the nearly identical masses of Ca and CaH. Ca atoms entering the interaction chamber were measured to have a forward velocity of 250 ± 200m/s. Currently, the CaH experiment is developing a detection scheme that utilizes a two photon excitation from the $X-A-E$ state to produce a background free signal at 490nm that can be used to perform velocity sensitive 45 degree measurements of the beam velocity. This method of detection will require purchasing a laser at 1665 nm to drive the $A-E$ transition, and we are deciding which laser will be most appropriate for this application.

The cooling region follows the velocity skimmer. This custom chamber has 12cm of optical access used to inject the cooling light, which was multipassed to maximize the interaction time by reflecting it between two 12cm custom mirrors. After cooling, some of the molecular population is left over in the $V = 1$ ground state, which we wish to recover in order to maximize the molecular signal available for imaging. We cleaned up this population in a separate chamber filled with only $V = 1$ repumping light. Finally, molecules propagate into the imaging region, where they are imaged using either $X - B$ or $X - A$ $V = 0$ fluorescence. The scattered photons are collected by a PMT to record the time of flight profile, and are simultaneously imaged with an EMCCD. I will discuss the EMCCD camera in more detail in the following sections. Images taken with the EMCCD are then fit with a 2D Gaussian curve to measure the effect of turning on and off the cooling light in the interaction chamber.

6.2.1 Molecular Transitions

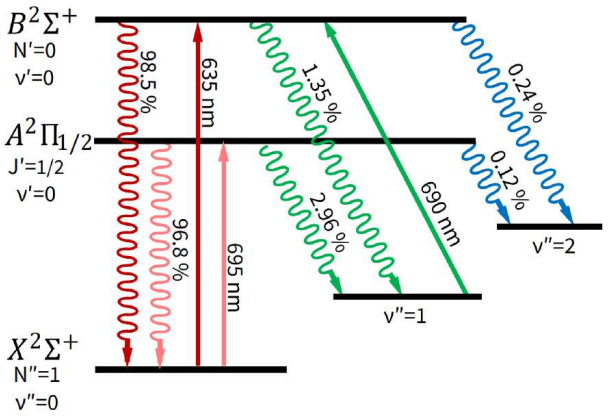

Figure 6.3: A diagram of the cooling (pink), imaging (red), and repumping (green) transitions used in this experiment. The decays from the excited states to the $V = 0, 1, 2$ states are represented as wavy lines.

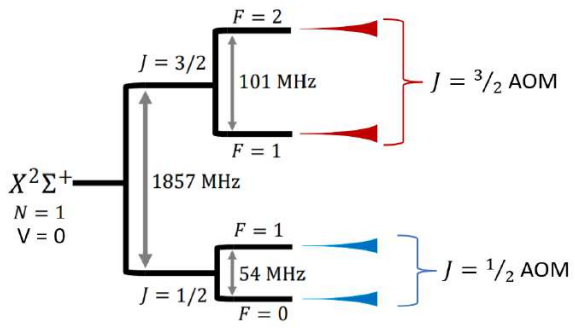

(a) Cooling Laser Sidebands

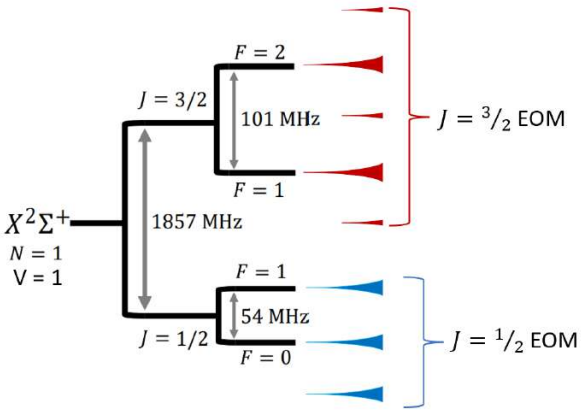

(b) Repumping Laser Sidebands

Figure 6.4: On top, I show the hyperfine structure for the two spin-rotation components of the $X^2\Sigma^+(V = 0)$ ground state. The $F = 1, 2$ states of the $J = 3/2$ state are split by 101 MHz, while the $F = 0, 1$ states of the $J = 1/2$ state are split by 54MHz. Each spin-rotation state is addressed with its own AOM. In the second plot, I show the hyperfine structure for the two spin-rotation components of the $X^2\Sigma^+(V = 1)$ ground state. Each spin-rotation state is addressed with its own EOM.

The transitions used for these measurements are shown in Figures 6.3 and 6.4. Molecules reside in the $X^2\Sigma^+$ electronic ground state of the $V = 0$ and $N = 1$ manifolds. The home-built laser system was used to excite the molecules to one of the two lowest lying electronic states, either the $A^2\Pi_{1/2}$ or the $B^2\Sigma^+$. We achieved rotational closure by using the $N = 1$ rotational state of the ground state, while exciting to the $N = 0$ state, requiring that the molecules' decay to the $N = 1$ state. The ground state possess two spin-rotation states corresponding to the projection of the spin onto the rotational angular momentum. The spin-rotation states are split by 1.86 GHz,

and we address the states with separate lasers that are combined on a PBS and coupled to the same fiber. In addition to the spin rotation splitting, each SR state is further split into two hyperfine manifolds that are addressed with AOMs in the case of the $A^2\Pi_{1/2}$ transition or EOMs for the $B^2\Sigma^+$ transition. We used both the $A^2\Pi_{1/2}$ or the $B^2\Sigma^+$ for cooling, but spent most of the time using the $A^2\Pi_{1/2}$ for cooling due to its shorter natural lifetime and higher scattering rate. The $B^2\Sigma^+$ was used primarily for imaging the molecules and as the upper state for our repumping scheme. Both excited electronic states, $A^2\Pi_{1/2}$ or the $B^2\Sigma^+$, can decay to the first excited vibrational level, with a 1% probability per cycle for the $B^2\Sigma^+$ state and a 3% probability for the $A^2\Pi_{1/2}$ state. We closed the leak to the $V = 1$ vibrational state to ensure that we could scatter enough photons to see the cooling effect. Repumping is made possible by the lasers and ILA's, which transfer molecules from the $X^2\Sigma^+(V = 1, N = 1)$ to the $B^2\Sigma^+(V = 0, V = 0)$ state. From there, they preferentially decay back to the $X^2\Sigma^+(V = 0, N = 1)$ state. The decay from the $A^2\Pi_{1/2}$ and the $B^2\Sigma^+$ to the $V = 2$ state was minimal ($\approx 0.3\%$), and it was not necessary to address this loss mechanism for transverse cooling.

In Figure 6.5, I show the optics system used to generate up to 300mW of $A^2\Pi_{1/2}$ and up to 150 mW of $X^2\Sigma^+(V = 1, N = 1) \rightarrow B^2\Sigma^+(V = 0, N = 0)$ laser power. The $A^2\Pi_{1/2}$ light is initially generated by two home-built ECDL seed lasers that each address a unique spin-rotation state, before AOM's are used to add the hyperfine structure appropriate for that spin-rotation state. The light from the AOM is fiber-coupled into four separate single mode fibers before seeding four home-built injection locking amplifiers. Each cooling amplifier addresses a single F state, while each repumping amplifier addresses one spin-rotation state - simultaneously addressing both hyperfine F states.

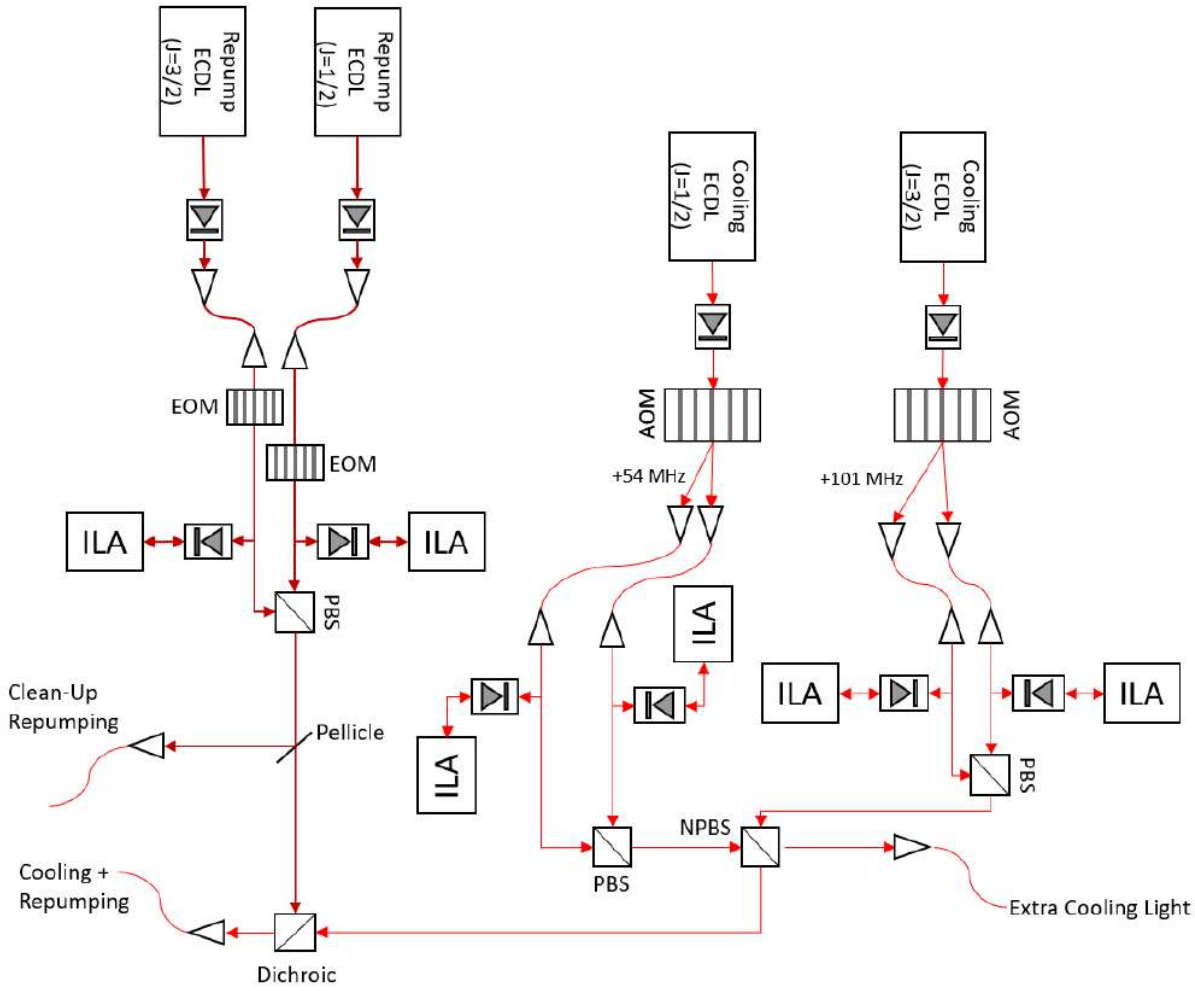

Figure 6.5: I show how each of the four cooling ILA's are seeded by the AOM sidebands added to two master ECDL's. I also show how the two repumping ILA's are seeded with EOM sidebands that are added a priori to two master ECDL's. The cooling hyperfine states of each spin-rotation manifold are combined with polarizing beam splitters, then the spin-rotation states are combined on a non-polarizing beam splitter. Waste light from the NPBS is coupled to a separate fiber to provide extra cooling light. I place a pellicle beam splitter on the repumping beam to provide light for the clean up region. Finally, the cooling light is combined with the repumping light using a dichroic, before all of the lasers are ultimately coupled to one single-mode fiber that carries the light to the experiment.

The hyperfine states are combined using a PBS and then the spin-rotation components are combined with a 50/50 non-polarizing beam splitter (NPBS) due to the fixed polarization angles between each hyperfine state. This would waste 50% of our cooling power, however, we recover the waste light from the NPBS by coupling it to a separate fiber that can also be injected into the cooling chamber to create two standing waves and maximize the power available. Cooling light

from the NPBS is then combined on a dichroic with the repumping light generated by two injection locking amplifiers, before this light is coupled to the same single mode fiber to ensure perfect overlap between the cooling laser and the repumping laser. The cycling and repumping light is coupled into the same fiber, so that during cooling the repumping light is perfectly coaligned with the cooling light. Ensuring that the cooling and repump light are perfectly coaligned minimizes the time molecules spent in the $V = 1$ state. Some repumping light is diverted with a pelicle beam splitter before the dichroic to provide the light for the final repumping in the clean-up region before the molecules are imaged.

6.2.2 Detection Scheme

We used a two-part out-of-vacuum imaging system to observe the molecules. This consists of a 60mm plano-convex lens bolted onto the 2.75 inch CF cross view-port that collimates light from the fluorescing molecules. Next we spectroscopically isolate the molecules' light from the background room light with a Semrock 690/8 nm BrightLine single-band band-pass filter. After passing through the filter the light is imaged onto the EMCCD chip with a 35mm focal length plano convex lens. commercial MVL35M1 camera lens.

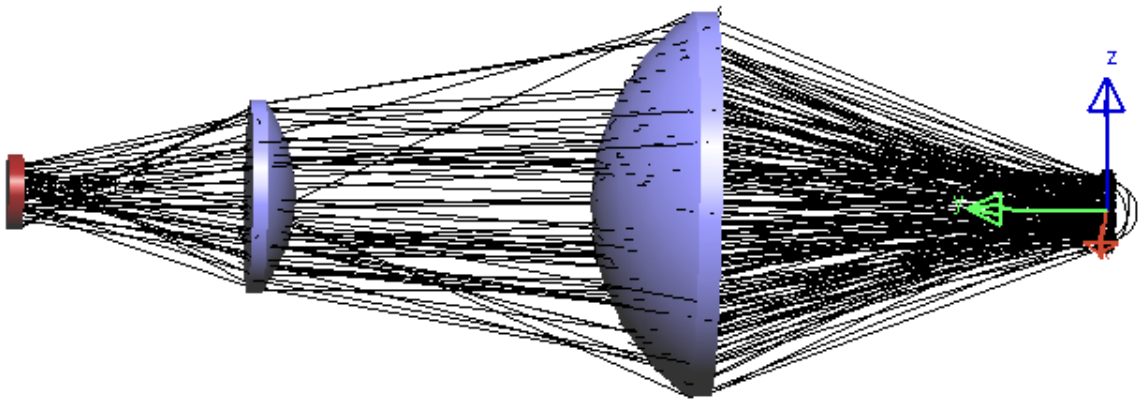

Figure 6.6: The optics used to collimate and then focus the detection light from the molecular beam onto the PMT surface.

The beam's signal is isolated by taking images of the background signal arising from the probe

laser scatter when they are not present in the chamber. This can then be subtracted off of beam images to eliminate the constant image offset from laser scatter off the windows that can washout images of the beam. One such image can be seen in Figure 6.7.

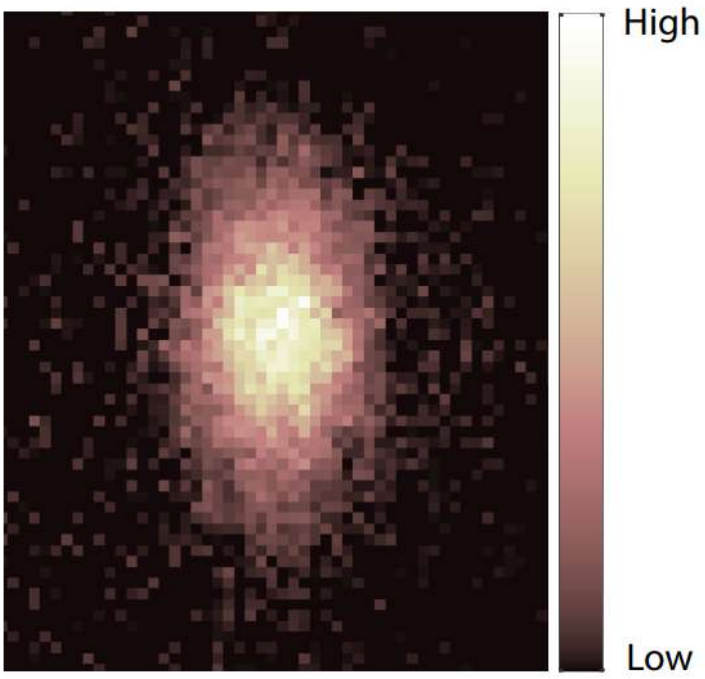

Figure 6.7: An example image of the molecular beam taken with the EMCCD. Images such as this one, were the basis of the measurements that demonstrated Doppler and Sisyphus cooling.

Calibrating the EMCCD is essential to extracting the experimental properties of the molecular beam. We converted pixels to mm during the data analysis by imaging a ruler with 1mm markings. The thread spacing is known and can be used to convert the distances in the image, from pixels to millimeters, i.e. the conversion is $0.02\frac{pixels}{mm}$. Simulations of the collection efficiency of the optics system were performed using LightTools. I imported the ThorLabs CAD files for the lenses into LightTools and defined the appropriate index of refraction based on the lens materials. My simulations revealed that our collection optics was only 1% efficient, which was largely limited by the distance of the collimating lens to the molecules beam. Improving this was deemed unnecessary for transverse cooling and would have required placing higher numerical aperture optics in-vacuum. The results of the simulation showing the total encircled energy on the EMCCD

surface and a simulated beam image can be seen below.

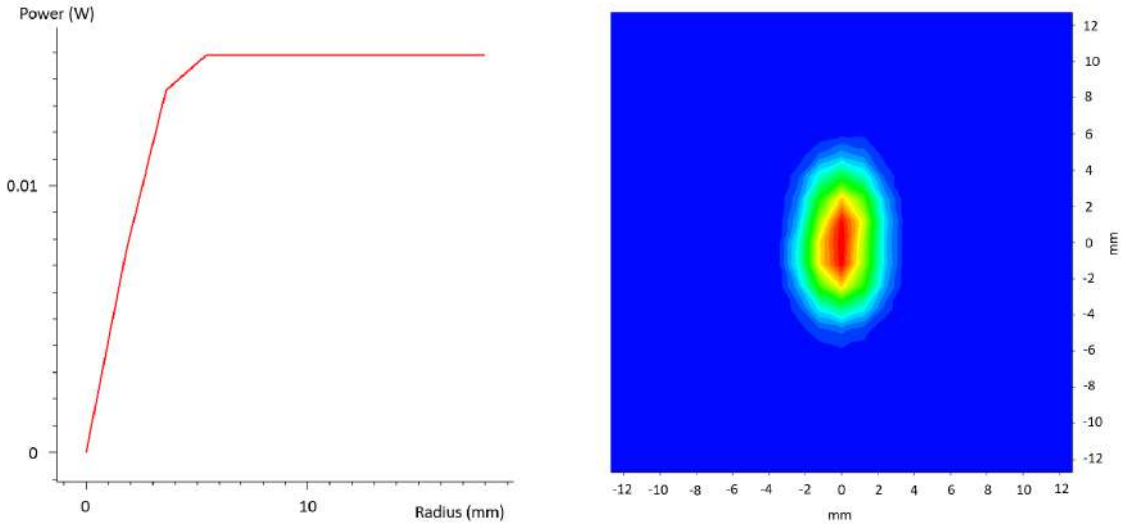

(a) Encircled energy

(b) Simulated beam image

Figure 6.8: A imaged simulated in LightTools which seeks to replicate the images of the beam as seen on the EMCCD camera is shown on the right. The plot on the left shows the integrated energy as a function of radius from the center of the detector for a total of 1W of fluoresced energy. The encircled energy divided by 1W, gives the percent efficiency of the collection optics.

The final step in imaging is to calculate the total number of molecules that are being imaged. We begin this calculation by extracting the total energy deposited on the sensor. According to the camera manufacturer this is given by:

$$E_{photon} = \left(\frac{Counts}{EM\ Gain}\right)\left(\frac{CCD\ Sensitivity}{CCD\ Quantum\ Efficiency}\right)(e^{-}Binding\ Energy)_{Silicon} \tag{6.1}$$

From the photon energy we can calculate the total number of molecules fluorescing in the field of view by combining the camera's quantum efficiency with the collection efficiency Ω and the molecule's scattering rate, Γ_{scat}. Thus the molecule number can be calculated as:

$$N_{mol} = \frac{E_{photon}}{h\nu \times \Gamma_{scat} t \times \Omega} \tag{6.2}$$

I would like to acknowledge and thank our newest grad-student Jinyu Dai for calculating these

essential conversions recently presented in our experiment's NJP paper [146].

Andor Solis

The iXon Ultra 888 by Andor is the most important piece of the data collection system that was instrumental in the observation of CaH laser cooling. This powerful piece of equipment, when correctly set up, provides remarkably clean images of the molecular beam with as little as a thousand photons. In Figure 6.9 show the results of a good image, fit, and residual.

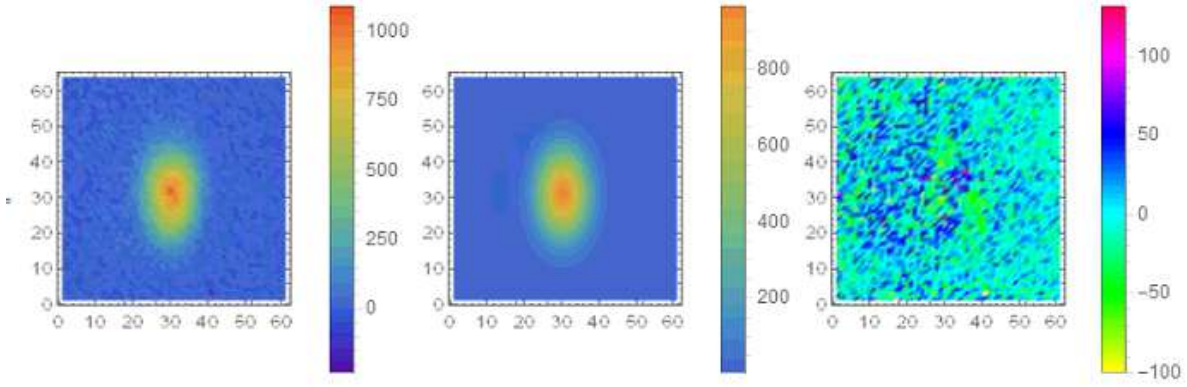

Figure 6.9: A raw EMCCD image of the molecular beam after background subtraction (left panel). The 2D Gaussian fit to that image (center plot). The fit residual (right panel) demonstrates that the image and the Gaussian are a good match.

The image quality is greatly affected by the multitude of settings within the Andor Solis program. Failure to correctly configure the camera will eliminate any chance of seeing effects from all but the strongest cooling. The primary settings that must be taken into account to acquire good images are the electron multiplying gain and the horizontal and vertical pixel shift speeds. The electron multiplying gain should be adjusted in response to the magnitude of the molecular fluorescence signal and the background scatter levels. If the gain is too low, one will not see molecules at all, while if the gain is too high, one risks damaging the camera. We determined the optimal gain level by gradually turning up the electron multiplying gain until the molecular beam images were clearly visible while not saturating the EMCCD. In our experiment, the EM gain was at about 300, whereas 200 and above is single photon counting mode.

Another camera setting that needed adjusting is the pixel readout speed. If the pixel readout is too slow, the experimental sequence becomes very long and gathering sufficient statistics becomes difficult. On the other hand, if the pixel read out speed is too high, then the amplified signal will begin to trigger adjacent pixels and introduce noise to the images. This effect is called "sloshing", and is characterized by the stripping effect shown in Figure 6.10. In our experience, the optimal horizontal shift speed was 500KHz (2.2uS shift speed), with the optimal vertical shift speed is 20MHz for an exposure time of 1ms.

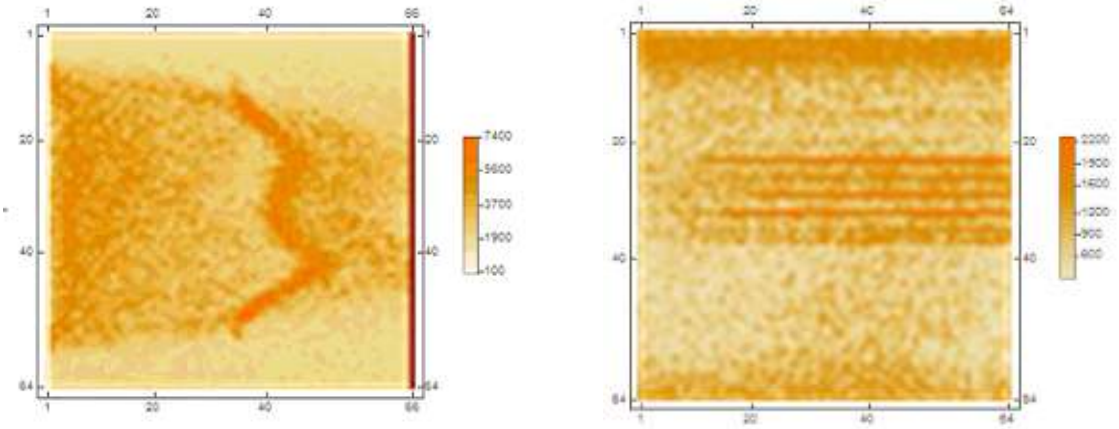

(a) label 2 (b) label 1

Figure 6.10: The effect of pixel shift speed on the EMCCD images. I show the effect of vertically reading out the pixels too quickly in the left panel. I show the effect of reading pixels out too quickly horizontally in the right panel. The aberrations seen in both images disappear when the camera read-out settings are optimized. No molecules were present for either image.

On a final note, not all image aberrations can be attributed to the EMCCD gain settings or read-out speeds. We spent quite some time investigating the source of the ring-like fit residual shown in Figure 6.11, only to find out that it was due to uncollimated background scatter light hitting the sensor. We assumed that light from the molecule beam was a point source when assembling the camera collection optics. In reality, the molecular beam is macroscopic enough that photons passing through the edge of the planoconvex collection lens are not be well-collimated and produce a ring in the image. We remedied this by moving the dichroic filter as close to the 60mm colimation lens as possible, and then using an optics tube to guarantee that all the light hitting the sensor was

passing through the dichroic. This decreased the collection efficiency, but greatly improved the image fit uncertainty.

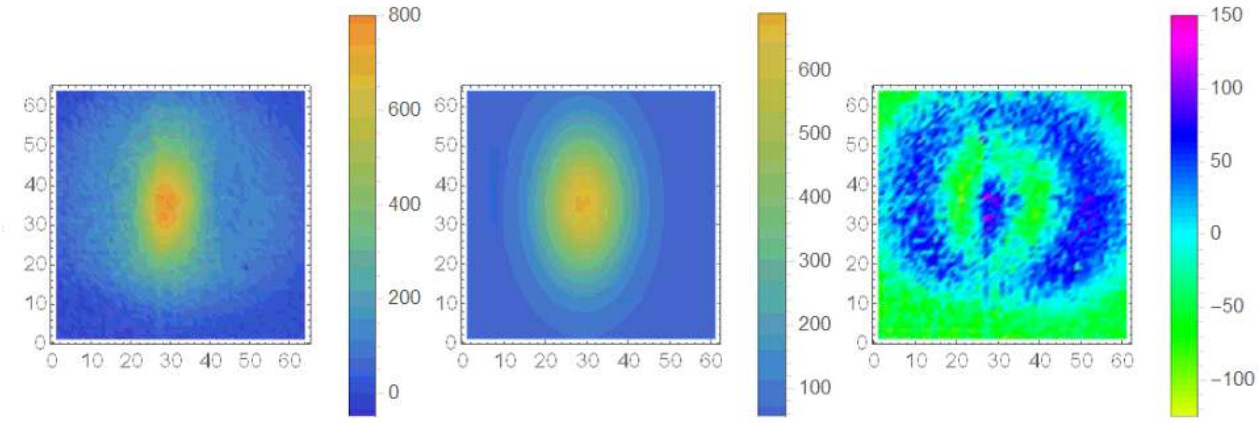

Figure 6.11: An EMCCD image from a poorly aligned optics system on the left. The middle panel shows the 2D Gaussian fit to the same image. On the right, the residual between the image and the fit is shown. It exhibits a clear ring structure. The ring is a product of placing the dichroic directly in front of the EMCCD sensor. This position maximizes the light hitting the sensor, but allows uncollimated light from the edges of the lens to also hit the EMCCD. This aberration was eliminated by placing a 1 inch dichroic immediately behind the 2 inch f=60mm collimation lens. This position ensures that only well collimated light passes through the center of the lens reaching the EMCCD.

We quantified the heating or cooling by using a program such as Matlab to fit a 2D Gaussian to the EMCCD images of the cloud. We then compare the width of a cooled beam to an unperturbed beam to calculate the change in the standard Gaussian width. We perform a spectrum and record the change in width as a function of frequency. The sisyphus effect produces heating for negative detunings and cooling for positive detunings, whereas the Doppler effect exhibits the opposite dispersion profile.

6.3 Laser Cooling

Laser slowing and magneto optical trapping uses the Doppler mechanism to scatter photons off a thermal atomic ensemble [180]. The scattering rate of this optical cycling is maximized by detuning the laser from the transition resonance to match the Doppler shift. The Doppler frequency shift is given by $\delta_{Dop} = \overrightarrow{k} \cdot \overrightarrow{v}$. There is a limit to the minimum temperature that can be reached with Doppler cooling, which arises from the natural lifetime of the excited state. This is called the Doppler limit, and written in terms of the excited state's natural lifetime, it is given by $T_{Dop} = \hbar/(2k_B\tau)$ [181]. Given the $A^2\Pi$ state's natural lifetime of 33 ns, we can calculate the Doppler limit temperature to be $T_{Dop} = 116\ \mu K$. Therefore, to cool the molecules further, we must employ techniques referred to as sub-Doppler cooling [5, 51, 50, 189]. We chose to pursue one such method, elegantly named magnetically assisted Sisyphus cooling. Sisyphus cooling is not required to slow and trap the molecules, but it demonstrates the ability to perform sub-Doppler cooling [4, 5, 6, 7, 135, 10, 11, 12, 13]. The most intuitive way to think of this effect is to imagine molecules with velocity v as they propagate through an optical standing wave that is slightly detuned from the cycling transition resonance. As the molecules traverse the standing wave, they experience a Stark shift dependent on the local intensity of the wave. By carefully choosing the detuning of the laser which forms the standing wave, one may select at which point in the periodic Stark potential the molecule is excited to the upper state. Blue detunings correspond to an excitation at the top of the Stark potential and radiate away the energy difference of the Stark potential (cooling). Red detunings are most likely to absorb at the bottom of the Stark potential and absorb the energy of the Stark shift (heating). The exact detuning that maximizes the heating or cooling effect depends on the magnitude of the Stark shift. Therefore, as the standing wave intensity increases, we expect the optimal detunings to grow in magnitude. This effect was clearly seen over the course of this experiment, as low power Sisyphus was maximized at ± 5MHz while the optimal detunings at high intensity were nearly ± 20MHz. The relatively low power available, combined with the high intensities required, forced us to maintain a very small laser diameter, which lead

to significant beam divergence as the cooling beam propagated. This expansion mades it easier to form a standing wave between the wings of the laser in adjacent retro-reflected passes, but limits the energy removal per Sisyphus cycle. Under experimental conditions we achieved a maximum laser intensity of $\approx 200\text{mW/cm}^2$.

Finally, I must address the effect of the "magnetic assistance" provided throughout the Sisyphus cycles. When the excited molecule relaxes, it can decay into a Zeeman dark state. Molecules must be remixed out of the dark states in order to continue the Sisyphus cycle. The appropriate magnetic field magnitude is dependent on the rate at which the molecules propagate through the standing wave; the optimal remixing rate matches the time is takes for molecule to transit through one quarter wavelength of the Sisyphus standing wave. This optimal remixing rate is calculated as $\lambda/(4v)$.

In the following section, I will detail my initial observation of Sisyphus cooling on the $X - A$ and $X - B$ transitions and I will describe the optimization process by which we maximized the cooling signature. In summary this involved varying the standing wave, minimizing the beam center-shift force asymmetry, optimizing the remixing magnetic field, and finally maximizing the laser power available, so as to produce the results ultimately published in my most recent paper, *Direct Laser Cooling of Calcium Monohydride Molecules* [146].

6.3.1 Initial Observation of Cooling on the $X^2\Sigma^+ \rightarrow B^2\Sigma^+$ Transition

I first observed this combined Doppler and Sisyphus cooling profile on the X-B cycling transition in September of 2020, after switching from BaH to CaH and three months after Columbia lifted its COVID lockdown policy banning in-lab research. This encouraging result was promising and inspired us to dedicate the following two years to improving the Sisyphus effect before ultimately publishing our best results [146]. I have included this first result out of a desire to be thorough in my description of my research, but also because this data is beautiful - showing both the Sisyphus and Doppler effects in the same plot.

The plot in Figure 6.12 shows a pronounced Doppler dispersion curve, with heating and cool-

ing and heating maximized at a detuning of ≈ -10MHz and ≈ +15MHz, respectively. The most significant feature of this plot is the small, but undeniable Sisyphus feature showing heating and cooling at ± 5MHz. The Sisyphus feature is small due to the low laser power available on the X-B transition, however this plot was the source of my conviction that carried me through following two years of experimental optimization of the Sisyphus signature.

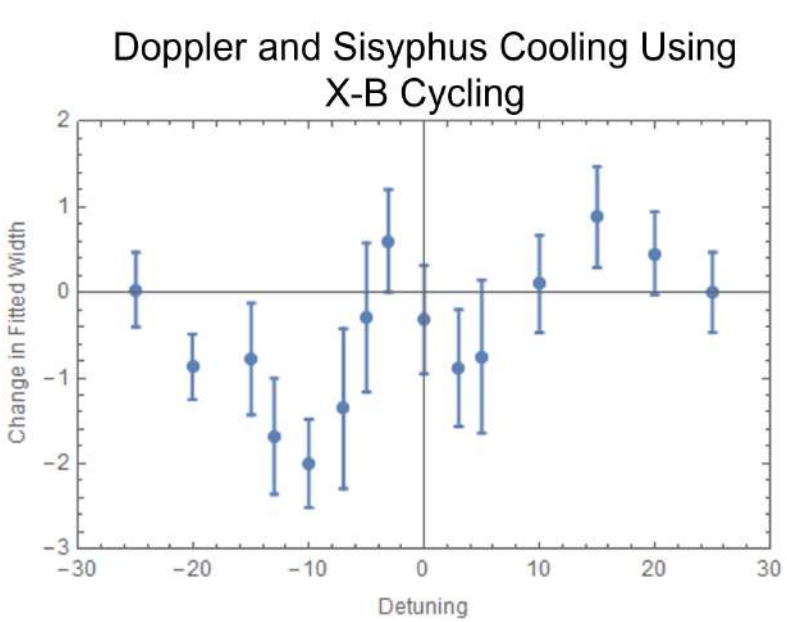

Figure 6.12: The first Sisyphus and Doppler feature measured on the X-B transition of CaH. The characteristic cooling and heating associated with the Doppler effect can be seen in the larger dispersion curve peaking at -10MHz and +15MHz. A smaller dispersion curve attributed to Sisyphus cooling can be seen perturbing the Doppler result. Note that the Sisyphus feature is of opposite sign with heating for negative detuning and cooling for positive laser detuning. The Sisyphus feature is narrower than Doppler due to the low laser power available at 635nm.

Despite these promising initial results, we decided not to pursue $X - B$ cooling for the future of the experiment for three reasons. First, the A state is a better candidate for cooling due to its shorter natural lifetime (33ns) as compared to the B state (58ns). A shorter natural lifetime leads to twice the scattering rate when cycling on the A state compared to the B state. I began with the B state due to the lack of high power single mode diodes for the $X - A$ transition at the time. Later we acquired 250mW diodes for the A state, which enabled us to switch to that transition. Second, by cooling and repumping through the same excited B state, we doubled the number of

ground states in which molecules can be distributed, halving the maximum attainable scattering rate. A slow scattering rate would make slowing and loading a MOT considerably harder. Third, we found that a small fraction of molecules were mysteriously lost when cycling on the $X - B$ transition. We fear that this was indicative of molecular pre-dissociation of the B state due to its very shallow molecular bonding potential. We measured the vibrational branching ratios to the $V = 2$ state and found that these vibrational losses could not account for the drop in population that we measured. The reason the B state predissociates is because it has the same symmetries as the X state. The A state offered a solution to this obstacle due to the different symmetry of the potential wavefunctions, thus suppressing the possibility of pre-dissociation while cycling.

6.3.2 Initial Observation of Cooling on the $X^2\Sigma^+ \rightarrow A^2\Pi_{1/2}$ Transition

In June of 2021, I detected the first signature of Sisyphus momentum exchange even with only 40mW of total cooling power. This first observation was the starting point for the optimization process by which we maximized the cooling signature on the X-A transition. The Sisyphus effect at such low power leaves no room for error, and any number of experimental imperfections will destroy the signature. These imperfections could include a lower than normal molecular yield, a poor laser lock, poor beam alignment, or a decrease in the cooling standing wave from a slight misalignment of the mirrors. Therefore, it took the rest of my team and myself some time to reproduce these results.

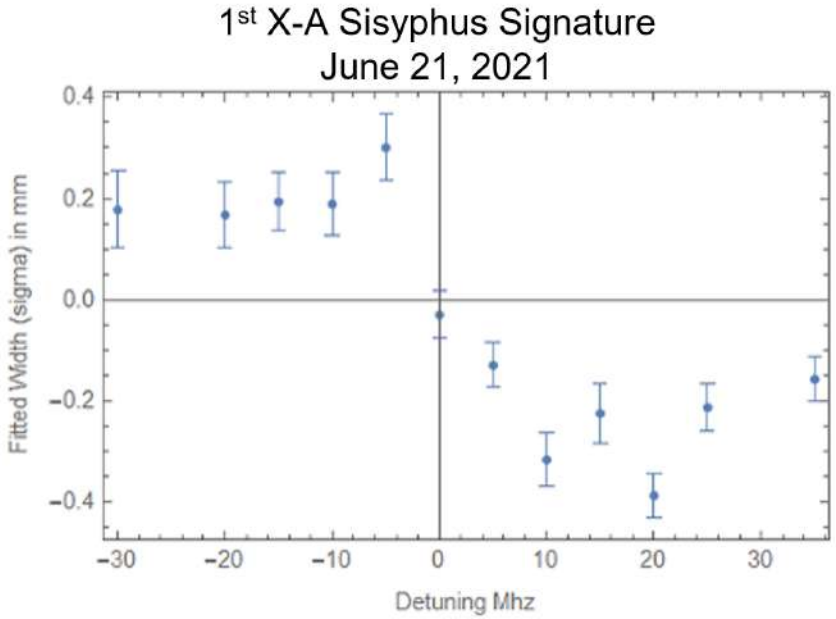

Figure 6.13: The first Sisyphus dispersion curve that I measured on the $X - A$ transition. Note the characteristic heating for negative detuning and cooling for positive detuning associated with the Sisyphus mechanism.

In troubleshooting the system, I made improvements to the experimental apparatus that lead to the robust Sisyphus signal which we see today. First and foremost, among the improvements was the addition of four home-built injection locking amplifiers. Each amplifier addresses one of the ground state hyperfine states. When the light of these amplifiers was combined and coupled to the same fiber, this system provided up to 300mW of Sisyphus cooling light. This order of magnitude increase in laser power was the single most important factor to observing Sisyphus, as I will demonstrate in the section on power saturating the Sisyphus effect. Another improvement that contributed to reproducing the Sisyphus effect was the use of AOMs to address the hyperfine components of the ground state rather than the EOMs used initially. The additional sidebands provided by EOM modulation would begin to approach resonance as the cooling laser frequency approached the optimal Sisyphus detuning. The final optimal detuning for Sisyphus was ± 20MHz, at which point the unnecessary EOM sidebands began to interact with the molecules and diminish the effects from the primary sidebands. The simpler spectrum from the AOM guaranteed that this

would not occur, since there were no extraneous sidebands to compete with.

Dependence on the Presence of a Standing Wave

Again limited by the available power, we were required to create an intensity standing wave between the wings of the multi-passed cooling lasers rather than the center of the beam. Access to costly high power commercial lasers can easily create very good standing wave through one pass of a perfectly retro-reflected laser. This approach is robust, as it is very clear when the retro-reflected beam is perfectly overlapped with first pass. However, a consequence of this is that this configuration provides very little interaction time. When operating at high powers, the incredibly strong Sisyphus force remains visible despite the lower interaction time. However, when the laser power available is low, one pass of a perfect standing wave does not produce an observable force given the signal to noise ratio of our experiment. We attempted this configuration many times, but never with success. We found that a weaker standing wave with a much longer interaction time produced the best Sisyphus effect. I do not doubt that if given watts of power, we may have been able to see the Sisyphus effect in one or two passes of the lasers.

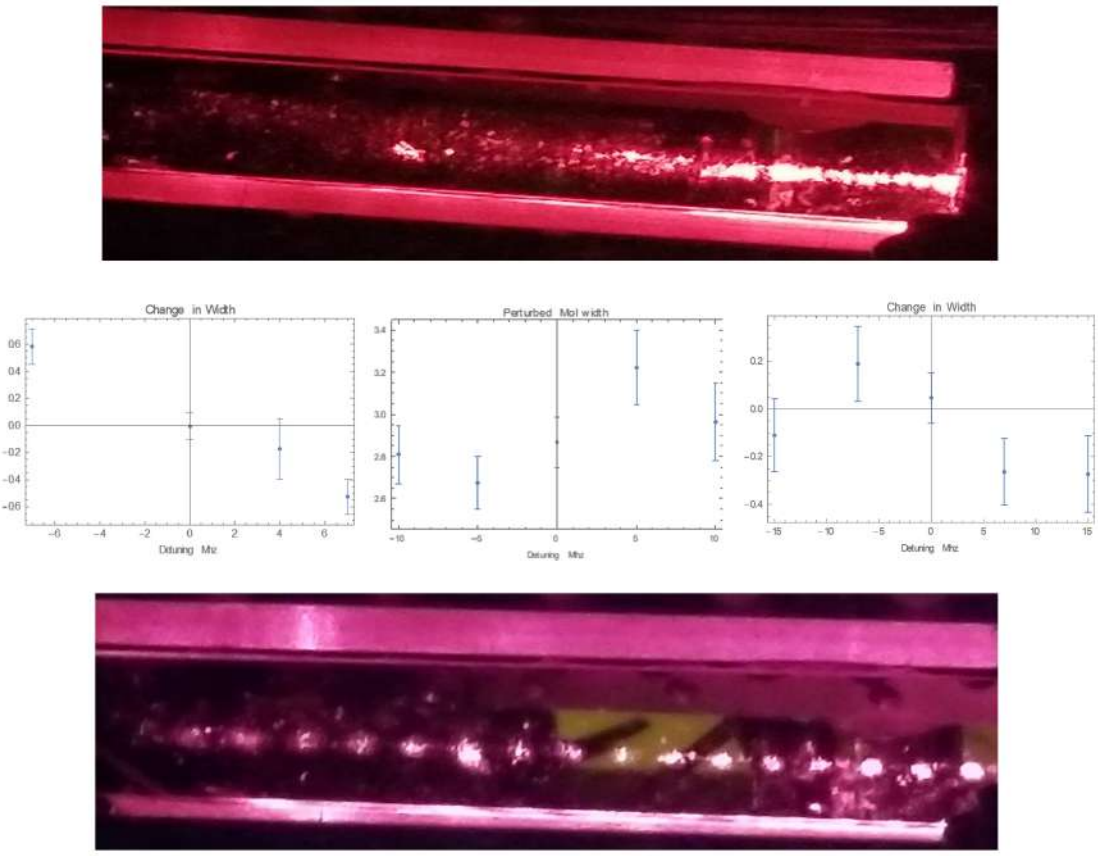

Figure 6.14: The effect of eliminating the standing wave on the detuning dependence of the heating and cooling features. A laser configuration where each laser pass overlaps with the wings of the passes adjacent to it, creating the standing wave required for Sisyphus (top). On the bottom, is shown a Doppler laser configuration which lacks a standing wave due to the large separation between the laser passes. The plot on the left shows Sisyphus heating and cooling taken with the lasers in the top configuration. In the center, plot I show the Doppler cooling and heating achieved with a laser configuration that lacks a standing wave. Finally (center right), is a demonstration that Sisyphus can be turned on again by realigning the mirrors to produce a standing wave.

Figure 6.14 shows data gathered on the same day. Here I was able to tune between Sisyphus and Doppler and back to Sisyphus again by eliminating the initial standing wave and then realigning it. I destroyed the standing wave, and produced a Doppler signature by spreading out the laser passes to guarantee no overlap between the wings of adjacent passes. These data demonstrate the clear dependence of the Sisyphus signature on the presence of a standing wave. This is one of the characteristic signatures of the Sisyphus effect.

Center Shift Minimization

Another key to producing a robust Sisyphus signature was to eliminate the force imbalance between left and right propagating laser passes. I noticed a large force asymmetry exerted by the left and the right propagating cooling beams, which manifested itself as a shift in the molecular beam center to the left or right, rather than a symmetric compression. A perfectly aligned transverse cooling beam produces the same force from the left vs the right propagating laser passes. However, a misalignment of the transverse cooling beams relative to the beam axis produces a Doppler shift of opposite signs between the left and right beams. This is due to the difference in the projection of the beam's forward velocity onto the laser k vector, that produces a Doppler shift of opposite sign for left vs for right passes. This means that left propagating beams can be Doppler shifted into resonance, while the right propagating passes are Doppler shifted away from resonance. Below I show the effect I observed in BaH [135], in which I was able to change the magnitude and sign of the Doppler shift by changing the alignment of the laser beam relative to the molecular beam axis. This phenomena was seen suppressing Doppler and Sisyphus alike; both effects were strongest when the force imbalance was minimized.

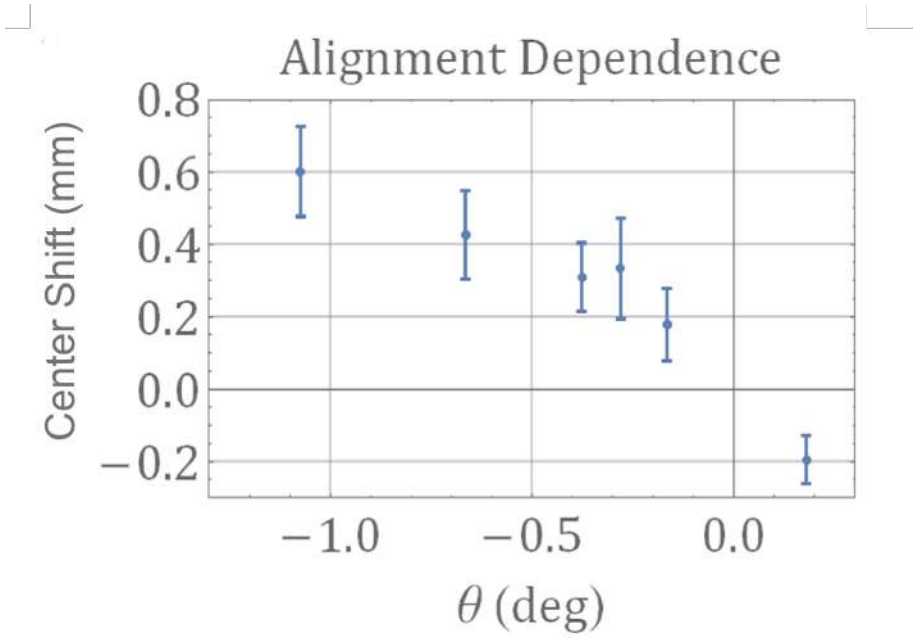

Figure 6.15: The effect of laser alignment on the center shift as measured on a beam of BaH. These results were published in my paper on BaH 1D cooling [135].

I first suggested and documented this effect when working on BaH [135] and hypothesized a simple explanation for the effect. Figure 6.16 shows two extreme cases of misalignment and the optimal alignment to help the reader develop an intuition for this effect. We optimized the mirror alignment by measuring and minimizing the center-shift of the molecular cloud when the laser resonance was a few natural line-widths away from resonance.

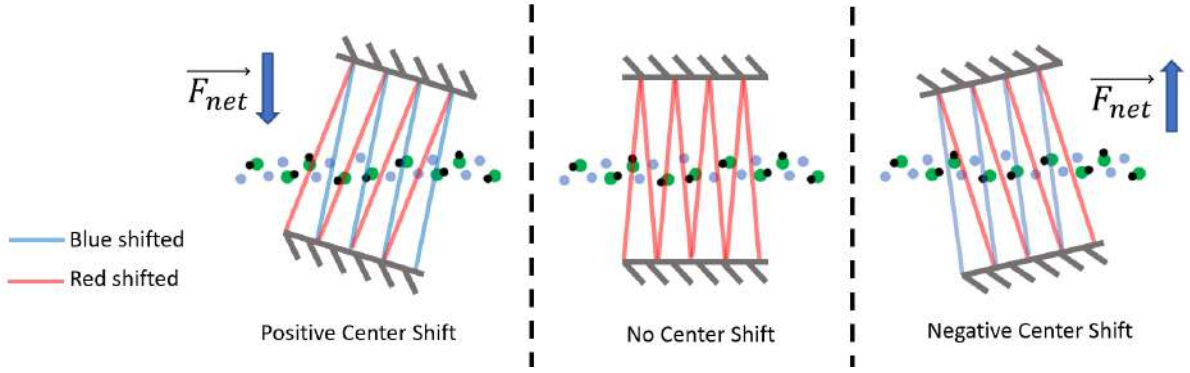

Figure 6.16: On the left and right, I show a diagram of severe misalignment of the cooling laser relative to the molecular beam. Both situations lead to a Doppler shift in the frequency of the left and the right lasers that shifts one direction into resonance, while moving the other laser passes away from resonance. This creates the force imbalance that leads to a center shift. A well aligned laser configuration is shown in the center where the Doppler shift is zero for left or right passing lasers and the cooling force is applied symmetrically. The correct alignment eliminates the center shift.

Magnetic Field and Intensity Dependence

The final parameter that is key to producing a robust Sisyphus effect is the magnetically assisted remixing of the $m_F = \pm 2$ dark states of the $J = 3/2, F = 2$ manifold and the $m_F = \pm 1$ dark states of the $J = 1/2, F = 1$ hyperfine manifold. Dark states form as a result of the linear laser polarizations used in this experiment. We were required to use linear polarization due to the use of polarizing beam splitters to combine the lasers addressing the $J = 1/2$ and $J = 3/2$ spin rotation states. As can be seen in figure 5.15, the optimal magnetic field feature is relatively broad, peaking at 2G with no remixing occurring at 0G as predicted by numerical solutions to the optical Bloch equations. Magnetic fields that are too high lead to a Zeeman splitting of the m_F states, which shifts states out of resonance. This effect is seen as a suppression of Sisyphus cooling for high field strengths. We were unable to experimentally resolve the 0G feature due to the uncompensated magnetic fields of the earth and the turbo pumps near the interaction chamber. However, the suppression of Sisyphus cooling at high field strengths is clearly visible in Figure 6.17.

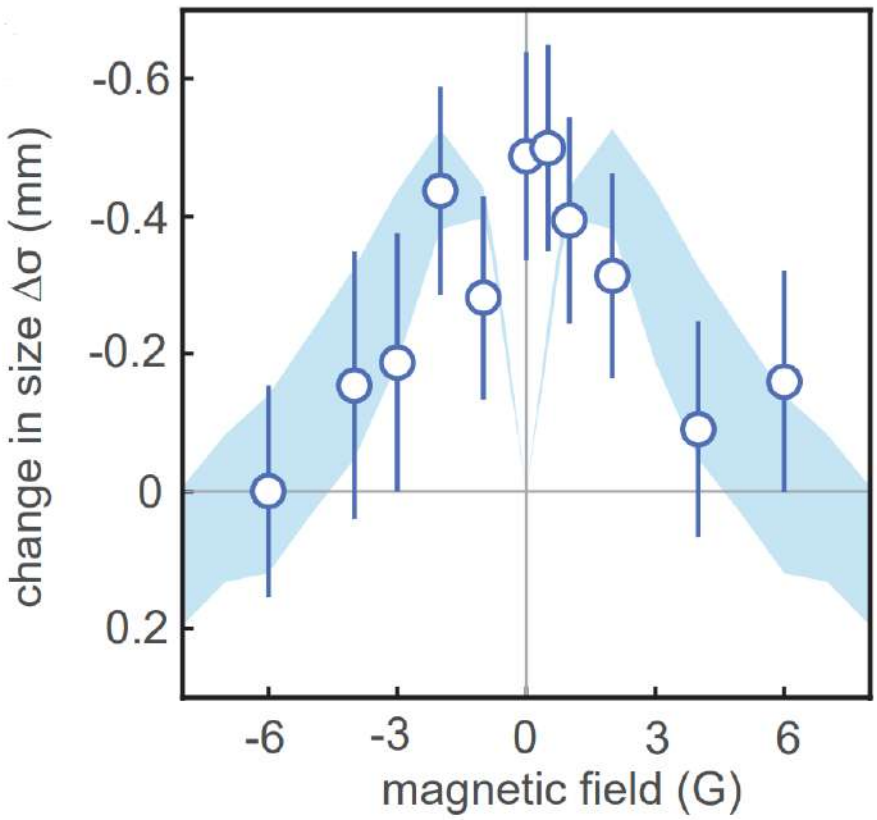

Figure 6.17: The effect of the externally applied magnetic field magnitude on Sisyphus cooling at the resonance frequency in addition to the theoretical magnetic field dependence as calculated through numerical solutions to the optical Bloch equations [146]. OBE simulations predicts strong suppression of the Sisyphus effect for $B = 0$, but this was not evident in the data because of the uncompensated magnetic fields in the lab from the Earth and adjacent turbo pumps. The data and simulation both demonstrate a strong suppression of the Sisyphus effect for large magnetic field strengths.

Intensity Dependence

Currently, we believe that cooling is still severely power-limited, as indicated by the linear improvement in Sisyphus cooling when we applied more laser power. The quality of our standing wave may have also been problematic, because we only create a standing wave in the wings of the beam where power is even further diminished. We attempted direct retro-reflection of the cooling laser onto itself in two identical interaction regions, but the low power of our laser system and the limited interaction time of such a configuration prevented us from seeing any improvement to the cooling signature. Solutions to the optical Bloch equations indicate that saturation of Sisy-

phus cooling should occur at greater than 600mW/cm^2, whereas at most we were able to produce 300mW/cm^2 [146].

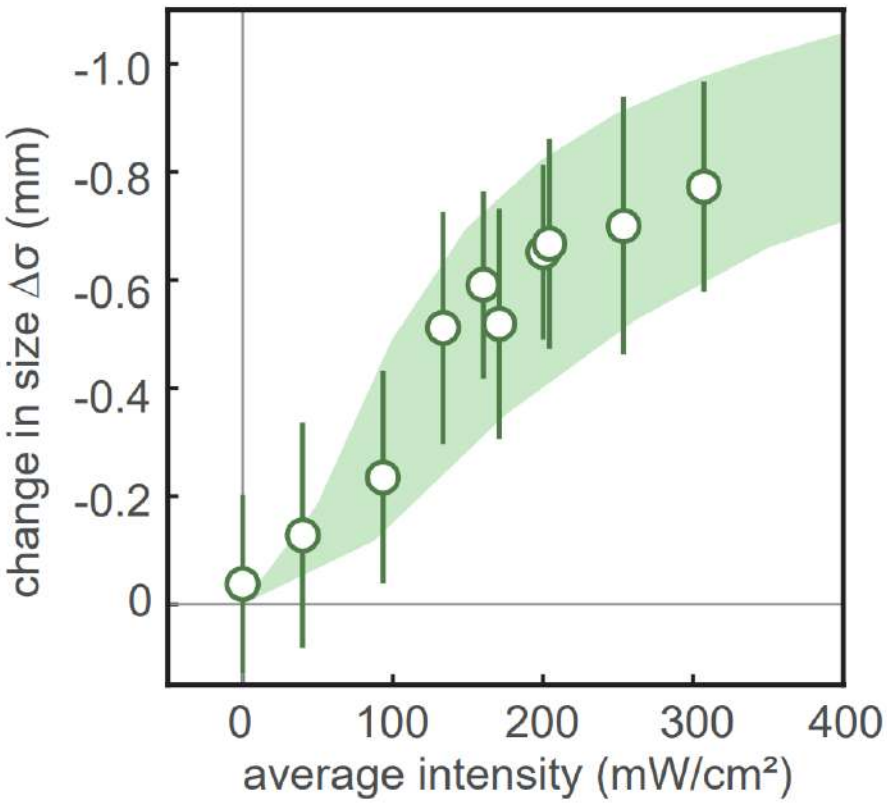

Figure 6.18: The experimentally measured Sisyphus cooling as a function of laser intensity shown as points. The theoretical dependence as predicted by numerical solutions to the optical Bloch equations are shown as the band plot [146]. As laser power increases, the Sisyphus effect grows in strength. The Sisyphus effect was predicted to saturate with intensity above 600mW/cm^2 which was well beyond the capabilities of our home-built laser system.

The relative laser polarization angles were restricted, due to the beam-combining techniques used in this experiment to combine the spin rotation states of the X state, separated by 1.86GHz. We chose to address these states with separate pairs of seed lasers amplified by separate injection locking amplifiers; combining these beams requires a PBS which sets the relative polarizations of the two spin rotation components. If our experiment had access to several watts of power from a fiber laser, or perhaps a Ti:Saph, we might have been able to waste some power and combine the lasers on a non-polarizing beam splitter. This would have allowed us to simultaneously optimize the magnetic remixing of both the $J = 1/2$ and $J = 3/2$ states. We are currently negotiating the

purchase of a high power fiber laser at 695nm, but supply chain disruptions arising from the recent pandemic have extended the lead time for the delivery of such a system to beyond my time as a graduate student at Columbia.

Funding gives a huge advantage in AMO physics. Buying professionally engineered high power laser systems or the best cryogenic components can greatly improve the experimental apparatus. Sisyphus effect relies on a Stark shift in the Zeeman sublevels that scales with power. Many of the experimental configurations used by other groups with access to high power laser systems could not be used in my attempt to observe the Sisyphus effect. Engineering a way around the power limitations of our optical systems represented a significant part of my research and a valuable part of my training.

Final Measurement of the Sisyphus effect

Having optimized our system to the experimental conditions, we recorded our best Sisyphus momentum transfer on the $X - A$ transition nearly two years after my first observation of Sisyphus on the $X - B$ transition. We achieved high intensities (peak 300 mW/cm^2) by keeping the laser waist to the minimum possible, while maintaining a relatively long Raleigh range. Despite this, the narrow beam waist limited the laser propagation distance to under 2 meters, and after 16 passes, the cooling laser expanded to a point where its intensity was two orders of magnitude lower than that with which it started. We applied an external magnetic field of 2G and rotated the laser polarizations to maximize the scattering rate. When the laser was +20MHz detuned from the transition we observed Sisyphus heating, while detuning the laser to -20MHz created Sisyphus cooling [146]. The width of the heating and cooling features is attributable to the power broadening of the excited state, which allowed us to see Sisyphus effect as far as ±50MHz from resonance.

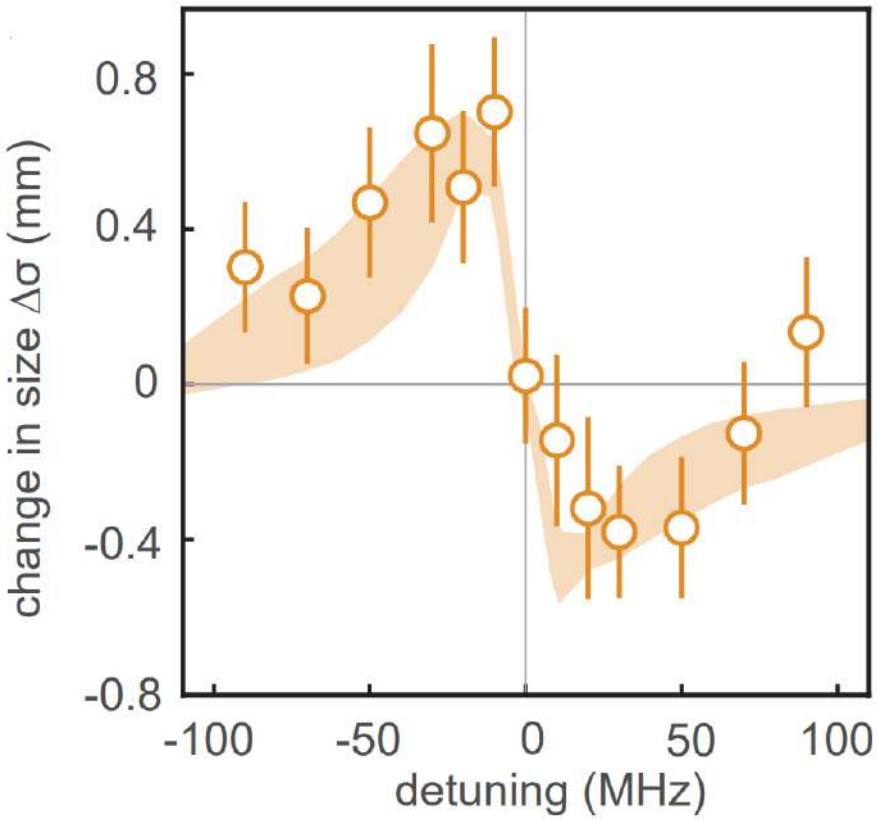

Figure 6.19: I show the strongest Sisyphus detected to date on CaH with the theoretically expected Sisyphus cooling shown as a band plot [146]. The theory curve was generated by numerical solutions to the optical Bloch equations that reflect the experimental laser intensities, interaction time, and magnetic field strength. Experimentally, the optimal Sisyphus force was observed at ± 20MHz.

Sisyphus cooling was observed through EMCCD camera images as compression of the molecular beam width. Similarly, Sisyphus heating was detected as a broadening of the molecular beam as the molecules' transverse velocities increased and caused a migration from the center to the wings of the beam. The 1D molecular beam profiles of an unperturbed beam and the most strongly heated/cooled beams is shown in Figure 6.20 [146].

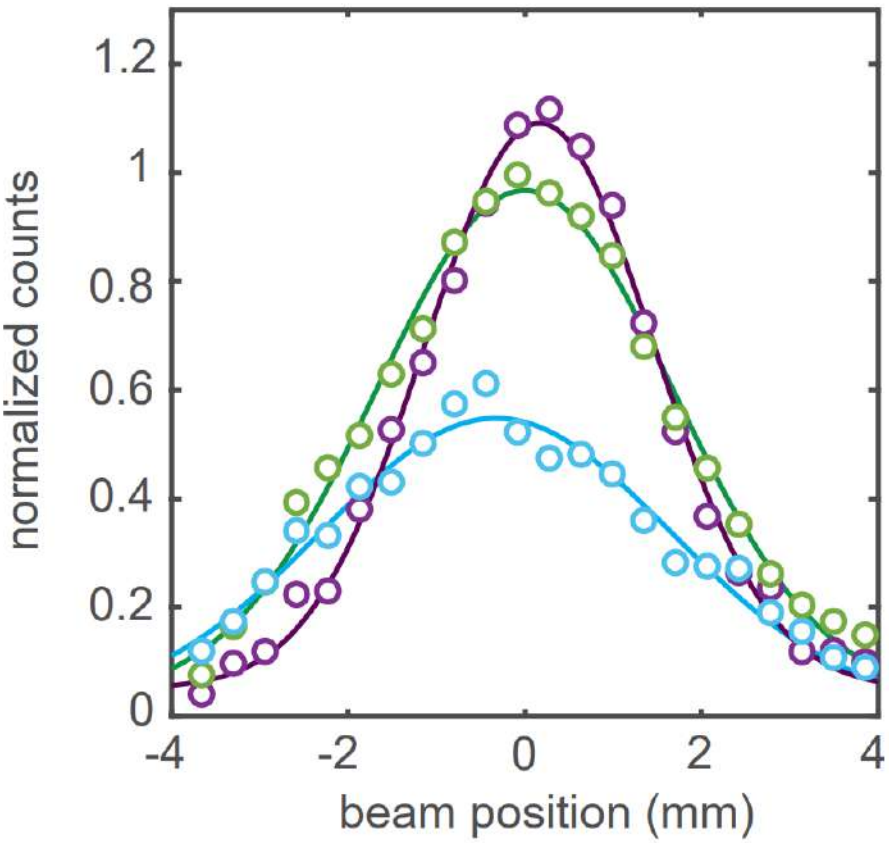

Figure 6.20: The 1D projection of the molecular beam's transverse profile for the unperturbed beam (green), the heated beam (blue), and the cooled beam (purple). Note the broadening of the molecular distribution in the heated beam and the compression of the cooled beam. The cooled beam's transverse temperature was reduced from 12.2(1.2) mK to a minimum temperature of 5.7(1.1)mK [146].

By combining these measurements with Monte-Carlo simulations of the expansion of the molecular cloud after passing through the transverse velocity filtering aperture at the start of the interaction chamber, we were able to extract the transverse velocity of the molecular beam. We conclude that the molecular beam transverse temperature was reduced from 12.2(1.2) mK to a temperature of 5.7(1.1)mK by scattering 140^{+400}_{-60} photons due to the Sisyphus effect.

Chapter 7: Outlook

7.1 The Path to Ultracold Hydrogen

The long-term goal of this experiment is to slow and trap CaH molecules and cool them past the Doppler limit. Then the molecule cooling experiment at ZLab will photo-dissociate CaH molecules to isolate and trap a sample of ultracold hydrogen. Once trapped, the transitions of hydrogen can be probed to an unparalleled precision. A dilute gas of hydrogen in the microkelvin regime would significantly reduce systematic errors arising form density and hyperfine state dependent collisional broadening that has dominated previous measurements [55]. Whereas, the long interrogation time provided by a trapped sample will significantly reduce statistical errors and enhance the precision of Hydrogen spectroscopy past the current state of the art [175]. However, there is still a great deal of work that must be done to accomplish this goal.

7.1.1 Slowing Experiments

The next immediate step will be to identify and address the $V = 2$ repumping transition. Slowing and trapping will require between 10^4 and 10^5 photon cycles, which will require closing the higher order vibrational leaks. This will require building additional lasers at 434.934065 THz and performing spectroscopy to find the $V = 2$ repumper. The new senior graduate student Qi Sun has promising data indicating that he has found the $J = 1/2$ component of this transition. The search is still ongoing for the $J = 3/2$ component of this transition.

Once the additional vibrational repumpers have been found, the experiment will be able to attempt longitudinal slowing to MOT capture velocities. Before I left, I helped build the MOT chamber that will also serve as a slowing chamber. As a part of this effort, I designed and built an in-vacuum high NA collection optics system that promises to improve the SNR of slowing mea-

surements. Nevertheless, slowing will present new challenges as the $X - A$ cooling transition will be severely power-limited without investing in a commercially manufactured laser system. The power limitation is a product of two experimental factors. First, the slowing laser must be broadened across hundreds of MHz to ensure that the laser remains resonant with the molecules as they decelerate and their transition frequency is Doppler shifted. Second, the laser's cross sectional area must be expanded to ensure that the laser can address the entire molecular beam. The molecular beam is 5 mm in diameter when it exits the cell, but quickly diverges due to the transverse velocity of the molecules in the beam. The laser profile needs to be wide enough to address all the molecules exiting that aperture. This will further lower the laser intensity that each molecule experiences, accentuating the power limitations posed by this laser system. The immediate solution to both of these power problems is to invest in a high power fiber laser technology. Alternatively, chirp slowing offers a solution to the frequency broadening challenge. In a chirp slowing system, the laser frequency is broadened less and the center frequency of the laser is tuned to match the deceleration of the molecular beam. Although possible, this adds significant complexity to the experimental sequence. The beam area problem could also be mitigated by building a 2D cooling system that takes advantage of the molecular beam compression via the Doppler or Sisyphus forces shown in this thesis. Again, this would add significant complexity to the system and delay the construction of a MOT. The fastest and simplest solution requires purchasing a commercial laser system for the main cooling transition at a minimum and possibly the first vibrational repumper.

There is also room for improving the molecular source. The forward velocity of the cell can likely be reduced to provide a molecular beam with a slower forward velocity. This would reduce the number of scattered photons needed to slow the beam to the trap capture velocity. Another cryostat upgrade could come in the form of optimization of the rotational temperature. As shown in this thesis, the $N = 1$ population could be improved upon by increasing the rotational temperature, transferring molecules out of $N = 0$ into $N = 1$. It is not immediately clear how to increase the rotational temperature, as I showed that simply heating the cell did not provide the intended result. My approach moving forward would be to try raising the temperature of the He buffer gas and

measure the effect on the rotational distribution. Heating the buffer gas could be accomplished by placing a cryogenic heater on the buffer gas bobbins. This change would not require significantly remodeling the cryostat, but other changes will likely require significant time and effort. The effects of modifications to the cryogenic cell are difficult to predict and it is unclear what will improve the rotational temperature. Improvements to the cryogenic cell risk a large investment of time without a guaranteed reward. However, it is possible to improve the molecular buffer gas source. I am certain that under the guidance of our post-doc Debayan Mitra, the graduate students Qi Sun and Jinyu Dai will find a solution.

References

[1] H. L. e. a. Bethlem, "Electrostatic trapping of ammonia molecules," *Nature*, vol. 406, pp. 491–494, 2000.

[2] J. D. Weinstein, R. deCarvalho, T. Guillet, B. Friedrich, and J. M. Doyle, "Magnetic trapping of calcium monohydride molecules at millikelvin temperatures," *Nature*, vol. 395, pp. 148–150, 1998.

[3] S. A. Moses *et al.*, "Creation of a low-entropy quantum gas of polar molecules in an optical lattice," *Science*, vol. 350, no. 6261, pp. 659–662, 2015. eprint: `https://www.science.org/doi/pdf/10.1126/science.aac6400`.

[4] S. Shuman, J. Barry, and D. DeMille, "Laser cooling of a diatomic molecule," *Nature*, vol. 467, pp. 820–823, 7317 2010.

[5] S. Truppe *et al.*, "Molecules cooled below the Doppler limit," *Nat. Phys.*, vol. 13, pp. 1173–1176, 2017.

[6] L. Anderegg *et al.*, "Radio frequency magneto-optical trapping of CaF with high density," *Phys. Rev. Lett.*, vol. 119, p. 103 201, 10 2017.

[7] A. L. Collopy *et al.*, "3D magneto-optical trap of yttrium monoxide," *Phys. Rev. Lett.*, vol. 121, p. 213 201, 21 2018.

[8] R. L. McNally, I. Kozyryev, S. Vazquez-Carson, K. Wenz, T. Wang, and T. Zelevinsky, "Optical cycling, radiative deflection and laser cooling of barium monohydride (^{138}Ba^{1}H)," *New J. Phys.*, vol. 22, p. 083 047, 2020.

[9] T. V. Andreev *et al.*, "Improved limit on the electric dipole moment of the electron," *Nature*, vol. 562, p. 355, 2018.

[10] B. Augenbraun *et al.*, "Laser-cooled polyatomic molecules for improved electron electric dipole moment searches," *New J. Phys.*, vol. 22, p. 022 003, 2020.

[11] I. Kozyryev *et al.*, "Sisyphus laser cooling of a polyatomic molecule," *Phys. Rev. Lett.*, vol. 118, p. 173 201, 17 2017.

[12] N. B. Vilas *et al.*, "Magneto-optical trapping and sub-doppler cooling of a polyatomic molecule," *arXiv:2112.08349*, 2021.

[13] D. Mitra *et al.*, "Direct laser cooling of a symmetric top molecule," *Science*, vol. 369, pp. 1366–1369, 2020.

[14] The ACME Collaboration: V. Andreev *et al.*, "Improved limit on the electric dipole moment of the electron," *Nature*, vol. 562, p. 355, 2018.

[15] W. B. Cairncross and J. Ye, "Atoms and molecules in the search for time-reversal symmetry violation," *Nat. Rev. Phys.*, vol. 1, p. 510, 2019.

[16] J. P. et al., "Second-scale nuclear spin coherence time of ultracold NaK molecules," *Science*, vol. 357, pp. 372–375, 2017.

[17] J. A. Blackmore *et al.*, "Ultracold molecules for quantum simulation: Rotational coherences in CaF and RbCs," *Quantum Sci. Technol.*, vol. 4, p. 014 010, 2019.

[18] R. Sawant *et al.*, "Ultracold polar molecules as qubits," *New J. Phys.*, vol. 22, p. 013 027, 2020.

[19] K. R. A. Hazzard *et al.*, "Many-body dynamics of dipolar molecules in an optical lattice," *Phys. Rev. Lett.*, vol. 113, p. 195 302, 19 2014.

[20] T. Aoyama, M. Hayakawa, T. Kinoshita, and M. Nio, "Tenth-order QED contribution to the electron g-2 and an improved value of the fine structure constant," *Physical Review Letters*, vol. 109, no. 11, 2012.

[21] D. Hanneke, S. Fogwell, and G. Gabrielse, "New measurement of the electron magnetic moment and the fine structure constant," *Physical Review Letters*, vol. 100, no. 12, 2008.

[22] L. D. Carr, D. DeMille, R. V. Krems, and J. Ye, "Cold and ultracold molecules: Science, technology and applications," *New Journal of Physics*, vol. 11, no. 5, p. 055 049, 2009.

[23] D. DeMille, "Diatomic molecules, a window onto fundamental physics," *Physics Today*, vol. 68, no. 12, Dec. 2015.

[24] C. Chin, V. V. Flambaum, and M. G. Kozlov, "Ultracold molecules: New probes on the variation of fundamental constants," *New Journal of Physics*, vol. 11, no. 5, p. 055 048, 2009.

[25] S. S. M. M. Kondov *et al.*, "Molecular lattice clock with long vibrational coherence," *Nature Physics*, vol. 15, no. 11, pp. 1118–1122, 2019.

[26] M. Safronova, D. Budker, D. DeMille, D. F. J. Kimball, A. Derevianko, and C. W. Clark, "Search for new physics with atoms and molecules," *Reviews of Modern Physics*, vol. 90, no. 2, 2018.

[27] I. C. Lane, "Production of ultracold hydrogen and deuterium via doppler-cooled feshbach molecules," *Phys. Rev. A*, vol. 92, p. 022 511, 2 2015.

[28] F. Biraben, "Spectroscopy of atomic hydrogen," *The European Physical Journal Special Topics*, vol. 172, pp. 109–119, 2009.

[29] C. L. Cesar *et al.*, "Two-photon spectroscopy of trapped atomic hydrogen," *Phys. Rev. Lett.*, vol. 77, pp. 255–258, 2 1996.

[30] P. Jansen, H. L. Bethlem, and W. Ubachs, "Perspective: Tipping the scales: Search for drifting constants from molecular spectra," *The Journal of Chemical Physics*, vol. 140, no. 1, p. 010 901, 2014.

[31] M. G. Kozlov and S. A. Levshakov, "Microwave and submillimeter molecular transitions and their dependence on fundamental constants," *Annalen der Physik*, vol. 525, no. 7, pp. 452–471, 2013.

[32] S. Truppe *et al.*, "A search for varying fundamental constants using hertz-level frequency measurements of cold CH molecules," *Nature Communications*, vol. 4, no. 1, 2013.

[33] O. W. Greenberg, *Small violations of statistics*, 1999.

[34] A. Shelkovnikov, R. J. Butcher, C. Chardonnet, and A. Amy-Klein, "Stability of the proton-to-electron mass ratio," *Physical Review Letters*, vol. 100, no. 15, 2008.

[35] J. B. et al., "A stringent limit on a drifting proton-to-electron mass ratio from alcohol in the early universe," *Science*, vol. 339, no. 6115, pp. 46–48, 2013. eprint: `https://www.science.org/doi/pdf/10.1126/science.1224898`.

[36] J. Bagdonaite, P. Jansen, C. Henkel, H. L. Bethlem, K. M. Menten, and W. Ubachs, "A stringent limit on a drifting proton-to-electron mass ratio from alcohol in the early universe," *Science*, vol. 339, no. 6115, pp. 46–48, 2013. eprint: `https://www.science.org/doi/pdf/10.1126/science.1224898`.

[37] E. R. Meyer and J. L. Bohn, "Prospects for an electron electric-dipole moment search in metastable ThO and $ThF+$," *Physical Review A*, vol. 78, no. 1, 2008.

[38] D. DeMille, S. B. Cahn, D. Murphree, D. A. Rahmlow, and M. G. Kozlov, "Using molecules to measure nuclear spin-dependent parity violation," *Physical Review Letters*, vol. 100, no. 2, 2008.

[39] J. Baron *et al.*, "Order of magnitude smaller limit on the electric dipole moment of the electron," *Science*, vol. 343, no. 6168, pp. 269–272, 2014. eprint: `https://www.science.org/doi/pdf/10.1126/science.1248213`.

[40] M. V. Romalis, W. C. Griffith, J. P. Jacobs, and E. N. Fortson, "New limit on the permanent electric dipole moment of ^{199}Hg," *Physical Review Letters*, vol. 86, no. 12, pp. 2505–2508, 2001.

[41] V. A. Dzuba, V. V. Flambaum, and J. S. M. Ginges, "Calculation of parity and time invariance violation in the radium atom," *Physical Review A*, vol. 61, no. 6, 2000.

[42] e. a. V. Andreev D. DeMille, "Improved limit on the electric dipole moment of the electron," *Nature*, vol. 562, 2018.

[43] W. B. Cairncross *et al.*, "Precision measurement of the electron's electric dipole moment using trapped molecular ions," *Physical Review Letters*, vol. 119, no. 15, 2017.

[44] I. Kozyryev and N. R. Hutzler, "Precision measurement of time-reversal symmetry violation with laser-cooled polyatomic molecules," *Physical Review Letters*, vol. 119, no. 13, 2017.

[45] M. Denis, P. A. B. Haase, R. G. E. Timmermans, E. Eliav, N. R. Hutzler, and A. Borschevsky, "Enhancement factor for the electric dipole moment of the electron in the BaOH and YbOH molecules," *Physical Review A*, vol. 99, no. 4, 2019.

[46] O Grasdijk *et al.*, "CeNTREX: A new search for time-reversal symmetry violation in the sup205/suptl nucleus," *Quantum Science and Technology*, vol. 6, no. 4, p. 044 007, 2021.

[47] S. K. Tokunaga, R. J. Hendricks, M. R. Tarbutt, and B Darquié, "High-resolution mid-infrared spectroscopy of buffer-gas-cooled methyltrioxorhenium molecules," *New Journal of Physics*, vol. 19, no. 5, p. 053 006, 2017.

[48] G. Drayna, "Novel application of buffer-gas cooling to cold atoms, diatomic molecules, and large molecules," *Harvard University*, 2016.

[49] E. T. Mengesha *et al.*, "Branching ratios, radiative lifetimes, and transition dipole moments for $YbOH$," *The Journal of Physical Chemistry A*, vol. 124, no. 16, pp. 3135–3148, 2020, PMID: 32227956. eprint: `https://doi.org/10.1021/acs.jpca.0c00850`.

[50] L. Caldwell *et al.*, "Deep laser cooling and efficient magnetic compression of molecules," *Phys. Rev. Lett.*, vol. 123, p. 033 202, 3 2019.

[51] L. Anderegg *et al.*, "Laser cooling of optically trapped molecules," *Nat. Phys.*, vol. 14, pp. 890–893, 2018.

[52] D. J. McCarron, M. H. Steinecker, Y. Zhu, and D. DeMille, "Magnetic trapping of an ultracold gas of polar molecules," *Phys. Rev. Lett.*, vol. 121, p. 013 202, 1 2018.

[53] X. W. et al., "The metastable q state of tho a new resource for the ACME electron EDM search," *New Journal of Physics*, vol. 22, no. 2, p. 023 013, 2020.

[54] I. C. Lane, "Production of ultracold hydrogen and deuterium via doppler-cooled feshbach molecules," *Phys. Rev. A*, vol. 92, p. 022 511, 2 2015.

[55] D. Fried *et al.*, "Bose-Einstein condensation of atomic hydrogen," *Phys. Rev. Lett.*, vol. 81, p. 8311, 1998.

[56] C. G. Parthey *et al.*, "Improved measurement of the hydrogen 1S−2S transition frequency," *Phys. Rev. Lett.*, vol. 107, p. 203 001, 20 2011.

[57] R. McNally, "Laser cooling of *BaH* molecules, and new ideas for the detection of dark matter," *Columbia Thesis*, 2021.

[58] A. Shayesteh, R. S. Ram, and P. F. Bernath, "Fourier transform emission spectra of the $A^2\Pi$-$X^2\Sigma^+$ and $B^2\Sigma^+$-$X^2\Sigma^+$ band systems of CaH," *J. Mol. Spectrosc.*, vol. 288, pp. 46–51, 2013.

[59] K.-K. Ni *et al.*, "Dipolar collisions of polar molecules in the quantum regime," *Nature*, vol. 464, no. 7293, pp. 1324–1328, 2010.

[60] S. Ospelkaus *et al.*, "Quantum-state controlled chemical reactions of ultracold potassium-rubidium molecules," *Science*, vol. 327, no. 5967, pp. 853–857, 2010.

[61] A. Kaufman and K.-K. Ni, "Quantum science with optical tweezer arrays of ultracold atoms and molecules," *Nature*, vol. 17, no. 12, pp. 1324 –1333, 2021.

[62] Y. Liu *et al.*, "Photo-excitation of long-lived transient intermediates in ultracold reactions," *Nature Physics*, vol. 16, no. 11, pp. 1132–1136, 2020.

[63] P. D. Gregory, J. A. Blackmore, S. L. Bromley, and S. L. Cornish, "Loss of ultracold $^{87}Rb^{133}Cs$ molecules via optical excitation of long-lived two-body collision complexes," *Phys. Rev. Lett.*, vol. 124, p. 163 402, 16 2020.

[64] J. W. Park, S. A. Will, and M. W. Zwierlein, "Ultracold dipolar gas of fermionic $^{23}Na^{40}K$ molecules in their absolute ground state," *Physical Review Letters*, vol. 114, no. 20, 2015.

[65] T. Takekoshi *et al.*, "Ultracold dense samples of dipolar RbCs molecules in the rovibrational and hyperfine ground state," *Phys. Rev. Lett.*, vol. 113, p. 205 301, 20 2014.

[66] X. Ye, M. Guo, M. L. Gonzá lez-Martínez, G. Quéméner, and D. Wang, "Collisions of ultracold ^{23}Na ^{87}Rb molecules with controlled chemical reactivities," *Science Advances*, vol. 4, no. 1, 2018.

[67] S. McArdle, S. Endo, A. Aspuru-Guzik, S. C. Benjamin, and X. Yuan, "Quantum computational chemistry," *Reviews of Modern Physics*, vol. 92, no. 1, 2020.

[68] G. Quemener and J. L. Bohn, "Shielding $^2\Sigma$ ultracold dipolar molecular collisions with electric fields," *Physical Review A*, vol. 93, no. 1, 2016.

[69] T. V. Tscherbul and R. V. Krems, "Controlling electronic spin relaxation of cold molecules with electric fields," *Phys. Rev. Lett.*, vol. 97, p. 083 201, 8 2006.

[70] T. V. Tscherbul, Y. V. Suleimanov, V Aquilanti, and R. V. Krems, "Magnetic field modification of ultracold molecule–molecule collisions," *New Journal of Physics*, vol. 11, no. 5, p. 055 021, 2009.

[71] T. V. Tscherbul and R. V. Krems, "Tuning bimolecular chemical reactions by electric fields," *Phys. Rev. Lett.*, vol. 115, p. 023 201, 2 2015.

[72] M. T. Hummon *et al.*, "Cold N+NH collisions in a magnetic trap," *Physical Review Letters*, vol. 106, no. 5, 2011.

[73] D. Jin and J. Ye, "Polar molecules in the quantum regime," *Physics Today*, 2011.

[74] S. A. Moses, J. P. Covey, M. T. Miecnikowski, D. S. Jin, and J. Ye, "New frontiers for quantum gases of polar molecules," *Nature Physics*, vol. 13, no. 1, pp. 13–20, 2016.

[75] "Accelerated chemistry in the reaction between the hydroxyl radical and methanol at interstellar temperatures facilitated by tunnelling," 2013.

[76] H. Bernien *et al.*, "Probing many-body dynamics on a 51-atom quantum simulator," *Nature*, vol. 551, no. 7682, pp. 579–584, 2017.

[77] W. S. Bakr, J. I. Gillen, A. Peng, S. Fölling, and M. Greiner, "A quantum gas microscope for detecting single atoms in a hubbard-regime optical lattice," *Nature*, vol. 462, no. 7269, pp. 74–77, 2009.

[78] M. Saffman, T. G. Walker, and K. Mølmer, "Quantum information with rydberg atoms," *Reviews of Modern Physics*, vol. 82, no. 3, pp. 2313–2363, 2010.

[79] D. DeMille, "Quantum computation with trapped polar molecules," *Physical Review Letters*, vol. 88, no. 6, 2002.

[80] P. Yu, L. W. Cheuk, I. Kozyryev, and J. M. Doyle, "A scalable quantum computing platform using symmetric-top molecules," *New Journal of Physics*, vol. 21, no. 9, p. 093 049, 2019.

[81] P. Krantz, M. Kjaergaard, F. Yan, T. P. Orlando, S. Gustavsson, and W. D. Oliver, "A quantum engineer's guide to superconducting qubits," *Applied Physics Reviews*, vol. 6, no. 2, p. 021 318, 2019.

[82] P. T. Brown *et al.*, "Bad metallic transport in a cold atom fermi-hubbard system," *Science*, vol. 363, no. 6425, pp. 379–382, 2019.

[83] L. Henriet *et al.*, "Quantum computing with neutral atoms," *Quantum*, vol. 4, p. 327, 2020.

[84] K.-K. Ni *et al.*, "A high phase-space-density gas of polar molecules," *Science*, vol. 322, no. 5899, pp. 231–235, 2008. eprint: https://www.science.org/doi/pdf/10.1126/science.1163861.

[85] L. R. Liu *et al.*, "Molecular assembly of ground-state cooled single atoms," *Phys. Rev. X*, vol. 9, p. 021 039, 2 2019.

[86] B. Yan *et al.*, "Observation of dipolar spin-exchange interactions with lattice-confined polar molecules," *Nature*, vol. 501, no. 7468, pp. 521–525, 2013.

[87] C. M. Tesch and R. de Vivie-Riedle, "Quantum computation with vibrationally excited molecules," *Phys. Rev. Lett.*, vol. 89, p. 157 901, 15 2002.

[88] D. Weidinger and M. Gruebele, "Quantum computation with vibrationally excited polyatomic molecules: Effects of rotation, level structure, and field gradients," *Molecular Physics*, vol. 105, no. 13-14, pp. 1999–2008, 2007. eprint: https://doi.org/10.1080/00268970701504335.

[89] C. M. Tesch and R. de Vivie-Riedle, "Vibrational molecular quantum computing: Basis set independence and theoretical realization of the deutsch–jozsa algorithm," *The Journal of Chemical Physics*, vol. 121, no. 24, pp. 12 158–12 168, 2004. eprint: https://aip.scitation.org/doi/pdf/10.1063/1.1818131.

[90] M. V. Ivanov, S. Gulania, and A. I. Krylov, "Two cycling centers in one molecule: Communication by through-bond interactions and entanglement of the unpaired electrons," *The Journal of Physical Chemistry Letters*, vol. 11, no. 4, pp. 1297–1304, 2020, PMID: 31973526. eprint: https://doi.org/10.1021/acs.jpclett.0c00021.

[91] R. Feynman, "Simulating physics with computers," *International Journal of Theoretical Physics*, vol. 21, pp. 467–488, 1982.

[92] S. Ebadi *et al.*, "Quantum phases of matter on a 256-atom programmable quantum simulator," *Nature*, vol. 595, no. 7866, pp. 227–232, 2021.

[93] B. B. et al., "Quantum computing with trapped ion hyperfine qubits," *Quantum Information Processing*, vol. 3, no. 1, pp. 45–59, 2004.

[94] D. Lu, A. Brodutch, J. Park, H. Katiyar, T. Jochym-O'Connor, and R. Laflamme, *Nmr quantum information processing*, 2015.

[95] T. Sowinnski, O. Dutta, P. Hauke, L. Tagliacozzo, and M. Lewenstein, "Dipolar molecules in optical lattices," *Phys. Rev. Lett.*, vol. 108, p. 115 301, 11 2012.

[96] R. Barnett, D. Petrov, M. Lukin, and E. Demler, "Quantum magnetism with multicomponent dipolar molecules in an optical lattice," *Phys. Rev. Lett.*, vol. 96, p. 190 401, 19 2006.

[97] P. Benioff, "The computer as a physical system: A microscopic quantum mechanical hamiltonian model of computers as represented by turing machines," *Journal of Statistical Physics*, vol. 22, 5 1980.

[98] A. J. Heinrich *et al.*, "Quantum-coherent nanoscience," *Nature Nanotechnology*, vol. 16, no. 12, pp. 1318–1329, 2021.

[99] C. M. T.D.Ladd, "Quantum computers," *Natural*, vol. 464, 7285 2010.

[100] S. Rasmussen *et al.*, "Superconducting circuit companion—an introduction with worked examples," *PRX Quantum*, vol. 2, no. 4, 2021.

[101] J. Preskill, *Quantum computing and the entanglement frontier*, 2012.

[102] C. Monroe *et al.*, "Large-scale modular quantum-computer architecture with atomic memory and photonic interconnects," *Physical Review A*, vol. 89, no. 2, 2014.

[103] C. D. Bruzewicz, J. Chiaverini, R. McConnell, and J. M. Sage, "Trapped-ion quantum computing: Progress and challenges," *Applied Physics Reviews*, vol. 6, no. 2, p. 021 314, 2019.

[104] A. Jenkins, J. W. Lis, A. Senoo, W. F. McGrew, and A. M. Kaufman, *Ytterbium nuclear-spin qubits in an optical tweezer array*, 2021.

[105] X. Wu *et al.*, "A concise review of rydberg atom based quantum computation and quantum simulation," *Chinese Physics B*, vol. 30, no. 2, 020305, p. 020 305, 2021.

[106] J. Roffe, "Quantum error correction: An introductory guide," *Contemporary Physics*, vol. 60, no. 3, pp. 226–245, 2019.

[107] R. H. Lavroff, D. L. Pennington, A. S. Hua, B. Y. Li, J. A. Williams, and A. N. Alexandrova, "Recent innovations in solid-state and molecular qubits for quantum information applications," *The Journal of Physical Chemistry Letters*, vol. 12, no. 44, pp. 10 742–10 745, 2021, PMID: 34758627. eprint: `https://doi.org/10.1021/acs.jpclett.1c03269`.

[108] L. Anderegg *et al.*, "An optical tweezer array of ultracold molecules," *Science*, vol. 365, no. 6458, pp. 1156–1158, 2019. eprint: https://www.science.org/doi/pdf/10.1126/science.aax1265.

[109] K. H. K. K. Leung *et al.*, "Transition strength measurements to guide magic wavelength selection in optically trapped molecules," *Phys. Rev. Lett.*, vol. 125, p. 153 001, 15 2020.

[110] N. R. Hutzler, H.-I Lu, and J. M. Doyle, "The buffer gas beam: An intense, cold, and slow source for atoms and molecules," *Chem. Rev.*, vol. 112, pp. 4803–4827, 2012.

[111] J. F. Barry, D. J. McCarron, E. B. Norrgard, M. H. Steinecker, and D. DeMille, "Magneto-optical trapping of a diatomic molecule," *Nature*, vol. 512, pp. 286–289, 2014.

[112] K. Wenz, I. Kozyryev, R. L. McNally, L. Aldridge, and T. Zelevinsky, "Large molasses-like cooling forces for molecules using polychromatic optical fields: A theoretical description," *Phys. Rev. Research*, vol. 2, p. 043 377, 2020.

[113] S. D. Hogan, "Rydberg-stark deceleration of atoms and molecules," *EPJ Techniques and Instrumentation*, vol. 3, no. 1, 2016.

[114] R. E. Smalley, L. Wharton, and D. H. Levy, "Molecular optical spectroscopy with supersonic beams and jets," *Accounts of Chemical Research*, vol. 10, no. 4, pp. 139–145, 1977. eprint: https://doi.org/10.1021/ar50112a006.

[115] S. E. Galica, L. Aldridge, and E. E. Eyler, "Four-color stimulated optical forces for atomic and molecular slowing," *Physical Review A*, vol. 88, no. 4, 2013.

[116] U. Even, "Pulsed supersonic beams from high pressure source: Simulation results and experimental measurements," *dvances in Chemistry*, 2014.

[117] N. Akerman, M. Karpov, L. David, E. Lavert-Ofir, J. Narevicius, and E. Narevicius, "Simultaneous deceleration of atoms and molecules in a supersonic beam," *New Journal of Physics*, vol. 17, no. 6, p. 065 015, 2015.

[118] M. Quintero-Pérez, P. Jansen, T. E. Wall, J. E. van den Berg, S. Hoekstra, and H. L. Bethlem, "Static trapping of polar molecules in a traveling wave decelerator," *Phys. Rev. Lett.*, vol. 110, p. 133 003, 13 2013.

[119] Y. Liu *et al.*, "Magnetic trapping of cold methyl radicals," *Physical Review Letters*, vol. 118, no. 9, 2017.

[120] N. Akerman, M. Karpov, Y. Segev, N. Bibelnik, J. Narevicius, and E. Narevicius, "Trapping of molecular oxygen together with lithium atoms," *Phys. Rev. Lett.*, vol. 119, p. 073 204, 7 2017.

[121] T. E. Wall, "Preparation of cold molecules for high-precision measurements," *Journal of Physics B: Atomic, Molecular and Optical Physics*, vol. 49, no. 24, p. 243 001, 2016.

[122] M. Zeppenfeld *et al.*, "Sisyphus cooling of electrically trapped polyatomic molecules," *Nature*, vol. 491, pp. 570–573, 2012.

[123] I. Kozyryev, L. Baum, L. Aldridge, P. Yu, E. E. Eyler, and J. M. Doyle, "Coherent bichromatic force deflection of molecules," *Physical Review Letters*, vol. 120, no. 6, 2018.

[124] I. Kozyrev, "Laser cooling and inelastic collisions of the polyatomic radical sroh," *Harvard University*, 2017.

[125] Y. Takahashi, D. Shlivko, G. Woolls, and N. R. Hutzler, "Simulation of cryogenic buffer gas beams," *Phys. Rev. Research*, vol. 3, p. 023 018, 2 2021.

[126] J. F. Barry, E. S. Shuman, and D. DeMille, "A bright, slow cryogenic molecular beam source for free radicals," *Phys. Chem. Chem. Phys.*, vol. 13, pp. 18 936–18 947, 2011.

[127] P. Hamilton, M. Jaffe, P. Haslinger, Q. Simmons, H. Müller, and J. Khoury, "Atom-interferometry constraints on dark energy," *Science*, vol. 349, no. 6250, pp. 849–851, 2015.

[128] D. Greif *et al.*, "Site-resolved imaging of a fermionic mott insulator," *Science*, vol. 351, no. 6276, pp. 953–957, 2016. eprint: `https://www.science.org/doi/pdf/10.1126/science.aad9041`.

[129] Z. Davoudi, M. Hafezi, C. Monroe, G. Pagano, A. Seif, and A. Shaw, "Towards analog quantum simulations of lattice gauge theories with trapped ions," *Physical Review Research*, vol. 2, no. 2, 2020.

[130] S. M. Dickerson, J. M. Hogan, A. Sugarbaker, D. M. S. Johnson, and M. A. Kasevich, "Multiaxis inertial sensing with long-time point source atom interferometry," *Physical Review Letters*, vol. 111, no. 8, 2013.

[131] A. D. Cronin, J. Schmiedmayer, and D. E. Pritchard, "Optics and interferometry with atoms and molecules," *Rev. Mod. Phys.*, vol. 81, pp. 1051–1129, 3 2009.

[132] V. Zhelyazkova *et al.*, "Laser cooling and slowing of CaF molecules," *Physical Review A*, vol. 89, no. 5, 2014.

[133] W. Bu, T. Chen, G. Lv, and B. Yan, "Cold collision and high-resolution spectroscopy of buffer-gas-cooled BaF molecules," *Physical Review A*, vol. 95, no. 3, 2017.

[134] T. A. Isaev, S. Hoekstra, and R. Berger, "Laser-cooled RaF as a promising candidate to measure molecular parity violation," *Physical Review A*, vol. 82, no. 5, 2010.

[135] R. McNally, I. Kozyrev, S. Vazquez-Carson, K. Wenz, T. Wang, and T. Zelevinsky, "Optical cycling, radiative deflection and laser cooling of barium monohydride," *New Journal of Physics*, vol. 22, p. 083 047, 2020.

[136] J. Barry, "Laser cooling and slowing of a diatomic molecule," *Yale University*, 2013.

[137] G. Herzberg, "Spectra of diatomic molecules," *Van Nostrand Books*, 1950.

[138] E. Hulthèn, "On the band spectrum of calcium hydride," *Phys. Rev.*, vol. 29, pp. 97–111, 1 1927.

[139] W. W. Watson and W. Bender, "The zeeman effect in the red CaH bands," *Phys. Rev.*, vol. 35, pp. 1513–1523, 12 1930.

[140] s. W. G. Liberale, "The zeeman effect in the red cah bandsetude du spectre d'absorption des systemes a2-x2 et b2-x2 de l'hydrure de calcium," *Physica*, vol. 41, 47 1969.

[141] L.-E. Berg and L Klynning, "Rotational analysis of the $A - X$ and $B - X$ band systems of CaH," *Physica Scripta*, vol. 10, no. 6, pp. 331–336, 1974.

[142] L. Berg and L Klynning, "New laboratory measurements of the a-x and b-x band systems of CaH," *Astr. Astophys Suppl.*, vol. 13, pp. 325–344, 1974.

[143] R. S. Mulliken and A. Christy, "Λ-type doubling and electron configurations in diatomic molecules," *Phys. Rev.*, vol. 38, pp. 87–119, 1 1931.

[144] A. Shayesteh, S. F. Alavi, M. Rahman, and E. Gharib-Nezhad, "Ab initio transition dipole moments and potential energy curves for the low-lying electronic states of cah," *Chemical Physics Letters*, vol. 667, pp. 345–350, 2017.

[145] Wikipedia contributors, *Morse potential*, [Online; accessed 22-May-2022], 2022.

[146] S. F. Vázquez-Carson, Q. Sun, J. Dai, D. Mitra, and T. Zelevinsky, *Direct laser cooling of calcium monohydride molecules*, 2022.

[147] M. Liu, T. Pauchard, M. Sjödin, O. Launila, P. van der Meulen, and L.-E. Berg, "Time-resolved study of the $A^2\Pi$ state of CaH by laser spectroscopy," *J. Mol. Spectrosc.*, vol. 257, pp. 105–107, 2009.

[148] L.-E. Berg, K. Ekvall, and S. Kelly, "Radiative lifetime measurement of vibronic levels of the $B^2\Sigma^+$ state of CaH by laser excitation spectroscopy," *Chem. Phys. Lett.*, vol. 257, pp. 351–355, 1996.

[149] A. N. Pathak and P. D. Singh, "Franck-Condon factors and r-centroids of the CaH ($B - X$) band system," *Proc. Phys. Soc.*, vol. 87, pp. 1008–1009, 1966.

[150] M. Ramanaiah and S. Lakshman, "True potential energy curves and Franck-Condon factors of a few alkaline earth hydrides," *Physica 113C*, vol. 113, pp. 263–270, 1982.

[151] P. Bernath, *Spectra of atoms and molecules*, 1995.

[152] M. Dick, "Spectroscopy of selected calcium and strontium containing polyatomic molecules," *University of Waterloo*, 2007.

[153] J. Lim *et al.*, "Laser cooled YbF molecules for measuring the electron's electric dipole moment," *Phys. Rev. Lett.*, vol. 120, p. 123 201, 12 2018.

[154] L. Baum *et al.*, "1d magneto-optical trap of polyatomic molecules," *Phys. Rev. Lett.*, vol. 124, p. 133 201, 13 2020.

[155] G. Iwata, "A cryogenic buffer-gas cooled beam of barium monohydride for laser slowing, cooling, and trapping," *Columbia University*, 2018.

[156] G. Z. Iwata, R. L. McNally, and T. Zelevinsky, "High-resolution optical spectroscopy with a buffer-gas-cooled beam of bah molecules," *Phys. Rev. A*, vol. 96, p. 022 509, 2 2017.

[157] Wikipedia contributors, *Turbomolecular pump — Wikipedia, the free encyclopedia*, [Online; accessed 29-May-2022], 2022.

[158] H. Finesse, *Ws7-60 series high precision wavelength meter*, [Online; accessed 22-May-2022], 2021.

[159] D. R. Paschotta, *Electro-optic modulators*, [Online; accessed 22-May-2022], 2022.

[160] Wikipedia contributors, *Electro-optic modulator — Wikipedia, the free encyclopedia*, [Online; accessed 22-May-2022], 2022.

[161] D. R. Paschotta, *Acousto-optic modulators*, [Online; accessed 22-May-2022], 2022.

[162] Wikipedia contributors, *Acousto-optic modulator — Wikipedia, the free encyclopedia*, [Online; accessed 22-May-2022], 2022.

[163] W. L. B. William Henry Bragg, "The reflection of x-rays by crystals," *Proceedings of the Royal Society A*, vol. 88, 605 1913.

[164] Wikipedia contributors, *Bragg's law — Wikipedia, the free encyclopedia*, [Online; accessed 22-May-2022], 2022.

[165] Newport, *Free-space optical receiver*, [Online; accessed 29-May-2022], 2022.

[166] D. R. Paschotta, *Photomultipliers*, [Online; accessed 22-May-2022], 2022.

[167] Wikipedia contributors, *Photomultiplier tube — Wikipedia, the free encyclopedia*, [Online; accessed 22-May-2022], 2022.

[168] Unknown, *Photodetector module p30pc-01)*, [Online; accessed 22-May-2022], 2021.

[169] C. Coates and A. Mullan, *What does ccd stand for, electron multiplying camera*, [Online; accessed 22-May-2022], 2021.

[170] Coates and Mullan, *Electron multiplying charge-coupled devices (emccds)*, [Online; accessed 22-May-2022], 2021.

[171] H.-I. Lu, J. Rasmussen, M. J. Wright, D. Patterson, and J. M. Doyle, "A cold and slow molecular beam," *Phys. Chem. Chem. Phys.*, vol. 13, pp. 18 986–18 990, 2011.

[172] D. Patterson and J. M. Doyle, "Bright, guided molecular beam with hydrodynamic enhancement," *J. Chem. Physics*, vol. 126, 2007.

[173] J. F. Barry, E. S. Shuman, and D. DeMille, "A bright, slow cryogenic molecular beam source for free radicals," *Phys. Chem. Chem. Phys.*, vol. 13, pp. 18 936–18 947, 42 2011.

[174] V. Singh, *Theoretical investigation of a two-stage buffer gas cooled beam source*, 2019.

[175] I. Kozyryev, T. C. Steimle, P. Yu, D.-T. Nguyen, and J. M. Doyle, "Determination of CaOH and CaOCHsub3/sub vibrational branching ratios for direct laser cooling and trapping," *New Journal of Physics*, vol. 21, no. 5, p. 052 002, 2019.

[176] B. K. Stuhl, B. C. Sawyer, D. Wang, and J. Ye, "Magneto-optical trap for polar molecules," *Phys. Rev. Lett.*, vol. 101, p. 243 002, 24 2008.

[177] M. D. D. Rosa, "Laser-cooling molecules: Concept, candidates, and supporting hyperfine-resolved measurements of rotational lines in the $A - X(0,0)$ band of CaH," *The European Physical Journal D*, vol. 31, pp. 395–402, 2004.

[178] Y. Wu, J. J. Burau, K. Mehling, J. Ye, and S. Ding, "High phase-space density of laser-cooled molecules in an optical lattice," *Phys. Rev. Lett.*, vol. 127, p. 263 201, 26 2021.

[179] Y. Gao and T. Gao, "Laser cooling of the alkaline-earth-metal monohydrides: Insights from an ab initio theory study," *Phys. Rev. A*, vol. 90, 2014.

[180] P. S. Harold J. Metcalf, "Laser cooling and trapping," 1999.

[181] K. D. F. D. D. P. Budker D., "Atomic physics : An exploration through problems and solutions," 2004.

[182] E. L. Raab, M. Prentiss, A. Cable, S. Chu, and D. E. Pritchard, "Trapping of neutral sodium atoms with radiation pressure," *Phys. Rev. Lett.*, vol. 59, pp. 2631–2634, 23 1987.

[183] W. D. Phillips, "Nobel lecture: Laser cooling and trapping of neutral atoms," *Rev. Mod. Phys.*, vol. 70, pp. 721–741, 1998.

[184] I. Bloch, J. Dalibard, and W. Zwerger, "Many-body physics with ultracold gases," *Rev. Mod. Phys.*, vol. 80, pp. 885–964, 3 2008.

[185] M. Morgado and S. Whitlock, "Quantum simulation and computing with Rydberg-interacting qubits," *AVS Quantum Sci.*, vol. 3, p. 023 501, 2021.

[186] T. Bothwell *et al.*, "Resolving the gravitational redshift across a millimetre-scale atomic sample," *Nature*, vol. 602, pp. 420–424, 2022.

[187] M. S. Safronova, D. Budker, D. DeMille, D. F. J. Kimball, A. Derevianko, and C. W. Clark, "Search for new physics with atoms and molecules," *Rev. Mod. Phys.*, vol. 90, p. 025 008, 2 2018.

[188] M. R. Tarbutt, "Laser cooling of molecules," *Contemp. Phys.*, vol. 59, pp. 356–376, 2018.

[189] S. Ding, Y. Wu, I. A. Finneran, J. J. Burau, and J. Ye, "Sub-Doppler cooling and compressed trapping of YO molecules at μK temperatures," *Phys. Rev. X*, vol. 10, p. 021 049, 2 2020.